Low-energy beam preparation for the next generation antimatter experiments

Thesis submitted in accordance with the requirements of the University of Liverpool for the degree of Doctor in Philosophy

2023

Volodymyr Rodin

Acknowledgements

My Ph.D. project became possible only thanks to many people that I had met along the way. Thanks to their inspiration, knowledge and expertise, but also their support helped me reach this point.

First of all, I would like to express sincere gratitude to Prof. Dr. Carsten Peter Welsch, my supervisor, for creating the AVA network. He provided me with an excellent opportunity to initiate and accomplish this exciting work. I also would like to extend my deepest gratitude to my supervisor Dr. Javier Resta-López for his continuous support and friendly guidance on this route for many years. A special thanks go to my supervisor Dr. Aaron Farricker who was always patient and helpful, bringing valuable improvements and comments. I had spent fantastic years with members of the QUASAR group and AVA fellows.

I would especially acknowledge James Robert Hunt, with whom I had the absolute pleasure of resolving the same challenges and with whom I shared great results and enjoyable times. I want to thank Milena, my great friend and office mate at Cockcroft Institute, who puzzled and inspired me from time to time. Ewa for all the great discussions that we had and all the fruitful requests for code improvement.

I am extending my gratitude to all my collaborators outside the UK, who believed in my ideas and helped in their further implementation, A. Kainz and W. Hortschitz from TU Wien, W. Bartmann, M. Doser and G. Khatri from CERN, code developers A. Oeftiger from GSI (PyHEADTAIL) and D. Sagan from Cornell (BMAD).

Finally, I would like to thank my family for their support and understanding during this project timeline. Thank you, especially to my twin brother Viktor Rodin for helpful discussions, review and feedback on parts of my work, and mom for always being there for me and pushing me to be my very best.

Abstract

Antimatter production facilities can serve as unique tools for examining fundamental physical theories and potential practical applications of antiparticles. Currently, Extra Low ENergy Antiproton (ELENA) ring at CERN's Antimatter Factory is the only place that provides low-energy (100 keV) antiprotons worldwide. Its deceleration capabilities provided a substantial efficiency increase for operating experiments by enabling capturing up to $\sim 60\%$ of the provided beam. However, recently proposed antimatter studies placed new requirements on the beam properties, such as ultra-short bunches or even lower beam energy (<10 keV), enhancing the impact of machine imperfections and collective effects. This introduced the necessity of developing more realistic tracking simulations for electrostatic storage rings, beam lines, and experiments to predict the behaviour of the beam under various conditions accurately and to gain a better understanding of the primary factors that limit beam lifetimes.

New simulation methods have been developed and employed on the electrostatic transfer lines, experiments from Antimatter Factory, and the ELENA storage ring to address this need. First, beam guiding elements were simulated to produce realistic 3D field maps. Some of them were simplified if there was no loss of tracking details. A state-of-art field measurement technique was proposed to benchmark quadrupole design and simulation results to ensure the quality of a model of electrostatic quadrupole from ELENA beam lines. A realistic 6D tracking simulation of the transfer line to the ALPHA experiment built in G4beamline and BMAD demonstrated perfect agreement with design models created in MAD-X, where the description of optical elements is simplified. Models have also shown the possibility of simultaneous dynamic tracking in multiple beam lines under the impact of a magnetic field produced by other experiments.

An interaction of low-energy antiprotons with light and heavy nuclear targets can provide fundamental knowledge about differential cross sections and nucleon densities. A light nucleus like helium is a perfect benchmark tool for studying dynamics inside the

many-body Coulomb problem since the number of possible reaction channels is limited. Such studies require ultra-short antiproton bunches ($\sim$1 ns) as a zero-time trigger for the setups utilizing a reaction microscope. Two routes were studied to achieve the desired bunch length. One demonstrated the feasibility of short bunch formation (1 ns r.m.s) using a single-pass experiment installed in the ALPHA transfer line, confirmed by tracking in G4beamline and BMAD. The more efficient but technically challenging path is based on collisions with an inner target embedded within the ELENA ring. It was demonstrated that the ELENA RF system can reduce bunch length from 75 to $<$5 ns r.m.s. Ultra-short antiproton bunches were observed to remain in equilibrium storage conditions if bunch intensities are kept below $\sim 3 \times 10^5$ to avoid the strong beam heating effects, e.g., space charge and intrabeam scattering (IBS).

For the near future experiments with bound systems of antiprotons and medium mass nuclei, a low-energy ($<$5 keV) injection system for the AEgIS experiment was designed and simulated. This will allow studying of properties of atomic nuclei and fragmentation processes with improved precision and extended lifetimes. The created beam line structure is also suitable for cold antiproton beam extraction into portable traps to facilitate antimatter experiments outside CERN.

Contents

Chapter 1

Introduction

1.1 Introduction

History taught us that one possible way to learn the structure of matter is to crack it with a highly energetic "hammer" - an elementary particle. Later on, researchers revealed the fact that faster is not always better. Neutrons and antiparticles demonstrated that unique processes happen at low energies - nuclear fission and low-energy annihilation. But before all these discoveries, many other fundamental bricks of the Standard Model were predicted theoretically. Dirac made the first prediction of an antiparticle in 1928 [1], and four years later, Anderson confirmed the existence of the positron experimentally. A few decades later, this particle finds a practical application in Positron Emission Tomography (PET) and Positron Annihilation Spectroscopy (PAS). In order to create the first anti-nucleon, the machine, according to the kinetic calculations, needs to provide kinetic energy of 6 m_p =5.6 GeV, where m_p =938.3 MeV is the rest energy of the proton. Thus the first antiprotons were discovered in 1955 at the Bevatron at Berkeley. Later, it was discovered that the actual production threshold in fixed targets is even lower (3.5 GeV if Cu) due to the presence of Fermi motion of the nucleons within target atoms. The detection of antiprotons ($\bar{p}$) was done via momen-

tum and time-of-flight (ToF) identification since most of the secondary particles from collisions were negatively charged mesons, produced in the reaction with higher momentum. The following year after $\bar{p}$ discovery, the antineutron, $\bar{n}$, was also identified at Berkeley, and today, for any new elementary particle, the corresponding antiparticle has also been found. The discovery of the first anti-atoms was first reported in 1965 [2, 3] at CERN, which however, passed entirely unnoticed until 1995 [4]. Researchers at CERN announced that they had successfully formed the first antihydrogen atoms at the Low Energy Antiproton Ring (LEAR) [5]. The antiprotons were circulating inside LEAR until collision with a heavy element target. Any antiprotons passing at a short distance to heavy atomic nuclei may create an electron-positron pair, and with low probability, the antiproton could bind with the positron to form an atom of antihydrogen. These antiparticles were highly energetic, travelling almost at the speed of light over a distance of 10 metres and then experiencing annihilation with ordinary matter. While creating the antihydrogen was a significant achievement, the atoms were too energetic — too "hot"— and did not lend themselves to be easy prey for study. It was required to perform meaningful and precise atomic collision experiments to understand the properties of an antiproton and anti-atom interaction.

1.2 Study of atomic and nuclear properties via particle collisions

More than a century ago, Rutherford performed his famous experiment [6], which marked the beginning of ion-atom collision research and holds fundamental significance for the development of modern physics, Fig. 1.1. It paved the way for a solid understanding of atomic structure. Initially, a "planetary" atomic model emerged from experimental observations, which could not explain the stability of atoms. However, with the development of quantum mechanics, this problem was resolved and atomic structure can now be regarded as being conceptually understood.

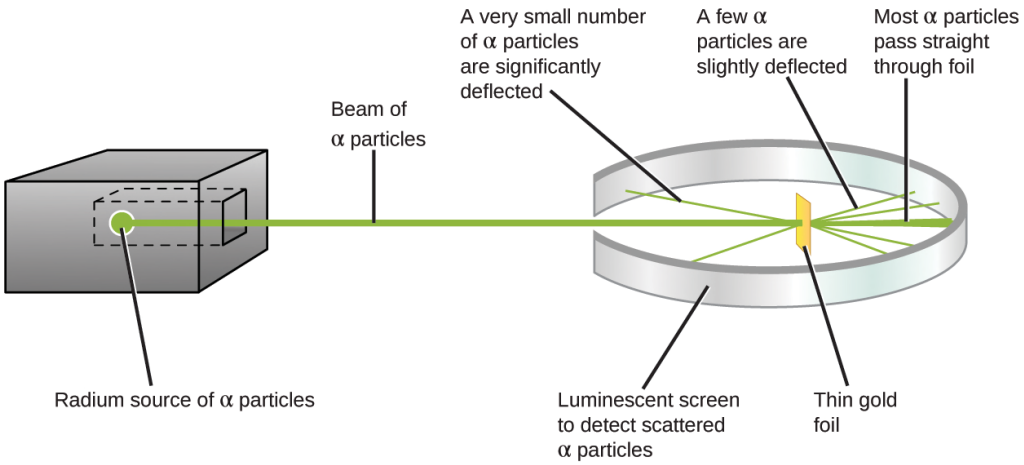

Figure 1.1: *Geiger and Rutherford fired α particles at a piece of gold foil and detected where those particles went [7].*

In the same way, an antiproton is a unique probe for atomic physics research. Having the same mass as the proton but with an opposite charge, it behaves as a "heavy electron" or as a "negative nucleus". This antiparticle gives a new test ground for studies of atomic collision dynamics and exotic atom formation. It is also known as a "theoretician's ideal projectile" because the lack of electron capture processes avoids complications in theoretical treatments. But to do these, one needs an antiproton beam of well-defined kinetic energy in the keV to MeV regime. This was not exactly the case in the 1960s.

1.2.1 Low energy region of interest. Antimatter physics.

Many experiments had been carried out with low-energy antiprotons at that time, in particular at Brookhaven and CERN in the 1960s and 1970s. However, in these early experiments, the antiprotons were part of secondary beams containing many negatively-charged pions and kaons and had a large momentum spread. Accordingly, antiproton beams need to be collected, slowed down and focused, which is also led to further beam growth. In the 1970s, Simon van der Meer and his colleagues at CERN and elsewhere imagined and developed the stochastic cooling method [8], which helped produce antiproton beams of high purity, sharp momentum resolution, and much higher

intensity than in the previous devices. The advent of cooling techniques in the 1980s changed this situation dramatically [9, 10]. It opened the door to fascinating studies in fields of matter-antimatter symmetry [11], first experiments related to ionisation of atoms or molecules by antiparticle impact [12], antiprotonic atom spectroscopy [13] and antimatter gravity [14]. In 1986 the first capture of antiprotons in a Penning trap for 100 s happened using 21 MeV antiprotons from the LEAR [15].

1.3 History of antimatter production at CERN

In the past, the antiproton production cycle was as follows: 1) antiprotons were produced by 26 GeV/c protons from the CERN Proton Synchrotron (PS) hitting an external target; 2) then they were then collected at their production optimum at 3.5 GeV/c in the Antiproton Collector(AC), then cooled and stored in the Antiproton Accumulator (AA), decelerated in the PS to 0.6 GeV/c before being transferred to LEAR. The antiprotons for LEAR were typically in a bunch of up to 3×10^9 particles. After

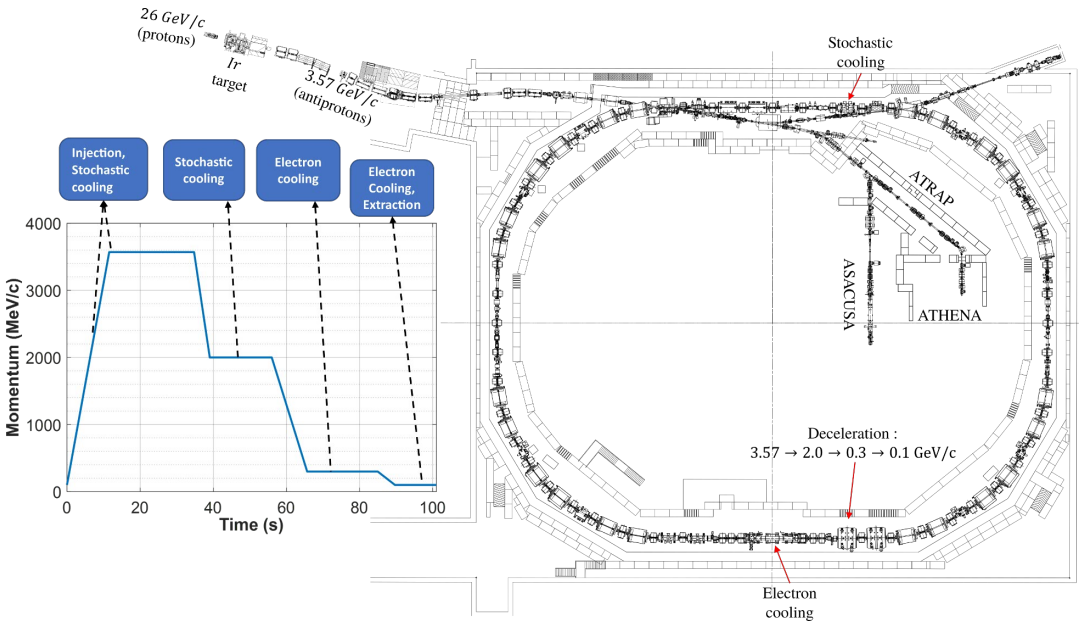

Figure 1.2: *Layout of the AD ring with its working cycle. Created using sketches sourced from [16].*

stochastic and electron cooling in LEAR, to improve the beam quality, the beam was either accelerated or decelerated to the required ejection momentum, ranging from 100 MeV/c to 1700 MeV/c. This ring was in operation from 1982 to 1996 for antiproton beams, and in 2000 it was replaced by the Antiproton Decelerator (AD), a cost-effective modification of the AC ring, which is still online. Figure 1.2 demonstrates the layout of the AD ring with the first set of experiments in 2005. The operation cycle on the left demonstrates the deceleration and cooling time periods.

The first experiments at the AD were mostly focused on a more efficient way to create and study antihydrogen atoms. The first two experiments, ATHENA (ApparaTus for High precision Experiments with Neutral Antimatter) [17] and ATRAP (Antiproton TRAP) [18] utilised improved techniques from the earlier TRAP experiment [15].

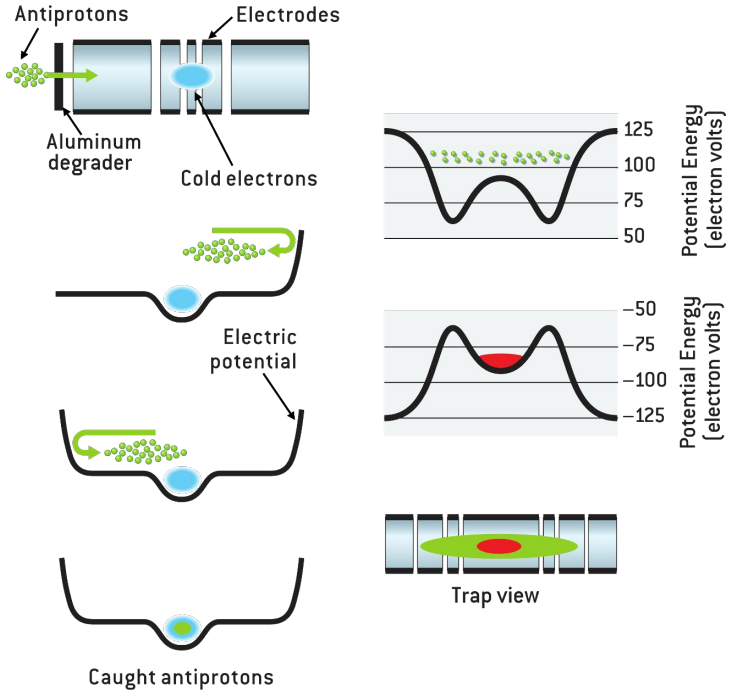

Figure 1.3: *Principles of antiproton trapping (left) and basic scheme of antihydrogen formation (right). (Adapted from [19].)*

To create cold antihydrogen in a controlled way, three particle species were required. At first, low-energy electrons were injected and confined inside the trap. After-

wards, the antiproton bunch from the AD was decelerated by aluminum degraders and negative potential before being captured. Electrons were used to cool down antiprotons in a similar way as in electron cooling. Then cold antiprotons were mixed together with positrons (possible reactions will be explained in a later Section 1.5). Thus, in order to operate with multiple species simultaneously, traps are usually designed with the ability to create a number of potential wells.

This working principle of particle mixing, displayed in Fig. 1.3, was pioneered by the ATRAP group and its predecessor, TRAP.

The third experiment, ASACUSA (Antiproton Spectroscopy And Collisions Using Slow Antiprotons) [20], was approved to study the formation of the antiproton-bound systems, energy loss for low-energy antiprotons, and ionisation processes involving antiprotons. ASACUSA has been utilising laser and microwave spectroscopy methods to characterise the properties of antihydrogen and antiprotonic systems.

1.4 Extra Low ENergy Antiproton (ELENA) ring

The creation of the cold antihydrogen and its further experimental study in AD configuration had tolerated two major drawbacks. The first one was a considerable inefficiency in terms of utilised antiproton beam: from initial 3×10^7 5.3 MeV antiprotons only 30,000 were trapped (0.1% efficiency) using degrader foils before a particle trap.

For example, to overcome this issue, in ASACUSA it was decided from the beginning to decelerate the antiproton bunch even further, below 120 keV. As a result, the total number of antiprotons available for the studies at ASACUSA was one to two orders of magnitude larger than for ATHENA or ATRAP. The second issue was the arrangement of beam delivery. A bunch of antiprotons extracted from AD was transported to only one experiment, switching to another experiment every eight hours.

A crucial solution for these problems was the design and construction of a smaller deceleration Extra Low ENergy Antiproton (ELENA) ring [21], whose layout is shown in Fig. 1.4. ELENA decelerates antiprotons further from 5.3 MeV to 100 keV applying

electron cooling technique to maintain beam quality. This extra step down significantly increased the number of trapped antiprotons by factor 100 for ATHENA, ATRAP and by factor 10 for ASACUSA.

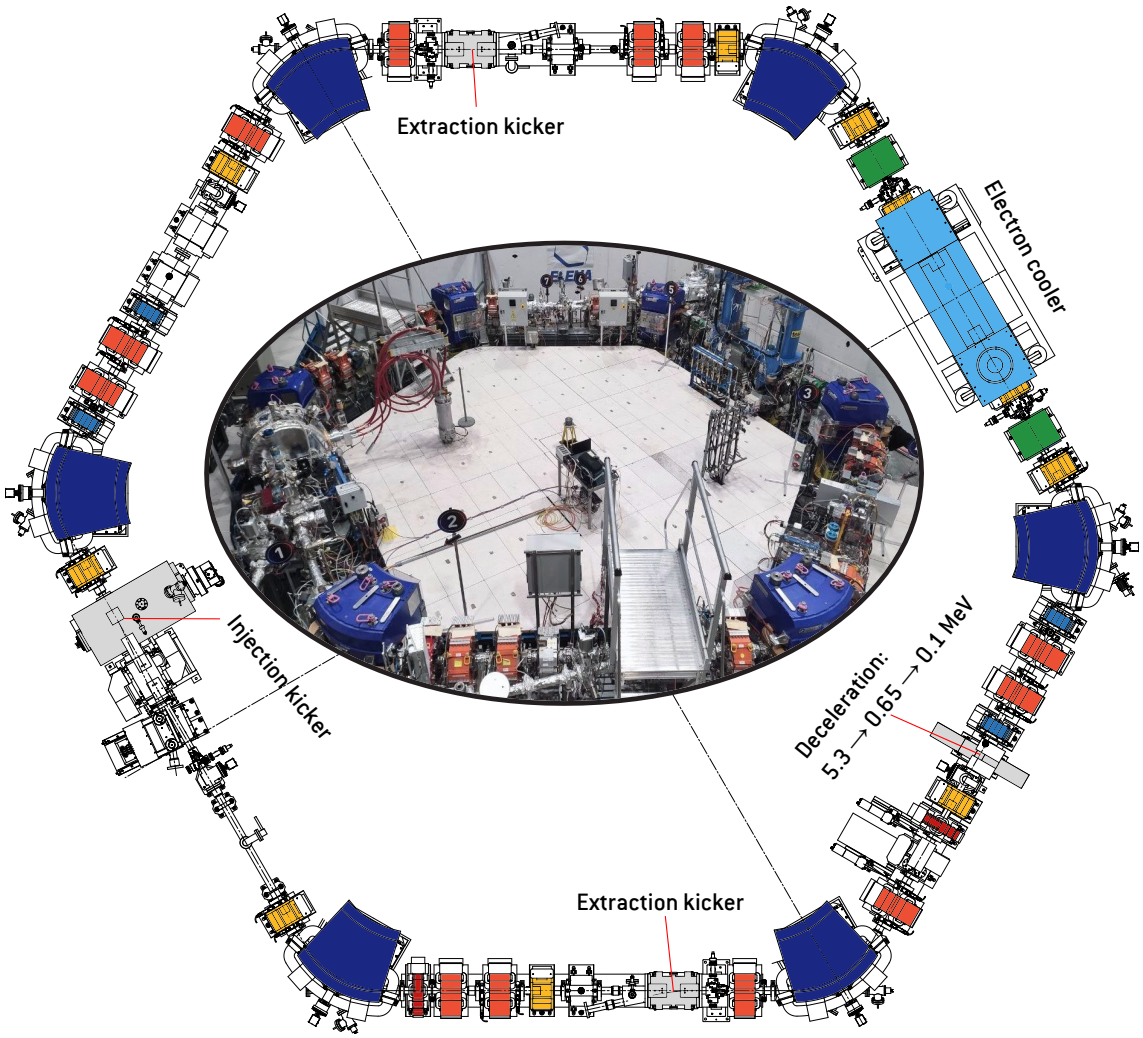

Figure 1.4: *Modified sketch and photo of the ELENA ring (private photo gallery). Created using drawings sourced from [22]. The colour of the elements represents different magnet families [23].*

Its operational cycle is similar to the second half of the AD cycle, Fig. 1.5. The bunch from AD is injected into ELENA where it is firstly decelerated to an intermediate plateau at 650 keV. After approximately four seconds of electron cooling, the antiproton beam is decelerated further to 100 keV. Finally, after three seconds of cool-

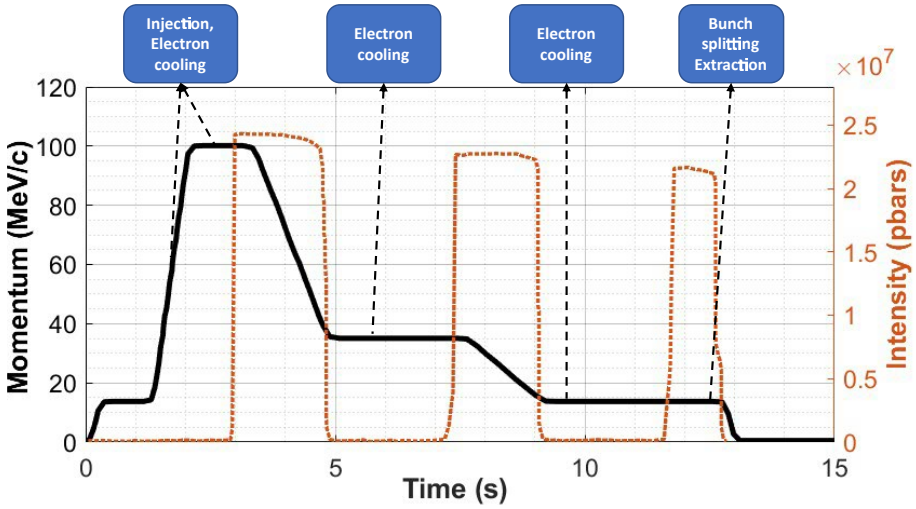

Figure 1.5: *An example of ELENA working cycle nowadays together with antiproton beam intensity.*

ing time, antiprotons are bunched and ready for extraction. Additionally, this ring can similarly operate with hydrogen anions produced from an embedded ion source. This allows machine optimisation and commissioning even without antiprotons.

The problem with beam availability for multiple experiments was solved by the extraction of multiple bunches in one turn (design value is 4) using two kickers shown on the scheme. This approach allows almost unlimited time for antimatter physics for a few experiments (depending on the number of bunches and requested intensity per shot). Further, to deliver these bunches to experiments in a more efficient way, a new design of transfer lines was proposed, which is briefly explained in the next section.

1.5 Experiments with antimatter nowadays

The new extraction capabilities of ELENA were fully utilised through a set of electrostatic beam lines installed during CERN's Long Shutdown 2 (LS2) phase. The full sketch with an earlier ELENA ring is demonstrated in Fig. 1.6. Additionally, this scheme includes elements that steer bunches in a vertical plane. This is especially beneficial for experiments on antimatter interaction with Earth's gravitational field. At

the time of writing, most branches were in the commissioning phase using antiprotons and hydrogen anions.

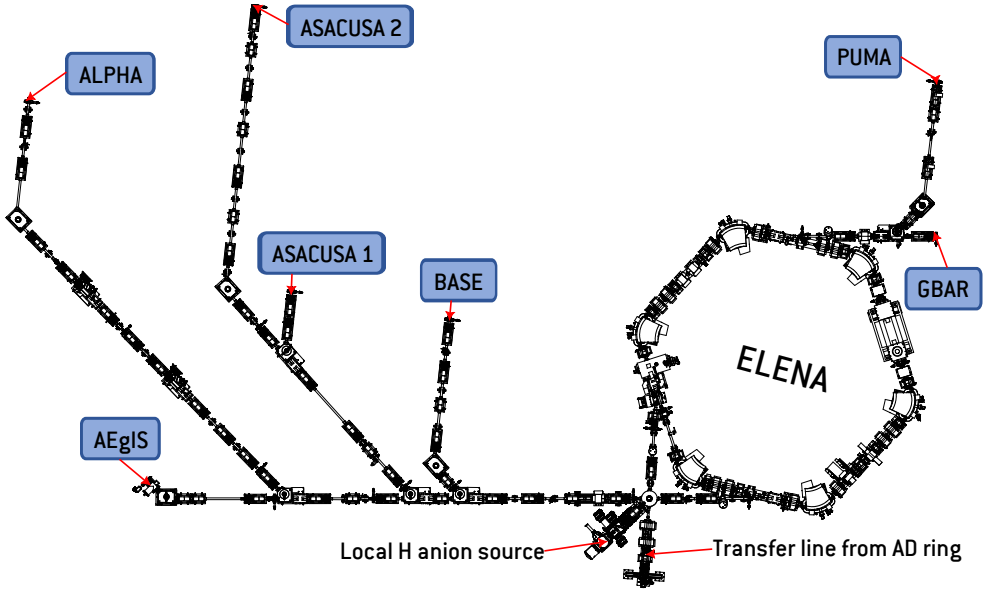

Figure 1.6: *Layout of extraction transfer lines from ELENA. Brunches to currently operating and planned experiments are highlighted.*

From experiments shown in Fig. 1.6, only ASACUSA remained in place and Antihydrogen Laser PHysics Apparatus (ALPHA)[24] was partially formed by the ATHENA team when that experiment concluded. They have been joined by Antihydrogen Experiment: Gravity Interferometry Spectroscopy (AEgIS)[25] with an aim to measure the gravitational interaction of antimatter. Another experiment with the same goal is the Gravitational Behaviour of Antihydrogen at Rest (GBAR)[26], which was used for the first ELENA commissioning period. The last in the list of currently installed experiments is the Baryon Antibaryon Symmetry Experiment (BASE)[27], which focuses on the high-precision measurements and comparison of the antiproton-to-proton charge-to-mass ratio as well as their magnetic moments. The newly approved experiment, the antiProton Unstable Matter Annihilation (PUMA)[28] experiment, is in the construction phase. It will focus on the studies of the interaction of trapped antiprotons with exotic heavy nuclei. It is also worth mentioning that the experimental goals of BASE (sub-project STEP[29]) and PUMA include the development of portable

traps for antiprotons. The timeline of previously mentioned experiments and machines utilised for antimatter studies is presented in Fig. 1.7.

The majority of these experiments require antihydrogen for their studies. It can be produced in several ways that may also require fulfilling certain conditions. Below are listed commonly utilised reactions for synthesis,

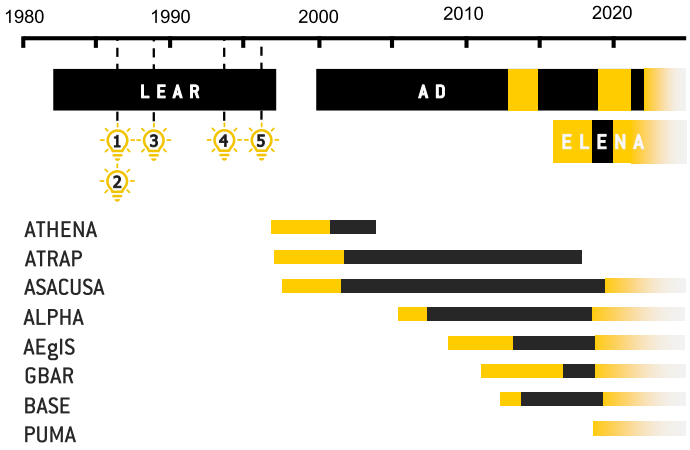

Figure 1.7: *Timeline of antimatter production experiments. Orange bars demonstrate approval and commissioning periods for machines and experiments; black bars represent operational periods. The light bulbs show several groundbreaking studies during the LEAR time. 1) (1986), first antiproton trapping [15]; 2) (1986), first atomic collision with slow antiprotons [30]; 3) (1988), magnetic moment measurements of antiprotons (using X-rays from Pb) [31]; 4) (1994), the first laser spectroscopy of antiprotonic He^* atom [32]; and 5) (1996), the first observation of fast $\bar{H}$ [4].*

- **Spontaneous recombination process**: for this reaction,

  $$\bar{p} + e^+ \longrightarrow \bar{H} + h\nu,$$

  $\bar{H}$ is formed in binary collisions between $\bar{p}$ and e^+ which is also accompanied by the emission of a photon that carries away the excess energy and momentum. The cross section of this process is small, for 1 eV antiprotons it is only 5×10^{-21} cm^2.

- **Laser induced recombination process**: in this reaction, a laser is applied to stimulate the recombination,

  $$\bar{p} + e^+ + h\nu \longrightarrow \bar{H}^* + 2h\nu,$$

  in which the antihydrogen formation rate in a particular quantum n-state is in-

creased by illuminating the interaction region with photons of appropriate energy $h\nu$ corresponding to this state ("*" denotes a Rydberg atom, like He^* in [32]). This method improves the initial cross section by two orders of magnitude.

- **Three-body recombination process**: involves an extra positron,

  $$\bar{p} + e^+ + e^+ \longrightarrow \bar{H} + e^+.$$

  Here excess energy and momentum are carried away by a positron. It requires high-density positron plasma and was successfully adopted by ATHENA, ATRAP and ASACUSA to produce the first antihydrogen atoms. Production rates have a strong dependence on the positron plasma temperature and a quadratic dependence on its density, $\rho_{e^+}^2 T_{e^+}^{-9/2}$, for which, however, production rates of 10^3 $\bar{H}$/s can be reached with $\mathcal{O}(10^5)$ antiprotons interacting with $\mathcal{O}(10^6)$ positrons.

- **Resonant charge-exchange**: which is also a three-body recombination process,

  $$\bar{p} + Ps^* \longrightarrow \bar{H}^* + e^-,$$

  involving positronium (Ps^*), the bound system of a positron and an electron (e^+e^-). This reaction was experimentally verified at ATRAP. The GBAR and AEgIS are also planning to utilise this reaction to create cold $\bar{H}$ for their studies. This scheme has a cross section of 10^{-16} cm^2, that however increases as $\propto n^4$ for a Ps^* occupying the excited state n. Therefore in practice, the cross section can reach values close to 10^{-8} cm^2. Other advantages of this process are the ability to choose the required n state and the significantly lower temperature of the resultant $\bar{H}$.

A further challenge after antihydrogen synthesis is how to study this "fragile" substance, annihilating after any interaction with the surrounding material. In this respect, experiments had been divided into two categories: performing a dynamic study of anti-atoms in-flight and magnetic capture inside an atomic trap for further investigation. The first approach had been employed by ATRAP, ATHENA, ASACUSA and AEgIS. One of the sub-branches of this method is a capture of further ionised antihydrogen, which was utilised by ATRAP [18]. One of the potential wells inside the

trap was carefully shaped so that its electric field ensures that no background $\bar{p}$ can be trapped except resulting from field ionisation of antihydrogen. GBAR also plans to trap ionised antihydrogen, $\bar{H}^+$, although in their case these ions will be produced via a two-step reaction process: 1) $(\bar{p} + Ps^* \longrightarrow \bar{H} + e^-)$ and 2) $(\bar{H} + Ps^* \longrightarrow \bar{H}^+ + e^-)$.

Magnetic capture of antihydrogen was accomplished on the same principles as with its common counterpart. The hydrogen atom possesses a small permanent magnetic dipole moment due to the spin of an electron. For antihydrogen atoms in an excited state, this magnetic moment increases even more, and thus, they can be trapped more easily. Similarly to hydrogen [33], $\bar{H}$ has two possible orientations, the so-called "low-field-seeking" (LFS) and "high-field-seeking" (HFS) states, depending on its spin orientation. The energies of the atoms in LFS states increase with the rise of the magnetic field of the trap so they tend to gather at the centre where the field is minimum. Conversely, the HFS states are pushed from the field minimum and can be ejected from the trap.

There are a few possible magnetic field configurations for trapping neutral atoms [34]. ALPHA and ATRAP experiments had chosen Ioffe–Pritchard trap design for their studies (Fig. 1c in [34]). It consists of so-called "pinch" coils with the same current direction combined with a multipole field for radial confinement of either one or both states. It creates a magnetic well with $\sim 1\,\mathrm{T}$ suitable for trapping LFS antihydrogen states. Instead, ASACUSA decided to utilise the so-called "cusp" magnet configuration (Fig. 1a in [34]), including initially two coils in the anti-Helmholtz configuration ($\uparrow\downarrow$ - current direction) and later upgraded to double "cusp" magnet with four coils. There are several reasons/advantages why this system was picked. First of all, it allows the investigation of both LFS and HFS states, resulting in a spin-polarised beam. Additionally, high-precision spectroscopy requires the absence of a magnetic field, which is achieved via the ASACUSA setup. Also, it allows a simple extension of the configuration via adding another set of coils, improving particle trapping efficiency and antihydrogen formation. In principle, it allows the confinement of neutral atoms in quantum states with large n numbers.

AEgIS has a similar approach concerning studies on the behaviour of antiprotons and antihydrogen in gravity. This experiment demonstrated the ability to resolve forces, acting on low-energy antiprotons, with high precision. It was done via passing antiprotons, which were released from the trap, through a Moiré deflectometer [35]. Comparison of the interference pattern from antiprotons against a pattern from photons gives a hint about the presence of an external force in a certain direction (impact of a magnetic field in [35]). The same exercise is planned to be performed with cold antihydrogen to demonstrate the impact of gravity in a field-free region. Also, recent experiment developments aim to create and study heavy antiprotonic atoms.

The last goal is set as a cornerstone of future PUMA studies. This project plans to capture decelerated antiprotons in a portable Penning trap setup and cool them down via electron cooling. After trapping around one billion antiprotons, the particle trap will be transported to the ISOLDE complex [36] at CERN. This facility can provide a wide range of exotic isotopes that PUMA targets. Different ion beams will be produced via varying target materials and their further conversion into positive(negative) ions for trapping with antiprotons. Mixing and cooling of nuclides with antiprotons will result in the formation of unstable antiprotonic atoms. utilising the decay of such antiprotonic systems through the annihilation of the antiproton with one of the nucleons on the nuclear surface, PUMA aims to provide a detailed characterisation of the neutron-to-proton structure of the nuclei of interest.

AEgIS experiment has a similar sub-project which will demonstrate proof-of-principle of such study with easily attainable ion species such as iodine or caesium. The decay of antiprotonic bound systems with selected nuclides can be easily detected and utilised for the characterisation of atomic nuclei [37]. Bunches of ions can be injected from a locally installed source. However, it requires a compact low-energy injection beam line and deceleration to trappable energies.

Future antimatter studies will require an even colder antihydrogen plasma for better precision. It is possible to decrease the energy of positrons and antiprotons via sympathetic cooling, as proposed by GBAR and demonstrated by ALPHA for positrons

[38]. In order to utilise the full capabilities of this technique, particle traps will need to be upgraded to a magneto-optic trap (MOT) configuration, applied originally for studying the ultra-cold matter (ions [39, 40] and molecules [41]). It will require a flexible laser system and source of ions for sympathetic and laser cooling.

Parenthetically, the interaction of antiprotons with different nuclides belongs to the unmarked territory, where collisions with light ions present a fundamental example of a few-body problem [42], a probe microscope for the structure of heavy ions and a perfect tool for theory benchmarks. Therefore, research facilities operating low-energy heavy-ion storage rings expressed a strong interest in the usage of antiprotons as the only missing ingredient.

1.6 Low-energy beams in heavy-ion storage rings

1.6.1 CSR

One of the suitable research places is the Cryostatic Storage Ring (CSR) [43] at the Max Planck Institute for Nuclear Physics in Heidelberg, which was proposed and constructed for collisional and laser-interaction studies over long storage periods with fast atomic, molecular, and cluster ion beams. CSR consists of four long sections, optimised for in-ring experiments, linked in a quadratic configuration, Fig. 1.8. All beam-guiding components of the ring are electrostatic, which is sufficient for operation in 20-300 keV energy range per charge unit. One of the straight regions contains an electron cooler in the middle. Besides the electron cooling option, the merged electron-beam device can be employed for electron-ion collision studies. Another section can be utilised for laser crossing or merging of a neutral beam with the circulating particles. One of the sections is dedicated to beam diagnostics devices. The last straight section is appointed for investigating collisional studies of the circulating ion beam with an integrated “reaction microscope” that serves as a sensitive detector for electrons and recoil fragments coming from a crossed-beam interaction area.

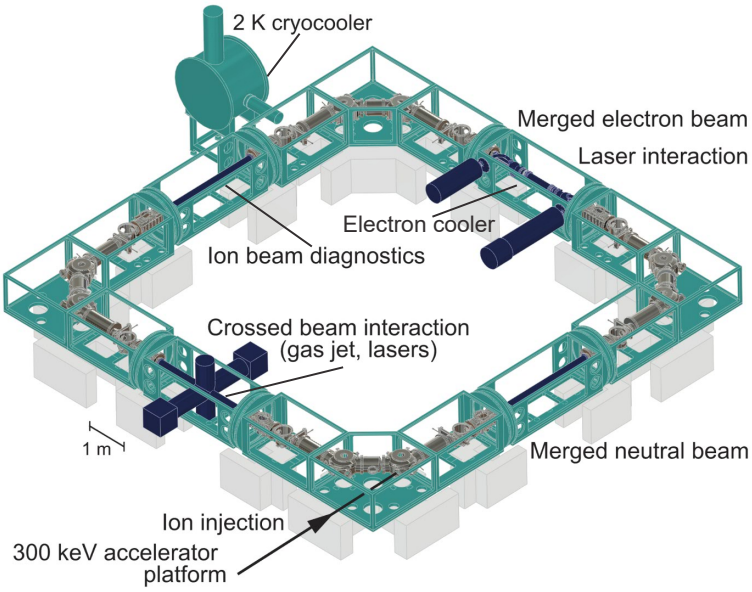

Figure 1.8: *Design structure of the CSR showing the main sections of the ring: the injection line, the electron cooler, and the location for the reaction microscope/laser system. Adapted from [43].*

Ring commissioning was also performed with (20-300 keV) low-energy protons, revealing the sensitivity of the circulating beam to Earth's magnetic field. To compensate for this, CSR is additionally equipped with vertical steering devices in beam-focusing assemblies.

Such powerful research capabilities create an outstanding platform for antimatter studies. Despite the fact that antiproton production infrastructure is missing in Heidelberg, one of the possible ways is to follow the ideas of PUMA and BASE-STEP and bring portable traps for injecting antiprotons inside CSR.

1.6.2 CRYRING@ESR

Another low-energy storage ring for heavy ions and protons, CRYsis-synchrotron-storage-RING (CRYRING) [44], was installed in 2013-2016 at the GSI accelerator complex in Darmstadt. Initially, it was constructed and operated from 1991 to 2010 at the Manne Siegbahn Laboratory at Stockholm University. In 2012 the storage ring was dismantled and shipped to Darmstadt as a Swedish in-kind contribution to

the FAIR project [45]. Currently, CRYRING is tailored with the existing Experimental Storage Ring (ESR)[46], which provides all naturally occurring elements in a range of charge states and energies (4 MeV/u to 500 MeV/u) - a project which is titled CRYRING@ESR.

Starting from the highest injection energy 30 MeV for protons, the CRYRING can further store, cool and decelerate particles down to 100 keV/u. An illustration of the present structure of this ring is displayed in Fig. 1.9. Similar to previously discussed machines, an embedded electron cooler compensates for beam growth after deceleration or serves as a dense electron target. On the opposite side of the electron cooler, an inner target is planned to be installed. It can be a thin metallic foil, droplet, or mentioned earlier, a reaction microscope. Additionally, a laser laboratory is under construction for atomic laser-spectroscopy experiments in visible and UV spectra. At

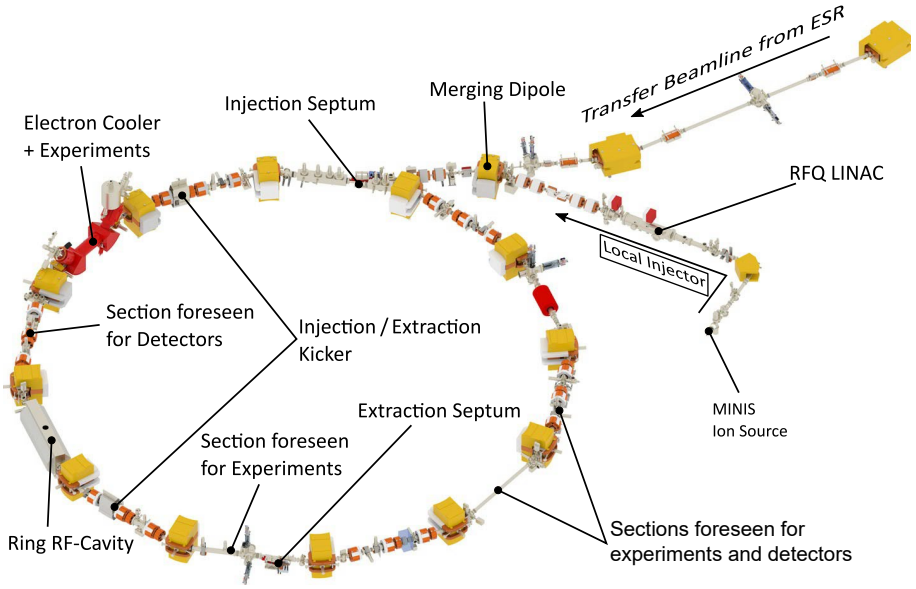

Figure 1.9: *Layout overview of the CRYRING@ESR facility demonstrating the injection line from ESR, the electron cooler, and locations for future experiments. Adapted from [44].*

the present moment, CRYRING does not have a source of low-energy antiprotons. At the FAIR project, the low-energy antiproton beam can be obtained by the use of the accelerator chain of High Energy Storage Ring (HESR), ESR and CRYRING, after

the construction of a dedicated transfer beam line from the HESR to the ESR [47, 48]. It may give a second wind to Low-energy Antiproton and Ion Research (FLAIR) collaboration project [49], which might get realised at the CRYRING@ESR facility.

Initially, the CRYRING was envisaged as a mid-to low-energy storage ring (LSR)[50] for antiprotons and ions as part of the FLAIR experimental complex of FAIR. FLAIR was proposed in 2004 to be the next-generation research facility for physics with low-energy antiprotons and antimatter, supplying antiprotons in energy from tens of MeV down to rest. A completely electrostatic ring, the Ultra-low energy Storage Ring (USR) [51] was developed to provide cooled beams of antiprotons and ions in the energy range of between 20-300 keV. The designed layout of the USR ring closely resembled the CSR ring, which was supposed to be its prototype. Given the success of the ELENA ring, which has effectively met the current demands of the antimatter research community, the potential outcomes for the FLAIR and USR projects remain uncertain.

1.6.3 Future plans: ultra-short bunches for exotic physics.

One of the main USR design goals was to provide ultra-short bunches in 1-5 ns regime as a trigger signal for the experiments within the embedded reaction microscope. For instance, it creates the possibility for correlated dynamics study of ionisation of He atoms by low-energy antiprotons, which may produce clean electromagnetic and sufficiently strong half-cycle pulses with a duration of a few femtoseconds down to a few tens of attoseconds [52, 53]. Such ultra-short XUV light pulses are of huge interest to unravel physical and chemical dynamical processes in matter with extraordinary time resolution. The lower energy is also preferable due to the large momentum spread of the 300 keV bunch. The stable operation strategy for 20 keV bunch compression can possibly be achieved with a set of procedures described in [54].

Finally, another unexplored and exotic study that can be performed with ultra-short antimatter pulses is the possibility of nuclear micro-fission/fusion, catalysed via the enormous energy released from the annihilation process [55, 56], ICAN-II space

project as an example [57].

1.7 Project aims and outline

The primary goal of this project is the optimisation of existing experiments and beamline design for recently proposed studies at Antimatter Factory, CERN. Multiple aspects of antiproton beam preparation were covered to evaluate the limiting factors. The largest part of the work focuses on the thorough description/implementation of beam guiding elements, beam manipulation and target interaction, which was done via a combination of various simulation tools. Some of the suggested ideas were firstly benchmarked and then applied in real life in low-energy antimatter research at CERN (ALPHA and AEgIS). Other parts of the project shed more light on the existing limitations and knowledge gaps regarding antiproton interaction with light atomic targets.

Each of the blocks of this work is appointed to a specific role. Chapter 2 gradually familiarises the reader with the theoretical base utilised for different parts of the project. Chapter 3 discusses various attributes of beam tracking methods and common approaches for the description of optical elements. In Chapter 4, the reader is introduced to a state-of-art device that was developed to map complex electrostatic fields to ensure in quality of the developed simulation model. A large piece of the work in Chapter 5 is dedicated to the realistic simulation of electrostatic beam lines, code development, and benchmarking of results in multiple simulation tools. It also covers the novel development of an injection line for future research at the AEgIS experiment, described in detail for the first time. Chapter 6 proposes new bunch compression schemes in beam transfer lines and ELENA, to achieve bunch properties required for short-pulse experiments. It also demonstrates equilibrium parameters for ultra-short bunches at 100 keV energy. Finally, Chapter 7 provides a summary of the work and outlook for further development routes.

Most of the results presented here were obtained within the framework of the ELENA ring and experiments in the AD hall. However, all the developed methods

and concepts can be applied to other antimatter experiments or low-energy machines mentioned above: CRYRING, CSR, and USR. Furthermore, simulation codes and techniques utilised here were extensively improved thanks to the extended functionality (by developers and myself) required for this project. Some of the findings may bring new insight into unknown antimatter physics and be beneficial for further optimisation of low-energy facilities.

Chapter 2

Essential Concepts of Beam Dynamics

2.1 Introduction

The design aspects of circular, linear accelerators and transfer lines have a comprehensive theoretical foundation known as beam dynamics. Commonly, accelerator physicists divide this field of science into a number of disciplines related to diverse working aspects of the machine. This chapter establishes the main concepts which describe the reference particle's motion together with collective effects from a bunch distribution in low-energy storage rings. For general understanding, the particle behaviour is split into longitudinal and transverse components without coupling. This compilation of the presented theory is based on various sources from experts in each discipline [58–62].

2.2 Transverse beam dynamics

2.2.1 Coordinate systems and phase space coordinates

A particle that is sent through a linear accelerator, storage ring or transfer line is commonly described via Frenet-Serret curvilinear coordinate system (CCS). Such a CCS

moves along a continuous, differentiable curve in the three-dimensional Euclidean space [58] (x, y, z) and helps to characterise all kinematic properties of a reference particle. Such an ideal path of the particle is called the *reference orbit* and is represented using Frenet-Serret CCS in Fig. 2.1. This track can be parametrised with the independent path length s. If we consider a homogeneous distribution of charged particles (with the same z), then any point in the transverse phase space can be expressed by $\vec{r} = \vec{r_0}(s) + x\vec{e_x}(s) + y\vec{e_y}(s)$, where $\vec{r_0}(s)$ is the reference orbit. The components x, y and z respectively are the horizontal (or radial), vertical and longitudinal (tangential) offsets from the reference orbit for a given s and are measured in units of length in the laboratory frame. Conventionally, x points outwards from the ring centre and s increases in the clockwise direction as viewed from above. Additionally, it is worth mentioning that beam dynamics codes may use various representations of particle coordinates: canonical with/without difference in longitudinal part (BMAD [63], MAD-X [64]) or non-canonical (PTC [65]) or global Cartesian (G4beamline [66], Geant4 [67]). To describe how the reference coordinate system is oriented within the Cartesian coor-

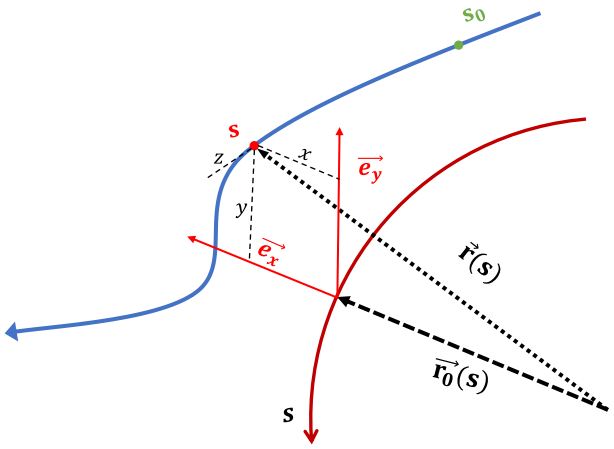

Figure 2.1: *The Frenet-Serret curvilinear coordinate system. The solid burgundy line represents the reference orbit. An actual particle track is shown with the solid blue curve.*

dinate system, each point on the s-axis is characterised by its (X, Y, Z) position and by three angles $\theta(s)$, $\phi(s)$, and $\psi(s)$ that describe the orientation of the reference axes as shown in Fig. 2.2.

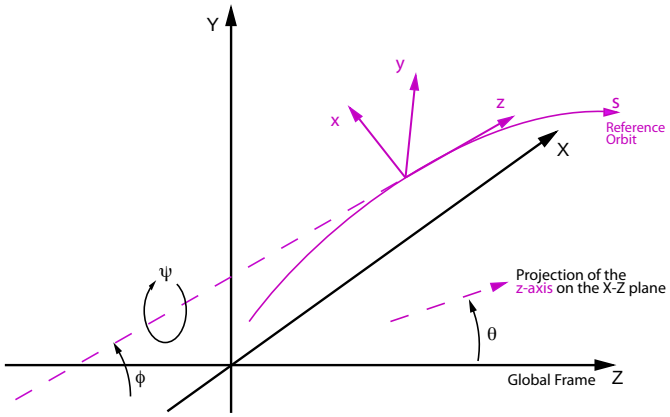

Figure 2.2: *Description of the reference orbit (purple) coordinate system in the global Cartesian coordinates (black) by position an (X, Y, Z) and by three rotation angles $\theta(s), \phi(s)$, and $\psi(s)$ [63].*

2.2.2 Charged particle motion in electric & magnetic fields

A beam of particles is steered and shaped utilising a combination of electromagnetic fields which are present in an accelerator or storage ring. In this case, a particle with mass m_p and charge q moving at a velocity $\vec{v}$ experienced the Lorentz force

$$\vec{F_L} = q(\vec{E} + \vec{v} \times \vec{B}), \tag{2.1}$$

where $\vec{E}$ and $\vec{B}$ are electric and magnetic field vectors respectively. If we relate the Lorentz force to the particle momentum $\vec{p}$ or kinetic energy E_{kin}, we know from classical mechanics that

$$\left.\begin{aligned} \Delta\vec{p} &= \int \vec{F_L}\, dt \\ \Delta E_{kin} &= \int \vec{F_L}\, d\vec{s} \end{aligned}\right\} \xrightarrow[d\vec{s}=\vec{v}\,dt]{} \vec{\beta}\Delta c\vec{p} = \Delta E_{kin}, \tag{2.2}$$

where $\vec{\beta} = \vec{v}/c$. Then $\vec{F_L}$ can be expressed in field components and the change of kinetic energy becomes

$$\begin{aligned}\Delta E_{kin} &= \int \vec{F_L}\, d\vec{s} = q \int [\vec{E} + \vec{v} \times \vec{B}]\, d\vec{s} \\ &= q \int \vec{E}\, d\vec{s} + \underbrace{q \int \vec{v} \times \vec{B} \vec{v} dt}_{=0}\,. \end{aligned} \tag{2.3}$$

It becomes evident that the kinetic energy of the particle changes whenever it travels in an electric field $\vec{E}$ and the acceleration occurs in the direction of the electric field. This acceleration is independent of the particle velocity and acts even on a particle at rest $\vec{v} = 0$. In contrast, the second component of the Lorentz force depends on the particle velocity and is mutually perpendicular to the direction of motion and the magnetic field. Combining equations (2.1) and (2.2) we can derive the equation of motion of a charged particle

$$\frac{d\vec{p}}{dt} = \frac{d}{dt}(m\gamma_L \vec{v}) \tag{2.4}$$

where $\gamma_L = 1/\sqrt{1-(v/c)^2}$ is the relativistic Lorentz factor.

In the simplest example of a circular machine the bending radius ρ_x is defined via equilibrium of centripetal and magnetic components of Lorentz forces

$$F_{centr} = F_L \;\Rightarrow\; \frac{m_p \gamma v^2}{\rho_x} = q|v_z B_y| \tag{2.5}$$

where B_y determines ρ_x and $v^2 \approx v_z^2$. After replacing the particle momentum $p = m_p \gamma v$ and discarding subscripts, we find an important parameter of the accelerator

$$|B\rho| = \frac{p}{q} \;\Leftrightarrow\; \frac{1}{\rho} = \frac{q|B|}{p} \tag{2.6}$$

which is called the *beam rigidity* $B\rho$ which is dependent of the charge and particle momentum. Using more practical units for a GeV energy storage ring, the expression

(2.6) becomes

$$\frac{1}{\rho}[m^{-1}] = 0.2998\frac{q_{eff}}{A}\frac{|B[T]|}{p[GeV/c]} \tag{2.7}$$
$$\frac{[eT]}{[GeV/c]} = \frac{[2.998 * 10^8 eVms]}{[m^2 10^9 eVs]} = 0.2998[m^{-1}]$$

where A is the particle nucleon number, p is the momentum per nucleon in units of GeV/c, and q_{eff} is the effective electric charge of the particle in the propagation medium. The general definition of deflection angle in a magnetic field is

$$\theta = \int \frac{d\vec{s}}{\rho_x} \tag{2.8}$$

or when it concerns a uniform field like in a dipole magnet of arc length l_d, the deflection angle is $\theta = l_d/\rho_x$. Much like the properties of light rays, particle beams are also prone to spread out due to an inherent beam divergence from the production source.

To keep the particle beam together and to obtain desired beam properties at selected points along the beam transport line or ring, focusing devices are required. A focusing feature can be provided for charged particle beams through the use of

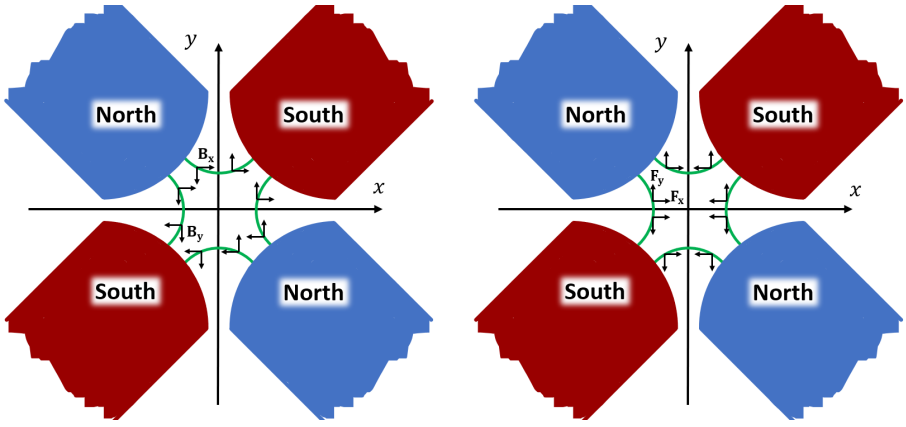

Figure 2.3: *Cross-sectional view of quadrupole magnet with components of the magnetic field (left) and forces towards positively charged particles (right).*

azimuthally varying magnetic fields, whose amplitude is zero on the reference axis,

whilst increasing linearly with the distance r from it. The most common device that provides a material-free aperture and the desired focusing field is called a quadrupole magnet is shown in Fig. 2.3. In Cartesian CCS horizontal and vertical focusing planes are usually considered

$$B_\phi = gr \xrightarrow[\text{Cartesian system}]{} B_x = gy \ , B_y = gx \tag{2.9}$$
$$\text{where } g = \frac{\partial B_x}{y} = \frac{\partial B_y}{x} \ [T/m]$$

is a field *gradient*. As evident from the right part of Fig. 2.3, the polarity of the magnet defines the horizontal focusing plane with its force components. In beam dynamics, it is customary to define an energy-independent focusing strength. Similar to the bending curvature in equation (2.6) we can define the focusing strength k as

$$k[m^{-2}] = 0.2998 \frac{g[T/m]|}{p[GeV/c]}. \tag{2.10}$$

But in reality, the magnet device produces additional components of the field. Thus, the more general definition of multipole strengths k_{n+1} can be introduced by the magnetic field expansion in a Taylor series. And in combination with (2.10), for the horizontal plane, we can obtain the next expression

$$B_y = \sum_n B_n \frac{x^n}{n!} \ \Rightarrow \tag{2.11}$$
$$B_y \frac{q}{p} = \underbrace{k_1}_{dipole} - \underbrace{k_2 x}_{quadrupole} + \underbrace{\frac{1}{2} k_3 x^2}_{sextupole} + \mathcal{O}(n \geq 3)$$

In addition, if the skew components of the n-th multipole are present, they are rotated by $\pi/2n$ in comparison with perpendicular components.

2.2.3 Hill's equation and transverse motion

Consider the machine layout consisting of periodic allocation of dipoles and quadrupoles (both focusing and defocusing). When particles move around the accelerator or storage ring, any time when their divergence (angle) causes them to drift too far from the reference orbit (in a horizontal or vertical plane) the quadrupole forces focus them back towards the reference orbit. Visually it looks like balls rolling through a potential valley with alternating gradients, see Fig. 2.4. These oscillations are known as the *betatron motion* of particles, a quasi-harmonic movement around the closed orbit which exists in both horizontal x and vertical y directions of the transverse plane u. Such behaviour can be explained with the second-order differential equation

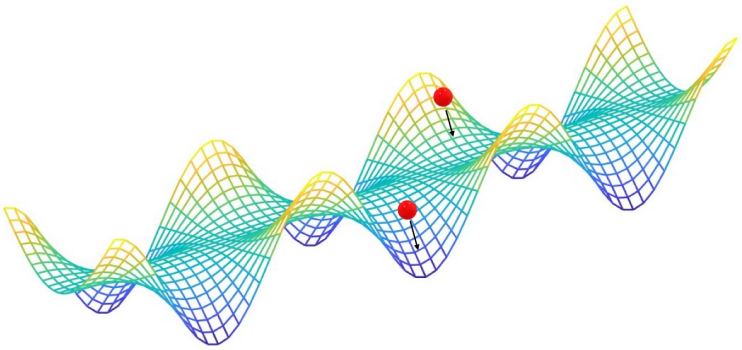

Figure 2.4: *Potential valley that represents the concept of alternate gradient focusing in one plane. One of the particles (red) moves towards the centre, and the other one away from the centre.*

$$\frac{du^2}{ds^2} + K_u(s)u = 0. \tag{2.12}$$

which is known as a homogeneous Hill's equation. The function $K_u(s)$ is the total focusing strength, which can be described as a combination of the weak focusing from the dipole and the strong focusing from quadrupole magnets,

$$K_u(s) = \frac{1}{\rho_u^2(s)} \pm k(s) \tag{2.13}$$

where $k(s)$ and $\rho_u(s)$ are the focusing strength and bending radius of the element respectively (plus sign for x, minus sign for y). Due to the fact that we consider motion in the circular lattice, both $K_u(s)$ and $\rho_u(s)$ are periodic in s and satisfy the conditions,

$$\begin{aligned} K_u(s+L) &= K_u(s) \\ \rho_u(s+L) &= \rho_u(s)) \end{aligned} \tag{2.14}$$

where L is the machine circumference. Equation (2.12) has a pair of linearly independent stable solutions of the form

$$u_{1,2}(s) = C_{1,2} w_u(s) e^{\pm i\psi_u(s)} \tag{2.15}$$

where $C_{1,2}$ are constants, $w_u(s)$ is the betatron amplitude function periodic with L and $\psi_x(s)$ is the phase advance. The general solution for horizontal motion $u(s) = x(s)$ can be written as a linear combination of the two principal trajectories

$$x(s) = C(s)x_0 + S(s)x_0' \tag{2.16}$$

where $C(s)$ and $S(s)$ are two independent solutions of Hill's equation called cosine-like and sine-line solutions.

Once we have these, we can define the transfer matrix between two positions in the accelerator as

$$M_{s_0 \Rightarrow s} = \begin{bmatrix} C(s) & S(s) \\ C'(s) & S'(s) \end{bmatrix}. \tag{2.17}$$

Furthermore, we can derive the connection between the principal trajectories and pseudo harmonic oscillations. Expressing (2.15) for the horizontal position and an-

gle functions

$$\begin{aligned} x(s) &= C_1\sqrt{\beta_x(s)}e^{i\psi_x(s)} + C_2 w_x(s)e^{-i\psi_x(s)} \\ &= A\sqrt{\beta_x(s)}\cos(\psi(s)-\psi_0) \end{aligned} \tag{2.18a}$$

$$x'(s) = -\frac{A}{\sqrt{\beta_x(s)}}\left(\alpha_x(s)\cos(\psi(s)-\psi_0) + \sin(\psi(s)-\psi_0)\right) \tag{2.18b}$$

$$\text{with} \quad \beta_x(s) = w_x^2(s) \text{ and } \alpha_x(s) = \frac{\beta_x'(s)}{2}$$

where A is a constant, ψ_0 being an initial value of phase advance and here we also have defined two *Twiss functions* β_x and α_x which depend on w_x and its derivative. Using equations (2.16) and (2.18), we can derive that

$$C(s) = \sqrt{\frac{\beta(s)}{\beta(s_0)}}\left(\cos(\Delta\psi(s)) + \alpha(s_0)\sin(\Delta\psi(s))\right) \tag{2.19}$$

$$C'(s) = \sqrt{\frac{1}{\beta(s)\beta(s_0)}}\left\{[\alpha(s)-\alpha(s_0)]\cos(\Delta\psi(s)) - [1+\alpha(s)\alpha(s_0)]\sin(\Delta\psi(s))\right\} \tag{2.20}$$

The solutions for S(s) and S'(s) can be computed in a similar way. The phase advance difference was given by $\Delta\psi(s) = \psi(s) - \psi_0$.

Hence, setting $\beta(s_0) = \beta_0$ and $\alpha(s_0) = \alpha_0$ the transfer matrix $M_{s_0\Rightarrow s}$ can be expressed as

$$M_{s_0\Rightarrow s} = \begin{bmatrix} \sqrt{\beta(s)} & 0 \\ \frac{\alpha(s)}{\sqrt{\beta(s)}} & \frac{1}{\sqrt{\beta(s)}} \end{bmatrix} \begin{bmatrix} \cos(\Delta\psi(s)) & \sin(\Delta\psi(s)) \\ -\sin(\Delta\psi(s)) & \cos(\Delta\psi(s)) \end{bmatrix} \begin{bmatrix} \sqrt{\frac{1}{\beta_0}} & 0 \\ \frac{\alpha_0}{\sqrt{\beta_0}} & \sqrt{\beta_0} \end{bmatrix} \tag{2.21}$$

from which horizontal position and angle evolve as

$$\begin{bmatrix} x(s) \\ x'(s) \end{bmatrix} = M_{s_0\Rightarrow s} \begin{bmatrix} x(s_0) \\ x'(s_0) \end{bmatrix}. \tag{2.22}$$

Such a matrix can be constructed for any guiding element of the machine. Thus the

whole lattice can be represented through the multiplication of a sequence of matrices. In accordance with Floquet's theory [68] the transfer matrix $M(s)$ over one period L may be written then as

$$M(s) = M_{s_0 \Rightarrow s} M^{-1}_{s_0 \Rightarrow s} = \begin{bmatrix} \cos(\psi(s)) + \alpha \sin(\psi(s)) & \beta(s) \sin(\psi(s)) \\ -\gamma(s) \sin(\psi(s)) & \cos(\psi(s)) - \alpha \sin(\psi(s)) \end{bmatrix} \tag{2.23}$$

with $\gamma(s)$ representing the third Twiss function which is defined using the previous two

$$\gamma(s) = \frac{1 + \alpha(s)^2}{\beta(s)}. \tag{2.24}$$

Further, we can show how the equations of motion (2.18) in the horizontal plane for a single particle may be used to describe the collective behaviour of a beam formed by many particles.

2.2.4 Emittance definitions

Using solutions of Hill's equation, an invariant of motion can be constructed if the total energy of the particle is unchanged after one machine period. Firstly, one can rewrite derivative of equation (2.18a) as

$$\begin{aligned} x'(s) &= -\frac{A}{\sqrt{\beta_x(s)}} \left(\alpha_x(s) \cos(\psi(s) - \psi_0) + \sin(\psi(s) - \psi_0)\right) = \\ &= -\frac{\alpha_x(s)}{\beta_x(s)} x(s) - \frac{A}{\sqrt{\beta_x(s)}} \sin(\Delta\psi(s)) \end{aligned} \tag{2.25}$$

or equally after rearrangement

$$\alpha_x(s) x(s) + \beta_x(s) x'(s) = A\sqrt{\beta_x(s)} \sin(\Delta\psi(s)). \tag{2.26}$$

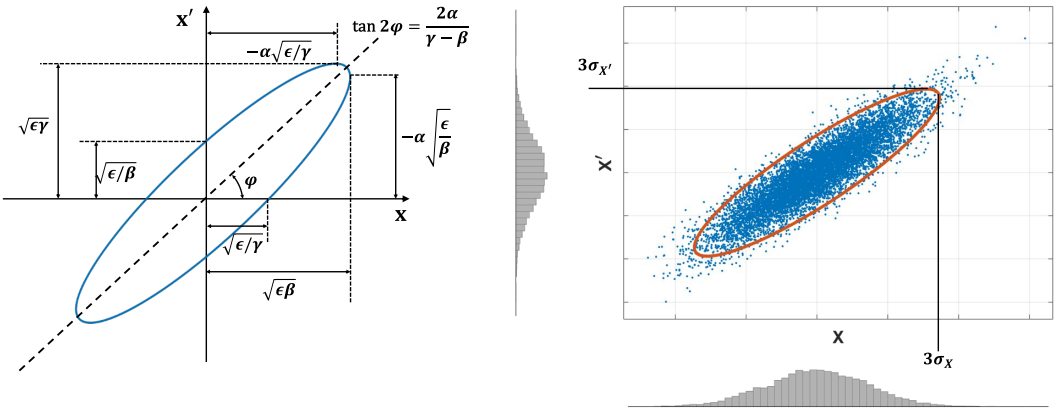

Figure 2.5: *Left: The beam emittance defined for a single particle using Twiss functions. Right: Statistical beam emittance for particle distribution. In this case, the ellipse includes 99.7 % of all particles or 3 r.m.s values.*

By squaring equation (2.18a) and its derivative (2.26) and then summing the products of both sides including the definition of γ from (2.24) we will obtain

$$\gamma_x(s)x(s)^2 + 2\alpha_x(s)x(s)x'(s) + \beta_x(s)x'(s)^2 = A^2. \tag{2.27}$$

This is a constant of motion known as *Courant-Snyder* invariant [69]. Geometrically it describes an equation of an ellipse in the (x, x') plane with area πA^2. The size and orientation of the ellipse are defined by Twiss parameters, α, β and γ, as demonstrated in the left part of Fig. 2.5.

By selecting a given fraction of the circulating particles enclosed within an arbitrary ellipse in the (x, x') plane, say $3\sigma_x$ or 95%, assuming Gaussian distribution at a certain point s, we obtain $\epsilon = A^2$ where the constant ϵ is called the *beam emittance*:

$$\int\int_{ellipse} dxdx' = \pi\epsilon. \tag{2.28}$$

The particle whose motion is described with such a phase ellipse includes all other particles which revolve on homothetic ellipses with amplitude $a < \epsilon$. Thus, we are able to describe the behaviour of the whole beam by the dynamics of a single particle. If the fraction of the particles inside the phase ellipse does not change on successive

machine turns, the beam emittance is conserved.

The transverse emittance of a particle distribution in the horizontal phase space can be described in the matrix notation of the ellipse equation

$$\begin{bmatrix} x & x' \end{bmatrix} \boldsymbol{\sigma}^{-1} \begin{bmatrix} x \\ x' \end{bmatrix} = 1 \tag{2.29}$$

where the symmetric matrix $\boldsymbol{\sigma}$ is the so-called *beam matrix* and is specified later in equation 2.31. This form may be extended further to the ellipse equation

$$\sigma_{22}x^2 + 2\sigma_{12}(s)xx' + \sigma_{11}x'^2 = \epsilon^2 \tag{2.30}$$

and if we compare it with equation (2.27), the beam matrix can be determined with Twiss parameters as

$$\boldsymbol{\sigma} = \begin{bmatrix} \sigma_{11} & \sigma_{12} \\ \sigma_{21} & \sigma_{22} \end{bmatrix} = \epsilon^2 \begin{bmatrix} \beta & -\alpha \\ -\alpha & \gamma \end{bmatrix}. \tag{2.31}$$

Such a definition of the beam matrix can be expanded to six or more dimensional planes adding, for instance, a spin of the particles. The ellipse area then is found from the determinant of the above matrix

$$\pi\sqrt{det\boldsymbol{\sigma}} = \pi\sqrt{\sigma_{11}\sigma_{22} - \sigma_{12}^2} = \pi\epsilon. \tag{2.32}$$

The right part of Fig. 2.5 represents a statistical definition of horizontal emittance when 99.7 % of all particles are included. Assuming a Gaussian distribution, the beam r.m.s (root mean squared) size in the horizontal plane can be found from the average

values of the selected n particles

$$\begin{aligned}\langle x^2\rangle &= \frac{1}{n}\sum_{n=1}^{n}(x_i - x_0)^2 = \epsilon\beta,\\ \langle x'^2\rangle &= \frac{1}{n}\sum_{n=1}^{n}(x'_i - x'_0)^2 = \epsilon\gamma,\\ \langle xx'\rangle &= \frac{1}{n}\sum_{n=1}^{n}(x_i - x_0)(x'_i - x'_0) = -\epsilon\alpha.\end{aligned} \tag{2.33}$$

Using the such definition, the r.m.s beam emittance statistically reads as

$$\epsilon^2 = \sigma_{11}\sigma_{22} - \sigma_{12}^2 = \langle x^2\rangle\langle x'^2\rangle - \langle xx'\rangle^2. \tag{2.34}$$

The beam emittance in a proton synchrotron is commonly measured in units of $\pi\cdot$ mm·mrad, but it varies from application, particle species and accelerator physics community.

2.2.5 Dispersion function

Thus far, it was assumed that all particles within the beam have momentum equal to that of the reference particle p_0. However, in practice, there will be always some small offset or momentum spread within the beam. To include this effect we need to extend our factor q/p from equation of motion in magnetic fields (2.6) as

$$\begin{aligned}\frac{q}{p} &= \frac{q}{p_0}(1-\delta)\\ \text{where}\quad \delta &= \frac{p-p_0}{p_0} = \frac{\Delta p}{p_0}\end{aligned} \tag{2.35}$$

is the first order *momentum deviation* from p_0. The resultant effect of non-zero momentum deviation is the variance of the trajectory in bending elements, as illustrated in Fig. 2.6. After the propagation of an off-momentum particle in a magnetic or electric dipole, both angular and positional offsets of the orbit are created. It also introduces

coupling between transverse and longitudinal phase space.

Replacement of the original term in equation (2.12) leads us to the inhomogeneous form of Hill's equation,

$$\frac{du^2}{ds^2} + K_u(s)u = \frac{1}{\rho_u(s)}\frac{\Delta p}{p} = \frac{\delta}{\rho_u(s)}. \tag{2.36}$$

Because the ODE is linear, the general solution for horizontal motion $x(s)$ is a sum of the general solution of the initial equation and a particular solution for the inhomogeneous part,

$$x(s) = x_\beta(s) + x_\delta(s) \tag{2.37}$$

where x_β is the betatron oscillation around the stable orbit for an off-momentum particle and x_δ is a displacement of this orbit from that of the reference particle (where $\delta = 0$). The particular solution is commonly written as

$$x_\delta(s) = D_x(s)\delta \tag{2.38}$$

where $D_x(s)$ is called *dispersion function* (for a horizontal plane in our case) and satisfies ODE similar to equation (2.36)

$$\frac{dD_x(s)^2}{ds^2} + K_x(s)D_x(s) = \frac{1}{\rho_u(s)} \tag{2.39}$$

and has the same properties as $K_x(s)$ and $\rho_x(s)$. Figure 2.6 demonstrates the impact of non-zero dispersion on the orbit and beam distribution. In practice, the dispersion function must be taken into account for r.m.s beam width calculations (equation (2.33)) in dispersive parts of the lattice

$$\sigma_x(s) = \sqrt{\epsilon_x\beta_x - D_x^2(s)\sigma_\delta^2} \tag{2.40}$$

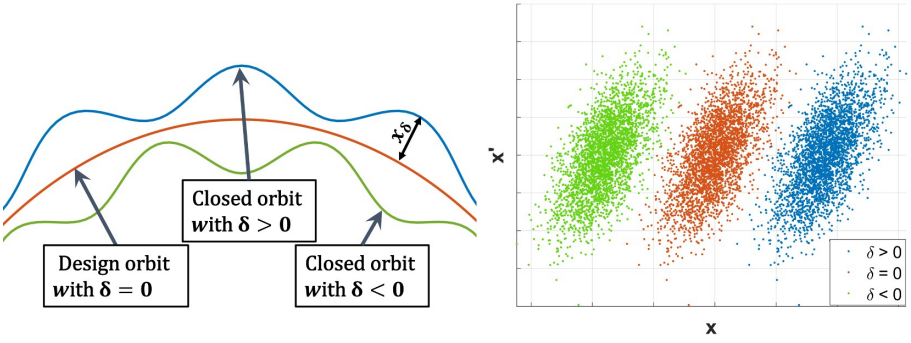

Figure 2.6: *Orbits with dispersion compared to the reference trajectory (left). Phase space ellipses of each particle in a horizontal plane (right).*

where σ_δ is the r.m.s width of the momentum spread.

2.2.6 Momentum compaction factor

Dispersion affects a phase space location of the reference orbit for off-momentum particles. Therefore, it also changes the orbit's path length. The total path length is consequently given by the sum of the ideal and deviation parts

$$L = \int (1 + \underbrace{\frac{D(s)}{\rho(s)}}_{\Delta L}) \mathrm{d}s \tag{2.41}$$

The change of the circumference L depending on the momentum spread δ is the so-called *momentum compaction factor*, calculated as

$$\alpha_c = \frac{\Delta L / L}{\Delta p / p_0} = \frac{1}{L_0} \int_0^{L_0} \frac{D(s)}{\rho(s)} \mathrm{d}s = \left\langle \frac{D(s)}{\rho(s)} \right\rangle . \tag{2.42}$$

where L_0 is the path length of the reference particle (δ=0). The momentum compaction factor is one of the transverse dynamics connections to the longitudinal dynamics of synchrotrons.

Naturally, the dependence of the path length on momentum deviation also yields a different revolution time of the particle. The reference particle with momentum p

travels around the nominal circumference L in time given by

$$T = \frac{L}{c\beta}. \tag{2.43}$$

The velocity here is defined in terms of the speed of light, $\beta = v/c$ (not to be confused with the betatron function). Accordingly, the variation of time with the path can be obtained by logarithmic differentiation

$$\frac{dT}{T} = \frac{dL}{L} - \frac{d\beta}{\beta}. \tag{2.44}$$

After replacing dL/L on $\alpha_c\delta$ and $cp = \beta E$, we obtain $\boxed{\mathrm{dp/p{=}d}\beta/\beta + dE/E}$ and knowing that $dE/E = \beta^2 dp/p$ we get $\boxed{\mathrm{d}\beta/\beta = (1/\gamma^2)dp/p}$ where γ is a Lorentz factor. Rewriting equation (2.44) with new components results in

$$\frac{dT}{T} = -\left(\frac{1}{\gamma} - \alpha_c\right)\frac{dp}{p} = -\eta\frac{dp}{p} \tag{2.45}$$

where η is called *slip-factor*. Also, the energy of a particle at which

$$\gamma_t = \frac{1}{\sqrt{\alpha_c}} \tag{2.46}$$

is called the *transition energy*. When a machine works below transition energy ($\eta > 0$), the arrival time depends on the velocity of the particles. However, above the transition energy ($\eta < 0$), the speed of the particle is so close to the speed of light that the circulation time of the particle with respect to other particles is more influenced by the change in path length due to its momentum change rather than its speed.

2.2.7 Tune and working point

Looking back at the phase advance and betatron oscillations of the particle which are defined as

$$\Delta\psi_{x,y}(s+L) = 2Q_{x,y}\pi \int_{s}^{s+L} \frac{dt}{\beta_{x,y}} \tag{2.47}$$

where the quantities $Q_{x,y}$ are called *betatron tunes* or a number of oscillations per turn. The operational state of the circular machine with the specific values of $Q_{x,y}$ is commonly called the *working point*. The betatron tunes are essential values used to analyse beam stability inside the circular machine. Particularly, fractional tunes of low order lead to coherent oscillation within the beam which can result in degradation and/or loss of the beam. This effect occurs due to resonance behaviour (similar to

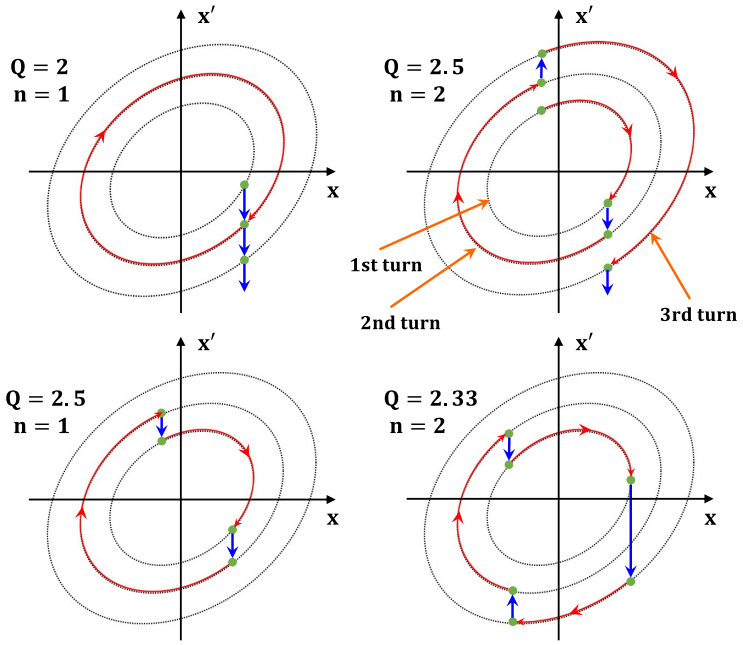

Figure 2.7: *Particle oscillation in a horizontal plane at different betatron values Q for field errors in dipole (left) and quadrupole (right). The two upper plots show unstable conditions when field errors cause amplitude growth. The two bottom plots demonstrate conditions when these errors self-cancelled every second (n=1) or every third turn (n=2).*

resonance disaster in mechanics) of oscillations led by multipole errors and illustrated

by an example of dipole and quadrupole fields in Fig. 2.7.

The general equations for resonance conditions of the betatron tunes can be written as follows:

$$mQ_x + nQ_z = sP \tag{2.48}$$

where m, n, s and P are integers, P is non-negative, and $|m| + |n|$ shows the resonance order, s is the periodicity of the lattice (a structure is built of s identical cells) and P is the order of the perturbation harmonic. These resonances are called *structural* or *systematic* resonances. High periodicity or symmetry of the lattice leads to the elimination of resonances where $s \times P$ is not an integer value, and thus increases a resonance-free area. In practice, each period has its own field or alignment errors which drive forbidden (random) resonances. Plotting the lines which satisfy the previous equation (2.48) for all possible values of m, n and P in the (Q_x, Q_y) plane results in the so-called *resonance* or *tune diagram* displayed in Fig. 2.8 for the periodicity equal one and four.

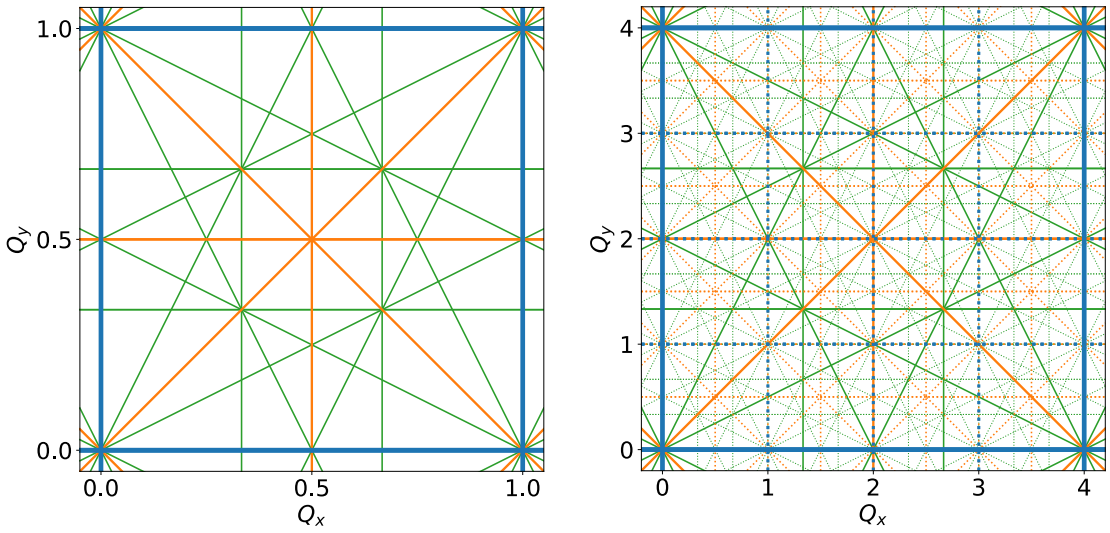

Figure 2.8: *Two examples of the resonance diagram for s=1 (left plot) and s=4 (right plot). Structural resonances of the first, second and third orders are shown with solid lines in blue, orange and green correspondingly. The dotted lines on the right side represent random resonances.*

For the positive values of m and n, the resonance is referred to as a *sum resonance* and it leads to a loss of the beam. If m and n are negative, the resonance is called a *difference resonance* or a coupling resonance and it does not result in a loss of the beam but instead leads to a coupling between the horizontal and the vertical transverse planes. Also, every resonance line from the tune diagram has some thickness, called the *resonance width*, in which the particle motion might be unstable, depending on the betatron amplitude. When the resonance is below the third order (linear), this width is called a *stop-band* because the entire beam becomes unstable if the operating point (Q_x, Q_y) reaches this region of tune values. The largest oscillation amplitude in the transverse plane where a particle is still stable is called the *dynamic aperture*. The lowest order resonances are the most dangerous because the "strength" of the resonances decreases with increasing order, and thus they must be carefully avoided by proper machine optics design and choosing an appropriate working point.

2.3 Longitudinal beam dynamics

In the previous sections, we focused our attention on the interaction of transverse electrical and magnetic fields with charged particles. The main function of these transverse fields is that they enable the possibility to steer these particles along a reference orbit but do not directly change the energy of the particle through acceleration. For particle acceleration, we must generate fields with force components that are in the direction of the desired acceleration. These fields are called longitudinal fields or accelerating fields. The momentum change in time of a particle that travels through these fields can be described as

$$\frac{d\vec{p}}{dt} = q\vec{E}(z,t). \tag{2.49}$$

The nature of such fields can be static, pulsed or they can be electromagnetic fields that oscillate at high frequency ($\approx$1 MHz–10 GHz).

Most commonly, the latter operational mode is used. Radio-frequency (RF) systems produce the required powerful electric fields in elements called *resonant cavities* or *loaded waveguides*. In this way, an alternating voltage helps to overcome earlier limitations imposed by corona formation and discharge in electrostatic accelerators.

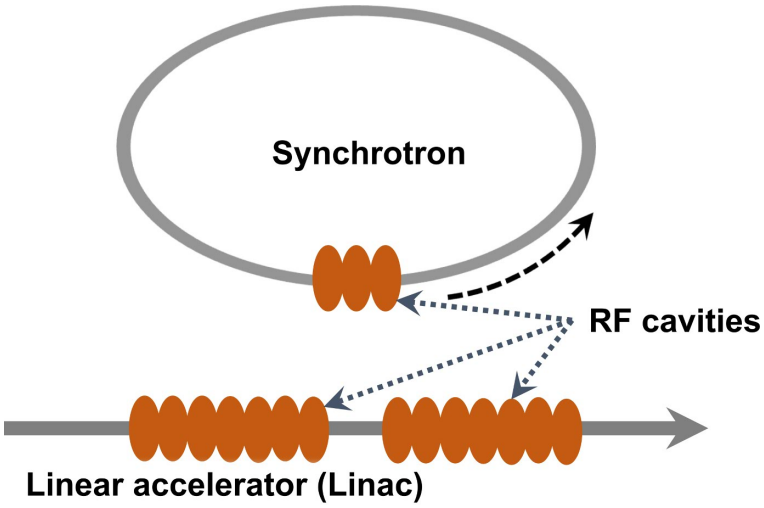

Figure 2.9: *Acceleration principle in circular and linear machines.*

2.3.1 Particle acceleration and synchrotron motion

Both linear and circular machines use the oscillating voltage in resonant cavities to achieve acceleration/deceleration and for the bunch manipulation in the longitudinal plane. In synchrotrons, particles guided by a magnetic field follow the orbit and return to the same accelerating cavity on every turn, while in linear accelerators, particles follow a straight path through a sequence of RF cavities.

The extent of acceleration for the particle travelling through a resonance cavity depends on the phase of the RF wave, which affects the particle. The RF cavity (Fig. 2.9) in a synchrotron should satisfy the synchronicity conditions and longitudinal phase stability criteria [58]. By synchronicity, it is meant that the frequency of RF system φ_{rf} should be locked to the frequency of particle revolution φ_s in the ring (otherwise, the accelerating voltage will be averaged to zero). It is expressed as $\varphi_{rf} = h\varphi_s$, where

the integer h is known as a *harmonic number*.

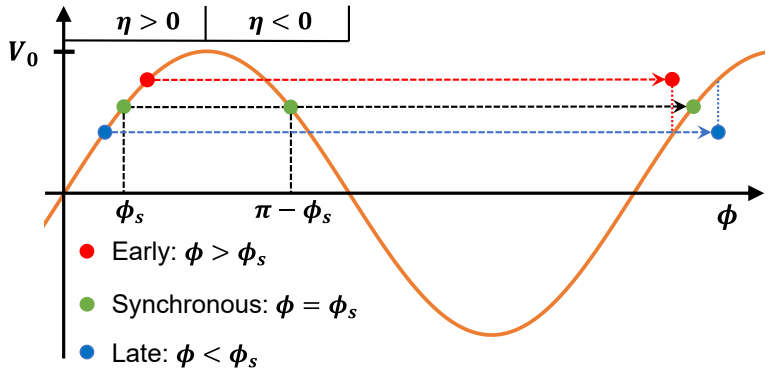

Figure 2.10: *RF time-dependent sinusoidal field with phase stability principle. Below transition ($\eta > 0$), the longitudinal focusing occurs if $\phi_s < \pi/2$ versus in $\pi - \phi_s$ field acts in a defocusing manner. And above transition ($\eta < 0$), both points act inversely.*

For a systematic acceleration, the phase of the oscillating RF field must reach a specific value at the arrival of the reference particle in the beam. This phase is called synchronous phase ϕ_s. The longitudinal phase focusing is achieved by choosing an appropriate synchronous phase. A particle that arrives earlier than the synchronous particle receives smaller acceleration than a later one below transition and vice versa above transition. The time-dependent electric field in the RF cavity gap, as shown in Fig. 2.10, is given by:

$$E_(z,t) = E_{z,0}\sin(2\pi\varphi_{rf}t + \phi_s). \tag{2.50}$$

By assuming that we know how the shape of the accelerating field changes over time, we can integrate equation (2.49) in terms of longitudinal position z over the gap length (L)

$$\Delta E = q\int_L \vec{E}(z,t)\mathrm{d}z \tag{2.51}$$

and obtain kinetic energy gain ΔE. Calculating ΔE it is found that

$$\Delta E = qV_0 T_{tr} \sin \phi_s \tag{2.52}$$

where V_0 is the maximum voltage across the cavity and T_{tr} is the transit time factor. The energy gain is time averaged over the length of time it takes the particle to traverse the field

$$T_{tr} = \frac{\sin(L\pi/\beta\lambda)}{L\pi/\beta\lambda}. \tag{2.53}$$

The transit time factor scales the change in kinetic energy of a particle according to how the electric field varies in time as a particle passes through the cavity. For example, if the phase of the electric field changes by more than π while the particle is in the cavity, then the particle will experience both accelerating and decelerating forces and the efficiency of the cavity will be reduced. This is why in machines where β varies, several types of cavities may be present, or the frequency of the cavity may be varied [60, 70].

2.3.2 Equation of motion in longitudinal phase space

To explain the behaviour of a non-reference particle, we define its relation to a synchronous particle as

$$c = c_s + \Delta c \tag{2.54}$$

where **c** can be any of the next particle parameters:

E, the kinetic energy

p, the momentum

ω, the angular revolution frequency ·

θ, the azimuthal orbital angle

ϕ, the phase angle

The last two, orbital and phase angles, are related by $\Delta\phi = \phi - \phi_s = -h\Delta\theta$ or in differential shape

$$-\frac{1}{h}\frac{\mathrm{d}\phi}{dt} = \frac{\mathrm{d}}{dt}\Delta\theta = \Delta\omega \tag{2.55}$$

The amount of energy that particle obtains per turn after passing through a cavity is defined as

$$\Delta E = qV_0 \sin\phi. \tag{2.56}$$

The change in energy between the test and the design particle after one turn is then given by

$$\Delta(E)_{turn} = E - E_s = qV_0(\sin\phi - \sin\phi_s). \tag{2.57}$$

If the energy gain in time is smooth with each turn, we can redefine the last equation as

$$\frac{\mathrm{d}(E)}{dt} \simeq \frac{\Delta E}{\tau_s} = \frac{qV}{2\pi}\omega_s(\sin\phi - \sin\phi_s) \tag{2.58}$$

and τ_s is the revolution time of the synchronous particle. Defining the variable $W = E/\omega_{rf}$ equation (2.58) becomes

$$\frac{\mathrm{d}W}{dt} = \frac{qV}{2\pi h}(\sin\phi_s - \sin\phi). \tag{2.59}$$

Equation (2.59) is *the equation of motion for energy difference* which also can be written in terms of momentum spread

$$\delta = \frac{\Delta p}{p} = \frac{\omega_{rf}}{\omega_{rf}} \frac{1}{\beta^2} \frac{\Delta E}{E} \tag{2.60}$$

as

$$\frac{\mathrm{d}(\delta)}{dt} = \frac{\omega_s}{2\pi\beta^2 E} qV(\sin\phi_s - \sin\phi). \tag{2.61}$$

To find the time evolution phase angle coordinate, using equation (2.55), we obtain

$$\frac{\mathrm{d}(\phi)}{dt} = -h\Delta\omega. \tag{2.62}$$

Then after rewriting equation (2.55) in terms of the revolution frequency

$$\frac{\Delta\omega}{\omega_s} = -\eta\delta \tag{2.63}$$

the phase equation result in

$$\frac{\mathrm{d}(\phi)}{dt} = h\eta\delta\omega_s = \frac{h\eta\omega_s^2}{\beta^2 E} W. \tag{2.64}$$

Finally the equations (2.64) and (2.59) form the *synchrotron equations of motion*. Assuming that the phase angle oscillation is small, they can be combined in order to construct a single second-order differential equation in the form of a harmonic oscillator

$$\frac{\mathrm{d}^2}{dt^2}(\phi - \phi_s) = \frac{h\omega_s^2 qV\eta\cos\phi_s}{2\pi\beta^2 E}(\phi - \phi_s) \tag{2.65}$$

with stability criteria

$$\eta\cos\phi_s < 0. \tag{2.66}$$

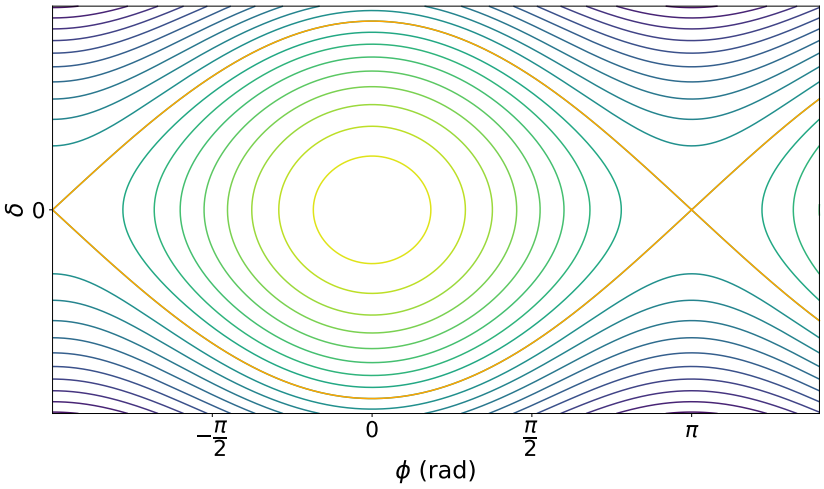

Figure 2.11: *Longitudinal phase space plotted for synchronous phases of 0 rad. Orange lines show a contour that separates two distinct kinds of particle motion - stable and unstable. A stable regime is observed when the phase of a particle is equal to the synchronous phase at $\phi_s = 0$, and the unstable behaviour occurs at $\phi = \pi$. Colours symbolise the energy of the particle "pendulum" with light green as the lowest value.*

The angular frequency for this oscillator is

$$\Omega_s = \omega_s \sqrt{\frac{hqV|\eta|\cos\phi_s}{2\pi\beta^2 E}} \tag{2.67}$$

with time for one synchrotron oscillation $T_s = 2\pi/\Omega_s$ and *synchrotron tune* Q_s defined as number of oscillation per one revolution

$$Q_s = \frac{\Omega_s}{\omega_s} = \sqrt{\frac{hqV|\eta|\cos\phi_s}{2\pi\beta^2 E}}. \tag{2.68}$$

Typical the order for the Q_s in ion rings is $\leq 10^{-3}$.

Plots of constant energy for equations of motion ((2.64) and (2.61)) are shown in Fig. 2.11 and demonstrate how particles can be expected to behave in longitudinal phase space. Two distinct kinds of motion can be seen and they are discussed in the next section.

2.3.3 Equations in Hamiltonian form. Bucket area.

The longitudinal phase space variables (ϕ, W) are canonical and can be derived from a Hamiltonian describing the total energy of the system

$$\begin{aligned} \frac{\mathrm{d}(\phi)}{dt} &= \frac{\partial H}{\partial W} \\ \frac{\mathrm{d(W)}}{dt} &= -\frac{\partial H}{\partial \phi} \end{aligned} \tag{2.69}$$

where H is

$$H = \frac{1}{2}\frac{h\eta\omega_s^2}{\beta^2 E}W^2 + \frac{qV}{2\pi}[\cos\phi - \cos\phi_s + (\phi - \phi_s)\sin\phi_s] \tag{2.70}$$

The Hamiltonian for adiabatic synchrotron motion has two fixed points. A stable fixed point is observed at ($\phi = \phi_s$, $\delta = 0$). The small amplitude trajectory in longitudinal phase space around a fixed point has the shape of an ellipse, and thus this point is also referred to as the elliptical point. An unstable fixed point is found at ($\phi = \pi$ - ϕ_s, $\delta = 0$). Trajectories near the unstable point conversely have the shape of a hyperbola and this point is referred to as the hyperbolic point. Hence, π - ϕ_s is an extreme amplitude for a stable motion that has a closed trajectory in phase space. This phase space trajectory separates the region of stable motion from the unstable region and is called the *separatrix*. The phase space enclosed within this separatrix is called the *RF bucket* and encloses an area of

$$A_B = \int \delta(\phi)\mathrm{d}\phi \tag{2.71}$$

know as the *bucket area*. The value for the Hamiltonian of the separatrix H_{sx} passing through unstable fixed point $(\pi - \phi_s)$ is

$$H_{sx} = \frac{\omega_s qV}{2\pi\beta^2 E}[-2\cos\phi_s + (\pi - 2\phi_s)\sin\phi_s] \tag{2.72}$$

and the phase-space trajectory is

$$\delta_{sx} + \frac{qV}{\pi\beta^2 Eh\eta}[\cos\phi - \cos\phi_s + (\pi - 2\phi - \phi_s)\sin\phi_s] = 0. \tag{2.73}$$

The separatrix has two turning points, $\pi - \phi_s$ and ϕ_m, the last one defined as

$$\cos\phi_m + \phi_m \sin\phi_s = -\cos\phi_s + (\pi - \phi_s)\sin\phi_s \tag{2.74}$$

Thus the bucket area A_B can be calculated from

$$A_B = \int \delta_{sx}(\phi)d\phi = 16\sqrt{\frac{qV}{2\pi\beta^2 Eh|\eta|}}\alpha_b(\phi_s) = 16\frac{Q_s}{h|\eta|\sqrt{|\cos\phi_s|}}\alpha_b(\phi_s) \tag{2.75}$$

where α_b is the ratio of the bucket area of the accelerating bucket and the stationary bucket,

$$\alpha_b(\phi_s) = \frac{1}{4\sqrt{2}}\int_{\phi_m}^{\pi-\phi_s}\left[\frac{|\eta|}{\eta}[\cos\phi + \cos\phi_s - (\pi - \phi - \phi_s)\sin\phi_s]\right]^{\frac{1}{2}} d\phi. \tag{2.76}$$

It can be approximated with a simpler relationship

$$\alpha_b \approx \frac{1 - \sin\phi_s}{1 + \sin\phi_s} \tag{2.77}$$

2.3.4 Stationary bucket

The RF bucket formed without acceleration is called the stationary bucket. In comparison with an accelerating bucket (where $\phi_s \neq 0$ or π), with the same machine parameters and RF voltage, it has a larger momentum width and bucket area. The shape of this bucket is symmetric relative to the RF phase (Fig. 2.12), which is either zero for $\gamma < \gamma_{tr}$ or π for $\gamma > \gamma_{tr}$. The full length of the bucket is 2π with respect to phase and $2\pi/h$ with respect to θ. The height of the bucket defines the maximum momentum deviation. In longitudinal dynamics, this height is also called momentum

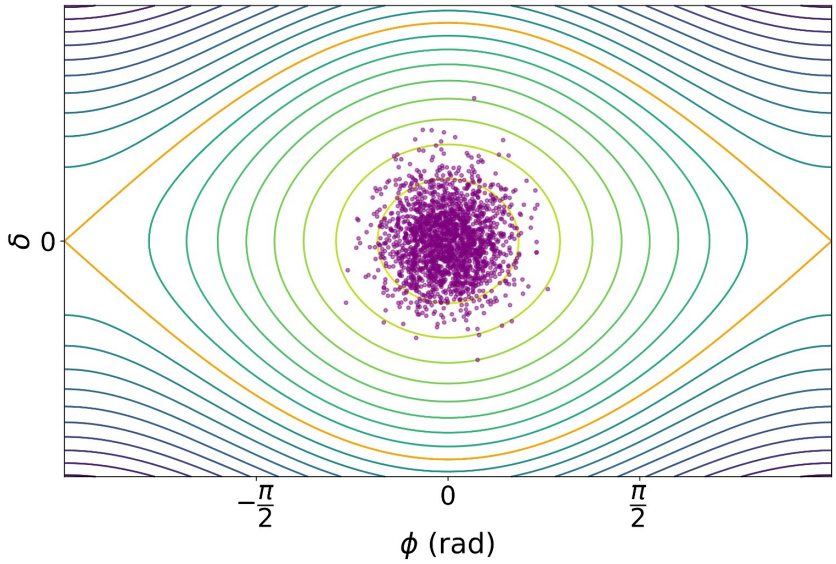

Figure 2.12: *The particle distribution (purple dots) inside stationary bucket below transition with* $\phi_s = 0$.

acceptance of the accelerator and is defined as,

$$\delta_B = \left[\frac{\Delta p}{p}\right]_{rf} = \frac{2Q_s}{h\eta} = \frac{1}{\beta}\sqrt{\frac{2qV}{\pi h\eta E}} \tag{2.78}$$

and comparing to equation of bucket area (equation (2.75)) when $\phi_s = 0$ gives a simple relationship between bucket area and bucket height

$$A_B = 8\delta_B = \frac{8}{\beta}\sqrt{\frac{2qV}{\pi h\eta E}}. \tag{2.79}$$

2.3.5 Longitudinal emittance

Similarly to the previously defined transverse emittance, the longitudinal emittance signifies the area of the beam in longitudinal phase space. The r.m.s emittance in the longitudinal plane is calculated, for example, in ESME [71] using its longitudinal

coordinates (θ, E) for a distribution of N macroparticles using

$$\epsilon = \frac{\tau_s}{2}\sqrt{\langle\Delta\theta\rangle^2\langle\Delta E\rangle^2 - (\langle\Delta\theta\Delta E\rangle)^2} \tag{2.80}$$

where the sums are over the macroparticles. Multiplying this by six gives an emittance value containing 95% of the particles. If both the r.m.s bunch length and the energy spread are known, then the emittance is

$$S_{95\%} = 6\pi\sigma_t\sigma_\delta. \tag{2.81}$$

The limitation of the presented methods is that they are not precise in the case when the particle distribution has a completely non-elliptical shape. The commonly used units again depend on simulation codes and regional accelerator physicists community, usually, these are $eV\cdots$ and mm·mrad.

2.3.6 Matching conditions

A requirement for matching in transverse phase space exists because of the need to inject the beam from one storage ring to another ring or transfer line with minimal losses. Similarly, matching conditions are also present in longitudinal phase space. Without compliance with the matching terms of the beam, particles may be lost due to a mismatch with the RF bucket, or severe phase space distortion may happen if the beam is injected into a larger RF bucket. If a continuous monochromatic beam, for example, is injected into an accelerator with too large a bucket as shown in Fig. 2.13, it will lead to an emittance distortion or "filamentation". This phenomenon occurs due to the fact that the synchrotron oscillation is non-linear and the frequency changes with the amplitude of the oscillation. In practice, the beam eventually occupies all available phase space.

The process is significantly different if the RF voltage is decreased and only spans the momentum spread of the beam. The phase space density for the central part of the

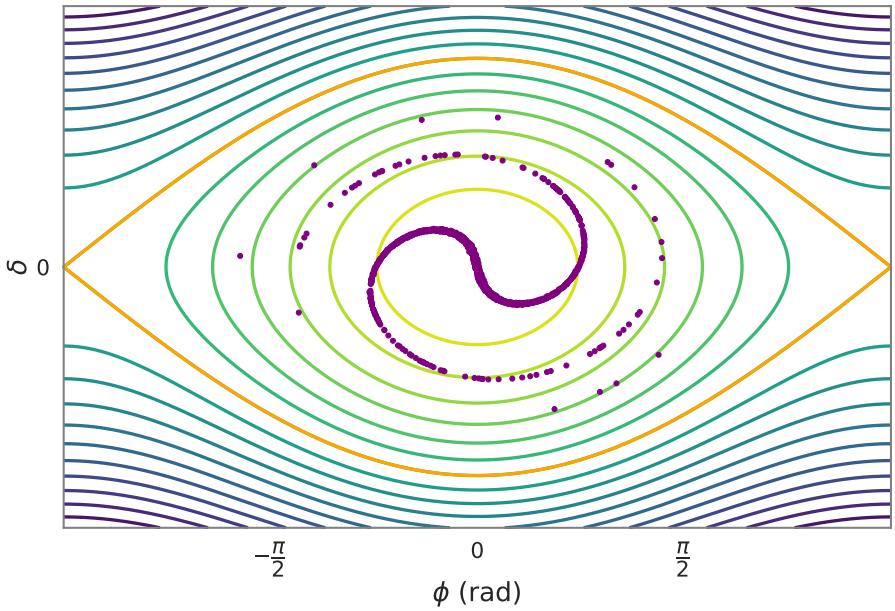

Figure 2.13: *Bunch filamentation in the case of mismatched injection.*

beam will not be distorted. However, some particles will not be captured, especially those near the unstable points of the separatrix.

The same type of problem also exists for bunched beams during injection or manipulation processes. The bunch length might be shorter than the RF wavelength or we may want to convert a bunch with a large momentum spread into a continuous beam with a small momentum spread. Regardless of the desired modification to the bunch distribution in phase space, there are methods to allow these transformations

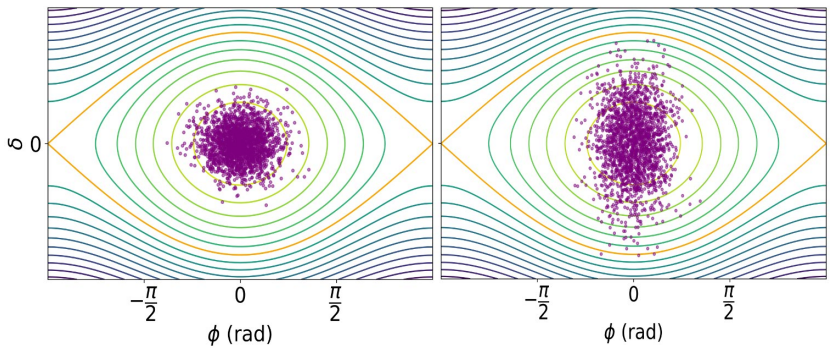

Figure 2.14: *Correctly matched particle bunch (left side). An incompatible bunched beam that requires RF voltage scaling (right side).*

while maintaining constant emittance.

For instance, to accept a bunched beam with a bunch length shorter than the RF wavelength, in the same way as the continuous beam by matching only the momentum acceptance shown in the right part of Fig 2.14 would cause phase space dilution. For the correct matching procedure, the RF voltage needs to be adjusted such that a phase space trajectory closely surrounds the injected beam. The same problems will happen if the distribution is injected off-energy or with a phase offset.

2.3.7 Adiabaticity

The most efficient method that allows almost all particles in a uniform longitudinal distribution to be captured is to raise the RF voltage very slowly [72] and is called *adiabatic capture*. To capture a beam adiabatically, without gain or loss of total energy, the RF voltage growth in time should be slow enough to achieve a linear variation of the phase space parameters, T_s and Ω_s, which helps to avoid emittance distortion. A number of parameters play an important role in how efficient this process is. The right selection of the shape of the voltage ramp, ramping time t_{ramp}, initial and final values of amplitude, V_i and V_f, phase angle ϕ and frequency ω_{rf} define the performance of adiabatic capture and various longitudinal manipulations. Figure 2.15 illustrates two commonly used voltage ramps.

Iso-adiabatic voltage ramp

The degree of the adiabaticity is assessed with the so-called adiabaticity parameter that defined as

$$\alpha_{ad} = \frac{1}{2\pi}\left|\frac{\mathrm{d}(T_s)}{dt}\right| = \left|\frac{1}{\Omega_s^2}\frac{\mathrm{d}(\Omega_s)}{dt}\right| \ll 1. \tag{2.82}$$

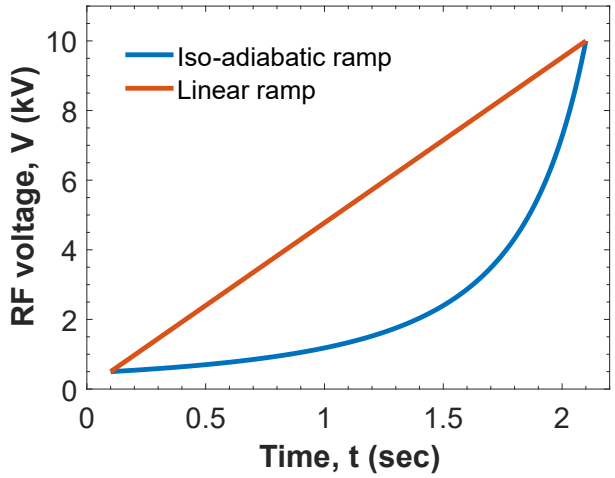

Figure 2.15: *A linear voltage ramp in comparison with an iso-adiabatic ramp.* $V_i = 500\,\mathrm{V}$, $V_f = 10\,\mathrm{kV}$ *and* $t_{ramp} = 2$ *seconds.*

From the last condition, we can obtain the equation for voltage dependence on time. Due to equation (2.67), we know that in the stationary case

$$T_s = 2\pi k \frac{1}{\sqrt{V}}, \text{where} \quad k = \omega_s \sqrt{\frac{2\pi\beta^2 E}{hq\eta}}. \tag{2.83}$$

Substituting T_s with the adiabaticity parameter, the ODE

$$\alpha_{ad} dt = \frac{1}{2} k \frac{dV}{V\sqrt{V}} \tag{2.84}$$

can be obtained.

Separation and integration of this equation results in the dependence of α_{ad} on ramp time and RF voltages

$$\alpha_{ad} = \frac{k}{T_{ramp}} \left(\frac{1}{\sqrt{V_i}} - \frac{1}{\sqrt{V_f}} \right). \tag{2.85}$$

The full solution obtained via indefinite integration defines the ramp form as $\alpha_{ad} t + C =$

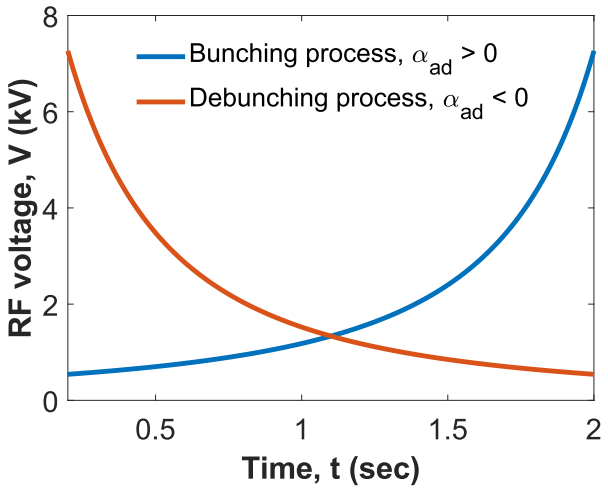

Figure 2.16: *Voltage ramps for bunching and debunching processes.*

$k/\sqrt{V}$ which gives a voltage profile of

$$V(t) = \frac{1}{\left(\frac{t}{T_{ramp}}\left(\frac{1}{\sqrt{V_i}} - \frac{1}{\sqrt{V_f}}\right) + C\right)^2}. \tag{2.86}$$

This solution can be written as a function of the initial value $V(t = 0) = V_i$ and the final value $V(t = T_{ramp}) = V_f$

$$V(t) = \frac{V_i}{\left(1 - \frac{t}{T_{ramp}}\left(1 - \frac{\sqrt{V_i}}{\sqrt{V_f}}\right)\right)^2}. \tag{2.87}$$

For decreasing synchrotron periods T_s, the amplitude V will increase, and α_{ad} is positive leading to a bunching process. For increasing synchrotron periods, the amplitude V will decrease and α_{ad} is negative resulting in a debunching process. Correspondingly, the voltage ramps are mirrored as shown in Fig. 2.16.

Linear voltage ramp

For other bunch manipulation techniques, the simple linear increase in RF voltage

amplitude is also considered

$$V(t) = V_i + \frac{t}{T_{ramp}}(V_f - V_i). \tag{2.88}$$

2.3.8 Bunch compression with RF systems

Whenever the adiabatic change of the RF voltage cannot be used to achieve the required beam characteristics, non-adiabatic methods are applied. The corresponding RF techniques are called *bunch compression*, *bunch rotation* and *phase rotation* [73–75]. The shared principle is to let the bunch, initially elongated in phase, rotate in a maximum height bucket, making it shorter. Even with a single RF system, various techniques can be used to compress the bunch.

Bunch rotation due to RF voltage increase

Consider a bunch with a very small momentum spread but a long bunch length as shown in Fig. 2.17a. To transform this bunch into a short bunch we could suddenly increase the RF voltage in a time short compared to the synchrotron period Ω_s. The

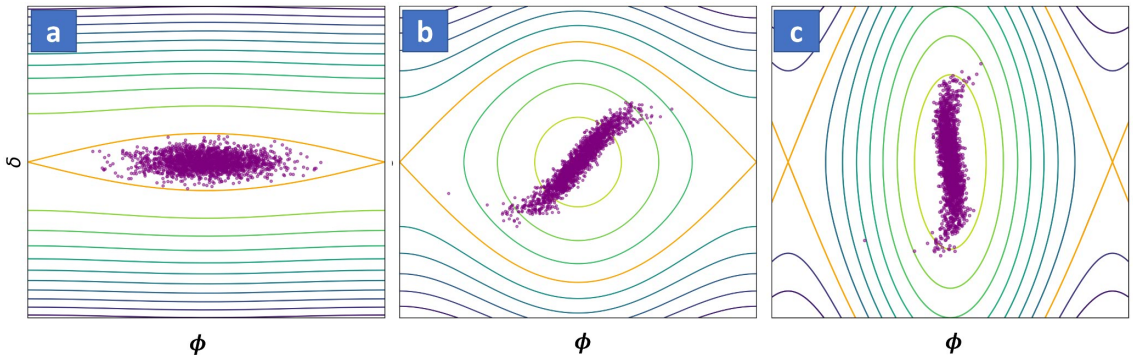

Figure 2.17: *a) An initial bunch with a long bunch length. b) The bunch rotation process after voltage increase. c) Adjusting the bucket to the new bunch.*

whole bunch then starts to rotate within the new bucket (Fig. 2.17b) exchanging bunch length for momentum spread. After 1/4 of a synchrotron period, the bunch length will reach its shortest value and starts to increase again through further rotation of the

bunch unless the RF voltage is suddenly increased a second time to stop the phase space rotation of the bunch (Fig. 2.17b). The continuous rotation happens because the bunch boundary does not coincide with a phase space trajectory. The RF voltage therefore must be increased to such a value that all particles on the bunch boundary follow the same phase space trajectory. The maximum momentum deviation $(\Delta p/p)_0$ and the maximum phase deviation ϕ_0 for the starting situation in Fig. 2.17a are linked as

$$\left[\frac{\Delta p}{p}\right]_0 = \frac{\Omega_{s0}}{\eta\omega_{rf}}\phi_0 \tag{2.89}$$

where Ω_{s0} is the starting synchrotron oscillation frequency for the RF voltage V_0. To start bunch rotation the RF voltage is increased to V_1 (Fig. 2.17b) and after a quarter synchrotron oscillation period at the frequency $\Omega_{s1} \propto \sqrt{V_1}$ the phase deviation ϕ_0 has transformed into a momentum deviation

$$\left[\frac{\Delta p}{p}\right]_1 = \frac{\Omega_{s1}}{\eta\omega_{rf}}\phi_0 \tag{2.90}$$

at the same time the original $(\Delta p/p)_0$ now corresponds to ϕ_1 given by

$$\left[\frac{\Delta p}{p}\right]_0 = \frac{\Omega_{s1}}{\eta\omega_{rf}}\phi_1. \tag{2.91}$$

Now we need to stop further phase space rotation of the whole bunch. This can be accomplished by increasing the RF voltage for a second time in a time short compared to the synchrotron oscillation period. This is done in such a way that the new bunch length or ϕ is on the same phase space trajectory as the new momentum spread $(\Delta p/p)_1$ shown in Fig.2.17c. The required RF voltage is then determined by

$$\left[\frac{\Delta p}{p}\right]_1 = \frac{\Omega_{s2}}{\eta\omega_{rf}}\phi_1. \tag{2.92}$$

After taking the ratio between equation (2.92) and (2.89) we obtain

$$\frac{\phi_1 \Omega_{s2}}{\phi_0 \Omega_{s0}} = \frac{(\Delta p/p)_1}{(\Delta p/p)_0}. \tag{2.93}$$

Replacing the ratio between momentum spreads by the ratio of equations (2.90) and (2.91), taking into account the fact that $\Omega_{0i} \propto \sqrt{V_i}$ and ϕ_i is proportional to bunch length l_i, we finally get a scaling law for the bunch length compression

$$\frac{l_1}{l_0} = \left(\frac{V_0}{V_2}\right)^{1/4}. \tag{2.94}$$

The bunch length can be reduced by increasing the RF voltage in a two-step process and the bunch length reduction scales like the fourth power of the RF voltage. This phase space manipulation is symmetric in the sense that a beam with a large momentum spread and a short bunch length can be converted into a bunch with a smaller momentum spread at the expense of the bunch length by reducing the RF voltage in two steps.

Alternatively, the bunch lengthening procedure can be carried out with a non-adiabatic decrease of RF voltage until the bunch area will be almost equal to the bucket area. Afterwards, a rapid increase to V_1 will initialise the bunch rotation process. If further capture/ejection procedure is not required, the bunch length ratio $l_1/l_0 \propto \sqrt{V_0/V_1}$. This technique is applied in most of the machines, mentioned in Chapter 1, enabling them to achieve shorter bunch lengths or smaller momentum spreads.

Bunch rotation because of RF phase jump

Once the maximum voltage amplitude is reached, bunch compression or stretching can be performed via the RF phase shift by π so the centre of the bunch will be located at the unstable fixed point (UFP) as shown in Fig 2.18a. This bunch will begin compressing in one direction and stretching in the other direction along the separatrix

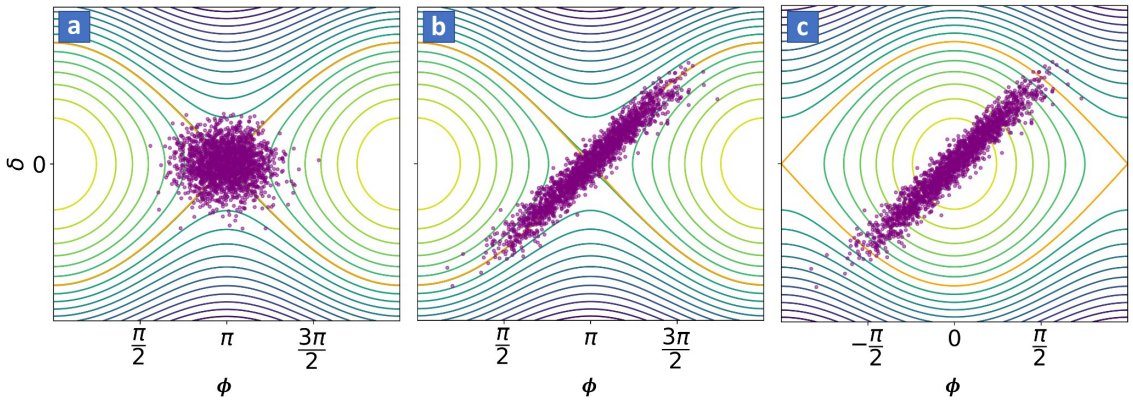

Figure 2.18: *RF compression: Phase rotation in unstable point. a) Matched bunch at the unstable fixed point. b) Bunch elongation procedure. c) Jumping back to the stable fixed point.*

orbit as shown in Fig 2.18b. In the linear approximation, the bunch length and bunch height will change according to

$$exp(\pm\Omega_s t_{UFP}) = exp(\pm\frac{2\pi t_{UFP}}{T_s}) \tag{2.95}$$

where T_s is the synchrotron period and t_{UFP} is time duration which bunch stays in the UFP. Afterwards we can bring the bunch back to the stable fixed point where the residual bunch rotation will happen, Fig. 2.18c.

Now we can find the optimal ratio of bunch compression through the phase shift method. For this, we will introduce momentum deviation in longitudinal phase space in the case of a stationary bucket of

$$\mathcal{P} = -\frac{|\eta|h}{Q_s}\delta. \tag{2.96}$$

The Hamiltonian in normalised coordinates then becomes

$$H_{st} = \frac{1}{2}Q_s\mathcal{P}^2 + 2Q_s\sin^2\frac{\phi}{2}. \tag{2.97}$$

Close to the UFP, the Hamiltonian separatrix can be approximated with two straight

lines crossing at 45°. From this, the maximum phase coordinate ϕ_{max} to which bunch phase can increase and stay within the bucket after another 180° phase jump is given approximately by

$$\frac{1}{2}\phi_{max}^2 + 2\sin^2\left(\frac{\phi_{max}}{2}\right) \approx 2. \tag{2.98}$$

Thereby we obtain $\phi_{max} = \sqrt{2}$. Due to longitudinal emittance conservation, we obtain a relation between emittance in UFP and stable fixed point

$$\pi\sigma_{\phi,i}^2 = \pi\sigma_{\phi,f}\sigma_{\mathcal{P},f}. \tag{2.99}$$

Then assuming 2σ of the particle distribution will reach $\phi_{max} = \sqrt{2}$, we find

$$\frac{\sigma_{\phi,i}}{\sigma_{\phi,f}} = \frac{\sigma_{\mathcal{P},f}}{\sigma_{\phi,i}} \approx \frac{\sqrt{2}}{\sqrt{3}\sigma_{\phi,i}}, \tag{2.100}$$

and the time to reach maximum bunch compression is

$$\Omega_s t_{UFP} = \ln\frac{1}{\sigma_{\phi,i}} - 0.203 \tag{2.101}$$

If we write the result of voltage compression [75] in a manner similar to equation (2.94), we obtain

$$\frac{\sigma_{\phi,i}}{\sigma_{\phi,f}} = \frac{A_B}{S_{95\%}} = \frac{2\sqrt{2}}{\sqrt{3\pi}\sigma_{\phi,i}}, \tag{2.102}$$

where we used the fact that the bucket area A_B in normalised coordinates is 16 and the bunch area is equal to $6\pi\sigma_{\phi,i}^2$. Consequently, we can find that voltage jump compression is more efficient by a factor $2/\sqrt{\pi}$. The major advantage of the phase jump technique is that only the RF phase needs to be manipulated.

Bunch splitting

Another possible way to decrease resulting bunch length is *bunch splitting* which is used to multiply the number of existing bunches by two or three depending on a number of available RF harmonics/systems [76, 77]. The reverse process aimed at increasing the resulting intensity is called *bunch merging*. Experimental confirmation of the bunch

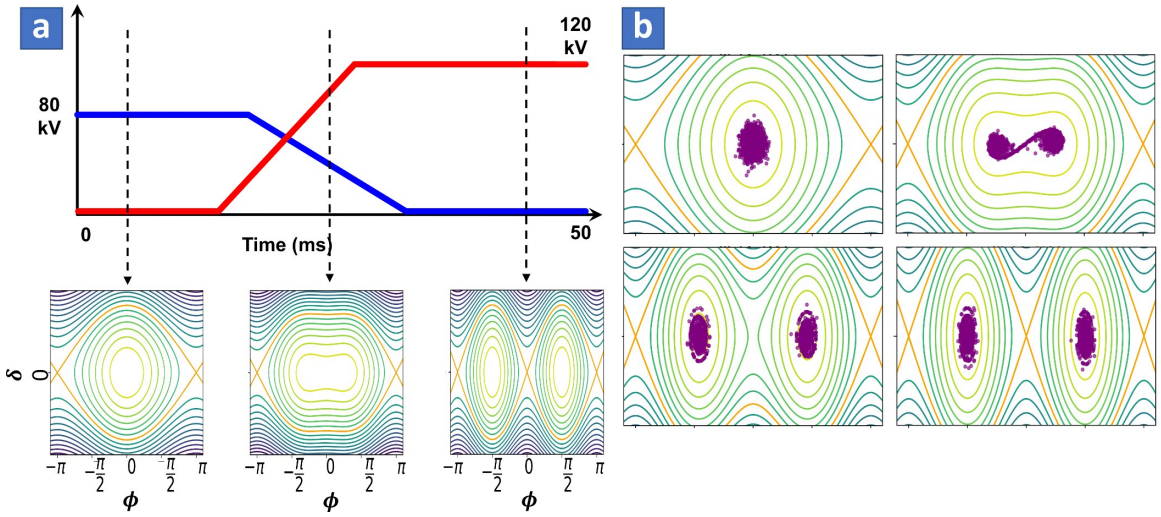

Figure 2.19: *Double splitting of the bunch. a) Voltage program for two RF cavities in time with corresponding evolution of the bucket. b) Four steps of the matched particle distribution evolution during the splitting process.*

splitting method was demonstrated and used for operation in the CERN PS [77] for increasing the number of circulating bunches in the ring. This has since become integral in the production of bunches in the PS (4+2 bunches–>72) for the LHC [78]. Despite the fact that the application of bunch splitting is limited in use, these processes have a notable advantage with respect to iso-adiabatic de-bunching/re-bunching of being able to stay quasi-adiabatic and preserve the emittance. Splitting of a single bunch into two happens using two RF systems simultaneously with a harmonic ratio of two. During this process, the potential well of the second RF system within the stable RF bucket is created together with slowly switching to a higher harmonic of RF system.

The initial bunch is captured by the first RF system (V_1, h_1) while the second $(V_2, h_2 = 2h_1)$ is disabled. The unstable phase of the second harmonic is centred

on the bunch. Then the voltage V_2 is slowly raised and V_1 is decreased, the bunch stretches in phase and progressively splits into two symmetric "bunchlets" as illustrated in Fig.2.19a. It is also worth noting that the best result is observed with $V_1 = V_{sep}$,

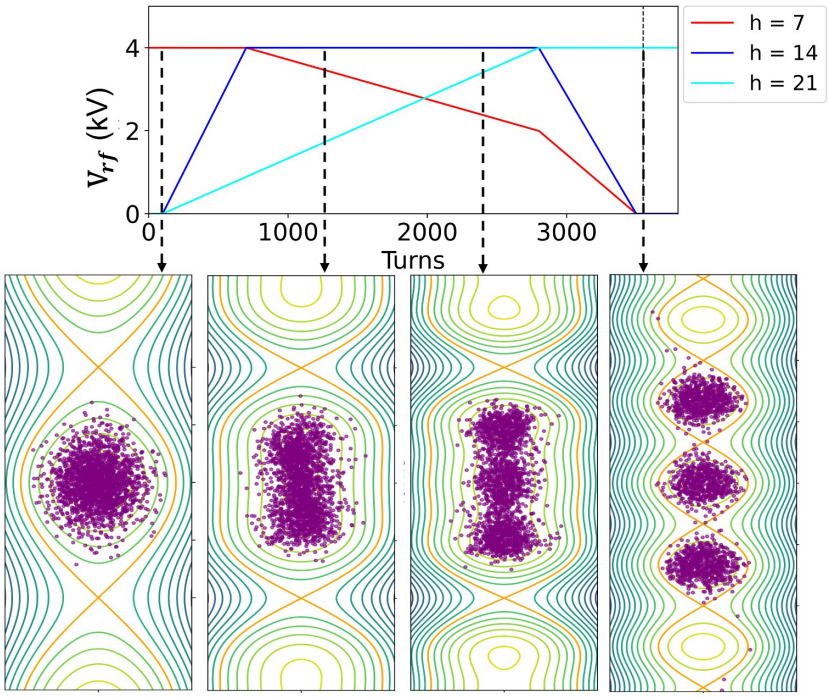

Figure 2.20: *Triple bunch splitting process. Voltage programme for three RF systems (top) and the corresponding evolution of the particle distribution in time.*

such that, at the time when two bunches have just formed from the splitting, the initial bunch would occupy an area in longitudinal phase space equal to 1/3 rd of the bucket acceptance when $V_2 = 0$. Voltage ramps are generally linear functions of time and the total duration of the splitting procedure should be larger than five synchrotron periods of the bucket with parameters $V_1 = V_{sep},\ h = h_1$. Each final "bunchlet" has half of the emittance of the initial bunch, and minimal blow-up is observed. A simulation example of a double splitting process in the PS performed in PyHEADTAIL [79] and shown in Fig. 2.19b has four evolution steps. A bunch at h=8 is split into two at h=16 within 25 ms, almost without emittance blow-up.

Similarly, the bunch splitting into three bunchlets requires three simultaneous RF

harmonics. The relative stable phases between harmonics as well as the voltage ratios, must be precisely estimated for the initial distribution to split evenly into the new bunches with longitudinal emittance mostly preserved. The evolution in longitudinal phase space and the voltages as a function of time for triple bunch splitting are illustrated in Fig.2.20. This combination, together with a bunch rotation afterward may decrease the achieved bunch length further. Another advantage of the bunch splitting technique is that it decreases the influence of heating effects caused by collective particle motion which is discussed next.

2.4 Collective effects in multi-particle distribution.

When the beam current increases, the beam can no longer be considered as a bunch of non-interacting single particles. As a result of the charge of the particles, the cross-over Coulomb interaction leading to the so-called *space charge* effect, *intrabeam scattering* (IBS) and *electron cooling* have to be considered. These collective processes can have a significant impact in comparison to single particle beam dynamics. Therefore the comprehension of relevant collective processes and the difficulties because of them are important for an optimal accelerator or experimental design. The IBS and space charge are considered as "incoherent" effects due to the fact that they result mainly in changes to the tune shifts and beam emittance without creating or amplifying core features within the beam.

2.4.1 Space charge effect.

Two space charge effects are distinguished: the direct space charge and the indirect (or image) one [80–83], and references therein. This section focuses mainly on the direct variant of the space charge. It comes from the interaction between the particles of a single beam and without interaction with the surrounding vacuum chamber.

Consider two particles with the same charge (for instance, protons) in a vacuum. At rest, they experience repulsion due to the Coulomb force. When travelling at velocity $v = \beta c$, they represent two parallel currents $I = vq$ in the lab frame, which attract each other by the effect of their magnetic fields. The diagram in Fig. 2.21 shows that the overall effect is still repulsive but decreases with velocity. Special relativity suggests that the forces become equal at the speed of light and thus cancel each other. To have a better understanding of the space charge effect, assume a collection of charged particles travelling in a coasting beam with a circular cross section, as shown in Fig. 2.22. The Coulomb repulsion pushes the test particle away from the beam centre; the overall force is zero in the beam centre and increases towards the edge. This behaviour

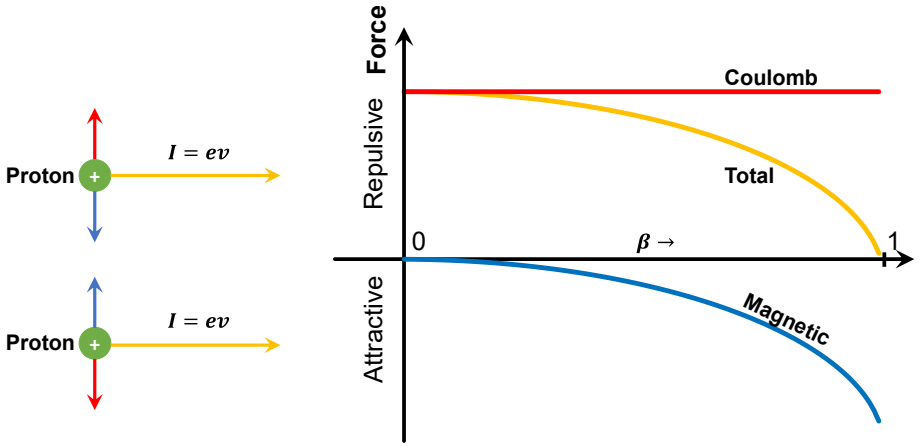

Figure 2.21: *Representation of two moving particles with two currents (left). A balance between attractive and repulsive forces (right) depends on the speed of particles.*

applies also to the test particle in a travelling beam, represented by parallel currents, except that the magnetic force vector is directed towards the beam centre. A circular coasting beam of radius r_b and uniform charge density η moves with constant velocity $v = \beta c$. It has a linear charge density (charge per unit length [C/m]) of $\lambda = \pi r_b^2 \rho$, a current density [A/m^2] of $J = v\rho$, and a total current of $I = v\lambda$. Figure 2.23 shows

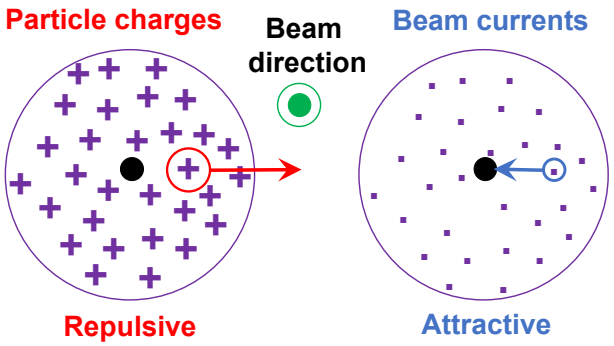

Figure 2.22: *Force directions within the uniform circular beam.*

such a beam. In the following, the electric $\vec{E}$ and magnetic $\vec{B}$ fields on the surface of a cylinder with radius $r < r_b$ are calculated (using polar coordinates r and ϕ). Due to symmetry, the electric field has just a radial component E_r, while the magnetic field lines are just circles around the cylinder, azimuthal B_ϕ component only. E_r can be

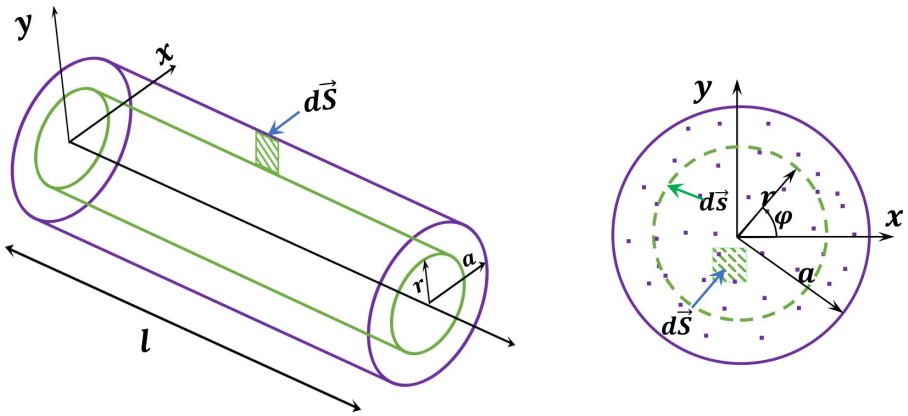

Figure 2.23: *Uniform circular beam representation.*

calculated then from the Maxwell equation

$$\boldsymbol{\nabla} \cdot \vec{E} = \frac{\eta}{\epsilon_0} \tag{2.103}$$

and its integral form, Gauss' law (integration over volume and surface of a cylinder with radius r and length l)

$$\iiint \boldsymbol{\nabla} \cdot \vec{E}\, \mathrm{d}V = \int \int \vec{E} \cdot \mathrm{d}\vec{S} \tag{2.104}$$

where dV is a volume element inside the cylinder, and $d\vec{S}$ an element of its surface (Fig. 2.23), yielding

$$\pi l r^2 \frac{\eta}{\epsilon_0} = 2\pi l r E_r \tag{2.105}$$

from which one can derive the radial electric field

$$E_r = \frac{I}{2\pi\epsilon_0 \beta c} \frac{r}{a^2} \tag{2.106}$$

Similarly, the azimuthal magnetic field B_ϕ is determined from another Maxwell equa-

tion

$$\boldsymbol{\nabla} \times \vec{B} = \mu_0 \vec{J} \tag{2.107}$$

and its integral form, Stokes' theorem (integral of the curl of a vector field over surface equals line integral of a vector field over closed boundary defined by this surface)

$$\oint \vec{B} \cdot \mathrm{d}\vec{l} = \iint (\boldsymbol{\nabla} \times \vec{B}) \cdot \mathrm{d}\vec{S} \tag{2.108}$$

where $\mathrm{d}\vec{l}$ is a path element in the cross-section along the circle with radius r, and $\mathrm{d}\vec{S}$ a surface element within this circle (Fig. 2.23). The integrals in equation (2.108) over the cylinder of radius r and length l result in

$$2_\phi = \mu_0^2 v \eta \tag{2.109}$$

yielding the magnetic field

$$B_\phi = \frac{I}{2\pi\epsilon_0 c^2} \frac{r}{a^2}. \tag{2.110}$$

Indeed, both electric and magnetic fields vanish at $r = 0$, and both increase linearly with r up to the edge of the cylinder ($r = a$).

These fields exert a force F_r on test particles at radius r, which is now calculated like the Lorentz force

$$\vec{F_r} = q(E_r + v_s \times B_\phi), \tag{2.111}$$

indicating that the force vector has a purely radial component F_r. Inserting E_r and B_ϕ from equations 2.106 and 2.110 one gets for the radial force on the test particle at

radius r

$$F_r = \frac{I}{2\pi\epsilon_0\beta c}(1-\beta^2)\frac{r}{a^2} = \frac{I}{2\pi\epsilon_0\beta c}\frac{1}{\gamma^2}\frac{r}{a^2} \tag{2.112}$$

In the $(1-\beta^2)$ term, the "1" represents the electric force, and the β^2 the magnetic one, and indeed they cancel at $\beta = 1$. It is replaced by $1/\gamma^2$ in equation (2.112). Replacing r by the transverse coordinates x and y results in the horizontal (F_x) and vertical (F_y)) forces which are linear in x and y, respectively:

$$\begin{aligned} F_x &= \frac{I}{2\pi\epsilon_0\beta c\gamma^2 a^2}x \\ F_y &= \frac{I}{2\pi\epsilon_0\beta c\gamma^2 a^2}y. \end{aligned} \tag{2.113}$$

Additionally, it is illustrative to compare the focusing effects of a quadrupole with the uniform high-intensity beam for which equation (2.113) applies. Figure 2.24 shows the

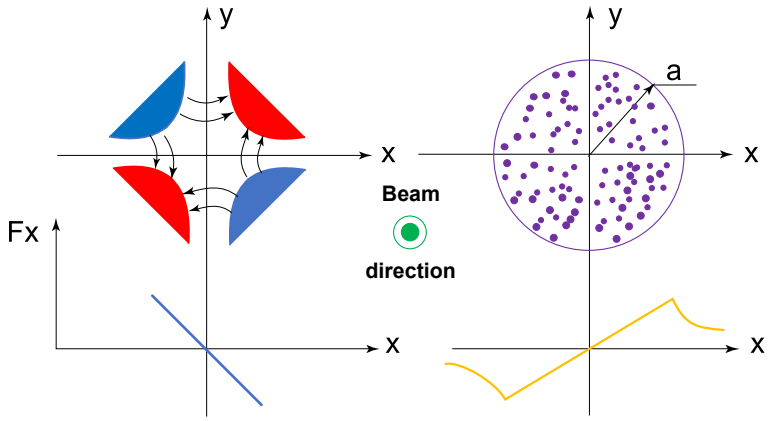

Figure 2.24: *Comparison of focusing/defocusing effect from a quadrupole (left) and from the direct space charge (right).*

force F_x vs x for a (horizontally focusing) quadrupole and for a space charge dominated uniform beam. While the quadrupole is focusing in one and defocusing in the other plane, direct space charge leads to defocusing in both planes.

As we know from Section 2.2, a focusing-defocusing (FODO) transport line is

described by Hill's equation

$$\frac{dx^2}{ds^2} + K_x(s)x = 0. \tag{2.114}$$

where $K_x(s)$ denotes the normalised gradients (positive if focusing, negative if defocusing) of the quadrupoles along the beam paths (here for the horizontal plane). To describe the continuous defocusing action of space charge, we can implement an additional perturbation term $K_{SC}(s)$:

$$\frac{dx^2}{ds^2} + (K_x(s) + K_{SC}(s))x = 0. \tag{2.115}$$

$K_{SC}(s)$ is derived by expressing dx^2/ds^2 in terms of transverse acceleration d^2x/dt^2 and thus of the force F_x from equation (2.113)

$$\frac{dx^2}{ds^2} = \frac{1}{\beta^2 c^2}\frac{d^2x}{dt^2} = \frac{F_x}{m_0\gamma} = -\frac{2r_0 I}{qa^2\beta^3 c\gamma^3}x \tag{2.116}$$

where $r_0 = q^2/4\pi\epsilon_0 m_0 c^2$ is the classical particle radius, 1.54×10^{-18} m for protons. For heavy ions of charge Z and atomic mass A the classical radius is $r_{ion} = r_0 Z^2/A$.

Hill's equation with space charge (for an unbunched beam with circular cross section and constant charge density) is then

$$\frac{dx^2}{ds^2} + (K_x(s) - \frac{2r_0 I}{qa^2\beta^3 c\gamma^3})x = 0. \tag{2.117}$$

Note the negative sign of the space charge term, reducing the overall focusing of the FODO sequence. The direct space charge leads to defocusing in either plane and therefore one would expect that particles in a high-intensity beam will experience a lowering of their betatron tune Q by ΔQ. The calculation below applies to the simplest (pretty explanatory only) case of an unbunched beam, circular cross section everywhere in the accelerator, and constant charge density. Applying equation (2.114) to a synchrotron lattice will yield the unperturbed horizontal Q_{x_0}, while equation (2.117) introduces a

space charge defocusing ΔQ_x which is readily calculated by integrating the weighted gradient errors around the circumference $2\pi R$:

$$\Delta Q_x = \frac{1}{4\pi}\int_0^{2\pi R} K_{SC}(s)\beta_x(s)\mathrm{d}s \tag{2.118}$$

Taking $K_{SC}(s)$ from equation (2.117) yields

$$\Delta Q_x = -\frac{1}{4\pi}\int_0^{2\pi R} \frac{2r_0 I}{q\beta^3 c\gamma^3}\frac{\beta_x(s)}{a^2}\mathrm{d}s = -\frac{2r_0 R I}{q\beta^3 c\gamma^3}\left\langle \frac{\beta_x(s)}{a^2(s)}\right\rangle. \tag{2.119}$$

The term $\langle\beta_x(s)/a^2(s)\rangle$ is just $1/\epsilon_x$, the inverse of the horizontal emittance, and thus an invariant. Replacing I by $Nq\beta c/(2\pi R)$ (with N the number of particles in the accelerator) and extending to the vertical plane (y) one gets for the direct space charge tune shift

$$\Delta Q_{x,y} = -\frac{r_0 N}{2\pi\epsilon_{x,y}\beta^2\gamma^3} \tag{2.120}$$

$\epsilon_{x,y}$ is the transverse emittance in either plane containing 95% of the particles. The main features are:

- The tune shift is proportional to the intensity.
- It scales with $1/\gamma^3$, so it becomes very small for all high-energy synchrotrons beyond 10 GeV.
- It does not depend on the machine radius R but on mostly the machine optics.

Realistic beams

In the preceding section, only the beam with constant charge density was considered. In what follows, an example of a non-uniform distribution, namely a multivariate Gaussian density in the elliptical beam cross section.

The local linear particle density λ_z for generic distribution is defined by

$$\lambda(z) = \iint \rho(x, y, z)\, \mathrm{d}x\mathrm{d}y \tag{2.121}$$

where $\rho(x, y, z)$ is the local particle density normalised to the total number of particles in the beam $\int_{-\infty}^{\infty} \lambda(z)\mathrm{d}s = N_p$. In the case of the bunched beam linear particle density is

$$\lambda(z) = \frac{N}{n_b\sqrt{2}\sigma_z}, \tag{2.122}$$

where N is the total number of particles in the machine, n_b is the number of circulating bunches and σ_z is the r.m.s bunch length for a Gaussian distribution.

For the transverse part only, $\rho(x, y)$ might be defined as

$$\rho(x, y) = \frac{\lambda}{2\pi\sigma_x\sigma_y} \exp\left\{-\frac{x^2}{2\sigma_x^2} - \frac{y^2}{2\sigma_y^2}\right\}. \tag{2.123}$$

The potential for a transverse bi-Gaussian charge distribution had been derived by Teng [84] and can be expressed as

$$U(x, y) = -\frac{q}{4\pi\epsilon_0}\lambda \int_0^{\infty} \frac{1 - \exp\left\{-\frac{x^2}{2\sigma_x^2+t} - \frac{y^2}{2\sigma_y^2+t}\right\}}{\sqrt{(\sigma_x^2 + t)(\sigma_y^2 + t)}}\, \mathrm{d}t. \tag{2.124}$$

From this potential, we obtain for example the horizontal electric field component by differentiation

$$E_x = -\frac{\partial U(x, y)}{\partial x} = -\frac{q}{4\pi\epsilon_0}\lambda x \int_0^{\infty} \frac{\exp\left\{-\frac{x^2}{2\sigma_x^2+t} - \frac{y^2}{2\sigma_y^2+t}\right\}}{(\sigma_x^2 + t)\sqrt{(\sigma_x^2 + t)(\sigma_y^2 + t)}}\mathrm{d}t. \tag{2.125}$$

No closed analytical expression exists for these integrals unless we restrict ourselves to a symmetry plane with $x = 0$ or $y = 0$ and small amplitudes $y \ll \sigma_y$ or $x \ll \sigma_x$, respectively. These assumptions are appropriate for most space charge effects and the

associated electric fields in horizontal and vertical mid-planes become

$$E_x = \frac{2\lambda}{4\pi\epsilon_0}\frac{x}{\sigma_x(\sigma_x+\sigma_y)}$$
$$E_y = \frac{2\lambda}{4\pi\epsilon_0}\frac{y}{\sigma_y(\sigma_x+\sigma_y)} \tag{2.126}$$

and the magnetic fields according to equation ($cB_{y,z} = \pm\beta E_{x,y}$) are from equation (2.126)

$$B_x = -\frac{2\mu_0\lambda c\beta}{4\pi}\frac{y}{\sigma_y(\sigma_x+\sigma_y)}$$
$$B_y = \frac{2\mu_0\lambda c\beta}{4\pi}\frac{x}{\sigma_x(\sigma_x+\sigma_y)}. \tag{2.127}$$

All fields increase linearly with an amplitude and we note that the field components in the horizontal mid-plane are generally comparable to those in the vertical mid-plane and $\sigma_y \approx \sigma_x$ because of the circular beam shape.

With these fields and the Lorentz equation, we formulate the transverse force acting on a single particle within the same particle beam. Since both expressions for the electrical and magnetic field differ only by the factor β we may, for example, derive from the Lorentz equation the horizontal force F_x on a particle with charge q

$$F_x = q(1-\beta^2)E_x = \frac{2q\lambda}{4\pi\epsilon_0\gamma^2}\frac{x}{\sigma_x(\sigma_x+\sigma_y)}. \tag{2.128}$$

This equation of the defocusing component of equation (2.117) might be rewritten as

$$K_{SC} = -\frac{2r_0}{\beta^2\gamma^3}\frac{\lambda}{\sigma_x(\sigma_x+\sigma_y)}. \tag{2.129}$$

Applying obtained expression to the formulae of tune shift (equation (2.120) and assuming Gaussian distributions for all planes after integration we result in

$$\Delta Q_{x,y} = -\frac{r_0\lambda}{2\pi\beta^2\gamma^3}\frac{\langle\beta_{x,y}\rangle R}{\sigma_{x,y}(\sigma_x+\sigma_y)}, \tag{2.130}$$

where, $\langle \beta_{x,y} \rangle$ are the mean lattice functions, $\sigma_{x,y}$ the horizontal and vertical r.m.s beam sizes, λ the linear peak density, R is the machine radius. Figure 2.25 demonstrates an example of the distribution of particles' tunes for a Gaussian bunch together with a design working point shown as a light green dot.

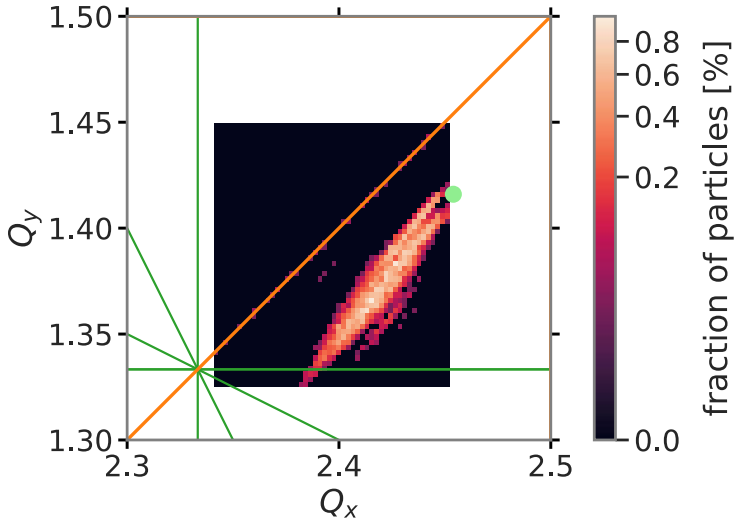

Figure 2.25: *Example of tune shift on a resonance diagram. Resonances of the second (orange) and third order (green) are shown.*

2.4.2 Intrabeam scattering

Intrabeam scattering (IBS) refers to the process of small angle multiple Coulomb scattering between charged particles within accelerator beams, resulting in the random transfer of the particle momentum and the expansion of the six-dimensional phase space. This is a relevant effect with the interplay between high beam density and particle energy in antiproton [85] and heavy ion [86] circular machines. In this section, commonly used IBS theories will be compared and summarised. Besides analytical theories, fully numerical approaches exist [87]. The particle momentum variation due to IBS process can be calculated by solving an equation of motion in the realistic optical structure considering interactions between particles. Since the calculation of the space charge effect is time consuming, one can use two methods to reduce the required particle number: 1) Molecular dynamics (MD) with periodic boundary conditions; and

2) Macroparticle simulation. For the MD method, the beam is divided into many 3D cells and the equations are solved for the particles from an individual cell.

Introduction to the theories

The first IBS theory description for accelerators was developed by Piwinski [88] and modified by Martini [89] establishing a formulation called the standard Piwinski-Martini (PM) method. Bjorken and Mtingwa (BM) [90] a few years later described the effect using a different approach and taking into account the strong focusing effect. These models of IBS analysis are based on a "Gaussian description" of the beam, which is assuming that distribution profiles are of Gaussian type for all degrees of freedom. Both BM and Martini's models are in good agreement and are compared against each other in later sections. One question that arises is "In what way is IBS in particle beams different from a similar scattering of gas molecules?". In circular accelerators, the curvature of the orbit produces a dispersion and due to this dispersion, the change of energy leads to a change in the betatron amplitude. In other words, we have a coupling of the longitudinal and transverse motion. Another consequence of this curvature effect is the negative-mass behaviour of particles so that the conservation law of beam temperature leads to a simple conclusion that below the transition energy one can have an equilibrium between the transverse and longitudinal temperatures while above the transition energy there is a continuous emittance increase in both transverse and longitudinal dimensions.

All theories and approximations calculate the horizontal (x), vertical (y) and longitudinal (p) growth rates and are defined as:

$$\begin{aligned} \frac{1}{\tau_p} &= \frac{1}{\sigma_p}\frac{d\sigma_p}{dt} \\ \frac{1}{\tau_{x_\beta}} &= \frac{1}{\sigma_{x_\beta}}\frac{d\sigma_{x_\beta}}{dt} \\ \frac{1}{\tau_{y_\beta}} &= \frac{1}{\sigma_{y_\beta}}\frac{d\sigma_{y_\beta}}{dt} \end{aligned} \tag{2.131}$$

Original Piwinski model

In his model, A. Piwinski derives the formulae for variations of the mean radial and vertical emittances, and the mean momentum spread per time unit due to a scattering event, neglecting the derivative of the beta and dispersion functions with respect to the longitudinal beam axis. For the smoothed focusing approximation only the mean values of the lattice functions are used and they are determined as follows:

$$\begin{aligned} \beta_{x,y} &= \frac{R}{Q_{x,y}}, \\ D_x = \frac{R}{Q_x^2},\ \alpha_{x,y} &= 0,\ D'_x = 0. \end{aligned} \tag{2.132}$$

here R is the ring mean radius, $Q_{x,y}$ are horizontal and vertical betatron tunes.

In the framework of this model, the growth rates are calculated in accordance with the following expressions:

$$\begin{pmatrix} \frac{1}{\tau_p} \\ \frac{1}{\tau_{x_\beta}} \\ \frac{1}{\tau_{y_\beta}} \end{pmatrix} = \begin{pmatrix} \frac{1}{2\sigma_p^2}\frac{d\sigma_p^2}{dt} \\ \frac{1}{2\sigma_{x_\beta}^2}\frac{d\sigma_{x_\beta}^2}{dt} \\ \frac{1}{2\sigma_{y_\beta}^2}\frac{d\sigma_{y_\beta}^2}{dt} \end{pmatrix} = \begin{pmatrix} nA_P\frac{\sigma_h^2}{\sigma_p^2}f(a,b,c) \\ A_P\left[f(\frac{1}{a},\frac{b}{a},\frac{c}{a}) + \frac{D_x^2\sigma_p^2}{\sigma_{x_\beta}^2}f(a,b,c)\right] \\ A_P f(\frac{1}{a},\frac{b}{a},\frac{c}{a}) \end{pmatrix} \tag{2.133}$$

where $n = 1$ for a bunched beam and $n = 2$ for an coasting beam, and constant

$$A_P = \frac{Z^4}{A^2}\frac{r_i^2 c N_b}{64\pi^2\beta^3\gamma^4\sigma_{x_\beta}\sigma_{x'_\beta}\sigma_y\sigma_{y'}\sigma_p\sigma_z} \tag{2.134}$$

with r_i, the classical particle radius, c the speed of light, N_b the bunch population, β the velocity over c, γ the Lorentz energy factor, and σ_z the bunch length. For a coasting beam, one has to use the substitution:

$$\frac{N_b}{\sigma_z} = \frac{2\sqrt{\pi}N}{C}. \tag{2.135}$$

The standard deviations are determined here as follows:

$$\sigma_{x_\beta,y} = \sqrt{\epsilon_{x,y}\beta_{x,y}},\ \sigma_{x'_\beta,y'} = \frac{(1+\alpha_{x,y}^2)\epsilon_{x,y}}{\beta_{x,y}}$$

and σ_p is the r.m.s. momentum spread. The function $f(a,b,c)$ is the following integral:

$$f(a,b,c) = 8\pi^2 \int_0^1 \left[ln\left(\frac{c^2}{2}\left(\frac{1}{\sqrt{p}}+\frac{1}{\sqrt{q}}\right)\right) - 0.577\right](1-3x^2)\frac{\mathrm{d}}{\sqrt{pq}}. \tag{2.136}$$

The following relations determine normalised parameters used in the formulae (2.136):

$$a = \frac{\sigma_h}{\gamma\sigma_{x'}},\ b = a = \frac{\sigma_h}{\gamma\sigma_{y'}},\ c = \beta\sigma_h\sqrt{2\frac{\rho_{max}}{r_i}},\ \frac{1}{\sigma_h^2} = \frac{1}{\sigma_p^2} + \frac{D_x^2}{\sigma_{x_\beta}^2}$$
$$p = a^2 + x^2(1-a^2),\ q = b^2 + x^2(1-b^2), \tag{2.137}$$

and the maximum impact parameter ρ_{max} is about 0.5 of the beam vertical size. The integral in equation (2.136) is calculated numerically.

Martini model

In accordance with the Martini model the longitudinal and transverse emittance growth rates for bunched beam averaged over the ring circumference (denoted by $\langle\rangle$ in equations) are then given by

$$\frac{1}{\tau_p} = \langle\frac{nA_M}{2}(1-d^2)f_z\rangle, \tag{2.138}$$
$$\frac{1}{\tau_{x'}} = \langle\frac{A_M}{2}[f_x + (d^2+\widetilde{d}^2)f_z]\rangle, \tag{2.139}$$
$$\frac{1}{\tau_{y'}} = \langle\frac{A_M}{2}f_y\rangle. \tag{2.140}$$

Here $f_{x,y,z}$ are so-called scattering functions and are calculated via numerical integration in each distribution dimension. After conversion to the polar coordinate system

(u,v,w) with the next relations,

$$u = \sqrt{z}\sin u\cos v,\ v = \sqrt{z}\sin v\sin u,\ w = \sqrt{z}\cos u$$

these functions are given by

$$f_i = k_i \int_0^{\infty}\int_0^{\pi}\int_0^{2\pi} \sin u g_i(u,v) exp[-D(u,v)w] ln(1+w^2) \mathrm{d}u\mathrm{d}v\mathrm{d}w \tag{2.141}$$

with coefficients $k_1 = 1/c^2, k_2 = a^2/c^2, k_3 = b^2/c^2$, where functions

$$D(u,v) = \frac{|\sin^2 u\cos^2 v + \sin^2 u(a\sin v - \widetilde{d}\cos v)^2 + b^2\cos^2 u|}{c^2}, \tag{2.142}$$

$$g_1(u,v) = 1 - 3\sin^2 uu\cos^2 v, \tag{2.143}$$

$$g_2(u,v) = 1 - 3\sin^2 uu\sin^2 v + \frac{6\widetilde{d}\sin u\sin v\cos v}{a}, \tag{2.144}$$

$$g_3(u,v) = 1 - 3\cos^2 u. \tag{2.145}$$

Normalised parameters are calculated from the following expressions:

$$a = \frac{\sigma_\xi}{\gamma\sigma_{x'_\beta}}\sqrt{1+\alpha_x^2},\ b = \frac{\sigma_\xi}{\sigma'_y},\ c = q\sigma_\xi,$$
$$\text{where } \sigma_\xi = \frac{\sigma_p\sigma_{x_\beta}}{\gamma\sigma_x} \text{ and } q = 2\beta\gamma\sqrt{\frac{\sigma_y}{r_i}}.$$

The terms d, $\widetilde{d}$ and A_M are given by:

$$d = \frac{\sigma_{x'}}{\sigma_p}D_x, \tag{2.146}$$

$$\widetilde{d} = \frac{\sigma_p}{\sigma_{x'}}(\alpha_x D_x + \beta_x D_{p_x}), \tag{2.147}$$

$$A_M = \frac{\sqrt{1+\alpha_x^2}\sqrt{1+\alpha_y^2}cr_i^2\lambda}{16\pi\sqrt{\pi}\sigma_x\sigma_{x'}\sigma_y\sigma_{y'}\sigma_p\beta^3\gamma^4}. \tag{2.148}$$

where $\lambda = N_b/(2\sqrt{\pi}\sigma_z)$ is the linear ion density, $\alpha_{x,y}$ are correlation Twiss functions, $x', y' = p_{x,y}$ are horizontal/vertical components of particle momentum, D' is the dispersion of x' and $\sigma_x = \sqrt{\sigma_{x_\beta}^2 + D_x^2\sigma_p^2}$ is the transverse-longitudinal coupled relation. In Martini's work, it was shown that the integrals (2.141) under assumptions in equation (2.132) are reduced to the Piwinski integral (equation (2.136)) and the Piwinski model is one possible simplification of the Martini model.

Bjorken-Mtingwa model

As Martini writes [91], the Bjorken Mtingwa approach of IBS theory, in contrast, is based on the scattering matrix (S-matrix) formalism related to quantum electrodynamics (QED), which relates transitions from an initial quantum state to the final state of a physical system experiencing the scattering process. The model develops the Fermi scattering "Golden Rule" and utilises it to compute the low-energy scattering amplitudes between particles, by evaluating the relevant Feynman diagram depicted in Fig.2.26. This approach is in some way similar to Moller theory [92] of scattering for electrons. The growth rates according to Bjorken-Mtingwa (with a $\sqrt{2}$ correction

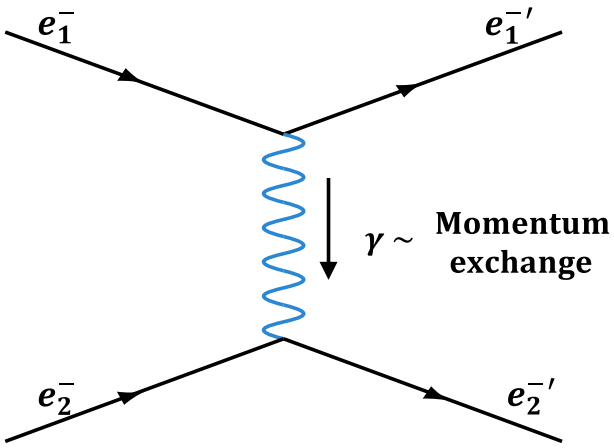

Figure 2.26: *Feynman diagram of the scattering process.*

factor [93], and including vertical dispersion) are

$$\frac{1}{\tau_i} = A_{BM} C_{log} \Big\langle \int_0^\infty \mathrm{d}\lambda \frac{\sqrt{\lambda}}{\sqrt{\det(L+\lambda I)}} \Big\{ \mathrm{Tr}(L^{(i)}) \mathrm{Tr}\big[(L+\lambda I)^{-1}\big] - 3\mathrm{Tr}\big[L^{(i)}(L+\lambda I)^{-1}\big] \Big\} \Big\rangle \tag{2.149}$$

where (i) represents p, x or y, and the Bjorken-Mtingwa scattering constant A_{BM} in analogy with Piwinski model is

$$A_{BM} = \frac{c r_i^2 N_b}{8\pi\beta^3\gamma^4\epsilon_x\epsilon_y\sigma_p\sigma_z} \,. \tag{2.150}$$

The main matrix $L = L^{(x)} + L^{(y)} + L^{(p)}$ is composed of the 3×3 matrices:

$$L^{(x)} = \frac{\beta_x}{\epsilon_x} \begin{bmatrix} 1 & -\gamma\phi_x & 0 \\ -\gamma\phi_x & \dfrac{\gamma^2 H_x^2}{\beta_x} & 0 \\ 0 & 0 & 0 \end{bmatrix}, \tag{2.151}$$

$$L^{(y)} = \frac{\beta_y}{\epsilon_y} \begin{bmatrix} 0 & 0 & 0 \\ 0 & \dfrac{\gamma^2 H_y^2}{\beta_y} & -\gamma\phi_y \\ 0 & -\gamma\phi_y & 1 \end{bmatrix}, \tag{2.152}$$

$$L^{(p)} = \frac{\gamma^2}{\sigma_p^2} \begin{bmatrix} 0 & 0 & 0 \\ 0 & 1 & 0 \\ 0 & 0 & 0 \end{bmatrix}, \tag{2.153}$$

where,

$$\phi_{x,y} = \frac{D_{x,y}\alpha_{x,y} + D'_{x,y}\beta_{x,y}}{\beta_{x,y}} \tag{2.154}$$

and,

$$H_{x,y} = \gamma_{x,y} D_{x,y}^2 + 2\alpha_{x,y} D_{x,y} D'_{x,y} + \beta_{x,y} D'^2_{x,y}. \tag{2.155}$$

In the previous equations the Coulomb logarithm C_{log} is defined in terms of the maximum r_{max}, minimum impact r_{min} parameters for which diverse definitions exist. The lower boundary of r_{min} can be the larger of the classical distance of the closest approach or the quantum mechanical diffraction limit from the nuclear radius. The high boundary r_{min} is taken to be equal to the smaller of the mean r.m.s beam size, or Debye length:

$$C_{log} \equiv \log\left(\frac{r_{max}}{r_{min}}\right)$$
$$\text{with } r_{max} = min(\lambda_D, \sigma_{x,y}) \text{ and } r_{min} = max(r_{min}^{CM}, r_{min}^{QM}) \tag{2.156}$$

These quantities are given by

$$\lambda_D = \frac{7.434}{Z}\sqrt{\frac{2E_\perp}{\rho}},\ \rho = \frac{N_b \times 10^{-6}}{\sqrt{64\pi^3 \langle\beta_x\rangle \epsilon_x \langle\beta_y\rangle \epsilon_y \sigma_p^2}},\ E_\perp = \frac{(\gamma^2 - 1)E_0 \epsilon_x}{2\langle\beta_x\rangle}, \tag{2.157}$$

$$r_{min}^{CM} = \frac{1.441 \times 10^{-9} Z^2}{2E_\perp},\quad r_{min}^{QM} = \frac{1.973 \times 10^{-13} Z^2}{\sqrt{8E_\perp E_0}} \tag{2.158}$$

in which ρ is the particle volume density in [m^{-3}] and $E_\perp$ is the transverse beam kinetic energy in the centre-of-mass frame [eV]. An original Bjorken-Mitingwa study takes the fixed Coulomb logarithm $g = 20$.

The expressions for the IBS growth rates in the Bjorken–Mtingwa equation (2.149) take a form that looks quite different from the equations for the growth rates in the PM method (equations (2.133) and (2.138-2.140)). However, Bane [93] also has shown that with certain assumptions, the Piwinski model and the Bjorken–Mtingwa model are in good agreement with each other. In the results chapters, the compared outcome for the ELENA ring provides good agreement between the two as well.

2.4.3 Electron cooling

Depending on the initial beam parameters (size, intensity, current and etc.), cooling techniques [94–97] can compensate for the impact of previously considered heating effects like IBS and space charge. It can also decrease the beam emittance and momentum spread by orders of magnitude. Also, cooling can reduce beam expansion after the crossing of the internal target by a coasting beam or after interaction with the residual gas. In the scope of this study, the electron cooling method was considered.

It was first proposed by Gersh Budker [97] in 1967 from the Budker Institute of Nuclear Physics (named after the inventor in 1994) to improve the luminosity of proton-antiproton collisions. The common scheme and working principle of an electron cooler are shown in Fig. 2.27.

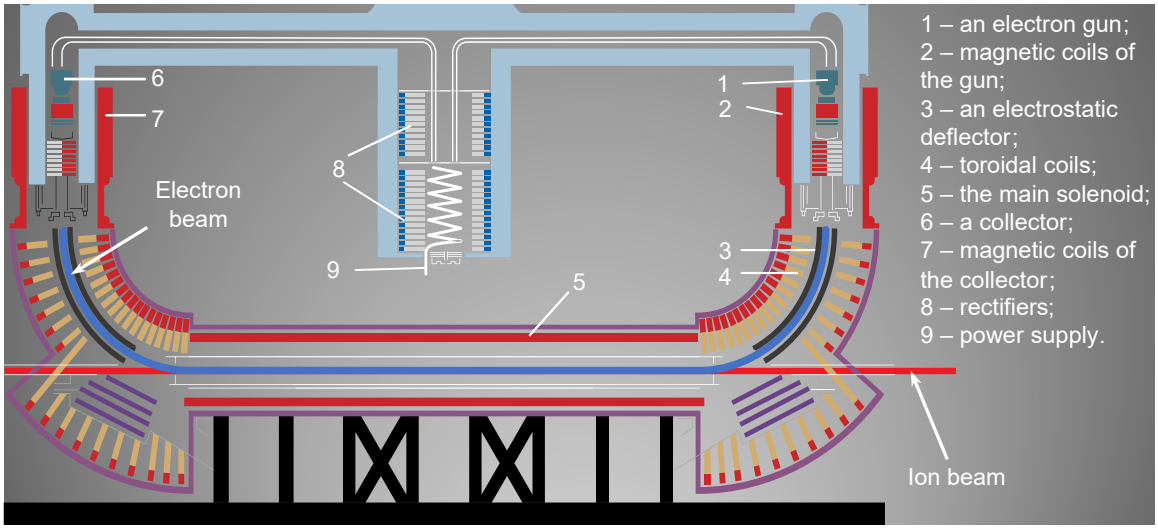

Figure 2.27: *Electron cooler structure. The electron beam (in blue) generated by an electron gun is directed with the help of a deflection system. After crossing with an ion beam (in red), it is directed outward and collected in a collector.*

Electron cooling, similarly to the IBS process, acts through a series of Coulomb collisions of the ions within a merged cold electron beam which results in the beam frame in a transfer of additional heating momentum from the individual ions to the electron beam. The Coulomb interaction in the electron cooling process is strongest for

small momentum deviations and the cooling rate increases with the reduction of the ion beam emittance and energy spread. In the traditional electron cooling systems the electrons are emitted from a thermal gun which is immersed in a longitudinal magnetic guiding field. It was experimentally and theoretically shown that the magnetic field affects the cooling power and increases the cooling force experienced by ions [98]. The thermal energy of the ions is transferred by Coulomb interaction to the electron beam which is continuously renewed and resembles a reservoir of cold electrons. An extensive introduction into electron cooling is given in [99–101]. In this study, BETACOOL [102] simulations were performed with use of practical semi-empirical formulae for magnetised cooling obtained by V. Parkhomchuk as a result of the fitting of experimental data [103, 104]

$$\vec{F} = -\frac{n_e e^4 Z^2 \vec{v}_{ion}}{m_e (v_{ion}^2 + v_{eff}^2)^{\frac{3}{2}}} \ln\left(\frac{\rho_{max} + \rho_{min} + \rho_{Lm}}{\rho_{min} + \rho_{Lm}}\right) \qquad (2.159)$$
$$\text{with : } v_{eff} = \sqrt{\delta v_{e\perp}^2 + v_{e\parallel}^2},$$

where eZ, with e as an electron charge, is the ion charge immersed in an electron beam with density n_e, m_e is electron mass, v_{eff} is an effective electron velocity, consisting of the sum of the longitudinal electron velocities $v_{e\parallel}$ component and the $\delta v_{e\perp}$ velocity component because of the presence of transverse magnetic and electric fields, $\rho_{Lm} = m_e \vec{v}_e / eB$ is the Larmor radius for electrons with velocity v_e in the magnetic field B of the cooler. The second part of the equation (2.159) is the Coulomb logarithm with ρ_{min} and ρ_{max} as limits of impact parameter ρ. The minimum boundary is a function of relative ion velocity and the maximum boundary is defined in terms of plasma

frequency ω_p and time of flight τ_c of the ion through the cooler with length L_c

$$\rho_{min} = \frac{Ze^2}{m_e(\upsilon_{ion}^2 + \upsilon_{eff}^2)} \tag{2.160}$$

$$\rho_{max} = \frac{\upsilon_{ion}}{\tau_c^{-1} + \omega_p} \tag{2.161}$$

$$\text{where } \omega_p = \sqrt{\frac{4\pi n_e e^2}{m_e}},\ \tau_c = \frac{L_c}{\beta\gamma c} \tag{2.162}$$

The cooling rate is proportional to the energy loss in the electron beam:

$$\frac{dE}{dt} = \vec{F}\vec{\upsilon_{ion}}. \tag{2.163}$$

It is evident from the previous equations (2.160-2.162) that the cooling rate is particularly sensitive to velocity deviations $\delta\upsilon_{ion}$ of the ion from the average electron velocity in all degrees of freedom. Consider as an example an ion beam having an emittance ϵ, the transverse velocities of ions will be

$$\upsilon_{ion,\perp} = \gamma\beta c\sqrt{\frac{\epsilon}{\beta_{x,y}}} = \gamma\beta c\theta_{ion} \tag{2.164}$$

where θ_{ion} is the ion beam angular spreads and $\beta_{x,y}$ are beta functions inside the cooler. Hence, for the regime of the tempered and moderately pre-cooled beam, the cooling rate τ, according to [104], is determined as

$$\frac{1}{\tau} = \frac{4J_e r_e r_{ion}}{\pi a_e^2 e\gamma^5\beta^4\theta_{ion}^3} L_c n_e \eta_e \tag{2.165}$$

where J is the current of the electron beam, r_{ion}, r_e are classical radii of the ion and electron, and a_e is the radius of the uniform cylindrical electron beam.

In reality, similar to the space charge, beam profiles of the electron and ion beam are not uniform. This impacts on the cooling efficiency in different regions of the primary beam and produces, in the general case, in bi-Gaussian distribution similar to that demonstrated in Fig. 2.28. This effect was observed in multiple storage rings

equipped with an electron cooler [105–107]

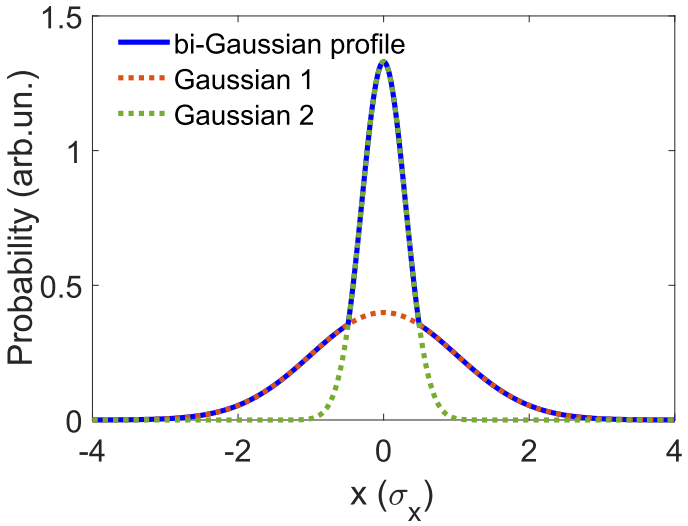

Figure 2.28: *Bi-gaussian beam profile as a combination of two Gaussian distribution.*

Another important parameter of the cooling system is the quality of the solenoidal magnetic field which defines the amplitude of transverse momentum components of an electron beam. Typically, the required field quality $B_{x,y}/B_0$ is of the order of 10^{-4}–10^{-5}, depending on the primary beam energy [108]. To measure field components with such precision along the cooler, a mapping device called *laser compass* is applied [109–111].

2.5 Summary

This chapter introduced important concepts for describing different parts of this study in a handbook style for accelerator physicists. Every subtopic begins with a simple concept that develops into practically applied formulae.

Firstly, an example of a single particle and beam distribution approaches, and concepts of the transverse and longitudinal dynamics were introduced. Further, collective effects caused by Coulomb interaction within multi-particle distribution were reviewed in the order:

- Space charge.
- Intra-Beam Scattering
- Electron Cooling.

Most of these heating/cooling effects are crucial in the design and operation of low-energy antiproton or high-intensity heavy-ion storage rings. In the next sections, practical simulation methods based on this theory are introduced, as well as beam interaction with the gas-jet target.

Chapter 3

Tracking methods and imperfections

3.1 Introduction

Various calculation methods might be employed to understand better the beam properties at any position of a circular machine or a transfer line at a given moment.

This chapter aims to explain different ways of simulating beam transport: using the transfer map method [69], particle tracking through field maps via Runge-Kutta algorithms [112] etc. Additionally, an algorithm for 6D bunch generation from the Twiss functions is demonstrated. The last section covers some of the common errors present in the elements of a storage ring.

3.2 Transfer maps

In the previous chapter, the general description of the transformation of particle coordinates was given (Eq. 2.22). In practice, a storage ring can be represented as a lattice of matrices. The most common elements are drifts, bending magnets, and quadrupoles. A particular transfer matrix can represent each of these elements. Many important aspects of beam dynamics in accelerators can be described in terms of Gaussian optics

and first-order ray-tracing matrices. These techniques are derived using the *paraxial approximation*. Also, similar to optical lenses, the thin or thick definition can be used for quadrupoles depending on their focal length and the length of the element. An example of a focusing-defocusing system as an optical sequence of two thin lenses and drift spaces is shown in Fig. 3.1.

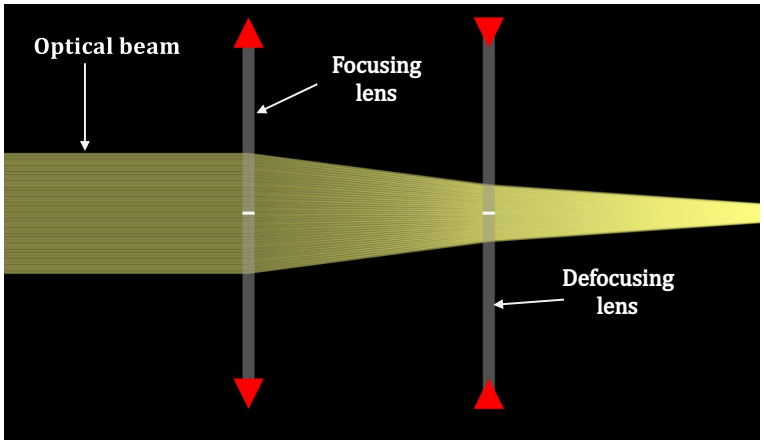

Figure 3.1: *FODO optical sequence.*

The impact of a drift space of the length $l = s - s_0$ or in a weak bending magnet for the horizontal plane, where $k(s)$ from Eq. 2.13 is close to 0, in the matrix formulation can be expressed by the 2×2 matrix

$$\begin{bmatrix} x(s) \\ x'(s) \end{bmatrix} = M_O \begin{bmatrix} x(s_0) \\ x'(s_0) \end{bmatrix} = \begin{bmatrix} 1 & l \\ 0 & 1 \end{bmatrix} \begin{bmatrix} x(s_0) \\ x'(s_0) \end{bmatrix} \tag{3.1}$$

.

When the focusing strength of the element $k = |k| > 0$, representing a pure focusing magnet, the transformation matrix for the element of length l is defined as

$$\begin{bmatrix} x(s) \\ x'(s) \end{bmatrix} = M_{QF} \begin{bmatrix} x(s_0) \\ x'(s_0) \end{bmatrix} = \begin{bmatrix} cos(\sqrt{k}l) & \frac{1}{\sqrt{k}} sin(\sqrt{k}l) \\ -\sqrt{k} sin(\sqrt{k}l) & cos(\sqrt{k}l) \end{bmatrix} \begin{bmatrix} x(s_0) \\ x'(s_0) \end{bmatrix} \tag{3.2}$$

and when $k = |k| < 0$ we will get the transformation for a pure defocusing element

$$\begin{bmatrix} x(s) \\ x'(s) \end{bmatrix} = M_{QD} \begin{bmatrix} x(s_0) \\ x'(s_0) \end{bmatrix} = \begin{bmatrix} cosh(\sqrt{k}l) & \frac{1}{\sqrt{k}} sinh(\sqrt{k}l) \\ \sqrt{k} sinh(\sqrt{k}l) & cosh(\sqrt{k}l) \end{bmatrix} \begin{bmatrix} x(s_0) \\ x'(s_0) \end{bmatrix} \tag{3.3}$$

.

Representing the transfer maps for different components in a beam line as matrices means that the maps can easily be combined through multiplication, to construct the (linear) map for any section of the beam line or ring. For example, the transformation sequence for a FODO cell in thin optics formalism is

$$M_{QD} M_O M_{QF} = \begin{bmatrix} 1 & 0 \\ \frac{1}{f_{QD}} & 1 \end{bmatrix} \begin{bmatrix} 1 & l \\ 0 & 1 \end{bmatrix} \begin{bmatrix} 1 & 0 \\ -\frac{1}{f_{QF}} & 1 \end{bmatrix} = \begin{bmatrix} 1 - \frac{l}{f_{QF}} & l \\ -\frac{1}{f^*} & 1 + \frac{l}{f_{QD}} \end{bmatrix} \tag{3.4}$$

where $f^* = \frac{1}{f_{QF}} - \frac{1}{f_{QD}} + \frac{l}{f_{QF} f_{QD}}$. The effect of the bending element in the first-order approximation can be treated as a combination of both a drift space (due to the fact that we work in a curvilinear coordinate system) and a focusing magnet.

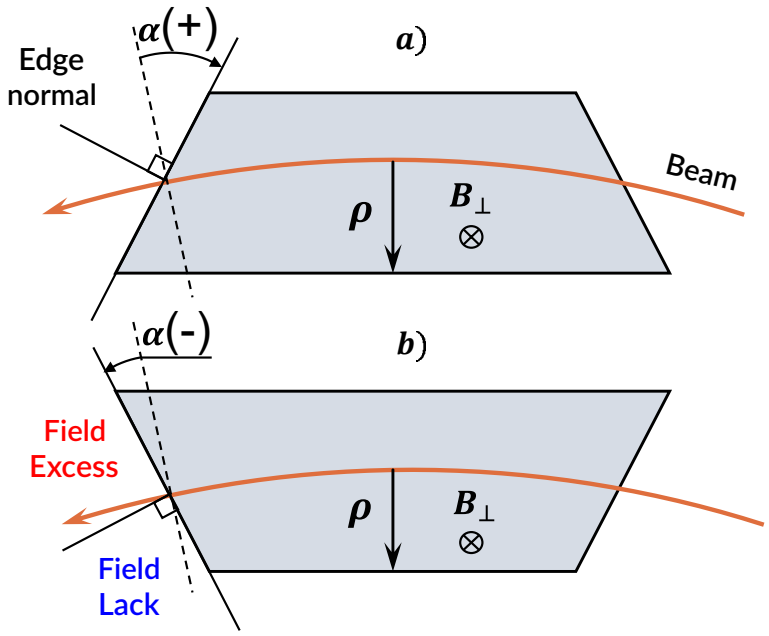

Figure 3.2: *The sector bend geometry with opposite angles for pole faces*

The focusing component appears in the boundary regions of the magnet for par-

ticles moving with a (transverse) offset distance from the reference trajectory. These can see either a "deficit" or an "excess" of the integrated transverse magnetic field. In the general case, the deflection angle $\Delta\theta$ caused by non-uniform dipole field $B(s)$ of length L is

$$\Delta\theta = \frac{1}{(B\rho)} \int_0^L B(s)ds \tag{3.5}$$

where ρ is a bending radius. Consequently, particles are deflected by an angle proportional to the traversed distance L in the boundary region, which in turn is to first order proportional to the transverse offset.

In practice bending magnets can also include focusing because of the geometry of their boundaries—*edge focusing*. Figures 3.2(a) and (b) show reference trajectories forming an angle α with the normal to the pole faces. The intermediate case between (a) and (b) is a sector magnet with $\alpha = 0$ not shown here where the reference trajectory enters and exits the pole faces along the normal to the faces. For the uniform field, in the simpler case of Eq. 3.5, focusing in the bending field changes depending on the edge angle α

$$\Delta\theta = \frac{B\tan\alpha}{(B\rho)}x. \tag{3.6}$$

By convention, the angle α for the magnet in Fig. 3.2(a) is positive, so Eq. 3.5 implies that a net defocusing is observed (i.e., a positive slope for particles moving from right to left). In contrast, the magnet in Fig. 3.2(b) has a negative α and yields a net focusing. To summarise, edge focusing in the transverse plane is represented by the matrices

$$M_{x,edge} = \begin{bmatrix} 1 & 0 \\ \dfrac{\tan\alpha}{\rho} & 1 \end{bmatrix}, \; M_{y,edge} = \begin{bmatrix} 1 & 0 \\ -\dfrac{\tan\alpha}{\rho} & 1 \end{bmatrix}. \tag{3.7}$$

For the sector magnet, where $\alpha = 0$, a weak focusing effect occurs in a horizontal plane, purely due to geometrical reasons in connection with Eq. 2.13. Thus, in matrix

form, a horizontal sector magnet is represented by the focusing matrix and drift matrix in the vertical plane

$$M_{SMx} = \begin{bmatrix} \cos\sqrt{k}L & \rho\sin\sqrt{k}L \\ -\dfrac{\sin\sqrt{k}L}{\rho} & \cos\sqrt{k}L \end{bmatrix}, \; M_{SMx} = \begin{bmatrix} 1 & \rho\theta \\ 0 & 1 \end{bmatrix}. \tag{3.8}$$

Matrices shown previously perform a transformation only on the horizontal or vertical phase space of the particles. In the more general form and in tracking codes each element (or the whole ring) has a so-called $R_{i,j}$ matrix. The matrix formalism discussed in this section can be also extended to higher orders as has been done in many classic particle accelerator matrix-based codes such as TRANSPORT, MAD-X and BMAD [113]. The transformation of the 6D vector $\vec{u} = [x, x', y, y', z, \delta]$ is calculated as

$$u_i(s_1) = \Delta u_i + \sum_{j=1}^{6} R_{ij} u_j(s_0) + \sum_{j=1}^{6}\sum_{k=1}^{6} T_{ijk} u_j(s_0) u_k(s_0) \tag{3.9}$$

where $i = 1 \ldots 6$.

It is worth mentioning the thick lens approximation of the lattice elements, which contrary to the thin lens approximations is inherently non-symplectic. This lack of simplecticity implies that the phase space volume is not preserved during the tracking and hence the emittances grow. Modern codes constantly develop various tracking methods to achieve symplecticity of tracking [114, 115].

3.3 Electrostatic optics

The transfer map methods can also be applied— with good agreement—to explain strong focusing and bending with an electric field. In the modern field of accelerator physics, where light and heavy ions are typically in the relativistic regime ($\beta \approx 1$), magnetic bending elements and quadrupoles are more prevalent than electrostatic counterparts due to their increased efficiency. With comparatively less focus on low-energy

accelerator physics, the use of electrostatic optical elements [116, 117] is more uncommon. However, in the extra low energy (<100 keV) antimatter and ion physics, that will be introduced by the new facilities such as FLAIR, ELENA, and low-energy experiments [24, 118, 119], this type of optics is the preferable option for particle transport.

The main difference between focusing electrostatic and magnetic quadrupoles is the orientation of their poles. Figure 3.3 shows this geometry structure and field lines for both types.

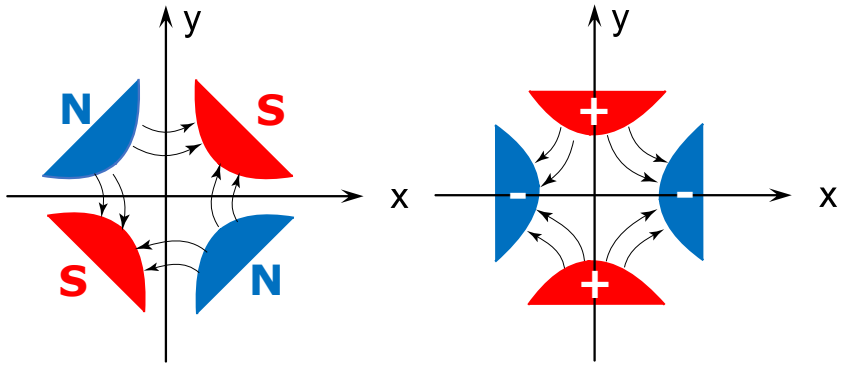

Figure 3.3: *Magnetostatic and electrostatic quadrupoles field lines*

The efficiency and feasibility of the use of electric and magnetic elements are mostly determined by cost and experimental requirements. The limiting factors are high-voltage breakdown at about 10^7 V/m in vacuum and saturation of ferromagnetic materials with the boundary at about 2 T [120] for electrostatic and magnetic elements, respectively. Another advantage is the independence from the mass of the ion for the electrostatic quadrupoles and dipoles, which can be seen from the next equations for their focusing strength k

$$k_B = \frac{q_{ion} B_0}{m_{ion} \upsilon r} = \frac{q_{ion} B_0}{\sqrt{2 E_k m_{ion}}} \tag{3.10}$$

$$k_E = \frac{q_{ion} E_0}{m_{ion} \upsilon^2 r} = \frac{q_{ion} E_0}{2 E_k} \tag{3.11}$$

where E_0 and B_0 are field amplitude at the pole of the magnet and r is an aperture radius. The kinetic energy is obtained from non-relativistic $E_k = m_{ion}\upsilon^2/2$ when $\gamma \approx 1$. The relation between these two, taking into account earlier limits from earlier is

$$\frac{k_E}{k_B} = \frac{E_{lim}}{\upsilon B_{lim}} = \frac{0.0167}{\beta}. \tag{3.12}$$

Thus below $\beta = v/c = 0.0167$ (for protons with energies less than 130 keV or for electrons with energies less than 70 eV), electrostatic quadrupoles are more efficient than magnetic quadrupoles. At higher energies, however, magnetic lenses are preferred.

Electrostatic bending can be demonstrated with a simple example of two parallel plates separated by a distance d with a voltage U between them, as shown in Fig. 3.4.

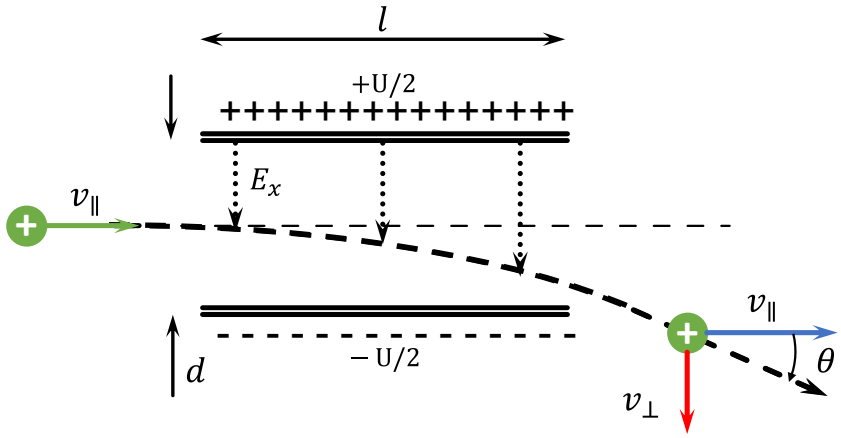

Figure 3.4: *Schematic illustration of charged particle deflection in a transverse electric field that is orthogonal to the direction of motion. The field is created by two conducting plates of length l separated by a distance d with a voltage U between them.*

This acceleration from the field perpendicular to the charged particle direction introduces an angular deflection. The perpendicular acceleration $a = q_{ion}U/m_{ion}$ and the time spent between the plates where the field acts is $t = l/v$ then bending angle θ for the small deflection is

$$\theta = \frac{v_\parallel}{v_\perp} = \frac{q_{ion}lU}{dm_{ion}v^2} = \frac{q_{ion}lU}{2dE_{kin}}. \tag{3.13}$$

Another practical case for electrostatic bending systems are cylindrical or toroidal electrodes that generate sector fields or different types of electrostatic lenses that are well described by Wolnik and Leibl [59, 121].

3.4 Field map methods

In case when a beam propagates in a field region that cannot be readily described with a set of multipoles, an alternative method exists. The field is described with a 3D grid of evenly spaced field points known as a *field map*. Each point may contain a 6-vector with three electric and three magnetic field components. These are commonly given in the Cartesian or cylindrical coordinate systems. Additionally, the field can vary with time and then each point of the field map also includes time or phase variables.

The use of an irregular grid is much less efficient for tracking purposes. This is because in order to track a particle in the region between two grid points where the field is undefined, the field values are identified with an interpolation algorithm. Two algorithms are generally applied—linear and cubic polynomial interpolations depicted in Fig. 3.5. The choice of algorithm depends on the smoothness of the original field.

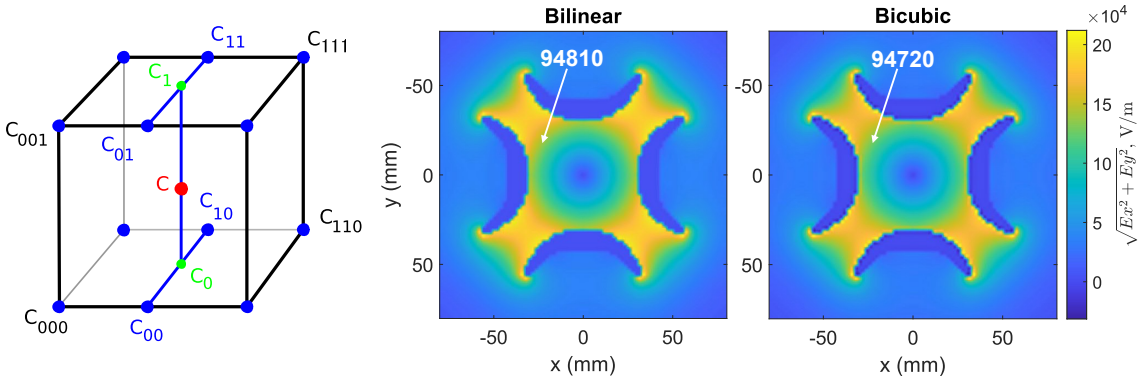

Figure 3.5: *Comparison of two interpolation methods. The left side shows an example of trilinear interpolation using 4 points. The difference in interpolated electrostatic field value in the case of bilinear and bicubic methods is shown on the right.*

In addition due to the 3D format of the field map, eight points are required for *trilinear* or *tricubic* interpolation.

3.5 Runge-Kutta tracking

The field map approach usually requires specific algorithms for particle tracking due to the fact that fields often cannot be described analytically in a simple way. To predict the position and velocity of the particle we can apply a numerical integration of the trajectory via Runge-Kutta (RK) method [112] used for solving of n^{th}-order ODEs. Hence, we can construct the required system of ODEs for the Lorentz force

$$\begin{aligned} \frac{d\vec{v}}{dt} &= \frac{F_L(\vec{\vec{x}},\vec{v})}{m} = \frac{q}{m}(\vec{E}(\vec{x}) + \vec{v} \times \vec{B}(\vec{x})), \\ \frac{d\vec{x}}{dt} &= \vec{v} \end{aligned} \tag{3.14}$$

where $\vec{x}$ and $\vec{v}$ are vectors of the particle position and velocity. In the simplest case (magnetic field only), the position and velocity of the particle are integrated. However, if a longitudinal electric field is present, the propagation is also integrated since the particle momentum changes along the integration step.

Next, a short explanation of the idea behind one of the most popular fourth-order RK method (RK4) is provided.

The general 1D (movement along t axis only) equation is

$$v_1 = v_0 + \frac{h}{6}(k_1 + 2k_2 + 2k_3 + k_4), \tag{3.15}$$

$$\begin{aligned} \text{where : } k_1 &= \frac{q}{m}F_L(x_0, v_0), \\ k_2 &= \frac{q}{m}F_L(x_0 + \frac{h}{2}, v_0 + \frac{h}{2}k_1), \\ k_3 &= \frac{q}{m}F_L(x_0 + \frac{h}{2}, v_0 + \frac{h}{2}k_2), \\ k_4 &= \frac{q}{m}F_L(x_0 + h, v_0 + hk_3). \end{aligned} \tag{3.16}$$

describes change in particle speed $v_0 \rightarrow v_1$ after time step $\Delta t = h$ where $k_1, .., k_4$ are

intermediate field evaluations of speed in time span Δt. Visually, the working principle of the RK method is depicted in Fig. 3.6 (left). You may notice how these additional evaluations define the final direction (slope) of v_1.

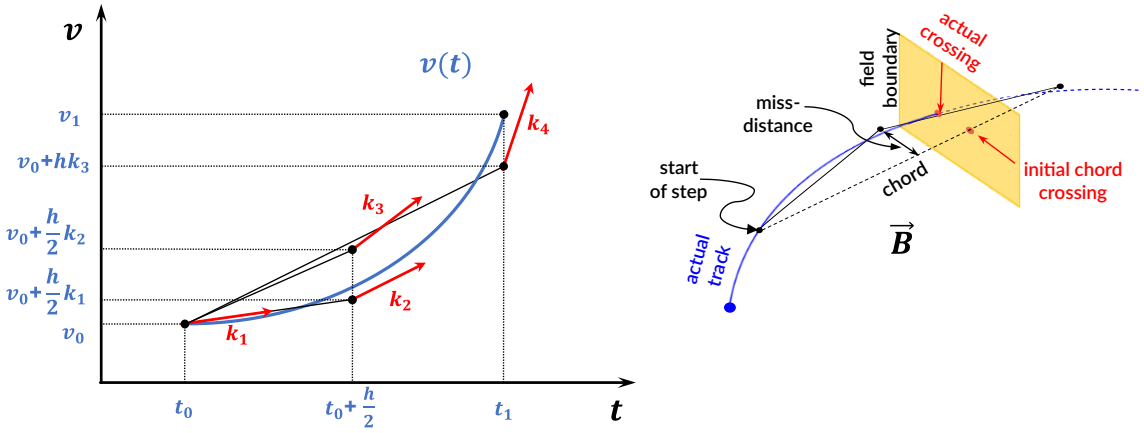

Figure 3.6: *Runge-Kutta working principle (left) and example of error accumulation in particle tracking during the single step (right).*

Many variations of the RK method have been developed to bring the best trade-off between performance and accuracy. The previously shown fourth-order method provides local accuracy of $\mathcal{O}(h^5)$. Geant4, for example, also provides higher order RK5..7 methods capable of converging the solution to $\mathcal{O}(h^{7--8})$ via adaptive integration steps.

An illustration of how a small error from integration misplaces the particle trajectory is demonstrated in Fig. 3.6 (right). As you may see, the curved path of the particle is broken up into linear chord parts. These chord segments are determined so that they closely approximate the curved path. The chords are then used to interrogate the particle as to whether its track has crossed a field boundary. This integration stage is the most computationally expensive because it requires many iterations to put the last point on the boundary with the same accuracy. This and the miss-distance between the chord and an actual arc are the main error contributors, leading to cumulative energy loss or gain.

Nevertheless, the Runge-Kutta method is quite an effective tracking method for relatively short distances or when a couple of thousand turns within the storage ring are required. It provides a robust way of tracking in intricate electromagnetic fields.

The extensive benchmarks against alternative integration methods were completed by [115, 122, 123] to demonstrate RK performance and applicability in various circumstances.

3.6 Bunch generation algorithm

As mentioned in Section 2.2.4 the 2D beam distribution can be represented with a beam matrix $\boldsymbol{\sigma}$. In general, a 6D expansion of this matrix is utilised. The six dimensions are three canonical conjugate coordinate pairs in three planes (two transverse and one longitudinal), and each particle can be represented by the vector $\boldsymbol{u} = (x,\, x',\, y, y',\, t,\, \delta)$. Six beam centroids are defined by the means of that distribution. The 6×6 matrix of second-order moments of the distribution can be represented compactly as $\Sigma_{ij} = \langle \boldsymbol{u_i}\, \boldsymbol{u_j} \rangle$ with the angle brackets denoting a central moment. More explicitly for a particle beam, this is:

$$\boldsymbol{\Sigma} = \begin{pmatrix} \langle x^2 \rangle & \langle x\, x' \rangle & \langle x\, y \rangle & \langle x\, y' \rangle & \langle x\, t \rangle & \langle x\, \delta \rangle \\ \langle x' x \rangle & \langle x'^2 \rangle & \langle x'\, y \rangle & \langle x'\, y' \rangle & \langle x'\, t \rangle & \langle x'\, \delta \rangle \\ \langle y\, x \rangle & \langle y\, x' \rangle & \langle y^2 \rangle & \langle y\, y' \rangle & \langle y\, t \rangle & \langle y\, \delta \rangle \\ \langle y' x \rangle & \langle y' x' \rangle & \langle y' y \rangle & \langle y'^2 \rangle & \langle y' t \rangle & \langle y' \delta \rangle \\ \langle t\, x \rangle & \langle t\, x' \rangle & \langle t\, y \rangle & \langle t\, y' \rangle & \langle t^2 \rangle & \langle t\, \delta \rangle \\ \langle \delta\, x \rangle & \langle \delta\, x' \rangle & \langle \delta\, y \rangle & \langle \delta\, y' \rangle & \langle \delta\, t \rangle & \langle \delta^2 \rangle \end{pmatrix}. \tag{3.17}$$

The $\boldsymbol{\sigma}$ here is in the top left 2×2 segment. The $\boldsymbol{\Sigma}$ is similarly linked to the Twiss functions $\beta_{x,y}, \alpha_{x,y}, \gamma_{x,y}$ and dispersions $D_{x,y}, D_{x',y'}$. These are used in combination with beam transverse emittances ϵ_x, ϵ_y and longitudinal parameters $\sigma_\delta, \sigma_\tau$. The combination of machine and beam parameters gives the physical observables such as the beam size. From a geometrical point of view, a combination of any three coordinates looks similar to a 3D ellipsoid shown in Fig. 3.7.

Because of the dispersion and energy spread present in the real beam longitudinal-

transverse and transverse-transverse couplings are introduced, which are defined as off-diagonal elements in the sigma matrix. To ensure that we have a positive variance in each dimension, the $\mathbf{\Sigma_{ij}}$ matrix must be positive definite. To obtain each term of the covariance matrix, we consider the effect of dispersion on single coordinates. For example, for an individual particle, the horizontal position is affected as follows: $x_i = x_{\beta i} + D_x\delta_i$, where x_i is the horizontal transverse coordinate,$x_{\beta i}$ is the betatron component and $D_x\delta_i$ reflects the change due to the particle's relative energy offset in a dispersive region.

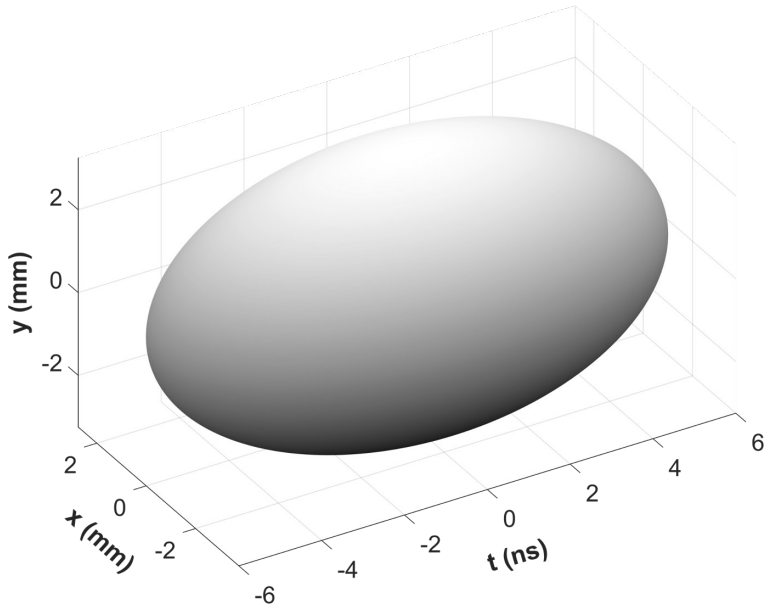

Figure 3.7: *Ellipsoidal shape of the bunch for a triplet of x, y and t coordinates.*

Due to independency and the random nature of $x_{\beta i}$ and δ_i , the second order moment in x_β can be derived from the properties of the variance: $\langle x^2 \rangle = \epsilon_x \beta_x +^2_x \sigma^2_\delta$, obtained by applying the Courant-Snyder equations and rewriting the variance in terms of standard deviation.

An interrelationship that involves two different variables affected by dispersion

has the same form. For example:

$$\begin{aligned}
&\langle x\, x' \rangle = \mathrm{cov}[x_\beta + D_x\delta,\, x'_\beta + D_{x'}\delta] = \\
&\langle x_\beta\, x'_\beta \rangle + D_x \langle x'_\beta\, \delta \rangle + D_{x'} \langle x_\beta\, \delta \rangle + D_x\, D_{x'} \langle \delta^2 \rangle = \\
&\langle x_\beta\, x'_\beta \rangle + D_x D_{x'} \langle \delta^2 \rangle = -\epsilon_x \alpha_x + D_x D_{x'} \sigma_\delta^2.
\end{aligned} \tag{3.18}$$

All other couplings can be shown in the same manner.

3.7 Stray fields

A low-energy particle beam (∼100 keV) may experience severe beam transport instabilities caused by field imperfections of different natures. For example, long (∼10 m), unshielded beam lines will not be able to transfer particles due to the natural Earth magnetic field or stray fields from closely located experiments, see example in Fig. 3.8. In the case of the storage ring, these additional fields will act like an extra multipole

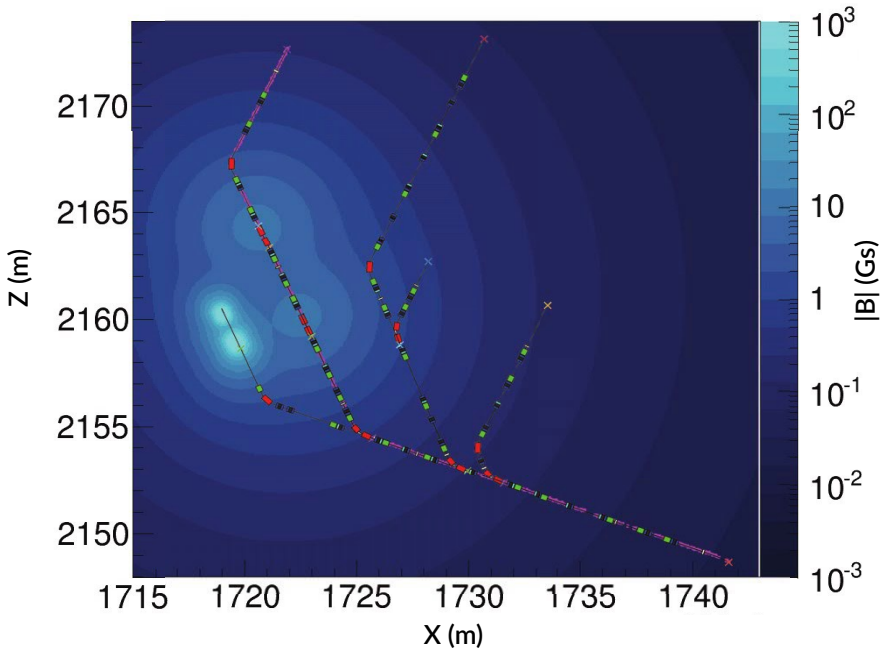

Figure 3.8: *Example of the stray field distribution from closely located experiments in AD hall [124].*

error.

These additional fields can be integrated into the model with the matrix or field map approaches. For the former, the field errors can be implemented into the model via horizontal or vertical kicks to a reference particle with a discrete sampling of the drift space between the existing elements of the optical lattice.

It is possible to go beyond this and overlap field points with a beam pipe utilising the conversion of the global field map into a reference coordinate system.

In order to mitigate the impact, most of the magnetic optics are usually replaced with electrostatic components, and efficient magnetic shielding and correction schemes are used.

3.8 Fringe fields

The previously mentioned matrix methods assumed ideal magnets with a uniform field over a given length. In fact, the geometrical length was assumed to be identical to the field length. In reality, the fields are generated by ferromagnetic poles and have a complex longitudinal profile that depends on the magnet aperture and field strength. Unlike the preceding topic that describes an extreme case of field leakage at a far distance, the fringe fields are stronger. They decay over an additional length which is usually shorter than the biggest aperture dimension [125]. Figure 3.9 demonstrates how the field distribution of a magnet extends over the iron length and an effective field length becomes larger than the geometric length of the magnet.

In beam dynamics codes such as BMAD or MAD-X the fringe field is taken into account via the splitting of the magnetic field into two parts. The first part is called the "hard edge field" and it provides a kick to the particle in the limit that the longitudinal extent of the fringe is zero. The second piece is the "soft edge" fringe field or "wing" that provides the fringe kick with the fringe having a finite longitudinal extent without the hard edge field.

The soft edge part is defined in terms of the field integrals F_{in} for the magnet

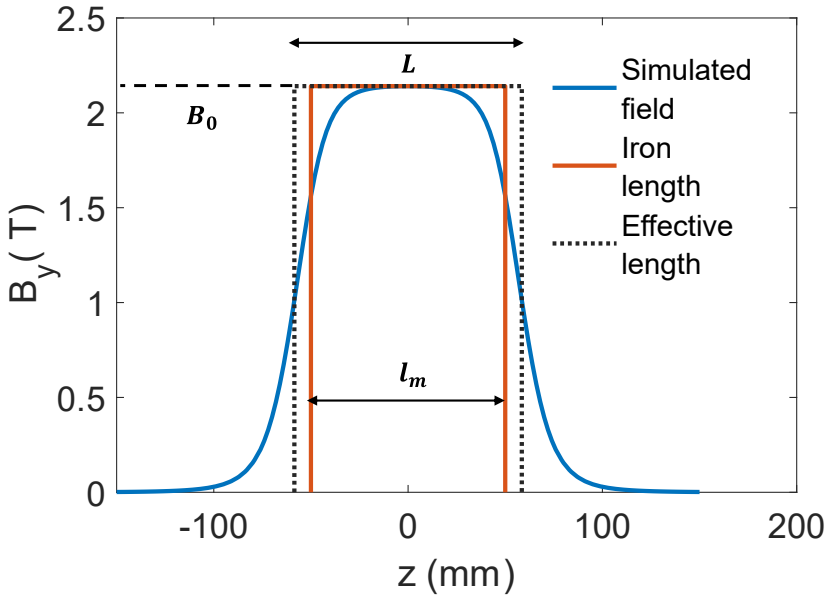

Figure 3.9: *Magnet field along the dipole length. The blue curve shows the simulated field by an element of length l_m with maximum field value B_0. The integrated field of this dipole corresponds to the hard edge ideal magnet with length L (black dashed curve).*

entrance and exit

$$F_{in} = \int_{-\infty}^{+\infty} \frac{B_y(s)(B_y(0) - B_y(s)}{h \cdot B_y^2(0)} \, \mathrm{d}s \tag{3.19}$$

where $B_y(0)$ is the field in the hard edge approximation and h is gap between the magnet poles.

This type of field can have an important impact on machine optics that has to be taken into account. Specifically, the fringe field created by a multipole of order n produces, in leading order expansion, $n+2$ order multipole fields, i.e dipole fringe fields create quadrupole fields, sextupole fringe fields create octupole fields, etc.

3.8.1 Fringe field in G4beamline

For more precise treatment of the magnetic field fall-off after the aperture, G4beamline utilises the Enge function [126] with six parameters $a_1 \ldots a_6$. This function is of the form

$$Enge(z) = \frac{B_0}{1 + \exp(a_1 + a_2(z/D) + ... + a_6(z/D)^5)} \tag{3.20}$$

where z is the distance perpendicular to the effective field boundary and D is the full aperture of the particle optical element.

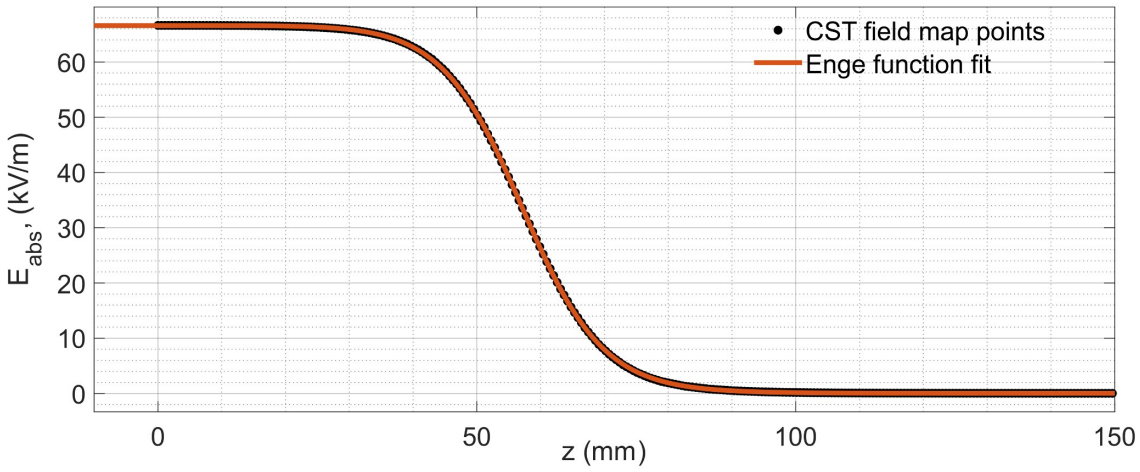

Figure 3.10: *Enge function fit (red) of an electrostatic quadrupole simulated in CST Studio (black dots).*

The description process requires a fitting procedure for mid-plane values of the analysed field and is suitable for magnetic and electrostatic elements. An example of the functional fit is shown in Fig. 3.10. The variation of the field outside mid-plane is taken into account by applying higher-order derivatives of the Enge function.

Recent developments of the Enge fringe field model have resulted in fully closed analytical expression for fringe fields in multipole magnets [127]. Expressions for the fields were obtained by solving the three-dimensional Laplace equation. Access to realistic analytical definitions of fringe fields provides a connection between studies of the dynamics of particles moving through the fringe fields, a particular magnet, and design studies of the magnet geometry.

3.9 Summary

In this chapter, the most common techniques for optical machine design were introduced. The matrix methods, where each magnetic/electrostatic element is described via 6×6 dimensional matrix are well suited for the design phase of an accelerator, a beam line or an experiment. In low-energy beam dynamics, however, the impact from the stray and fringe fields becomes more visible due to the lower rigidity required to steer the beam away from the design orbit. It is generally harder to design uniform fields with low amplitude. Hence, field map methods become handy and they can describe almost any shape of the field. To track 6D beam distribution based on initial Twiss functions various symplectic and non-symplectic algorithms were applied. One of them is the classical Runge-Kutta method. This method is indistinguishable from symplectic ones on small time scales and with a higher order of integration. Thanks to the tracking methods, backward improvement of the analytical description of the field can be performed.

Chapter 4

Measurements of electrostatic quadrupole field

4.1 Introduction

The previous chapter discussed the benefits of using electrostatic optics for low-energy physics. We can confidently describe the effect of each designed element on the beam using an approximated matrix or field map methods. However, until recently, there was no equipment available to precisely measure and check the electric field shape generated by these elements. Instead, one had to trust simulations and depend on extremely tight manufacturing tolerances. Unlike the widespread usage of Hall and NMR sensors for 3D mapping of a magnetic field, there was no practical tool for an electrostatic field. To address this issue, I established collaboration with the authors of the following research, [128]. Initially, their sensor was designed to measure the strength of electric fields and alert workers of potential breakdown hazards in areas close to high-voltage power lines. Fortuitously, by design, the device was non-invasive and had the capability of measuring the amplitude of the electrostatic field along a single axis that was sufficient for field mapping.

In this chapter, a novel non-invasive way to experimentally probe the electrostatic

field in a 3D volume with an improved micro-sensor is presented. Furthermore, the working principle of the sensor and the experimental setup are described. Using the example of an electrostatic quadrupole focusing component, excellent agreement between the simulated and real field was found. This study was done in a collaboration established during the course of this work between the Cockcroft Institute, CERN and Technische Universität Wien (TU Wien). The obtained results provided a crucial benchmark for the simulation of elements and beam optics.

4.2 Quadrupole design

A comprehensive analysis of a focusing component from the ELENA transfer line quadrupole assembly was performed. A CAD model of the quadrupole was created using the technical design report and drawings of element's components from EDMS, CERN's Drawing Directory (CDD) [129]. Figure 4.1 demonstrates the full FODO

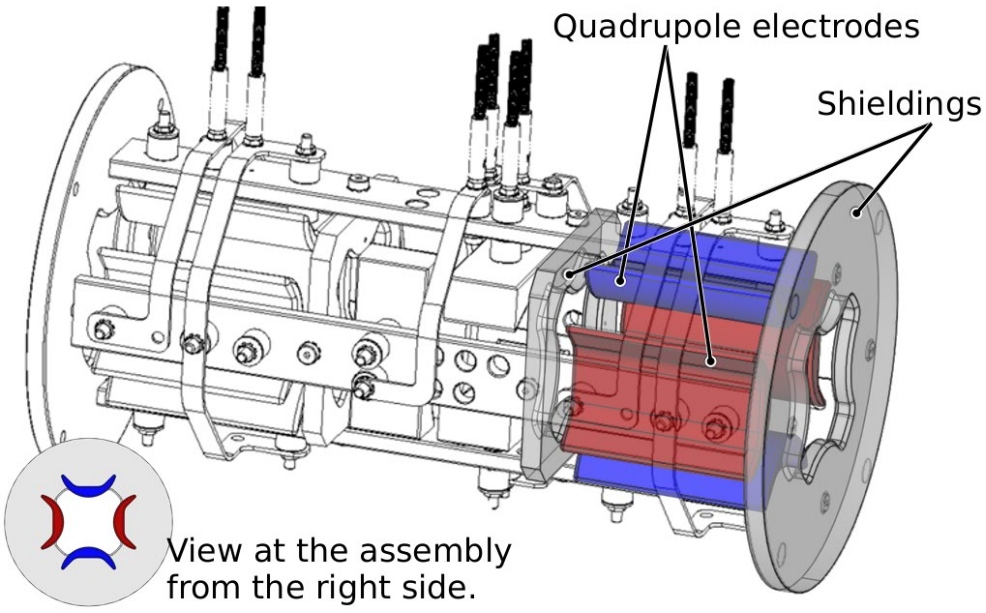

Figure 4.1: *Drawing of the FODO assembly. Created elements of the simplified model are highlighted. Colours symbolise the applied voltage at the poles: red for positive and blue for negative potential. Frontal and rearward shielding plates for mitigating of the fringe field influence are highlighted in grey.*

assembly with quadrupole assembly parts highlighted. In the next chapter, a more detailed sketch of the longitudinal section will be given. The simulated model of the quadrupole consists of four electrostatic plates, a large forward (part of the vacuum tank) and smaller internal shielding. All these components are made of AISI 316L stainless steel. In Fig. 4.2, a photograph of the frontal view of the assembly is shown.

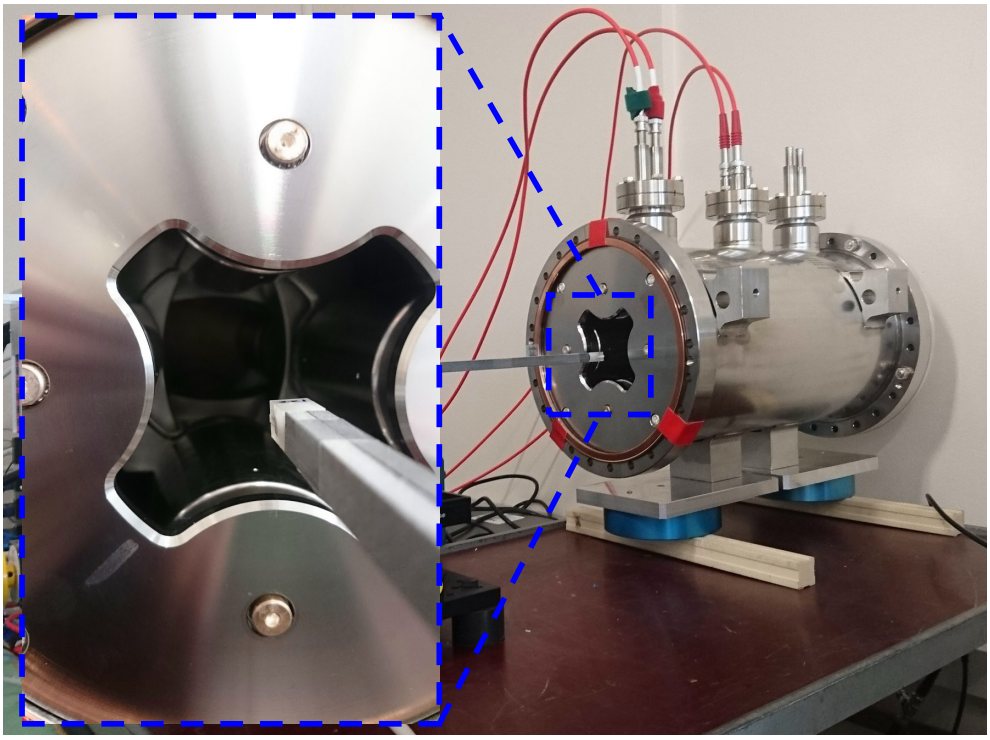

Figure 4.2: *The FODO assembly that was examined. The front side is highlighted and shows a plastic holder for the sensor.*

4.3 FEM electro-mechanical simulations

Using the 3D CAD model, electrostatic FEM simulations were performed in CST. During beam line operation, the FODO assemblies are located inside a tank under an ultra-high vacuum, limiting access to the electrodes. As a first step, CST was used to calculate the field in both vacuum and air. Evaluation of the field distribution confirmed that there is no significant difference in field gradient measured in the air

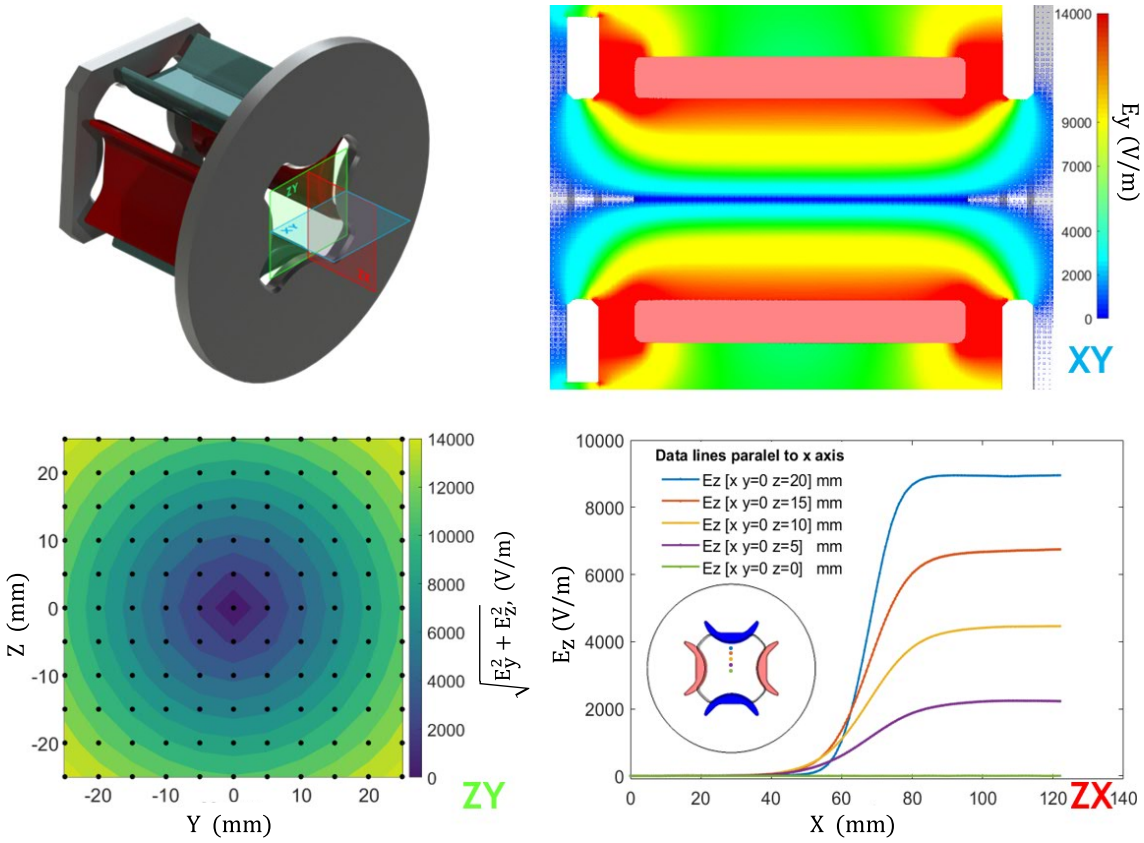

Figure 4.3: *Electrostatic field analysis. The x-coordinate here is along the quadrupole axis. xy-section: perpendicular y-component of the field, highest intensity is observed near the electrodes and shielding; zy-section: the transverse field* $E_\perp = \sqrt{E_y^2 + E_z^2}$ *obtained at the centre cross section plane of the electrodes. The black dots represent the measurement step of the field scan (5 mm); zx-section: change in intensity of the longitudinal component of the field at various distances from the z-axis.*

as opposed to vacuum, for a range of voltages up to the maximum design voltage of ±6 kV (relative permittivity of air is 1.0006). Detailed analysis of the quadrupole field is shown in Fig. 4.3. The top left part demonstrates a CAD model with three section planes: XY, ZY and ZX. Applied potentials, in this case, were ±200 V.

For the next step, the measurement process using a micro electro-mechanical system (MEMS) was benchmarked in a combined electro-mechanical simulation utilising COMSOL [131] by A. Kainz. All simulations involving the MEMS were performed the same way using the electrostatics module of COMSOL. The electric field was gener-

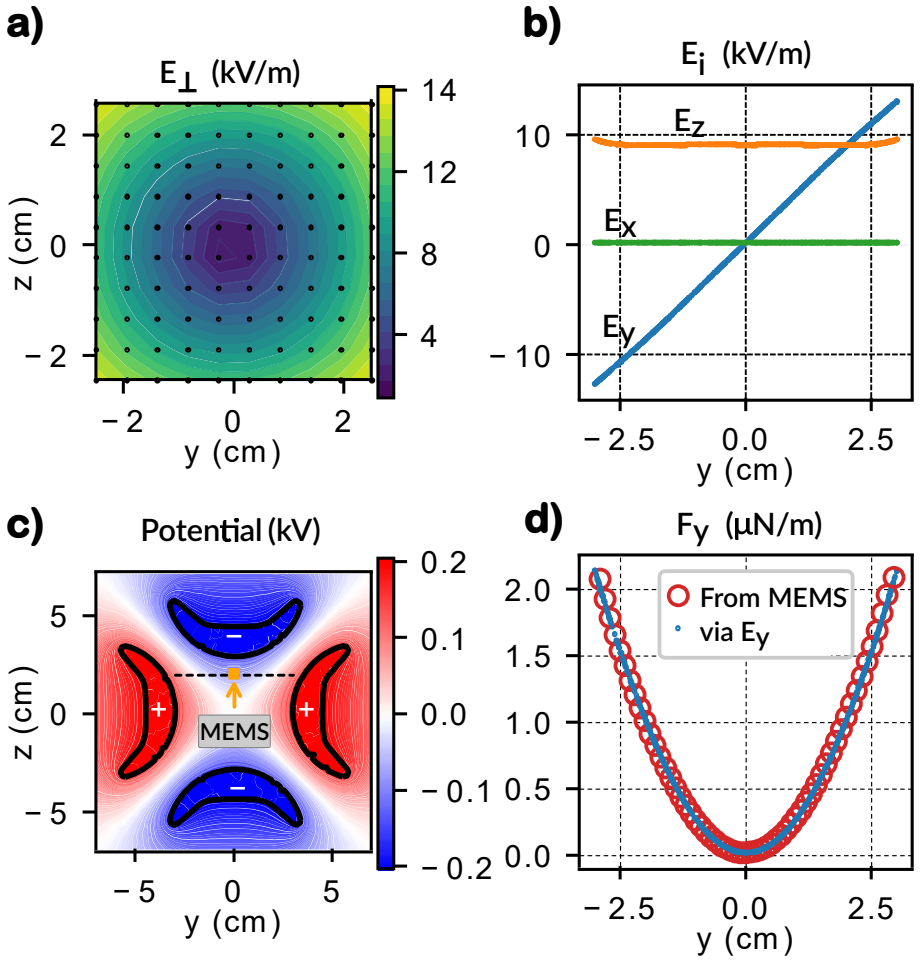

Figure 4.4: *a) Cross section of the E field obtained from F_y and F_z force calculation on the yz plane in the quadrupole centre. The black dots correspond to the scan positions performed by MEMS. In all other coordinates the result is linearly interpolated. b) Field components obtained on the line between points (0,-3,2) cm and (0,3,2) cm. c) Potential at the cross section with analysis line. d) Force obtained in the simulations (red circles) compared to the force calculated from the data in (c) by $F_y = \alpha E_y^2$ [130].*

ated by setting the same potentials of electrodes as in CST and the micro-structure was treated as an ideal conductor by applying a floating potential boundary condition to it. The electrostatic force was then calculated simultaneously considering the movable mass inside the sensor. As an example, Fig. 4.4 demonstrates vertical force evaluation between two aperture points (0,-3,2) cm and (0,3,2) cm in the middle of the quadrupole. The next section describes the working principle of MEMS in general.

4.4 Working principle of MEMS from TU Wien

The operational approach of MEMS is to sense an electric field based on the principle of electrostatic induction [128, 130, 132]. This process is a natural consequence of the mobility of free charges in conducting solids. If a conductor is placed in an electric field $\vec{E}$, the free charge carriers inside the conductor redistribute. This polarization is a result of field compensation inside the body. Thus, oppositely charged regions occur at the conductor's surface. Each of these surface regions experiences an outward force due to the E field while the total force on the body remains zero. If one separates these oppositely charged regions, keeping their only connection in the form of a conducting spring, one can observe an elongation of the spring due to the electric field (Fig. 4.5)a,b. This happens due to the electrostatic force pulling on the individual charged surfaces and the conductivity of the spring by which the polarization of the body is maintained. The simplest example of this behaviour is a conducting sphere with a radius R inside a uniform field $\vec{E} = E_0\vec{e_z}$ pointing in the z-direction, where $\vec{e_z}$ is the unit vector in the z-direction, the total electrostatic force experienced by the right hemisphere, which is a positively charged region, can be calculated analytically [133] to be

$$\begin{aligned} \vec{F_{es}} &= F_e s\vec{e_z}, \\ F_{es} &= \frac{9}{4}\pi R^2 \varepsilon_0 E_0^2 = \alpha_s \varepsilon_0 E_0^2 \end{aligned} \tag{4.1}$$

where $\alpha_s = 9\pi R^2/4$ takes into account the symmetric geometry of the sphere and ε_0 is the electric permittivity of free space. The force acting on the left hemisphere is equally strong and points in the opposite direction. Therefore, the total force on the full sphere equals zero.

In a similar way, this force can be used to deflect the spring-suspended proof mass of the MEMS and can be represented as $\vec{F}_{\text{es}} = Q\,\vec{E}$. Here, Q is the induced charge on one side of the conductor, and the whole body remains neutral. Since linear dependence of Q on $\vec{E}$, $\vec{F}_{\text{es}} \propto \vec{E}^2$. The schematic cross section of the MEMS and

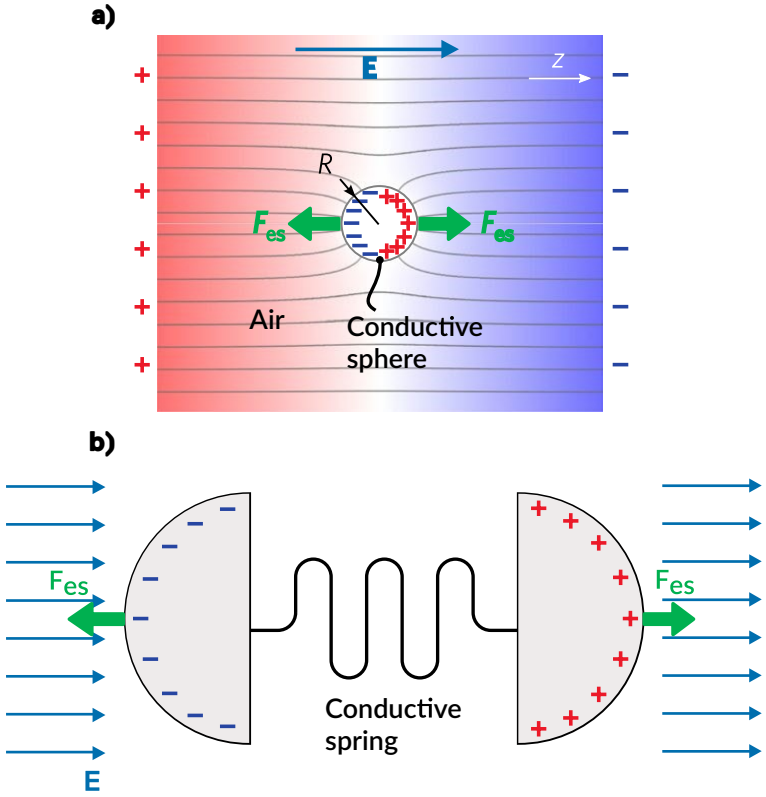

Figure 4.5: *a) Forces and field lines of a conducting sphere with radius R in field E. The electric field polarizes the sphere. b) A conductive spring connecting the oppositely charged regions of the sphere elongates due to electrostatic force F_{es} while maintaining polarisation [128].*

operating principle are shown in Fig. 4.6. The deflection is read out optically via a shutter consisting of two identical arrays of holes where one is etched into the moving proof mass of the Si chip, while the stationary one is made of Cr deposited onto a glass chip. The shutters collimate the light flux coming from the LED depending on the electrostatic force applied. The light intensity is then detected by a reverse-biased photodiode leading to a current. This current, in turn, is converted into the output voltage for analysis.

Note that the MEMS structure was designed to deflect only in one direction and is sensitive only to the corresponding component of the field. In a first calibration simulation, the relation between force and field strength, $\vec{F}_{\mathrm{es}} = \alpha \vec{E}^2$, was established, i.e. the coefficient α. A value of $\alpha = 1.29 \times 10^{-14}\,\mathrm{N/(V/m)^2}$ was obtained inside a

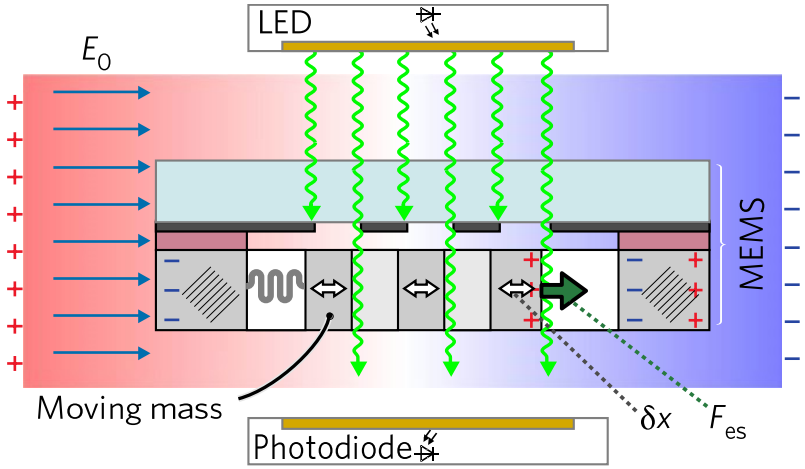

Figure 4.6: *Schematic cross-section of the electric field transducer. Light flux emitted by an LED is modulated by two micro-sized optical shutters. The output signal of the photodiode depends on the deflection δx of the movable aperture, which is induced by an external electric field E_0 [130].*

uniform field ranging from 0 to 83.3 kV/m and a least-squares fit (R-square: 0.9993) shown in Fig. 4.7.

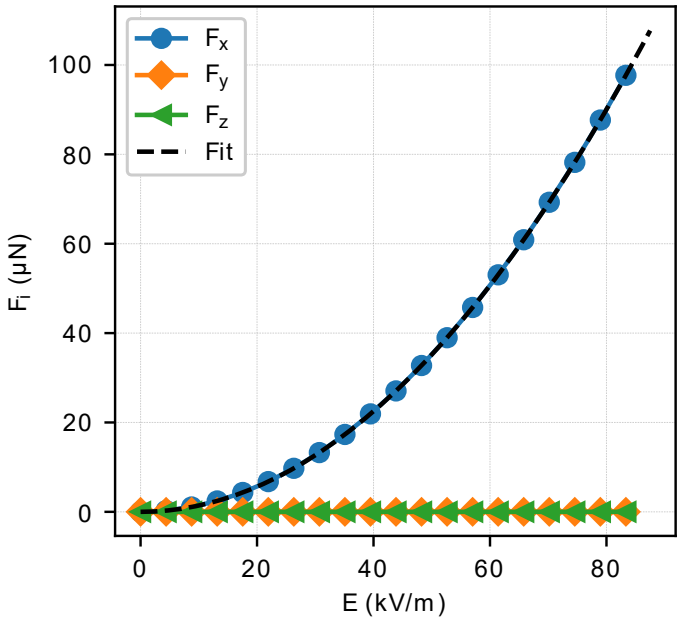

Figure 4.7: *Relation between the electrostatic force F_{es} and E in a uniform field of varying strength obtained in FEM calibration simulations via COMSOL. From [130].*

4.5 Measurement setup

In order to probe the quadrupole field, the MEMS chip was encapsulated within a 3D-printed acrylic holder and connected via optical fibres to the readout electronics placed at a shielded location away from the quadrupole. Except for the Si part of the MEMS chip, only dielectric materials are used in the probe to avoid additional field distortions. The light coming from the LED is guided through the chip and reflected back by a small right-angle prism into the output fibre. Figure 4.8 depicts the fully

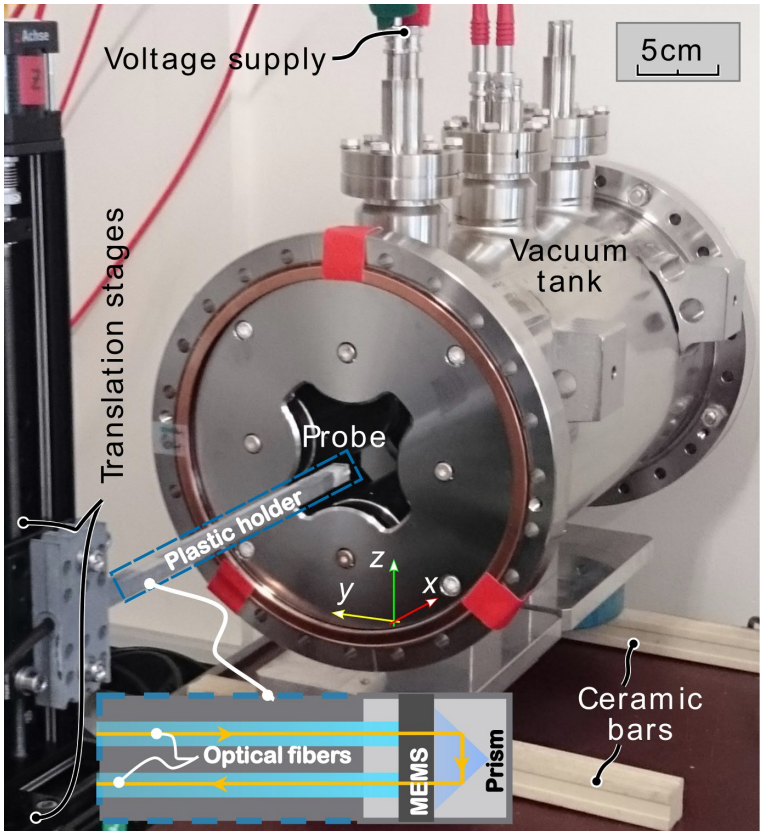

Figure 4.8: *Measurement setup for analysis of the quadrupole electric field. The dashed rectangle depicts how the light passes through the MEMS in the probe holder.*

assembled measurement setup. The two-axis linear stage was controlled via a single-board computer and used to position the sensing tip within the quadrupole. The quadrupole was supplied with a sinusoidal voltage of $\pm 200\,\mathrm{V}$ and $f = 150\,\mathrm{Hz}$ using a

two-channel high-voltage amplifier controlled by a waveform generator. An AC supply was chosen over a DC supply to rely on the lock-in method for the sake of improved results. Furthermore, this low frequency was used to excite the mechanical resonance ($f_0 = 300\,\mathrm{Hz}$) of the MEMS that did not affect the shape of the field.

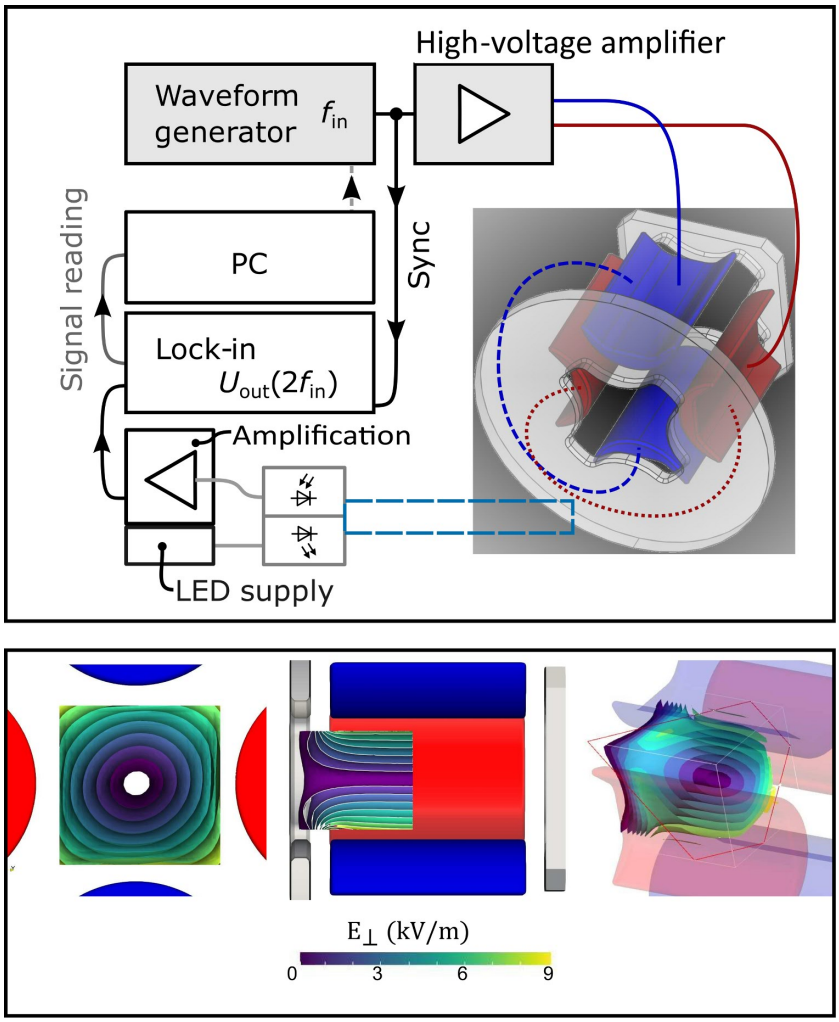

Figure 4.9: *Connection schematics of the E-field measurement setup (top) and views of 3D map of the field strength $E_\perp$ in the front half of the quadrupoles (bottom). The scanned data points were interpolated and represented as set of iso-surfaces.*

Before the actual measurement of the quadrupole field, the probe was calibrated for both the y and z-directions in a uniform field provided by parallel plate electrodes. Sinusoidal voltages at 150 Hz ranging from 500 mV to 200 V were applied to the plates,

which were 3.4 cm apart. This amounts to a field range of 15–5,900 V/m. The full connection scheme of the experiment is shown in the upper part of Fig. 4.9.

In the next step, the 3D volume from the center plane to the outer edge of the shielding plate of the quadrupole was studied. It was $8 \times 5 \times 5\,\mathrm{cm}^3$ in size and with a step size of 2 mm in each direction, a total of $39 \times 25 \times 25 = 24,375$ points were scanned. The time to achieve reasonable statistics for a single point was 15–30 seconds. The bottom part of Fig. 4.9 shows the resulting 3D field map of the field amplitude $|\mathbf{E}|$ composed of the individual y and z-component results.

4.6 Benchmark with FEM simulations

To compare the measured field shape against FEM simulations, the probe was used to map the most ideal field in the centre cross section of the quadrupole. Figure 4.10 shows the corresponding interpolated results for field strength of the y and z-components. The

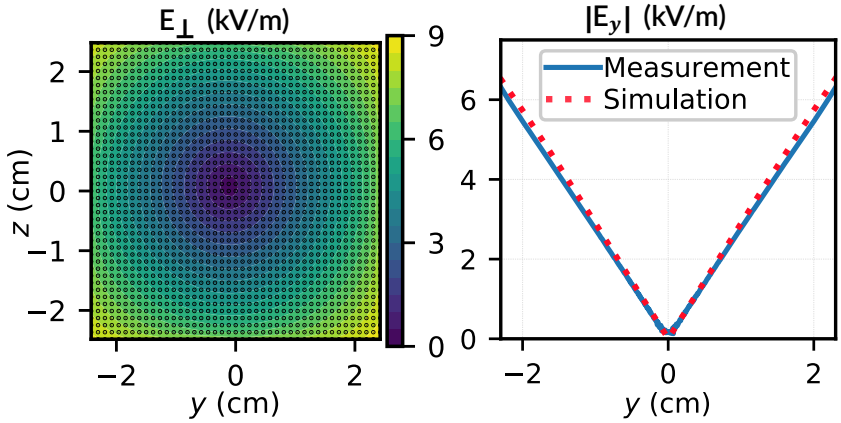

Figure 4.10: *(Left) The field strength $|E|$ was obtained from the output voltage converted from the intensity of the light signal. The black dots denote the positions of the probe in 2D plane. A linear interpolation has been applied between the dots. The MEMS was moved along a line as in Fig. 4.4c with a step size of 100 µm. (Right) $|E_y|$ recalculated from the data and compared to the FEM simulation in COMSOL.*

deviation from the simulated data is of the order of 3 %, which can be attributed to the makeshift holders for the fibres and probe tip, and calibration differences between

the quadrupole and parallel plates.

It had been concluded from these measurements that the quadrupole behaves as the simulations predict, which is one of the major benefits of using electrostatic components and beam line design. However, unforeseen effects can occur if the produced geometry deviates from the requirements. For this reason, extremely tight fabrication tolerances of $\delta = \pm 50\,\mu m$ are required for the individual components.

For future improvements of this type of measurement, one of the aims will be to combine three sensor elements to measure all three field axes simultaneously. Additionally, commonly used spatial averaging for magnetic field mapping, handled by so-called Quad Hall plates [134], could be adapted to enable symmetry of the mapping and an active compensation. In an ideal case, the effect of the spatial offset should be completely eliminated by utilizing this technique.

4.7 Summary and Outlook

In this chapter, work on an efficient way to analyse and measure a complex 3D electric field strength was reviewed. This work used a modified version of MEMS from [128]. It has been shown that exceptional spatial resolution ($\sim 10\,\mu m$) can be achieved for fields with sufficiently low curvature. The field of an electrostatic quadrupole from the FODO assembly of the main components of low-energy antimatter beam steering and control in the ELENA electrostatic transfer lines at CERN was mapped.

The results confirmed experimentally that such electrostatic components behave like FEM simulations performed in CST and COMSOL predict. This is one of the advantages over magnetic components and simplifies their design. Nevertheless, this reliability is linked to tight fabrication tolerances and very accurate production. Future accelerator physics projects proposed at CERN involve electrostatic elements in a storage ring, where due to the beam passing through the element multiple times, the required field homogeneity is tighter than for the measured electrostatic quadrupole. For the ongoing study of an electrostatic ring to measure the electric dipole moment

[135, 136], a field homogeneity of 1×10^{-4} is required, which corresponds to mechanical fabrication tolerances of a few micrometers. While the requirements of the ELENA electrostatic transfer line quadrupole (tolerance of $\mathcal{O}(100\,\mu\text{m})$) are still feasible, it will be challenging to produce electrostatic ring elements with such precision cost-effectively. Therefore, precise field analysis of the element would provide vital information for mitigation methods such as sorting elements and active compensation.

The next chapter demonstrates how based on detailed element description, such a correction can be applied to the ELENA transfer lines.

Chapter 5

Electrostatic transfer line simulation

5.1 Introduction

Beam facilities operating at low energies have proven to be invaluable tools for carrying out atomic and molecular physics research. Because of comparatively less focus on low-energy physics, and the usage of electrostatic optical elements, these experiments are much less widespread than magnetic-based ones at higher energy. However, their output will become even more advanced in the new era of extra-low energy (<100 keV) physics, brought in by new facilities such as FLAIR, CSR, ESR and ELENA. Beam transfer lines attached to these rings are usually also based on electrostatic optics and fast deflectors. It is a cost-effective solution for an extraction system into multiple experiments simultaneously. In this chapter, simulation work on realistic and computatively efficient descriptions of beam behaviour and various aspects of electrostatic beam line operation were investigated. The main focus was given to ELENA transfer lines that were recently upgraded with electrostatic optics. These simulations are based upon previous simplified methods of beam line design [124, 137] and refine the previous findings [138].

To meet these requirements, a major portion of this work related to the 3D simulation of the longest ELENA beam line taking beam towards the ALPHA experiment has been carried out in a modified version of G4beamline. For the benchmark of obtained results, additional simulations were performed in BMAD.

G4beamline is a Geant4-based project, similar in philosophy to the simulation tool as BDSIM [139], utilised for beam-matter interaction studies in storage rings and linacs. A large number of experiments use Geant4 and FLUKA for predictions of the interaction of various species particles with detectors or dose deposition with surrounding material [140–142]. Geant4 provides various theoretical models in its physics lists supplemented with experimental data for an accurate treatment of low-energy particles [143]. It also has the capability to export beam distribution for usage in external simulations of antimatter experiments.

This chapter covers the description of the main components of ALPHA and AEgIS transfer lines as well as their impact on 6D beam transport. It also provides an example of efficient optimisation of inherited imperfections, namely fringe and stray fields. Finally, an insight into an extension of the AEgIS experiment is provided.

5.2 ELENA Transfer Lines

To improve the availability to multiple experiments to the decelerated antiproton beam from ELENA, the design of the transfer lines envisages simultaneous operation of the experiments. This is achieved by bunching of ELENA beam at the fourth harmonic (h=4) after the final cooling plateau. Bunch splitting also helps to dilute the impact of the collective effects on a single bunch of high charge.

Figure 5.1 shows the layout of the ELENA ring with a system of four beam line branches that have been commissioned. The main focus of this work is the neighbouring transfer lines (solid lines) between ELENA, the ALPHA and AEgIS experiments. The transfer lines are split into sections labelled as LNE00, LNE01,..., LNE04. This division into sections separates space between horizontal or vertical bending elements specified

as red dots, which will be described later in this chapter.

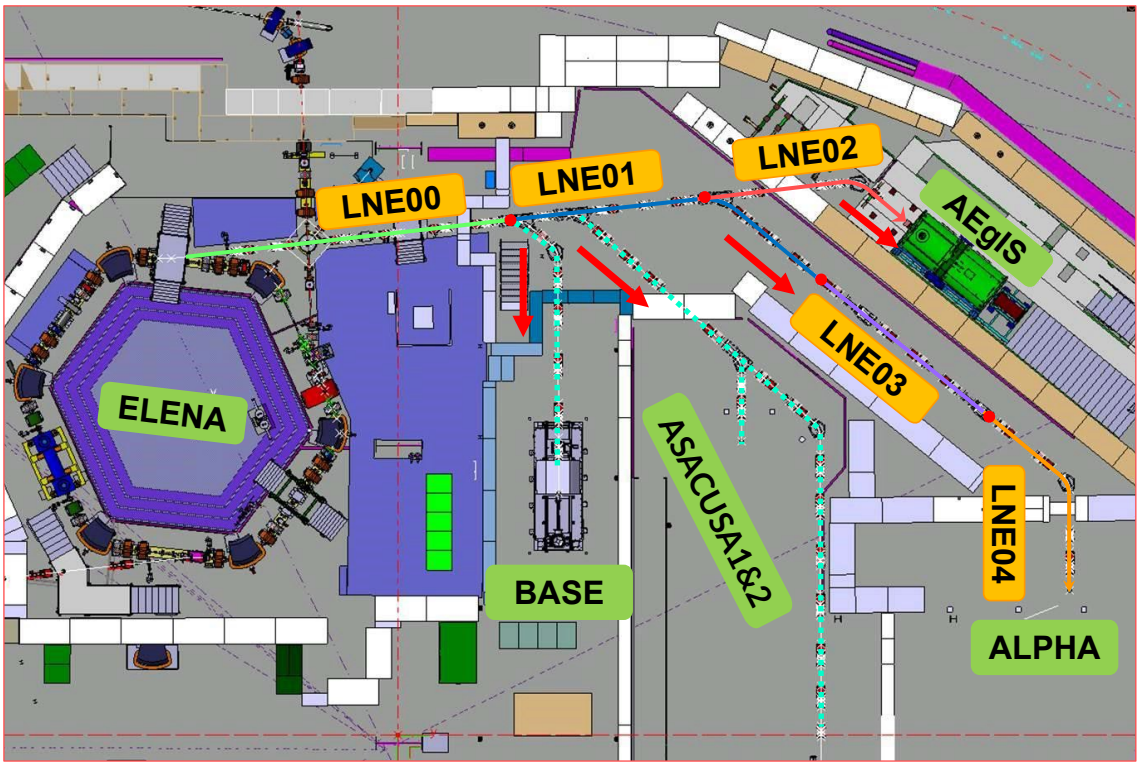

Figure 5.1: *Schematic of electrostatic transfer lines within the AD hall. Solid lines are in the main focus of interest.*

The transfer lines to all experiments are built in a modular fashion i.e. they are designed mostly from repetitions of several identical elements.

The beam correction and focusing is done using electrostatic quadrupole doublet assemblies (equipment code ZQNA) mentioned in the previous chapter, seen as a symmetrical drawing cut shown in Fig. 5.2. To steer the beam in horizontal and vertical directions, a set of two electrostatic corrector kickers (ZCH and ZCV) are installed in the middle of the assembly and separated from quadrupoles via internal shielding. Each quadrupole part is powered independently either with a focusing (ZQMF) or defocusing (ZQMD) polarity arrangement or with the same polarity if more strength is required. In a few places where only a single quadrupole is enabled, this design also serves as redundancy in case of internal electrical connection faults. In total, about 60 assemblies of this type will be used in the ELENA transfer lines.

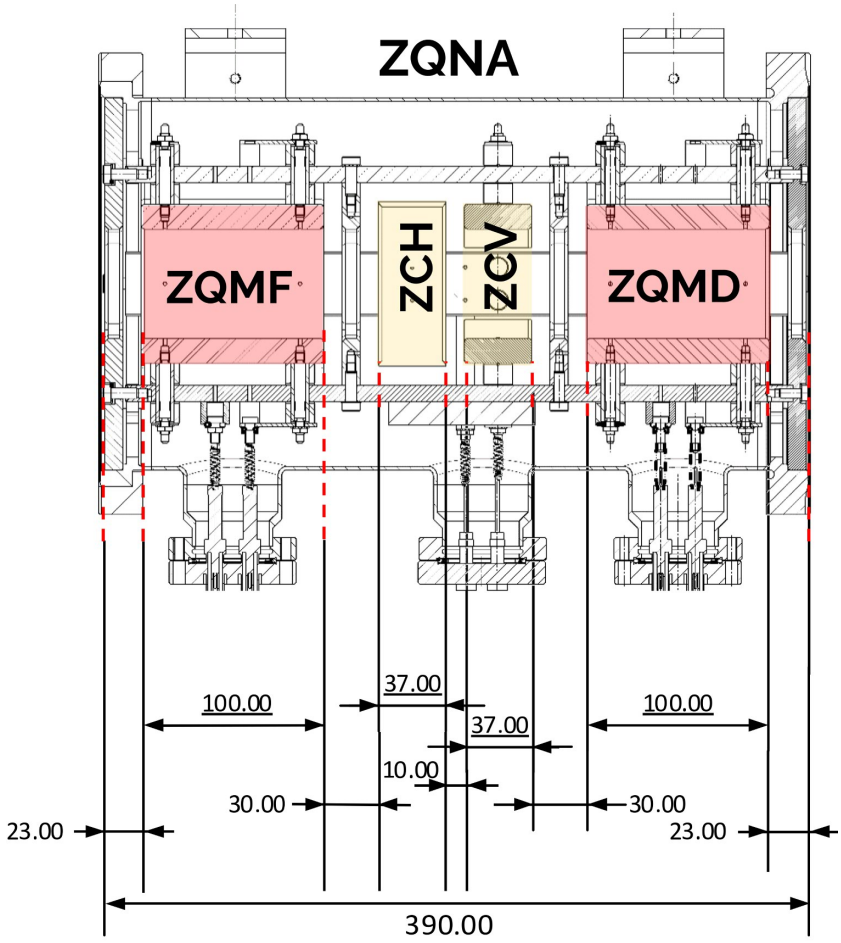

Figure 5.2: *ZQNA assembly drawing with dimensions displayed in millimetres. Electrostatic quadrupoles are highlighted in red, while kickers are marked in yellow colours.*

The main requirements were an optical strength of the quadrupoles up to $6\,\mathrm{m}^{-1}$ and the deflection strength of kickers up to 10 mrad. They are achievable by applying up to $\pm 5\,\mathrm{kV}$ to 100 mm electrodes of quadrupole and $\pm 2\,\mathrm{kV}$ to 37 mm kicker plates. The mechanical aperture of 60 mm satisfies the conditions for safe beam passage for all designs. The large distance between quadrupole and corrector electrodes (30 mm) and inner shielding minimise field leakage between elements. A beam position monitor (BSGWA) can be rigidly coupled to the ZQNA on its downstream side, minimising the monitor-quadrupole alignment errors.

To perform bunch train splitting and transfer of a single bunch to one of the

experiments, a number of pulsed fast deflectors are utilised (ZDFA). They are identical in design to the two extraction deflectors within the ELENA ring. For further bending downstream of a branch of the transfer line electrostatic slow deflectors are used (ZDS). Four of these elements are also coupled with fast deflectors for greater bending angles.

Depending on the operational function, three main designs of slow deflectors are distinguished—ZDSA, ZDSB and ZDSC:

- The ZDSA type is combined with the fast deflector ZDFA in a common vacuum chamber and performs horizontal bending towards BASE, ASACUSA and ALPHA experiments (locations at Fig. 5.1).
- The ZDSB type is a standalone slow deflector that is utilised for horizontal bending within beam line branches toward all experiments.
- The ZDSC type is also coupled with ZDFA and was designed for the ATRAP experiment that had been completed. It is identical to ZDSB but performs bending in a vertical plane.

With the intention to assist with the design, manufacture and replacement of broken components, identical toroidal electrodes are used in each deflector type with slightly different voltage settings to account for the different bending angles.

5.3 Modelling of beam line elements in G4beamline

In order to interpret each operational component of the highlighted beam lines with the required level of detail, CAD assemblies, based on available drawings of main components [129] were constructed. An example of such a model for the electrostatic quadrupole was presented in a previous chapter (Fig. 4.1).

A detailed description of the element implementation inside the G4beamline simulation and various modifications of the original code are presented here.

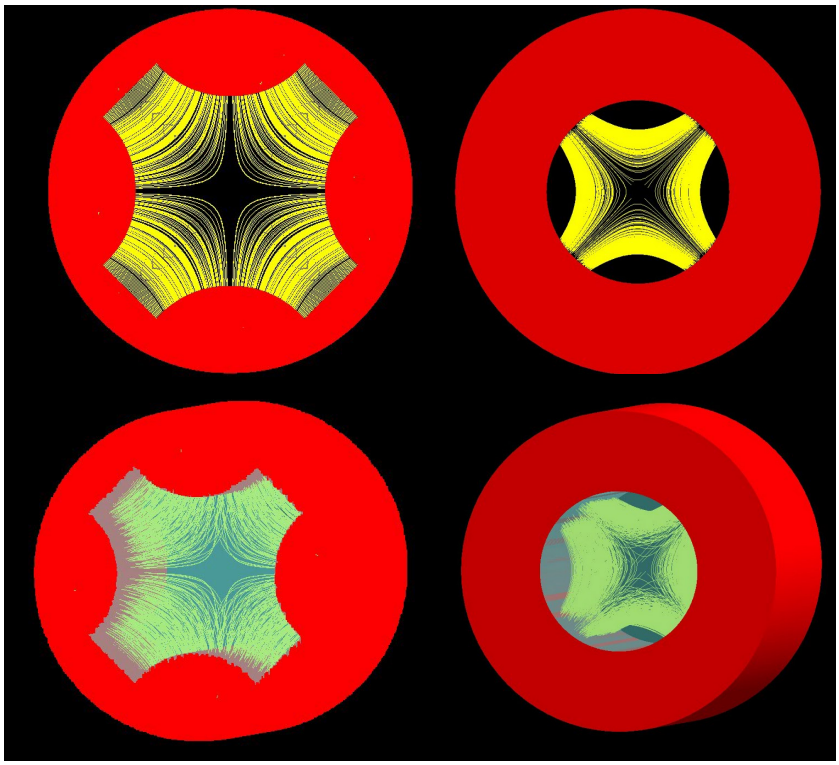

Figure 5.3: *Comparison of an electrostatic "+" quadrupole geometry (left) against cylindrical magnetic version (right). Red iron body collimates the incoming beam. Field lines are partially shown in yellow colour, aperture volume can be defined with a custom material (transparent light blue).*

5.3.1 Electrostatic quadrupoles

To accurately simulate the transfer line quadrupoles, firstly, the basic description of field components in G4beamline coordinates had to be reviewed and extended.

The Geant4 serves as a base library for the G4beamline and thus inherits its methodology for the simulation of electromagnetic fields. The simulation area is initially divided into 3D voxels consisting of single bin field maps of size $200 \times 200 \times 200$ mm. Any of them may include beam line elements with the superior resolution of the field. Globally, it is a large field map with varied point increments for local elements.

In the case of a magnetic quadrupole, represented inside the code with **generic-quad** element, field components, which affect a moving particle, are estimated analyt-

ically depending on the particle position inside the element aperture using

$$B_r = \frac{B_0 r}{a} \sin 2\theta, \quad B_\theta = \frac{B_0 r}{a} \cos 2\theta, \tag{5.1}$$

in polar coordinates, or

$$B_y = B_0 \frac{x}{a}, \quad B_x = B_0 \frac{y}{a} \tag{5.2}$$

in the Cartesian coordinate system. B_0 is the field strength on the magnet pole, r and θ correspond to position of the particle, a is the magnet aperture.

An electrostatic version of such a quadrupole can be implemented by adding the corresponding field components

$$E_r = \frac{E_0 r}{a} \cos 2\theta, \quad E_\theta = \frac{E_0 r}{a} \sin 2\theta, \tag{5.3}$$

or in the Cartesian coordinate system

$$E_x = -E_0 \frac{x}{a}, \quad E_y = E_0 \frac{y}{a}. \tag{5.4}$$

Correspondingly, E_0 is an electric field strength defined as $E_0 = 2V_0/a$, where V_0 is a potential on the quadrupole electrode. To incorporate this definition, two additional parameters were introduced for the **genericquad** class: ***gradientM*** and ***gradientE***. The definition of quadrupole strength for both field types was used in terms of normalised quadrupole strengths $k_{B,E}$ using the conversions in Eq. 3.11.

G4beamline includes two geometric configurations of quadrupole, cylindrical and plus ("+") shaped. Both variants are shown in Fig. 5.3 together with their field lines. The major difference is a slightly increased collimation of particles, outside the aperture dimension a, for the cylindrical design.

To confirm the accurate implementation, particle tracking of the optically matched distribution, with an emittance of 2.5 mm was performed through a FODO lattice con-

sisting of five magnetic/electrostatic quadrupoles. Both types had the same integrated focusing strength and used a hard edge model approximation.

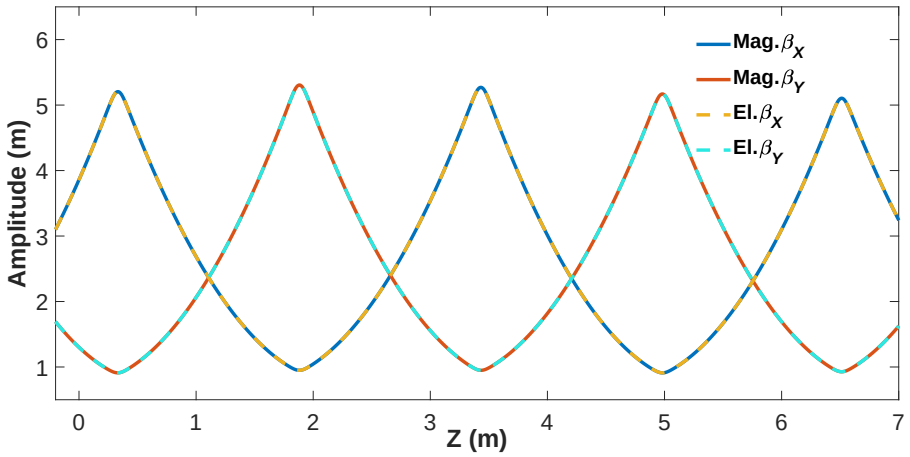

Figure 5.4: *Benchmark of magnetic and electrostatic beam lines consisting of 5 quadrupoles. Horizontal and vertical beta functions ($\beta_{x,y}$) are displayed.*

The comparison of obtained optical beta functions, $\beta_{x,y}$, is shown in Fig. 5.4. Optical functions were calculated using **profile** G4beamline command based on covariance matrix formalism from Chapter 2. These are in perfect agreement because of the absence of a longitudinal field. Additionally, the particle distributions have been

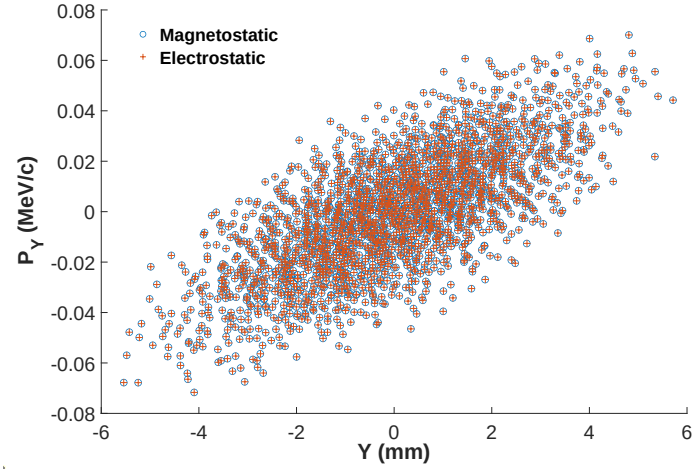

Figure 5.5: *Benchmark of magnetic and electrostatic beam lines consisting of 5 quadrupoles. Vertical phase space plots of 2000 particles at* 200 mm *distance after the last quadrupole.*

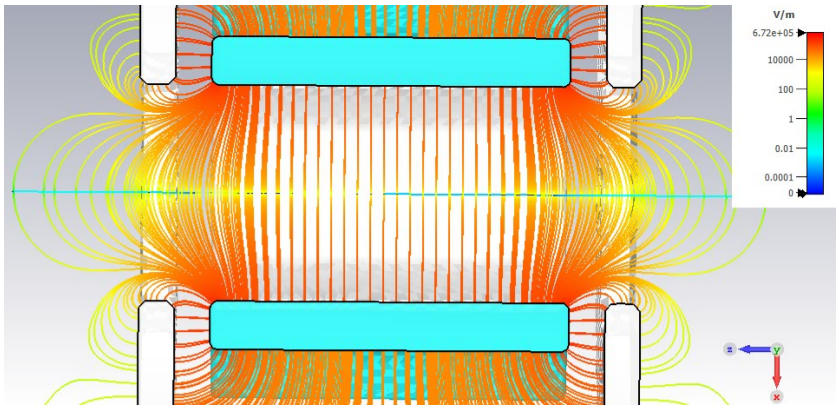

Figure 5.6: *Field lines in the middle of quadrupole with* 1 mm *offset in y for cut, voltage of* 1.5 kV *applied on electrodes.*

compared and are shown in Fig. 5.5. Minimal offsets can be explained by the numerical precision of the Runge-Kutta method and rounding errors.

A more realistic G4beamline model of an electrostatic quadrupole was implemented based on the CST model described in Chapter 4. It utilises the additional description of fringe fields with the Enge function, mentioned in Chapter 3. Figure 5.6 shows a quadrupole ZX-cut with 1.5 kV applied and shows how the fields propagate beyond its electrodes (light blue). To approximate this shape, the dependence of an

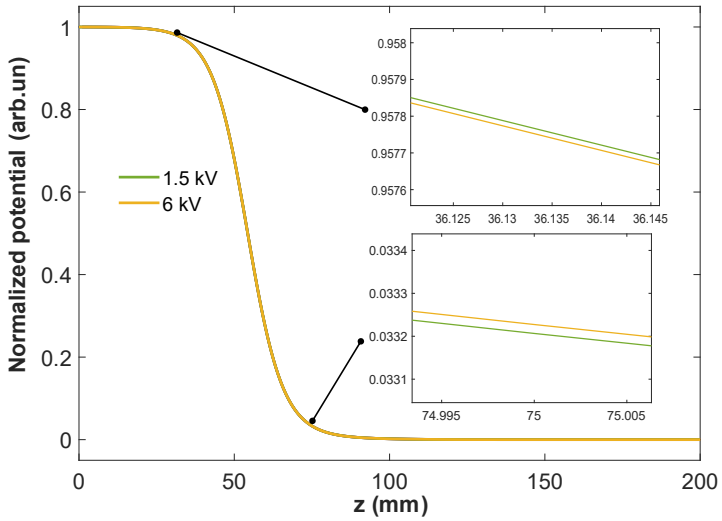

Figure 5.7: *Comparison of Enge function fits for various voltages.*

electrostatic potential V on the quadrupole length was characterised at a radial dis-

tance of 20 mm from the central axis. This distance represents the size of the good field region, described in the quadrupole technical specification. The procedure was repeated with 6 kV voltage to ensure confidence in the quality of the field description. The obtained data was then fitted with the Enge function ($R^2 = 1$) using MATLAB's Curve Fitting Toolbox [144].

The shape of the potential across the quadrupole is independent and naturally scales with the applied voltage. The potential difference comes mostly from the numerical precision of CST field simulation and, in the normalised case, is $\approx 1 \times 10^{-4}$, as displayed in Fig. 5.7. All six coefficients, $a_1 \dots a_6$, are very similar and may be found in Table 5.1. It also means that the shielding performance is sufficient and that a single Enge fit can be used for the simulation of any quadruple in the ALPHA beam line.

Table 5.1: *Enge coefficients for different electrode potentials.*

Voltage, V	a_1	a_2	a_3	a_4	a_5	a_6
1500	-0.7528	10.45	0.3205	-3.219	-3.102	3.321
6000	-0.7529	10.45	0.3324	-3.234	-3.215	3.475

5.3.2 Fast and slow deflectors

The fast extraction devices, in their turn, aim to satisfy multiple requirements. The goal is to extract a beam by 220 m and have good field region of size ∅52 mm with quality of ±1%. The total beam acceptance is ∅60 mm. It was achieved with the geometry displayed in Fig. 5.8. The electrodes of length 400 mm are not parallel and slightly follow the extracted beam in order to decrease the required voltage from ±7.3 kV to ±6.1 kV [145]. The material used in the electrodes and shielding is AISI 316LN stainless steel.

To implement this deflector in G4beamline simulation, firstly, a CST model was created using CERN's Engineering Data Management Service (EDMS) database drawings [146]. The most important parts: electrodes, vacuum vessels and inner shielding

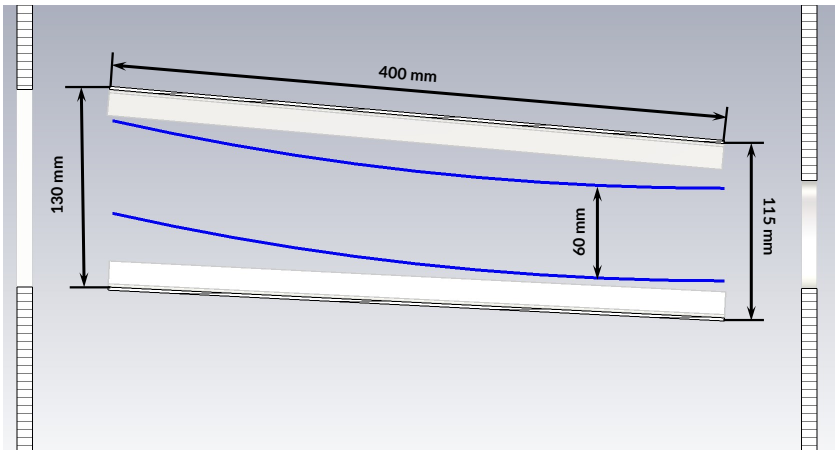

Figure 5.8: *Geometry of ZDFA deflector electrodes. Blue lines represent the total beam acceptance.*

were simulated. The shape of the surrounding vacuum vessel has a noticeable impact on the created electrostatic field configuration. To confirm the practicality of the design values, beam tracking was performed and the result is shown in Fig. 5.9. The total

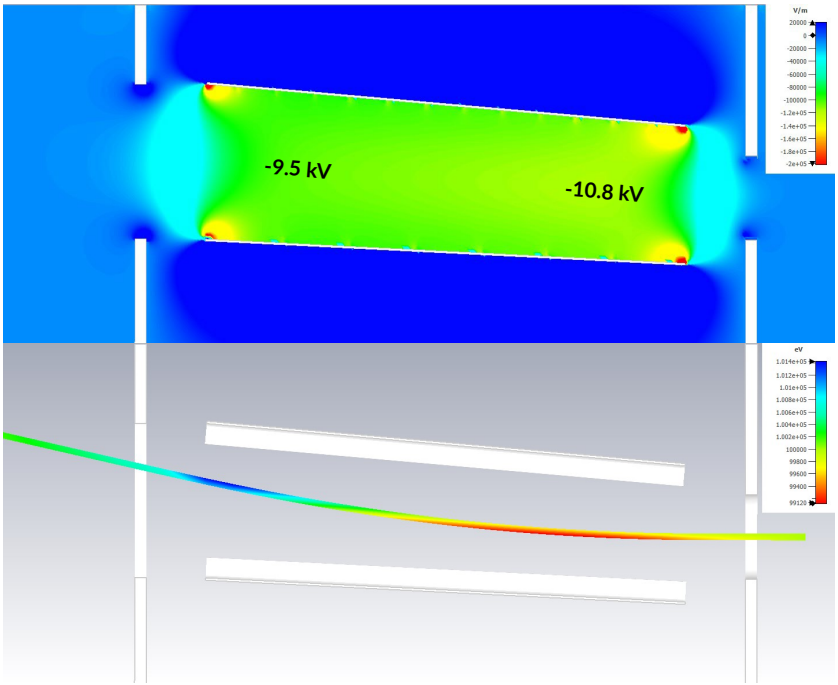

Figure 5.9: *CST model of ZDFA deflector electrodes. The distribution of the horizontal field component E_x is quite uniform (Top). Tracking of* 100 keV *antiproton beam through electrodes.*

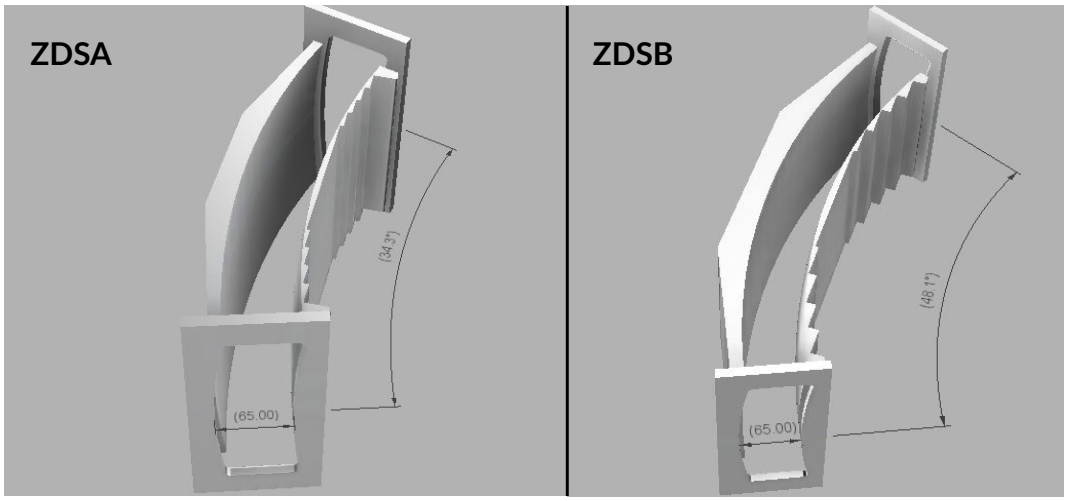

Figure 5.10: *CAD models of ZDSA and ZDSB deflectors.*

deviation from the ideal bending angle is less than 0.25%. An extracted field map with a dimension of 160×40×700 mm and step of 2 mm provided the realistic description of ZDFA element in G4beamline simulation. This includes two 150 mm drift regions before and after deflector.

In a similar manner, the two types of slow deflectors: ZDSA and ZDSB were simulated. As you can see from Fig. 5.10, both types share a toroidal design and the ZDSB deflector is an elongated version of the ZDSA deflector. The curved beam orbit has a radius of 600 mm. The aperture between the electrodes of 65 mm provides a bending angle range of ±1.2° for ZDSA and ±2.3° for ZDSB depending on the applied voltage. The nominal bending angle voltages are ±10.078 and ±10.54 kV respectively. The material used for the electrodes and shielding plates is AISI 316N stainless steel.

By analogy with the ZDFA deflector, CST models were created and Fig. 5.11 demonstrates the beam tracking performed with the aforementioned parameters. Afterwards, field maps with dimensions of 250×40×600 mm and 284×40×730 mm were produced for G4beamline.

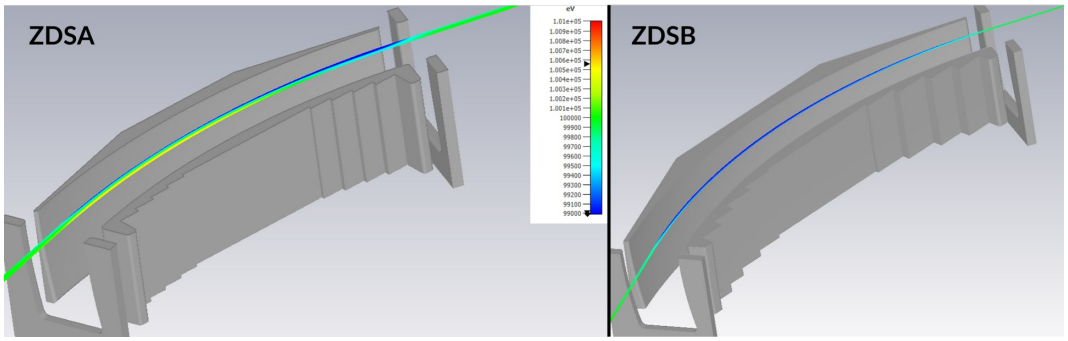

Figure 5.11: *CST models of ZDSA and ZDSB deflectors. Tracking of* 100 keV *antiproton beam through both geometries.*

5.3.3 Complete model and G4beamline improvements

Using the descriptions of the beam line elements described in the previous section, the transfer line to ALPHA was modelled in G4beamline. The lattice was constructed on the basis of the transfer line design from CERN report [147] and adjusted accordingly to the latest available MAD-X model [137].

Figure 5.12 shows an interactive 3D visualisation model using OGLSQt driver with antiproton beam tracking shown in red. Bending elements and beam line sections are also highlighted. The colour of the deflector electrodes represents an applied voltage polarity in the CST model. After the reference particle and the beam have been tracked

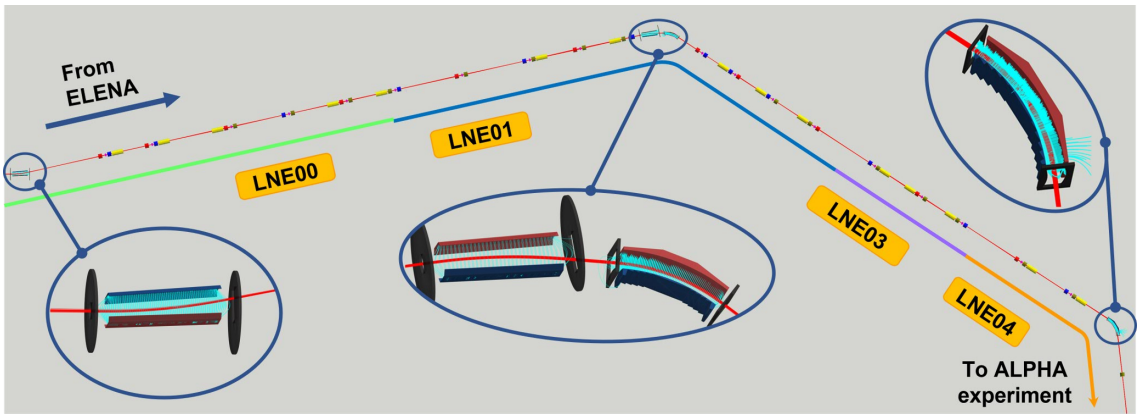

Figure 5.12: *3D visualisation of ALPHA branch in G4beamline. The deflector elements are highlighted. Field lines are shown in cyan.*

through the lattice, the user may request to store beam distribution in predefined

locations via the virtualdetector (does not affect beam) or detector (physical detector with the defined material) commands, these can calculate many useful accelerator physics quantities based on the beam's behaviour. The profile command can store the emittance and optical functions along the lattice, amongst other parameters in the requested reference coordinates. The trace command allows the user to record information on individual particles at defined equidistant steps, for instance, to store the field type, strength and components seen by the particles as a function of s and the transverse coordinates. This information can be used for the custom calculation of optical functions or for extraction to another code.

Apart from adding electrostatic quadrupoles, the default G4beamline 3.06 Geant4 project was additionally modified to improve the demonstrated simulation model as well as the efficiency of the tracking code in general. Here is a brief list of the most important modifications with a short description of each:

- Added capability to import or export CAD geometries (physical properties) into G4beamline in GDML format, as shown in the example of the deflectors in Fig. 5.12. This simplifies error checks during field map insertion and provides realistic apertures and accurate beam dose deposition. It also enables the capability for the model to be transferred between different codes [148].

- The material command was modified by adding `ionpotential` parameter, which allows the ionisation losses to be redefined inside a material according to measurements. The default value is calculated using the Geant4 algorithms.

- G4beamline was updated to Geant4.10.07 version. The field manager class was modified to enable a range of the latest field integrators instead of the one default 4^{th} order Runge-Kutta method. The Dormand and Prince 5^{th} order stepper was used as the new default option because of the fewer evaluations of the derivative (and field) than the previous classical 4^{th} order method. The ability to set a specific field stepper to any element was another addition to the code. The best choice overall depends on the smoothness of the field.

5.4 Input beam distribution

The input beam distribution was generated using a Matlab script developed on the basis of the sigma matrix methods described in Section 3.6. It also allows forward and backward conversion to the BMAD bunch format. The optics parameters used were the same as in the MAD-X simulation provided by CERN. The generated 6D phase space bunch population of 128,000 macro-particles has a 3D Gaussian shape truncated at 3.5σ, where σ is the standard deviation. Full properties of the created bunch are shown in table 5.2 These values were assumed in accordance with the latest ELENA scraper

Table 5.2: *Bunch parameters for the injected bunch.*

Parameter	Value
Bunch length r.m.s $\sigma_{z,t}$ (m, ns)	$0.3282, 75$
Relative momentum spread $\Delta P/P_0$	1×10^{-4}
Reference momentum P_0 (MeV/c)	13.7
Horizontal/vertical emittance $\epsilon_{x,y}$ (mm mrad)	2.55, 2.5
Horizontal/vertical size r.m.s $\sigma_{x,y}$ (mm)	3.25, 3.7
Relativistic beta β	0.0146

measurements for a coasting beam at the extraction plateau without cooling [149] (Table VI). These are closer to the latest obtained beam profiles at LNE50 obtained via micro-wire monitors [150] (Figure. 12). The measured transverse beam distributions were well described by Gaussian distributions with the same input parameters. Beam tracking was performed with a maximum step of 1 mm in elements containing the field and 10 mm in the drift sections. An artificial cutoff of 35 mm (termination of particles) was implemented to mitigate the impact on statistical calculations by rare events when particles leave the beam line.

5.5 Comparison with BMAD implementation

To fully trust the simulation results, an additional benchmark of the ALPHA beam line was performed in BMAD. This is a subroutine library written in FORTRAN for charged-particle and X-ray simulations in high-energy accelerators, storage rings and low-energy injection transfer lines. Each individual element can be assigned a particular tracking method in order to maximise the speed or accuracy of the program. In addition, a Python interface has been included [151] to simplify the bunch conversion to other codes at any stage of tracking. The same CST field maps were assigned to the bending elements after conversion into BMAD format. Quadrupoles were defined as electrostatic multipoles with focal strengths as in the MAD-X model.

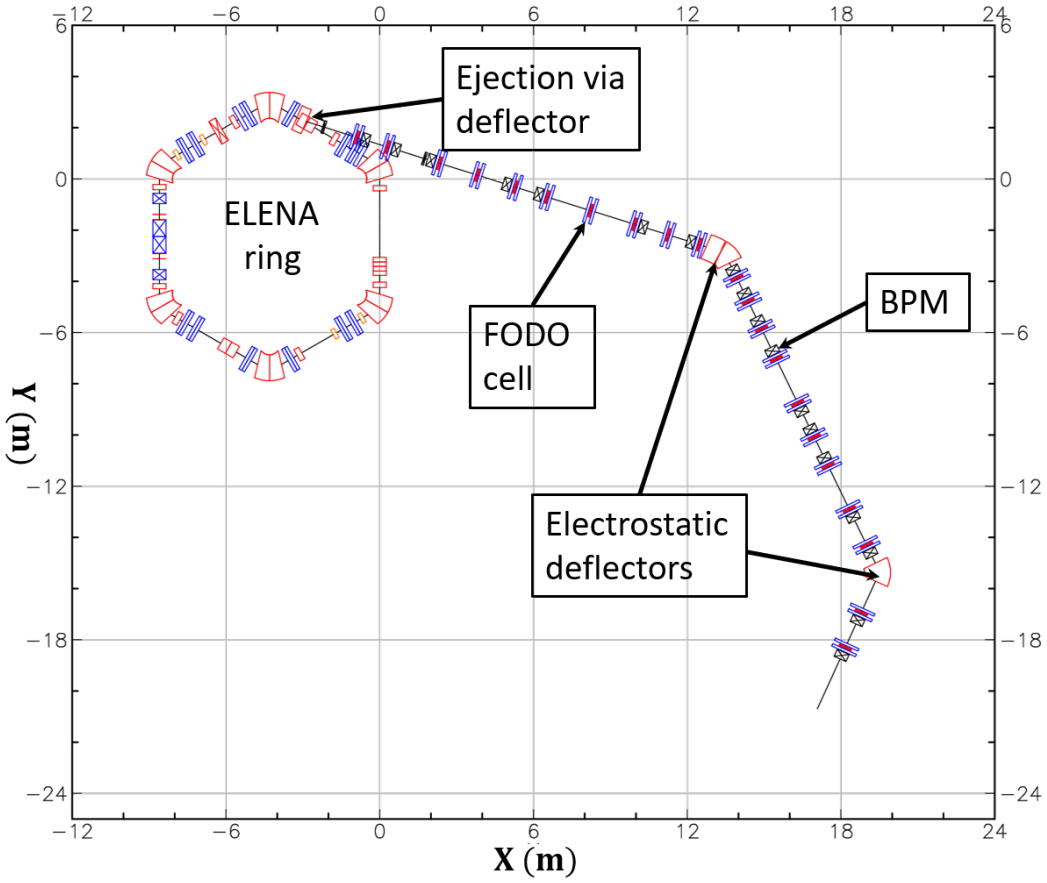

Figure 5.13: *2D layout of ALPHA transfer line linked with ELENA from BMAD simulation*

Produced in BMAD, a 2D visualisation of the calculated lattices for the ELENA ring and the transfer line to the ALPHA experiment is depicted in Fig. 5.13. Such a model allows the seamless injection of the bunch from the ring. The bunch distribution was generated with the same parameters as for G4beamline and tracked through the transfer line section. The beam propagation method for field map elements was set to 5^{th} order Runge-Kutta and the rest of the elements were using the default BMAD tracking algorithms. BMAD, similarly to MAD-X, allows the calculation of many beam and lattice quantities. Beam optics and orbits were scored and compared against results from the above-mentioned simulation tools. Figure. 5.14 shows a comparison of the beta functions and orbits for; G4beamline, BMAD and an initial MAD-X simulation where the first-order Taylor maps were used to represent the fast and slow deflectors. Overall, there is a good agreement between the three simulation codes. The small

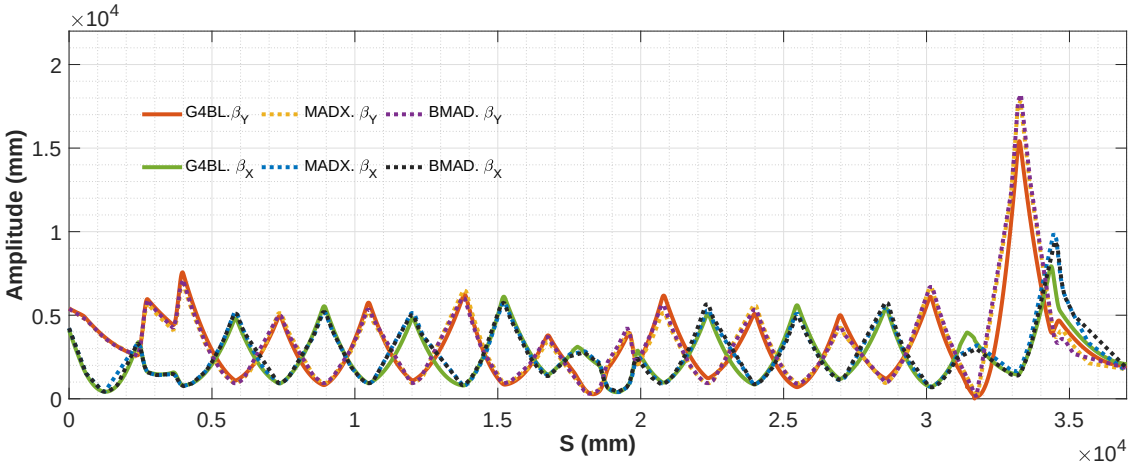

Figure 5.14: *Comparison of beta functions in G4beamline, BMAD and MAD-X.*

discrepancy in G4beamline comes due to the technical reason mentioned before. Only the G4beamline simulation of transfer line electrostatic quadrupoles contains a realistic distribution of fringe fields. Thus, a small mismatch in optics accumulates towards the end of the beam line when MAD-X quadrupole strengths are used, leading to differing final results.

Interestingly enough, the BMAD simulation agrees with MAD-X, despite the fact

that it uses field maps from G4beamline. This means that the deflectors that were simulated are in close agreement with the initial design.

To further compare these simulations, beam quality tests had been performed with the same input beam, described in the previous section. These were defined within an initialisation file for BMAD and after tracking, the same distribution was exported into G4beamline. Figure 5.15 shows a bunch after ejection from ELENA and the final distribution delivered to the ALPHA experiment. Growth of the beam r.m.s emittance at a level of 1% had been observed due to small geometric aberrations after deflectors. The r.m.s beam widths at the end of the beam line from simulations in

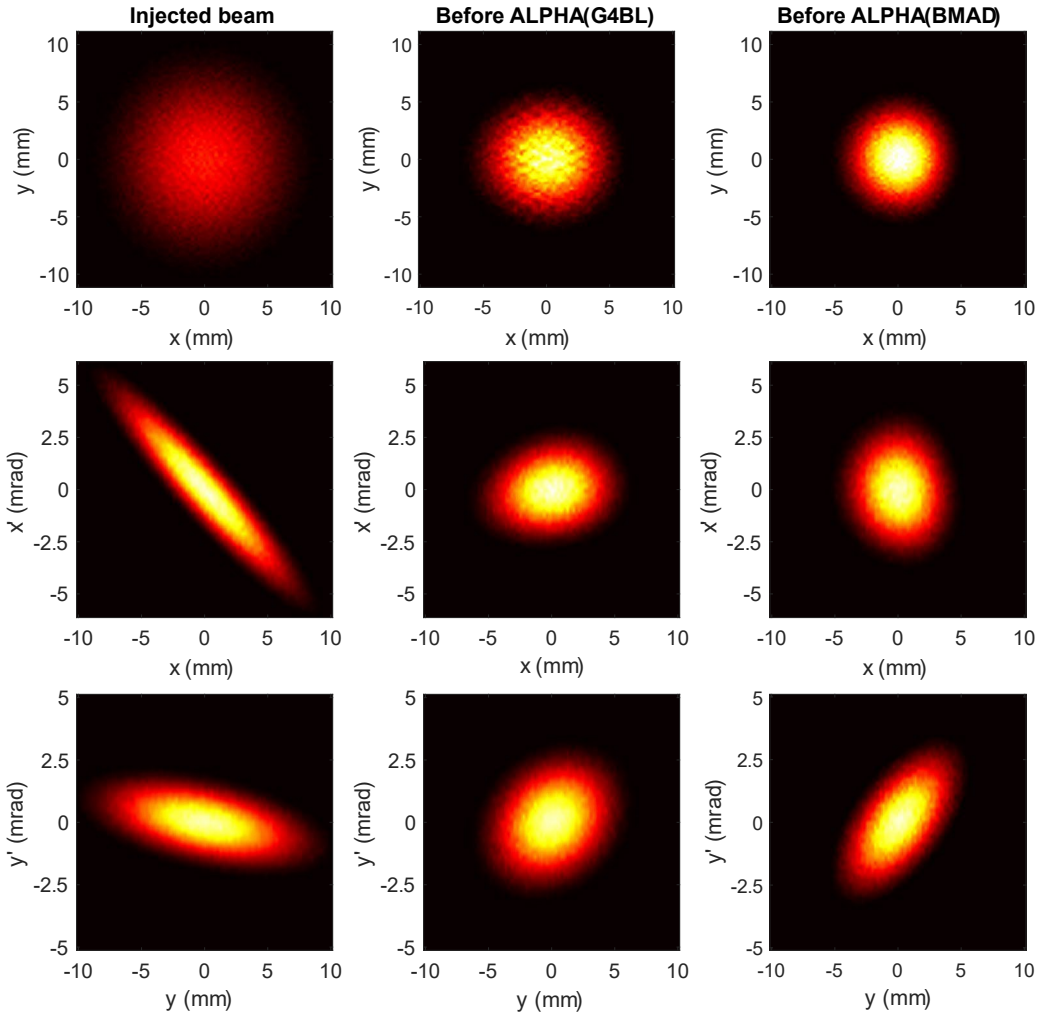

Figure 5.15: *Comparison of transverse beam phase spaces at the start and end of the beam line to ALPHA.*

G4beamline(BMAD) are $\sigma_x = 2.25\,\text{mm}$ (1.9 mm) and $\sigma_y = 2.15\,\text{mm}$ (2.08 mm) which is close to the design values of $\sigma_{x,y} \approx 2\,\text{mm}$. A small difference in distributions is observed due to optics mismatch and it is possible to obtain exact results via quadrupole strength tuning. Evidence of this linear effect can be demonstrated with an extra increase of the horizontal focusing in the G4beamline model. The comparison of the horizontal distribution before and after this adjustment in G4beamline is shown in Fig. 5.16. The resulting beam width is almost identical to BMAD output where quadrupole length is unaffected by fringe fields.

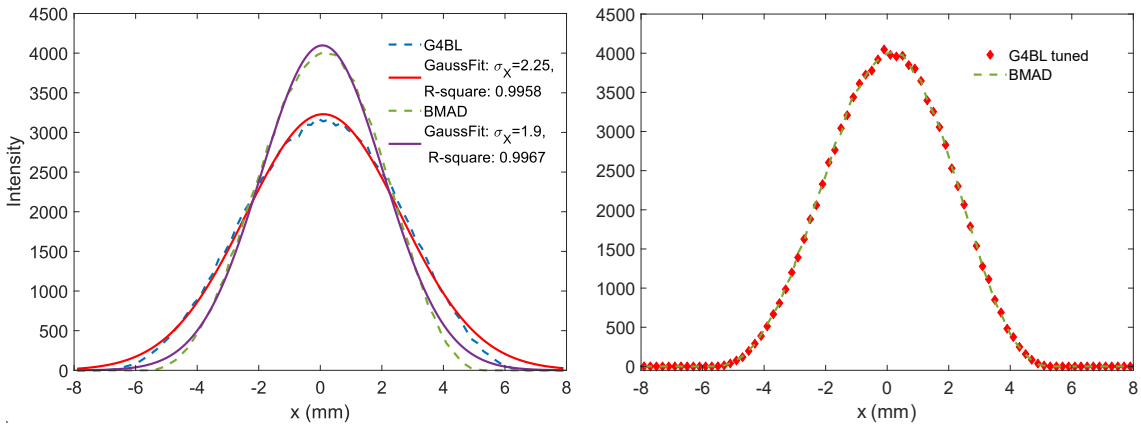

Figure 5.16: *Comparison of the horizontal beam distribution at the end of the beam line to ALPHA before and after quadrupole tuning. Tracking data provided from BMAD and G4beamline.*

5.6 Tuning process in G4beamline and BMAD

The previous section did not discuss one important fact about field maps. Because of the field simulation tool settings (mesh size, boundary conditions, etc.), field interpolation method or tracking algorithm, an output field value naturally varies to some small extent. However, a variation on a large scale may significantly affect a beam that is tracked through the map. To reduce inconsistency, an additional tuning of the field maps was performed in G4beamline and BMAD.

G4beamline provides a simple tuning algorithm ("Golden-section search") for

bending elements, RF cavities and field maps via the `tune` command. It uses iterations of a reference particle that travels from s_0 to s_1 beam line position to evaluate and minimise a defined expression at s_1, based on some default particle properties (x, Px, t, etc.) and varying typically an element's field amplitude, particle momentum or phase of RF wave. For instance, to tune a ZDFA kicker, the reference particle passes through it, from s_0=0 m to s_1=2 m, adjusting the gradient of the provided field map to minimise the x position of the particle at s_1. When the output value is lower than the tolerance settings, the field gradient is used for full beam tracking. This was done to set the field amplitudes for all four bending elements to steer the beam by the correct angle. The multiple `tune` instances were utilised to have a combined effect of all bending elements.

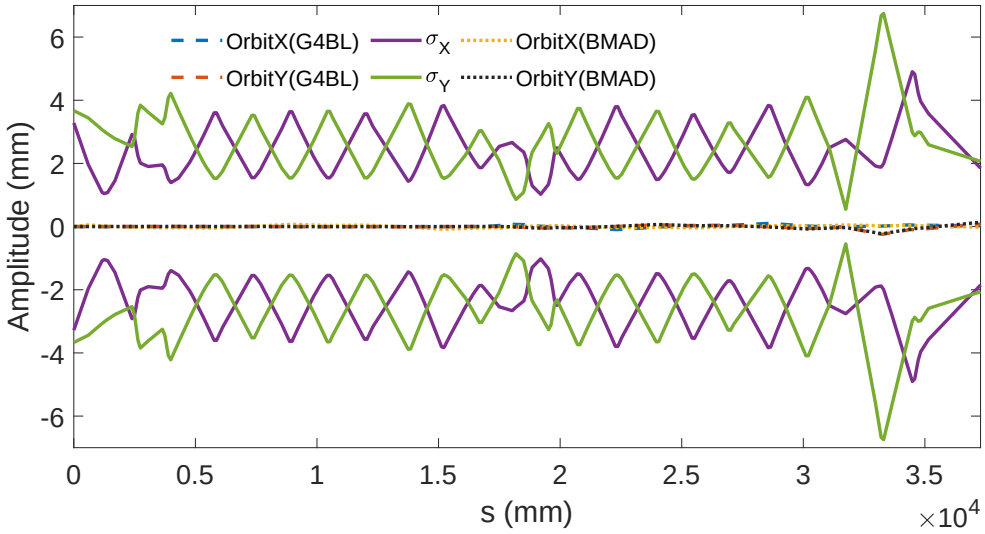

Figure 5.17: *An orbit of the simulated beam in G4beamline and BMAD together with an r.m.s beam width.*

BMAD has the capability to tune almost every aspect of the beam line or beam, except for parameters with inter-dependencies. For example, the bending radius and deflection angle of a magnet cannot be tuned simultaneously. Like G4beamline, the BMAD sub-program Tao itself implements "single objective optimisation" methods. The `lm` and `lmdif` optimisers, based on the Levenberg-Marquardt algorithm [152], provide fast minimisation of the defined problem but mostly find a local minimum.

The differential evolution method (`de`) [153] finds the global minimum but has longer evaluation times. During field map tuning, a combined strategy was applied with the usage of `lm` and `de` optimisation one after the other.

Amplitude values obtained after field map tuning in comparison to the design numbers were lower by 0.35%, mostly due to extended fringe regions in BMAD and G4beamline. Figure 5.17 provides an illustration of obtained beam orbits together in scale with r.m.s beam envelopes. A residual effect of tracking through deflector field maps was a small momentum offset of $\delta = 3.6 \times 10^{-4}$ (70 eV as kinetic energy shift) shown in Fig. 5.18. This is most likely due to field interpolation errors and field asymmetry at the entrance and exit of the deflector field map. In terms of practical aspects for particle trap experiments, to remove this momentum excess, an extra foil thickness of roughly 1 nm (for aluminum) is needed—this is one order smaller than the error during foil thickness measurements [154]. So overall this error is insignificant.

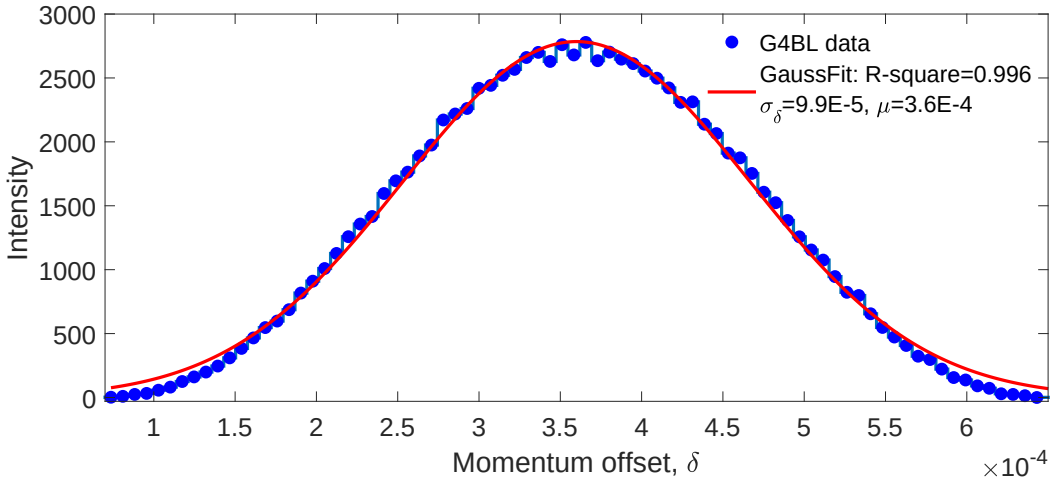

Figure 5.18: *Distribution of momentum offset at the end of the ALPHA beam line (blue) and applied Gaussian fit (red).*

For multiple objective optimisation, BMAD/G4beamline can be linked to Python/Matlab and utilise the existing optimisation algorithms such as the genetic and paretosearch algorithms [155]. Additionally, for this purpose, the BMAD distribution contains a sub-project `moga` that is based on a genetic algorithm.

5.7 GUI application

Analysis of the G4beamline output can be time consuming and repetitive. Initially, to aid this the installation of G4beamline contained the HistoRoot sub-program [156] that allowed data to be displayed from ASCII or ROOT files. However, due to limited support, it works only with a specific ROOT version. To improve this, a Matlab-based interface was developed using `appdesigner` and available Matlab language functions. An image of the developed GUI is shown in Fig. 5.19.

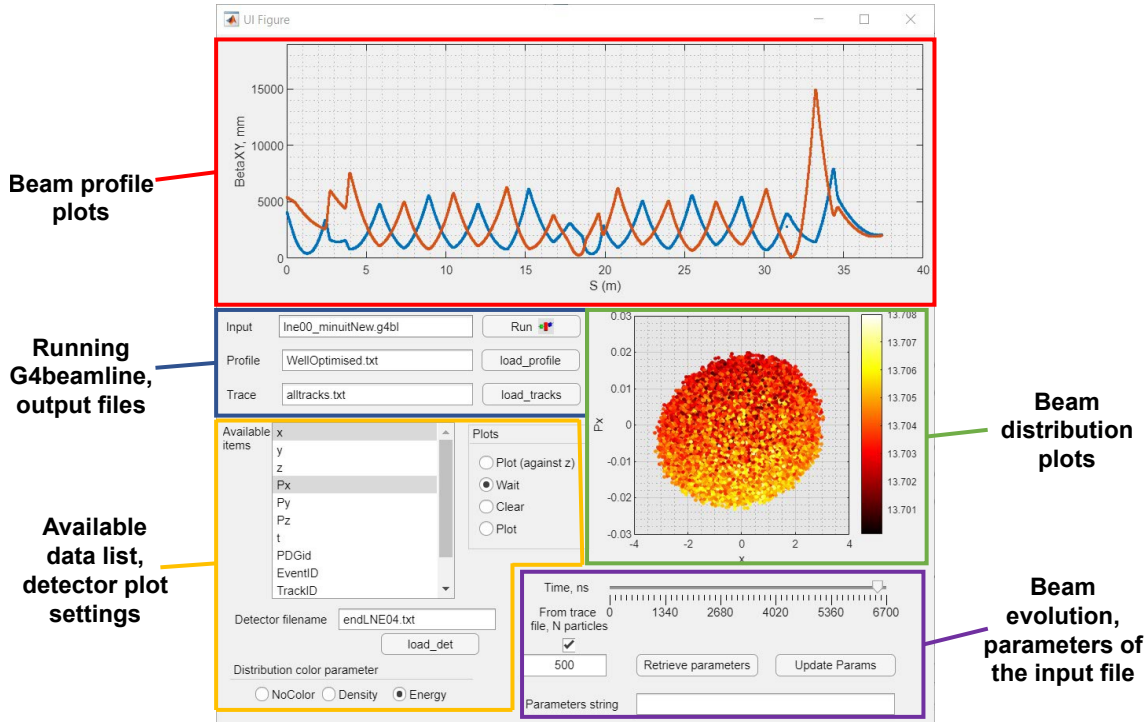

Figure 5.19: *Developed GUI and the provided functionality.*

Readout and G4beamline initialisation functions are contained behind the Matlab scripts which receive input from the GUI. The list of available data is flexible and updates depending on the number of columns in the output file. Plots appear in one of the two windows depending on the type and number of simultaneously selected by user data entries. The distribution plots allow a colouring scheme based on the particle energy (momentum) or particle density per 1 mm. Alternatively to `detector`

output, the distribution can be plotted from a `trace` file, that allows the user to see the beam at a specific time (or location s). A parameter line defined within the input file parameters via `param` command is also shown. This GUI provides easy and intuitive access to all simulation data and can be distributed to any operating system where a standalone set of Matlab Runtime libraries is installed [157].

5.8 Impact of stray fields from AEgIS

The impact of the stray magnetic field was discussed in Section 3.7. Figure 3.8 demonstrates a situation when all experiments in the AD hall work simultaneously. In the previous studies of transfer lines, the solenoids from particle traps were described as a single point source and adopted an analytic approach [124, 158]. The impact of the field components was included in the transfer line model via transverse kicks to the reference particle with 10 cm sampling of the available drift space.

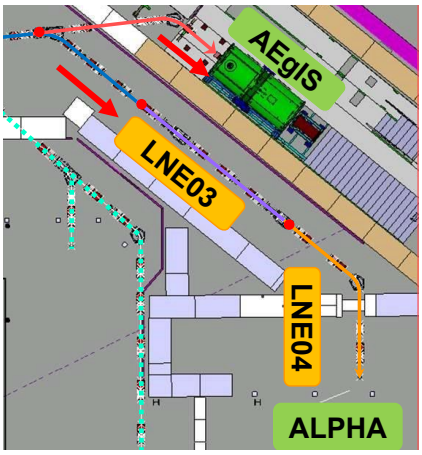

Figure 5.20: *The relative location of AEgIS and ALPHA.*

To improve the previous somewhat simplified model, in this study [159], a combined G4beamline model of ALPHA and AEgIS solenoids was constructed to apply a realistic 3D distribution of the stray fields. The location of these two experiments is highlighted in Fig. 5.20. The magnetic contributions from the AEgIS trap are generated by two main coils and 21 low-field correction coils. The main barriers between

the transfer line and the experiment are the stainless steel vacuum vessels and concrete wall which have minimal shielding capabilities ($\mu < 1.01$). Any extra shielding effects could be produced by a ferromagnetic material located in the space between the solenoid and the ALPHA beam line.

5.8.1 Model of the particle trap solenoids

All solenoidal coils were simulated in CST to include the external field coming from the trap at a significant distance. An additional simplified benchmark had been performed between CST and G4beamline utilising `coil` and solenoid elements. The magnetic

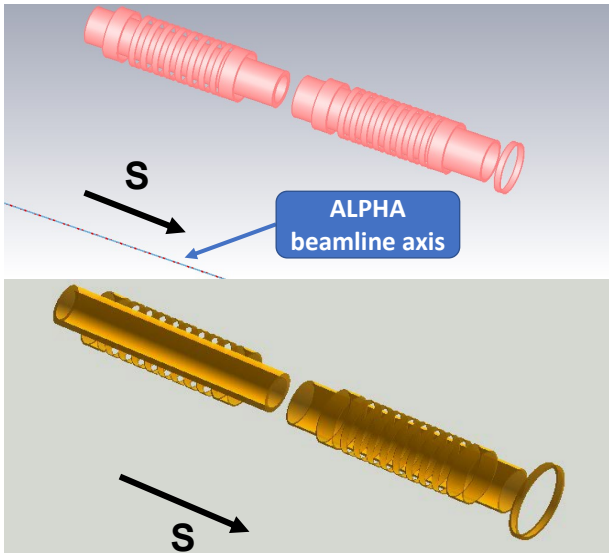

Figure 5.21: *Geometry of AEgIS coils. (Top) CST model with a dashed line indicating the position of the ALPHA transfer line. (Bottom) Model of the coils modeled using G4beamline.*

field produced with these `coils` is computed for a set of infinitely thin current sheets spread evenly radially. The `solenoid` provides the working current to a set of nested coils. The size of the simulation region for the CST had been chosen to obtain the field components down to the level of the Earth's natural magnetic field amplitude.

A comparison of the model geometries is shown in Fig. 5.21. The top part of the image shows coils simulated in CST. The neighbouring beam line directed towards

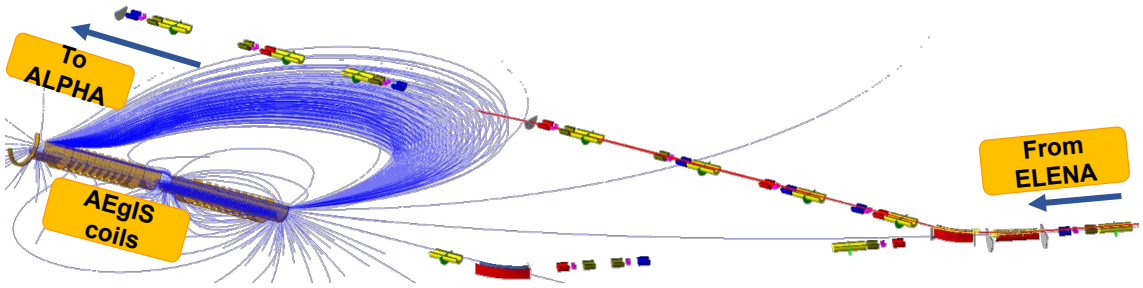

Figure 5.22: *Antiproton beam (in red) loss in front of AEgIS solenoid line due to stray fields (blue lines) impact.*

ALPHA is located at ∼3 m from the solenoid axis. The bottom image demonstrates the geometry of the coils created in G4beamline. To maximise tracking performance, only a small volume of the simulated field was used which encompassed the relevant vacuum chambers. The field map was of size 0.024 m × 0.024 m × 13 m and was exported and implemented into the G4beamline simulation in such a way that the antiproton beam passes through the middle part of the field. The use of the whole map is not computationally efficient when the fine mesh (2 mm) is used. The same 6D beam distribution with a momentum of 13.7 MeV/c was used as an input for tracking. Due to the presence of the magnetic fields the beam is deflected immediately after bending towards the ALPHA branch. The beam trajectories from tracking are shown in Fig. 5.22. The beam is terminated in space due to reaching the artificial radial cut-off distance of 35 mm corresponding to the beam pipe aperture. The position of the first coil entrance was obtained by combining data from [147] and distance measured during the visit to the AEgIS experiment.

5.8.2 Comparison of field map and analytic method

To benchmark the field obtained from CST and G4beamline, one can track a particle with zero charge with a 1 mm step through the straight section of the ALPHA beam line. The field components witnessed by such track can be stored via `trace` command. The stored field for both solenoid representations is shown in Fig. 5.23. For comparison, it is worth highlighting the absolute value of the Earth's magnetic field amplitude in

the CERN region is 4×10^{-5} T [160], which is shown with a straight line.

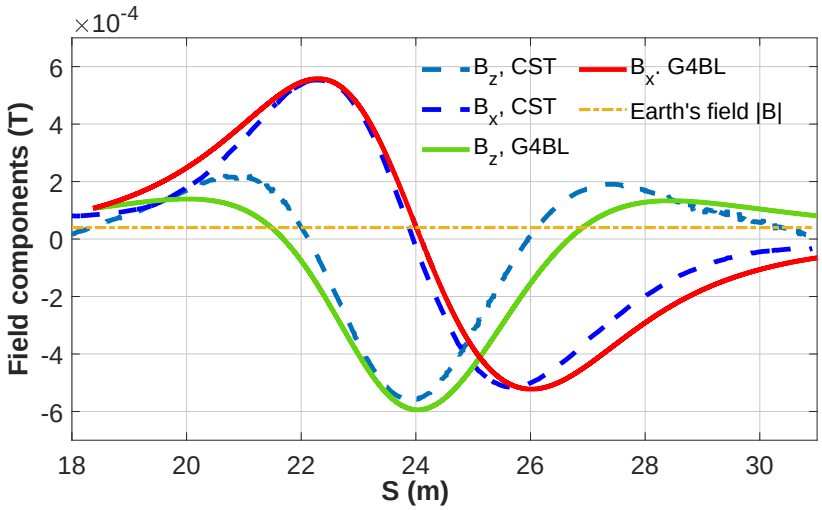

Figure 5.23: *Benchmark of the largest stray field components: B_z going along the beam line axis and B_x is a transverse component.*

5.8.3 Field mitigation with a passive shielding

An additional passive shielding of the beam line in the region with the highest stray field amplitude may be used to help mitigate their impact. The volume fully enclosed

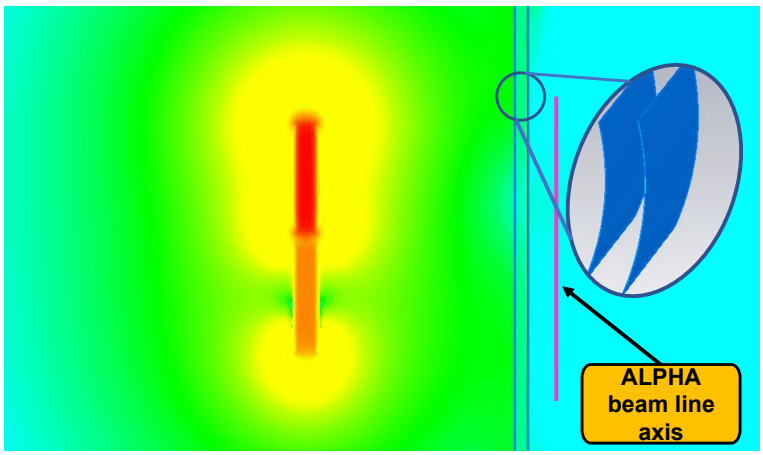

Figure 5.24: *The magnetic field from AEgIS coils and passive shielding influence. The geometry of two thin sector shields is highlighted.*

or partially covered with a thin layer (multi-layer) structure composed of the material

with high magnetic permeability (μ_r) may provide the region with a decreased field amplitude. A best practice is to use a fully enclosed cylinder or box made of mu-metal ($\mu \sim 80000$), multi-layer film nanostructures or permalloy, that help to shield, for example, photo-multiplier tubes [161–164]. In theory, the coating of beam pipes in the drift sections with thin foils made from these materials may be considered. An alternative option can be lightweight modular shields that will increase the curvature of magnetic field lines. The such preliminary design had been studied and is shown in Fig. 5.24. The two thin cylindrical sectors in this picture are made of mu-metal. One can see that the field distribution—created via solenoidal coils—is quite asymmetrical when the shield is installed on the left from the ALPHA line. The design provides easy access to beam line elements or to the particle trap components and it is relatively movable. Further, the impact of the shield has been investigated depending on the distance from the main coil axis. Results for B_x component are shown in Fig. 5.25. The efficiency of the shielding increases with the distance from the trap for the reason that a smaller portion of the field bypasses these mu-metal foils

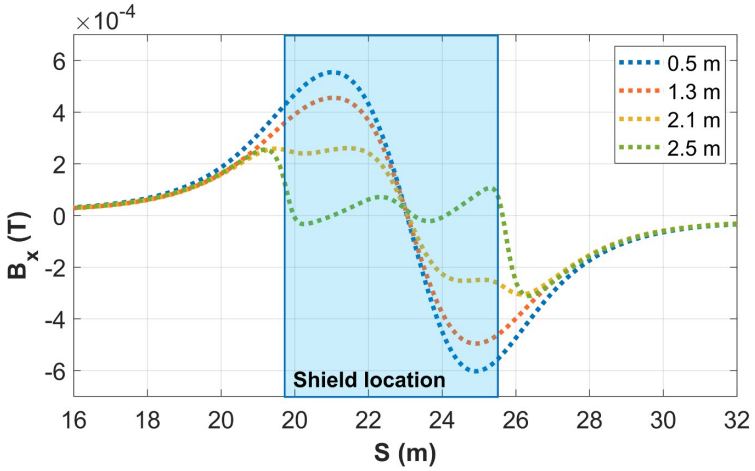

Figure 5.25: *An amplitude of magnetic field component B_x at ALPHA line axis depending on the distance between the solenoid and the shield.*

The low field region from 20 m to 26 m is hidden behind mu-metal foils and corresponds to 6 m in length. Other possibilities to attenuate stray fields can be the synchronisation of re-powered solenoid magnets in such a way that zero field time gaps

will allow the bunch to pass downstream unaffected.

5.9 Proposal of ion injection scheme into AEgIS trap

In Chapter 1, experiments involving low-energy negative ions (up to 5 keV) were discussed. In the context of this work, the upgrade of the injection beam line for the AEgIS collaboration was created from the ground up. Figure 5.26 shows the current situation from the different angles after the handover point from the LNE02 transfer line. As is shown, there is an available space of dimensions 2.4 m by 1.0 m. The ex-

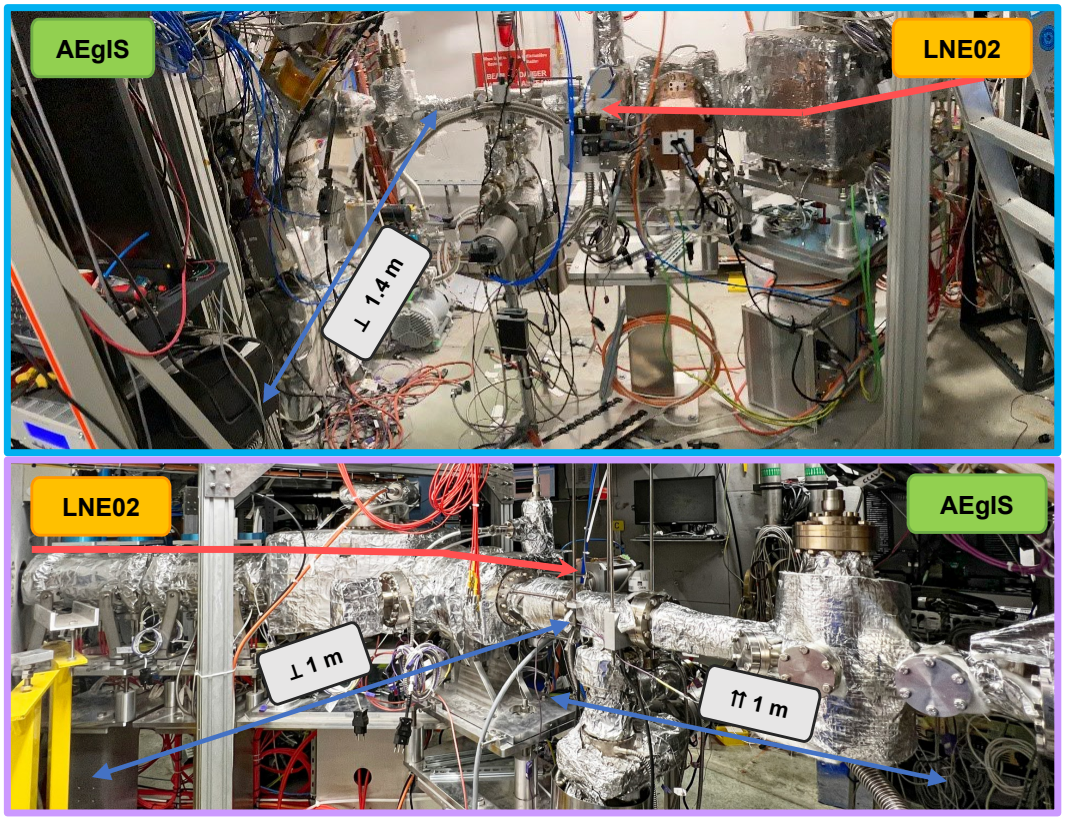

Figure 5.26: *The end of LNE02 electrostatic line and downstream AEgIS beam line section. (Top) View of the concrete wall between AEgIS and LNE03. (Bottom) Sight from the concrete wall.*

perimental plans include the capability to operate with two different anion production

schemes, a Paul trap storing iodine and Cs sputter sources.

Thus, the new beam line should allow the passage of an antiproton bunch and provide bending for both anion species, without simultaneous operation. Another functionality that is highly requested is backward extraction from the trap. The initial relative position and junction points for both ion sources are shown in Fig. 5.27. In

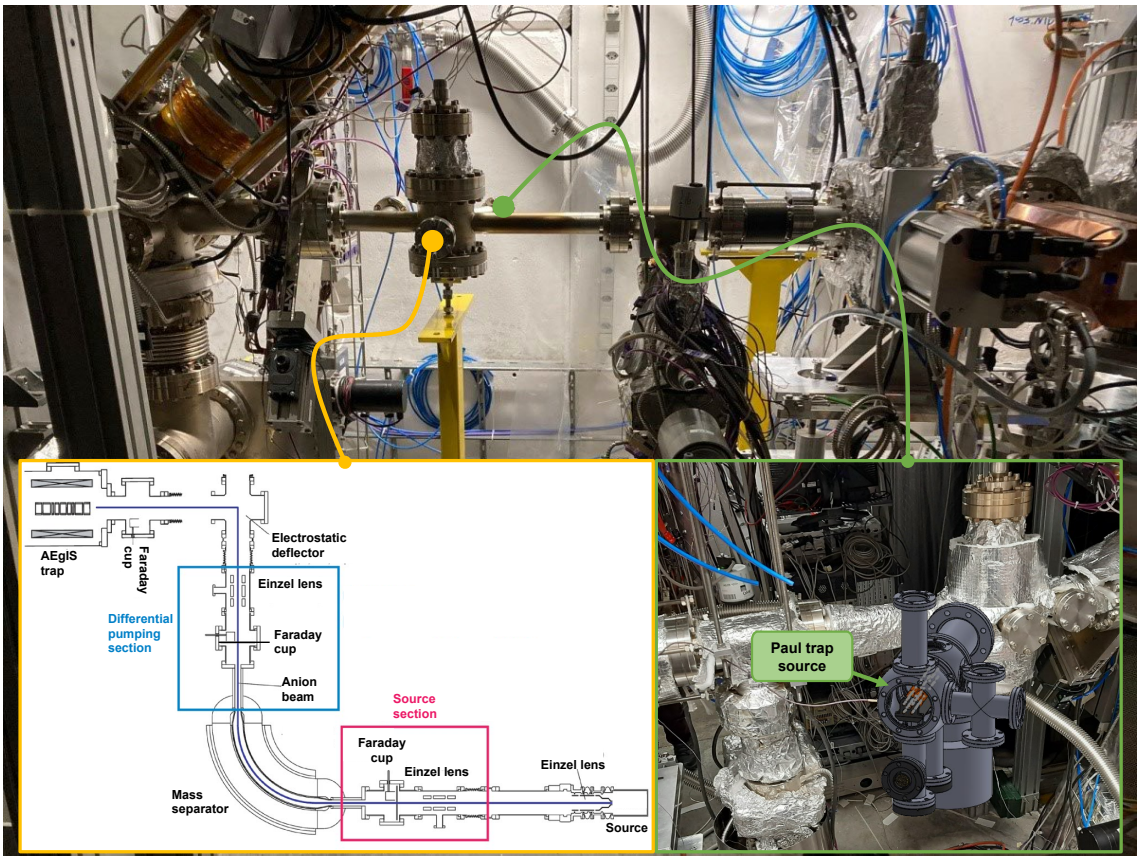

Figure 5.27: *Suggested connection points for anion sources. Branch schematics for Cs sputter source (Bottom left). The first vision of the future connection for the Paul trap source (Bottom right).*

order to provide more space for inner optical and bending elements it was suggested to replace a junction chamber with a larger one. Additionally, due to space limitations, the initial connection at 90° for the Cs source was decreased to 75°. Electrostatic focusing and deflection were chosen as the preferable option due to low energy of the anions and mass independence. The suggested beam line design should be able to handle low anion currents up to 10 µA in continuous mode and provide deceleration

before injection to the trap.

5.9.1 Deflection chamber design

Due to the standalone nature of the ion beam line setup and its small dimensions, the design development was performed in CST with anion beam tracking available. An intermediate stage of the bending section is shown in Fig. 5.28. Most of the optical and bending elements are separated via shielding apertures which are grounded. The design

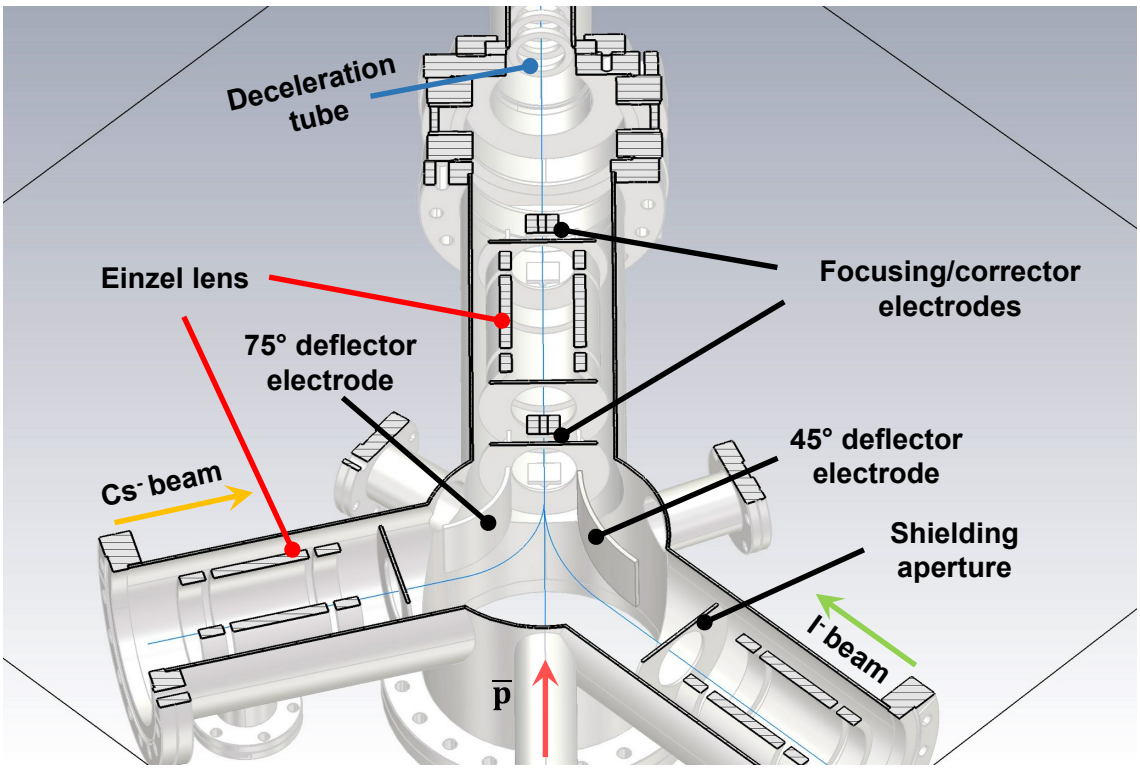

Figure 5.28: *Cut of the deflection chamber design created in CST. The main components are labelled. Thin blue lines correspond to an ideal trajectory of the particle from both branches. Two sets of corrector electrodes help with additional steering or focusing.*

of the vacuum chamber and beam pipe was limited by practical aspects (vacuum level of the LNE02 beam line, accessibility, voltage limits) and the required functionality.

Einzel lenses

The scheme in Fig. 5.28 includes three Einzel lenses. These are made of three cylindrical electrodes for the round beam operation. These lenses are always focusing and do not change the energy of the transmitted particle. The focusing properties of this type of lens are symmetrical, so focal distances before and after the lens are the same $f_1{=}f_2{=}f$. The first and the third electrodes are at the same beam line potential V_0 and the middle electrode has a different potential V_M. The Einzel lens focusing properties depend on the geometry of the lens and voltage ratio V_0/V_M.

When a charged particle passes through the electric field configuration created via such a lens, it enters into a region with a larger electric field and then it gets repelled/attracted to the inner side of the middle electrode. The trajectory inside this lens depends on the middle electrode's voltage, incident angle, charge and energy of the particle. This is similar to the effect of the thick optical lens on the light ray of different wavelengths entering from air into media with higher refractive index (glass for example). The particle velocity here plays the role of the refractive index which is proportional to a square root of the potential value or particle kinetic energy, $E_0 = qV_0$, where q is a charge of the particle. Thus we may construct the charged-particle analogy of the optical Snell's Law

$$\sqrt{E_0}\sin\alpha_0 = \sqrt{E_M}\sin\alpha_M \tag{5.5}$$

where $\alpha_{0,M}$ are incident and "refraction" angles of the particle. Another useful relation that was used during the design was the Helmholtz-Lagrange Law. It links the linear magnification M and angular magnification m of rays through the Einzel lens to the ratio of the kinetic energies between the two ends of the lens

$$\sqrt{\frac{E_0}{E_M}} = Mm. \tag{5.6}$$

The linear magnification $M = r_2/r_1$, where r_1 and r_2, are the widths of the beam at

object and image locations. Angular magnification is defined similarly, $m = \varphi_2/\varphi_1$, where φ_1 and φ_2 are angular spreads at object and image points.

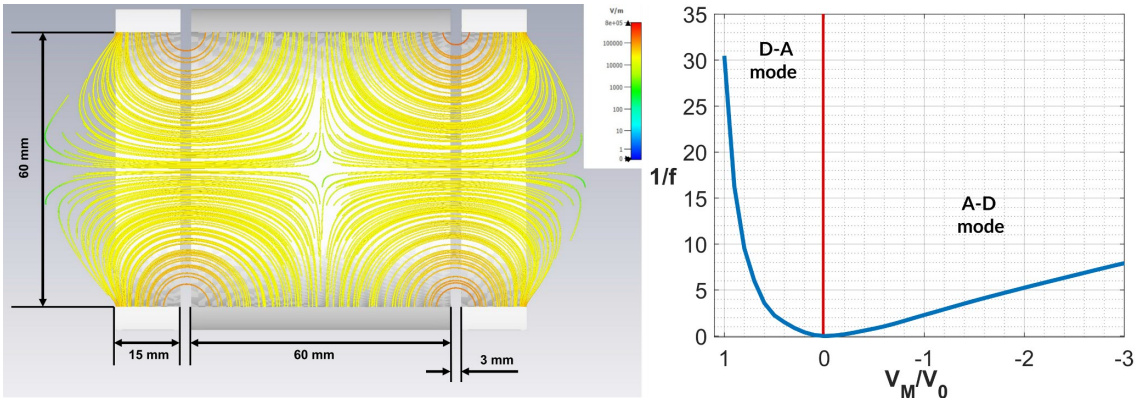

Figure 5.29: *Cut of the Einzel lens designed in CST (left). The highest field is created near gaps between electrodes. Dependence of the focusing strength of this lens from the potential ratio (right).*

The Einzel lens has two operating modes depending on the V_M/V_0 ratio. When we consider negatively charged particles and $(V_M/V_0) < 0$, the lens works in acceleration-deceleration (A-D) mode: the first gap between electrodes accelerates the beam and the second gap decelerates. Conversely, the lens works in deceleration-acceleration (D-A) mode. The second mode has higher refractive power (shorter focal length) compared to the A-D mode for the same voltage amplitude applied to the middle electrode. However, the A–D mode has the advantage when the required focal length is not very small, as in our case. In this mode both the spherical and the chromatic image aberrations are smaller than in the D–A mode [165]. These imperfections are smaller because the trajectories are closer to the main axis of the lens, whereas the transverse field has a more linear behaviour. Figure 5.29 shows the geometry of the lens present in the proposed design and focal strength dependence on the central electrode voltage.

Deflection elements

The big space that nests both bending electrodes is a cylinder with CF160 flange and height of 180 mm. Both bending electrodes have cylindrical geometry with the same

height ±20 mm relative to the chamber horizontal middle plane shown in Fig. 5.28. The bending electrodes were designed to have 20 mm of available distance before and after the electrode. Hence, an arc radius for the 75° bend is 65 mm and for the 45° branch this radius is 121 mm. Further, these values were scaled down into radii of electrodes in order to have ≈20 mm of available beam aperture. The voltages that are required to bend the 2 keV iodine beam are 4.6 kV and 2 kV for the 75° and 45° branches, respectively. Due to the asymmetric nature of the bending system, an uncompensated acceleration was provided via the 75° electrode after the exit from the left branch. As a result, the beam was guided only through 2/3 of the electrode's length. To mitigate this effect, the distance to the electrode at the entrance to the bending section was increased to 24 mm (equal to +2.5° electrode rotation around the downstream arc point).

Tracking through the beam line for both angles had been performed and it is shown in Fig. 5.30. The 2 keV iodine beam with radius of 10 mm was utilised. Potentials were applied to one of the sides at a time (Einzel lens and bending electrode). The

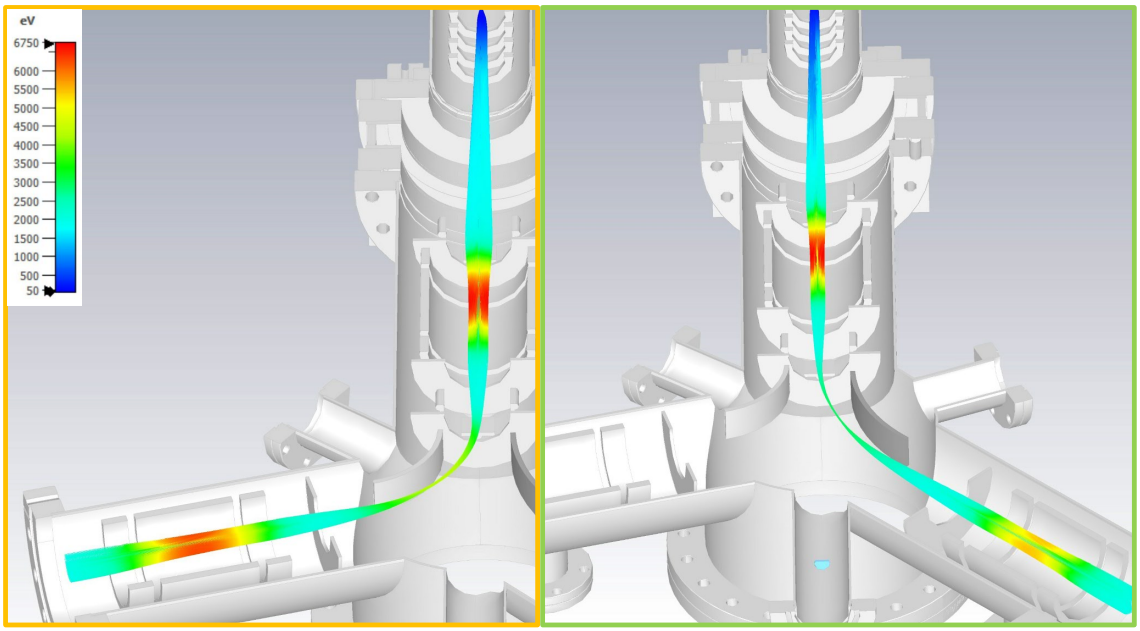

Figure 5.30: *Tracking of* 2 keV *iodine beam in CST. Focusing in both deflection cases,* 75° *(left) and* 45° *(right), occurs close to the middle of the electrode.*

focusing power of the first Einzel lens before bending is also different. This is due to another level of acceleration of each of the bending electrodes. The voltage at the middle electrode for 75° is 5 kV and for the 45° branch it is 4 kV. The Einzel lens after the bending is kept on the level of 5.5 kV. For more energetic anion beams, all voltages can be simply scaled up by a known factor. Two sets of correctors, the first after the deflection and the second after the last Einzel lens will help to keep the orbit close to the designed path. Alternatively, they allow an additional horizontal or vertical focusing in quadrupole mode. The last section is a deceleration tube that brings beam energy down to a few hundred eV depending on the experimental requirements. In the future, the deceleration section might be reconsidered for the pulsed operation of an anion beam. At the time of writing, the AEgIS team had submitted a grant application (OPUS22 №2021/43/B/ST2/01948) to cover further development of ion sources. The main parts of the deflection chamber were designed and successfully manufactured. Figure 5.31 shows the produced deflection chamber called "Starship", and inner assembly, which includes an ion lens and correctors that are mounted onto ceramic holders.

5.10 Summary

In this chapter, an advanced approach to low-energy beam line description was presented. It was tested on the electrostatic transfer lines and experiments from Antimatter Factory at CERN. The main focus was given to the ALPHA beam line and the external impact coming from the AEgIS experiment. For the latter, a new complex merging section dedicated to anion injection was also designed to allow anion injection.

The first section described the building blocks of the transfer line: electrostatic quadrupoles and bending elements. Further, a description and modifications of the G4beamline code that were made to enable this work have been introduced. It allowed the creation of a realistic representation of electrostatic quadrupoles via Enge functions and built upon experimental measurements. CAD models of the electrostatic deflectors helped to simulate their behaviour in an accurate manner utilising the CST software

Figure 5.31: *The "Starship" deflection chamber together with one of the inner ion lens assemblies (private photo gallery).*

suite.

The whole beam line model was simulated in G4beamline with some additional improvements. Further, benchmarks against previous MAD-X results and another beam tracking tool - BMAD, were performed using the same input beam and field maps. Overall, all models agreed quite well and the quality of the beam is close to the design values. The behaviour of the beam orbit after field map tuning was also very close to zero in BMAD and G4beamline. A small momentum offset was observed at the end of the beam line, which is negligible at the experimental level. For better data input and result output from G4beamline, a dedicated GUI interface was developed to replace HistoRoot.

Afterwards, the beam line model was extended with the AEgIS branch to simulate the impact of stray fields from the closely located particle trap. The field observed via neutral particle tracking through CST produced field map demonstrated close agree-

ment in amplitude with the G4beamline approach, which can be used as a faster alternative. To reduce the impact of these fields, a preliminary design of passive shielding was suggested. It showed the best performance when the distance between the beam line and shielding material was small (0.5 m).

In the end, the newly proposed design of an anion injection system for the AEgIS experiment was presented. Its geometry aims to maximise transmission for the ELENA antiproton beam and for the beams coming from two short branches with envisioned ion sources. The scheme utilised Einzel lenses and asymmetrical cylinder sectors for bending. The suggested ideas fully satisfied the needs of the AEgIS team for the upcoming experiments. It will allow a first-time demonstration of the formation of medium antiprotonic atoms (iodine anions) inside the AEgIS setup. The flexible functionality of the designed beam line will also include the possibility of extraction of trapped species into portable particle traps.

Chapter 6

Bunch compression and target interaction

6.1 Introduction

Atomic collision with low-energy antiprotons is the ideal candidate for studying multiple physical processes occurring when antimatter and matter interact. Additionally, it can help to investigate possible discrepancies between the behaviour of the proton and antiproton. Some of these discrepancies were discussed in Section 1.5.

Due to the length limitations of the particle traps, it will be beneficial to have variable antiproton bunches. In addition, to perform target collision measurements in the low energy regime ($\leq$100 keV), the bunches must be short enough to allow the triggering of an interaction from which the subsequent reaction fragments can be associated. This increases the signal-to-noise ratio (SNR), meaning a lower integration time is needed.

Bunch length also puts other strong limitations on the beam. For stable storing of short bunches, bunch intensities on the order of 10^4–10^5 are required to stay below the stability threshold defined by beam heating effects, e.g., space charge and IBS, leading to emittance degradation. One of the ways to compensate for emittance growth inside

the ring is the well-understood electron cooling technique [97]. Currently, bunch compression in the ELENA, AD and CSR rings is based on the bunch rotation approach, discussed in Chapter 1. This method has demonstrated bunch compression using an in-built RF system. Additionally, the same bunch compression technique can be applied within an electrostatic transfer line from the ELENA storage leading from the ring to one of the experiments. In this case, it is also called `velocity bunching` [166] in the drift space.

The purpose of this chapter is to demonstrate possible mechanisms to reduce the bunch length in ELENA and its transfer lines. It also gives practical limitations of the intensity of the compressed bunch due to space charge and IBS. Careful benchmarks of analytic estimation and results from the tracking provide confidence in these findings. In addition, an example of gas-jet target crossing with short and long bunches will be studied, providing the expected reaction rate. Although the simulations demonstrated in this chapter were done for the specific case of the ELENA ring, the same principles and tools can be applied to any low-energy machine.

6.2 Velocity bunching principle

When a storage ring operates at low energy with $v \ll c$, one of the practical techniques to perform longitudinal bunch compression is utilising an RF cavity and a free particle drift space. In this case, the phase-dependent voltage pulse introduces a correlation between position and energy within the bunch and in the drift, compression occurs due to velocity differences. This principle is equivalent to bunch rotation described in Subsection 2.3.8 but in this section, it will be shown for a single particle. Velocity bunching is schematically illustrated in Fig. 6.1, which represents the longitudinal phase space of a bunch with z, the longitudinal position of particles and $\delta \equiv \Delta E/E$ the energy difference relative from the reference particle values. Consider a particle in three different propagation stages: before entering the RF cavity, (z_1, δ_1); after the

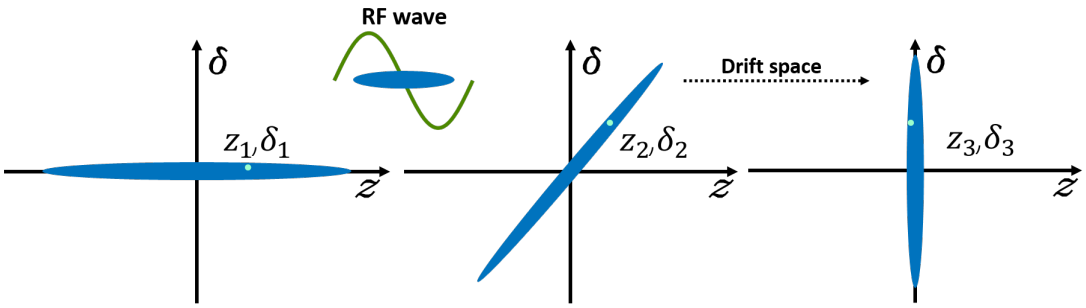

Figure 6.1: *Principle of velocity bunching with antiprotons.*

cavity, (z_2, δ_2); and at the end of the drift space, (z_3, δ_3). These points are related by

$$z_2 = z_1 \qquad \delta_2 = \delta_1 - \frac{qV_0}{E_i} \sin\varphi, \tag{6.1}$$

$$z_3 = z_2 + R_{56}\delta_2 \qquad \delta_3 = \delta_2, \tag{6.2}$$

where q is the particle charge, V_0 is the cavity voltage, E_i is the initial particle energy, φ is the relative phase of the particle with respect to the zero crossing of the cavity voltage and R_{56} is the transfer matrix element which denotes relative energy deviations. The initial and final stages are linked by

$$z_3 = z_1 + R_{56}(\delta_1 - \frac{qV_0}{E_i} \sin\varphi), \tag{6.3}$$

$$\delta_3 = \delta_1 - \frac{qV_0}{E_i} \sin\varphi. \tag{6.4}$$

The phase φ can be rewritten as a function from longitudinal position z_1 in the form $\varphi = -\omega z_1/v$, with ω being the angular frequency. Considering this, an energy "chirp"

$$\chi = -\frac{2\pi qV_0}{\lambda E_i} \sin\varphi, \tag{6.5}$$

can be introduced where v is the particle velocity and λ is the wavelength. Due to the small phase difference within a bunch, a Taylor expansion can be applied to the sine function, and the final values for bunch length and energy spread of particle distribution

can be written as

$$\sigma_{z_f} = \sqrt{(1+\chi R_{56})^2\sigma_{z_i}^2 + R_{56}^2\sigma_{\delta_i}^2}, \tag{6.6}$$

$$\sigma_{\delta_f} = \sqrt{\sigma_{\delta_i}^2 + \chi^2\sigma_{z_i}^2}. \tag{6.7}$$

Full compression is achieved at $R_{56} = -1/\chi$, so called "over-compression" can be obtained at $1+\chi R_{56} > 0$ and "under-compression" when $1+\chi R_{56} < 0$.

The main advantage of this method is its flexibility. It might reasonably be applied to any in-ring cavity system, and significant compression will occur after an optimal number of turns.

6.3 Multi-harmonic cavity

To achieve the requirements of a slowly controlled deceleration process, the ELENA ring is equipped with a low voltage, wide-band normal conducting cavity. The RF system provides voltage in a range extending from 144 kHz to above 2 MHz in 100 V and 500 V levels of amplitude respectively as shown in Fig. 6.2. The cavity design

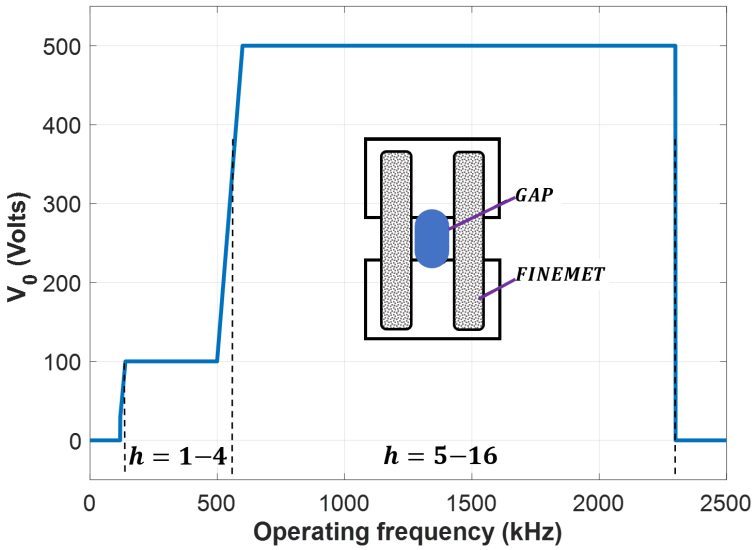

Figure 6.2: *Working voltage curve for 0–2.5 MHz frequency range and schematic structure of the ELENA RF system.*

is in the form of a coaxial resonator with the accelerating gap in the centre and two Finemet® [167] type magnetic alloy (MA) cores on each side. By varying the magnetic permeability of cores, the total inductance of the cavity is changed, therefore varying the operating frequency and bandwidth of the cavity.

The first systems using a similar type of MA and working principle were installed in KEK JHF synchrotrotrons [168], LEIR [5] and recently replaced the existing RF cavities in the PS Booster during the Long Shutdown 2 (LS2) at CERN [169]. The

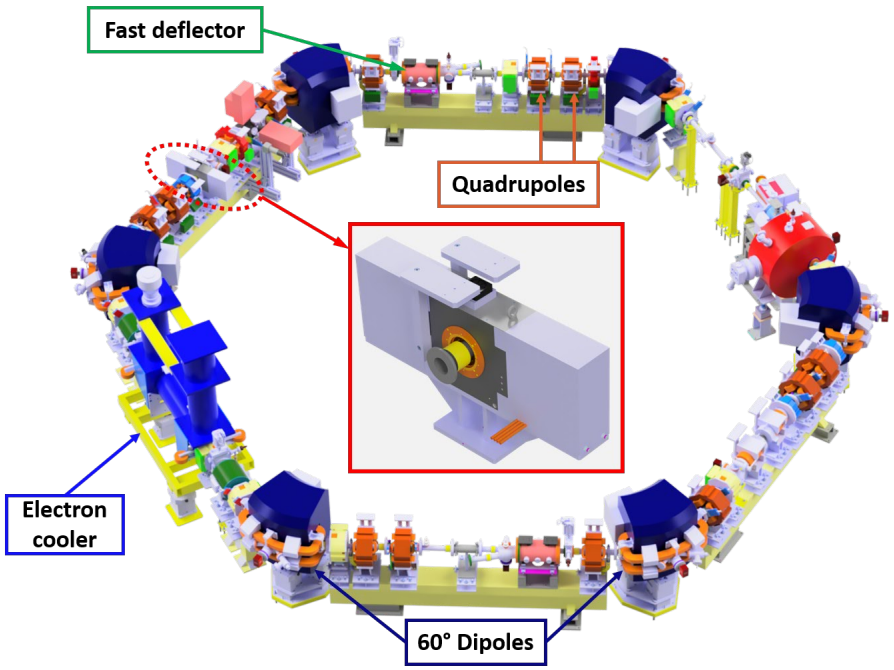

Figure 6.3: *CAD model of ELENA with main elements highlighted. The RF system installed inside the ring is depicted in the centre.*

cavity decelerates a bunch from AD at h=1 (h1) and is turned off for electron cooling. After sufficient cooling time (of the order of seconds), the beam is bunched again and extracted to the electrostatic transfer lines going to a number of experimental areas. Using bunch rotation or bunched beam cooling prior to extraction may provide shorter bunches. The first measurements showed that using two combined processes at h1, a bunch length was reduced from initial an 600 ns to around 200 ns [170]. Further investigation of this phenomenon in the next sections will highlight the limitations in

obtaining even shorter bunches.

6.4 Bunch Compression in ELENA ring

To understand the behaviour of a particle distribution as a function of the RF system parameters and the initial bunch charge, I performed simulations using BMAD. In addition, a Python interface has been included to simplify the bunch transfer to other codes at any stage of tracking. Previously, studies of the ELENA ring (Fig. 6.3) were thoroughly carried out via the MAD-X simulation code, which provides a good reference point. The latest version of MAD-X optics [137] was successfully converted into the BMAD format utilising an embedded converter and linked with other simulation tools within the Python program. Figure 6.4 shows the corresponding transverse betatron functions and the first-order horizontal dispersion inside the ELENA ring when the RF voltage is equal to zero. Calculations were made in two modes: single-particle beam dynamics at the reference energy (solid lines) and via tracking a generated beam distribution (dots). The effect of the lattice on the longitudinal plane has been evaluated by tracking a bunch distribution generated with BMAD and matched to the optical parameters at injection. The full properties of the bunch are summarised in table 6.1. In order to account for collective effects later, this distribution consisted of

Table 6.1: *Simulation parameters for the ELENA and an injected bunch.*

Parameter	Value
Bunch length r.m.s $\sigma_{z,t}$ (m, ns)	$0.3282, 75$
Relative momentum spread $\Delta P/P_0$	1×10^{-4}
Reference momentum P_0 (MeV/c)	13.7
Horizontal/vertical emittance $\epsilon_{x,y}$ (mm mrad)	2.5, 2.5
Nominal working tunes $Q_{x,y}$	2.454, 1.416
Total charge C (pC)	0.72
Horizontal/vertical size r.m.s $\sigma_{x,y}$ (mm)	3.55, 3.35
Revolution period T (μs)	6.95
Relativistic beta β	0.0146

128,000 macro-particles with a charge of $q_m \approx 0.06$ fC that corresponds to bunch intensity of N_b=0.45 $\times$ 10^7 antiprotons. Similar to the beam initialisation from Chapter 5, the bunch generated in 6D had a 3D Gaussian shape truncated at 3σ, where σ is the standard deviation. After bunch tracking had been performed with different RF volt-

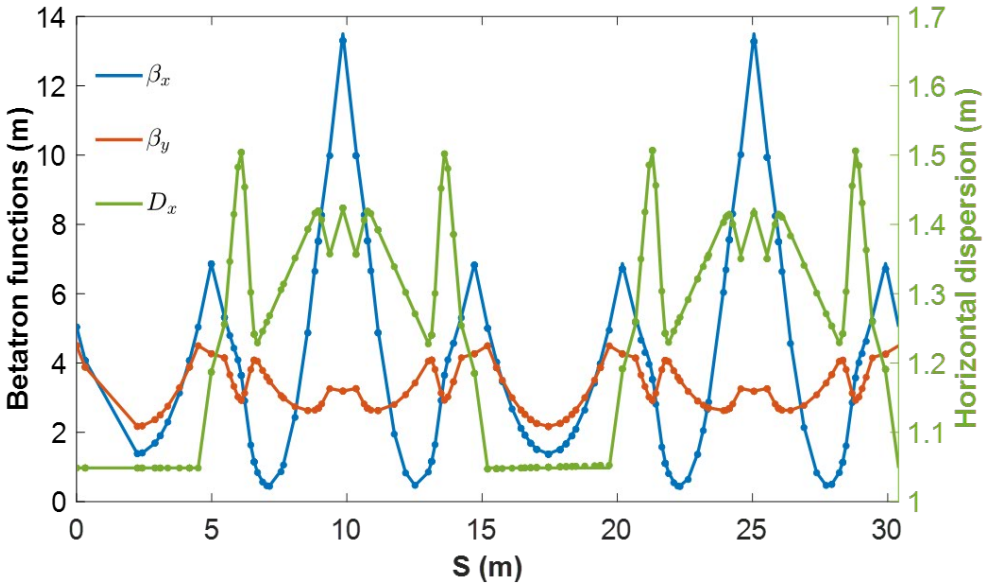

Figure 6.4: *Optical functions of ELENA combined with horizontal dispersion. Solid lines represent values from single-particle dynamics and dots values obtained from bunch tracking.*

ages, an optimum number of turns was estimated without any collective effects. The first harmonic of RF and 100 V voltage creates stable bunch rotation with a maximum compression which occurred every 34 turns with σ_z=4.6 cm or in time units $\approx$ 10 ns, this is shown in Fig. 6.5. The number of required turns, as expected, corresponds to one quarter of the ELENA synchrotron period. A higher voltage and harmonic number may provide faster compression but result in bunches with higher momentum spread. Experimental benchmarks of the results can be achieved by utilising sensitive beam current transformers for low bunch charge operation with antiprotons or H^- ions.

Alternatively, this compression can be carried out in the transfer line. This is analysed and discussed in the next section.

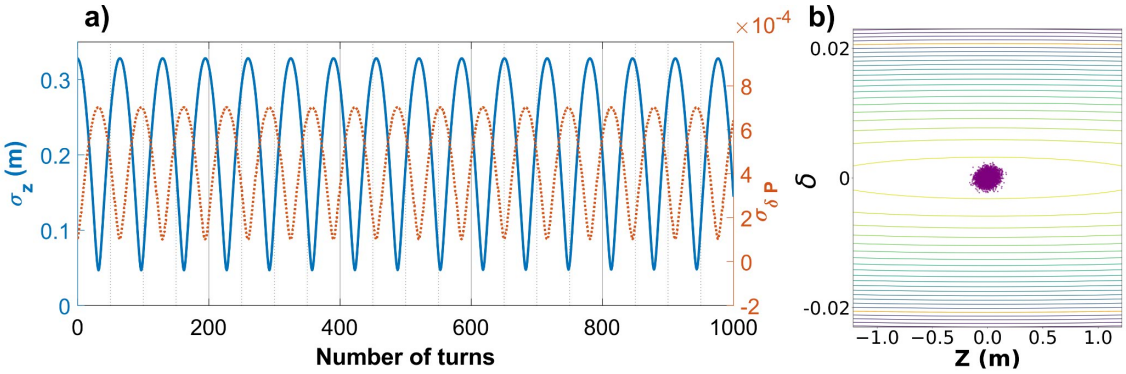

Figure 6.5: *Evolution of bunch parameters during 1,000 turns for the first RF harmonic. (**a**) Standard deviations of bunch length and momentum spread from tracking distribution with an RF voltage* 100 V*. (**b**) Longitudinal phase-space of the fully compressed bunch (34 turns) within a stable separatrix bucket.*

6.5 Bunch Compression in ALPHA transfer line

In the previous chapter, the layout of the transfer lines was shown. The lines naturally have drift spaces between the focusing and bending elements. These spaces could allow for the installation of additional beam instrumentation or RF cavities which can be used for the proposed beam manipulation.

As an alternative to the in-ring bunch compression method, I had also considered bunch compression in one of these transfer lines with the one-time crossing of a high-gradient normal conducting or ferrite loaded/MA cavity [171, 172], similar to that installed in ELENA. Additionally, it could also provide higher flexibility of bunch length manipulation for existing experiments. Firstly, the bunch compression distances had been analytically examined for cavity voltages in the range 30–60 kV, which corresponds to 15–35 m drift distances using equations 6.6 and 6.7. In Fig. 6.6, we can see that the momentum spread in the bunch is strongly dependent on the cavity voltage. However, it only has a small impact on the minimum attainable bunch length. To verify these predictions, benchmark simulations in BMAD and G4beamline were performed using extended models of the ALPHA beam line described in the previous chapter. Figure 6.7 shows a detailed 3D layout of the transfer line indicating the pro-

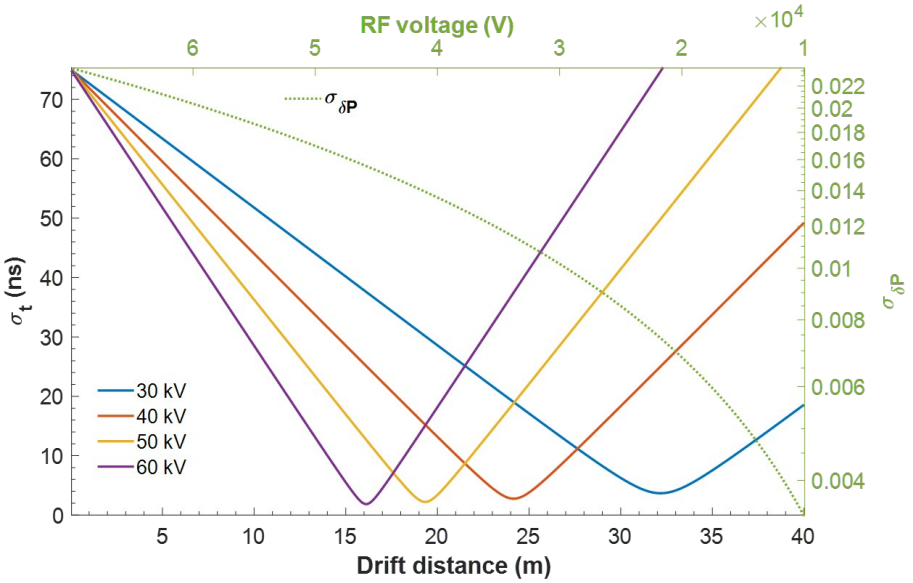

Figure 6.6: *Evolution of bunch properties for different RF voltages applied.*

posed RF system location and the beam monitor located 19.4 m apart. Both models treat the RF cavity element (Fig. 6.7b) in a similar manner when the zero-crossing of the sinusoidal voltage curve is synchronous with the reference particle. The initial

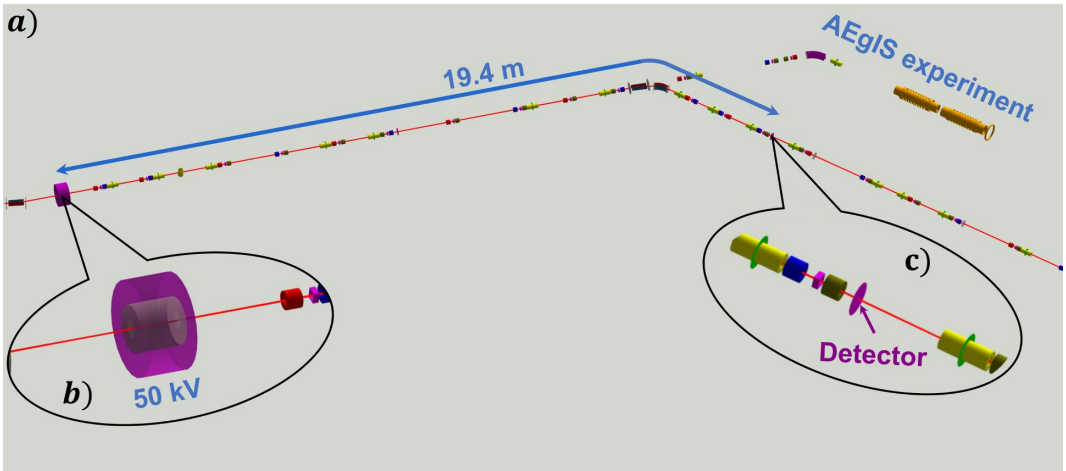

Figure 6.7: *(**a**) The visualisation of transfer lines simulation model constructed in G4beamline. (**b**) The RF system with 30 cm accelerating gap.(**c**) Detection of the compressed bunch.*

6D tracking distribution was generated in BMAD combining transverse values from table 6.1 for this transfer line and the experimentally measured bunch length from

[170]. Figure 6.8 shows the benchmark of G4beamline and BMAD after compression for the bunch parameters mentioned above. Both codes had the same description of the electrostatic deflectors—3D field maps created utilising CST. Table 6.2 compares the

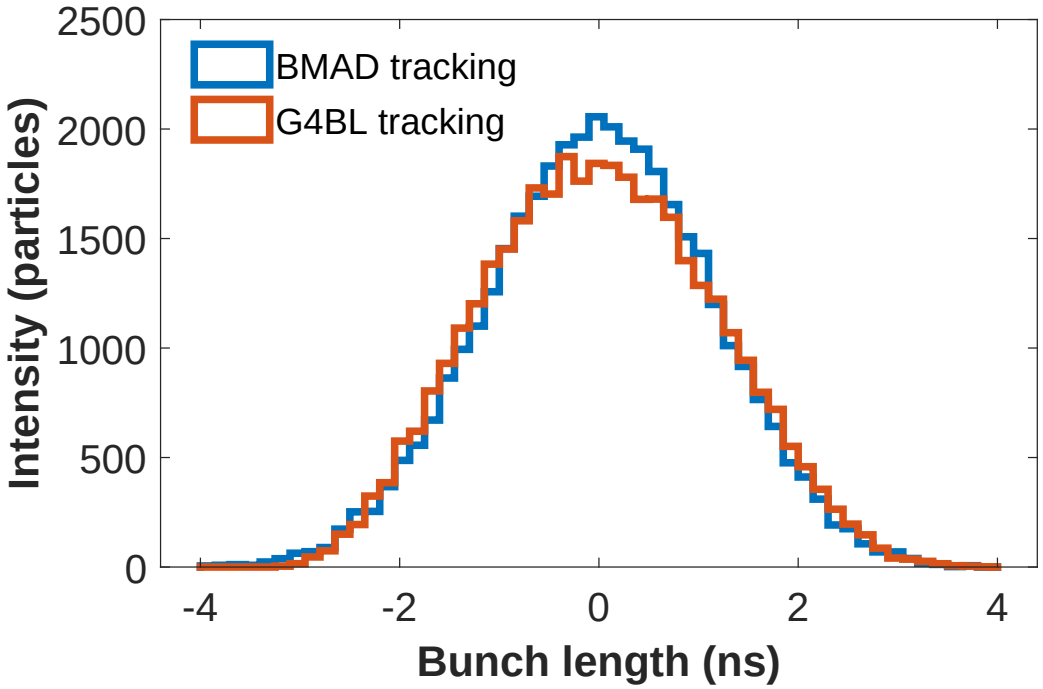

Figure 6.8: *Bunch length at the detector obtained from G4beamline and BMAD. Times are relative to the reference particle.*

bunch length and intensity at the location of the bunch length minima during bunch rotation. The transmission intensity of the beam decreases from the initial value due

Table 6.2: *Compressed bunch at the detector*

Parameter	G4BL(f.map)	BMAD(f.map)
Bunch length σ_t (ns)	1.15	1.13
Momentum spread $\Delta P/P_0$	0.0054	0.0054
Transmission (%)	38.0	38.5

to the limited energy acceptance of the slow deflector, in addition to physical aperture limitations. Further optimisation of the optics and orbit correction may help to decrease beam losses downstream of the experimental line. An additional obstacle

considered in the next sections is beam instabilities caused by increasing space charge impact which limits the stable bunch intensity and compression efficiency.

6.6 Space charge limitations

So far, bunch compression was considered without taking into account the collective effects. In the next sections, it will be shown how the bunch length, beam emittance and bunch intensity affect the stability of the beam. For this study two simulation methods were utilised: 3D PIC model from BMAD, which allows longitudinal tracking of unmatched bunches, and the frozen space charge model (a semi-analytical Bassetti-Erskine model [173]) in SixTrackLib with PyHEADTAIL space charge kicks. This type of study was previously suggested and performed for SIS100 [174, 175]. The shrinking of the bunch with an initial charge of 0.72 will inevitably lead to IBS leading to emittance growth and longitudinal decompression. The 0.72 bunch length and charge are critical limitations resulting in an incoherent tune shift $\Delta Q_{x,y} \approx -0.12$ for the nominal working tunes. This value was estimated from equation 2.130.

6.6.1 Space charge effect: BMAD models

The simulation aspects of 3D space charge tracking are described by Mayers in [176]. The physical space of the bunch is meshed in three dimensions and the mean charge density at each node of the mesh is calculated by counting the number of particles that are located close to it. After the density function is obtained, the electric and magnetic fields at each node are computed by solving Poisson's equation. The most precise BMAD solver uses a Fast Fourier transform (FFT) method when EM field of the node is presented as the convolution of the charge density and a Green's function. The number of 3D grid cells for space charge calculation was set in order to to reduce the PIC-dependent noise [177] and checked by obtaining a smooth space charge force.

Convergence studies for BMAD were performed to ensure the results were accu-

rate. Figure 6.9 (left) demonstrates horizontal emittance change depending on the number of tracked particles and resolution of the mesh. The right side of the image shows the number of particles per cell. For these tracking studies, a bunch consisting of 128,000 macro-particles and a mesh of $40 \times 40 \times 80$ cells was considered as sufficiently precise. This corresponds to the density of 1 macro-particles per cell.

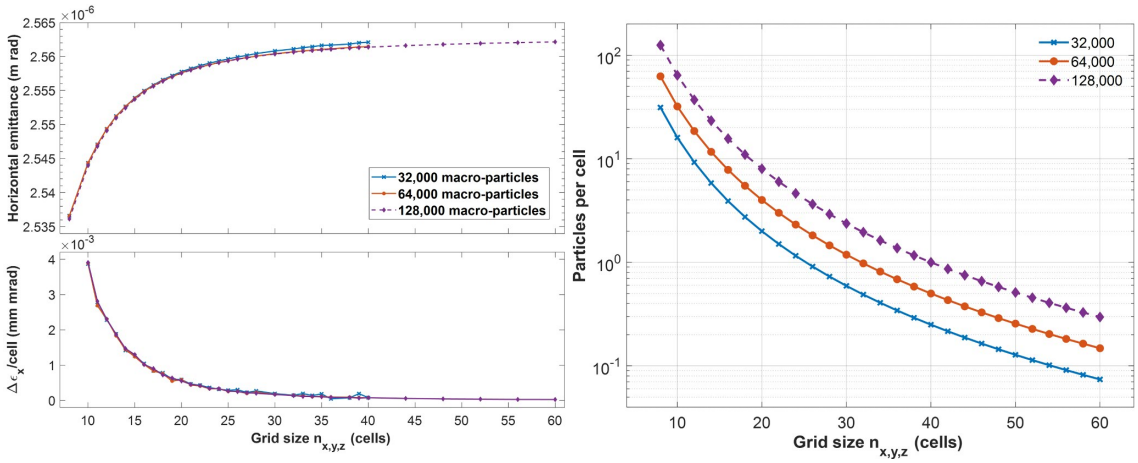

Figure 6.9: *Dependence of horizontal emittance growth as a function of grid size and macro-particle number (Top Left). Relative change of emittance per cell at each configuration (Bottom Left). Particle density dependence on grid size.*

Tracking has been performed in BMAD for 200 turns within the ELENA ring and additionally in the ALPHA transfer line for two different assumed bunch intensities. Figure 6.10 shows the evolution of horizontal emittance and length of the bunch for both compression scenarios. The horizontal emittance reversible growth during the bunch rotation inside the ring is understood quite well and happens due to transverse-longitudinal coupling in PIC simulation. Very similar behaviour was previously thoroughly studied in [178] on an example of 180-degree rotation for the heavy-ion synchrotron.

Next, the same simulation of bunch rotation in BMAD was performed with a simplified representation of space charge impact in PyHEADTAIL.

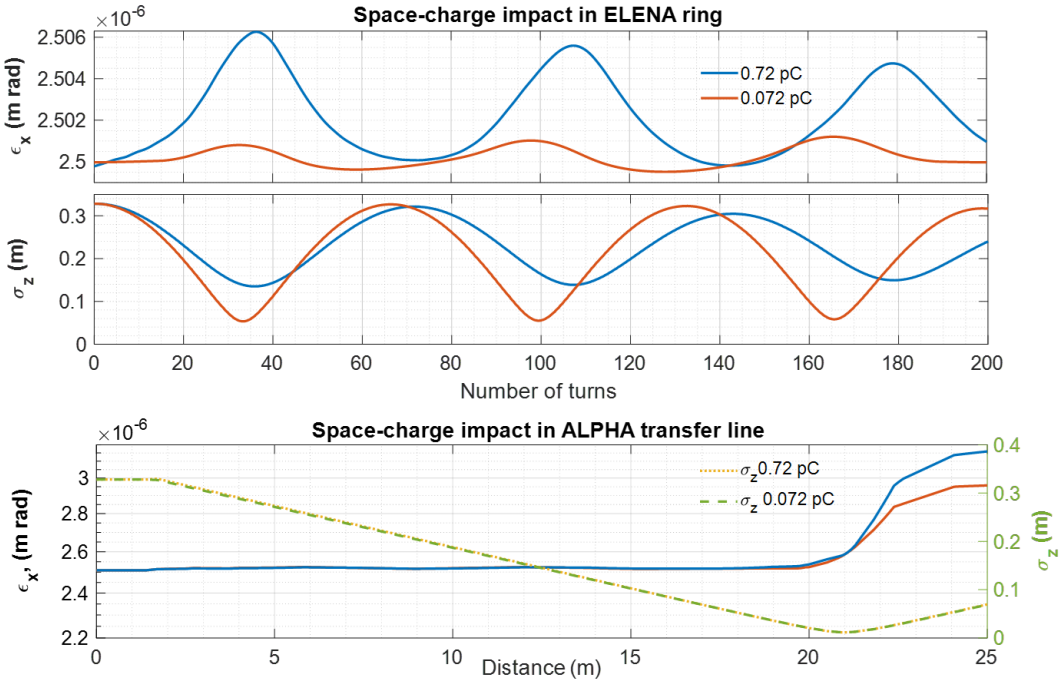

Figure 6.10: *Evolution of bunch parameters with space charge enabled. (Top) Horizontal emittance variation for 200 turns. The nominal charge of the bunch* 0.72 *considerably increases the shortest length value. (Middle) The distribution with lower, 10 % particle density has non-linearities but is closer to bunch length values without space charge. (Bottom) Higher cavity voltage in the transfer line leads to equally effective compression for both intensities. Difference occurs close to longitudinal focus point at distance* 19.6 m.

6.6.2 Frozen & 3D PIC space charge models in PyHEADTAIL

In order to obtain much faster space charge calculations in simulation tools one often imposes assumptions on the shape of the space charge fields, while the simulated results should ideally resemble the self-consistent results. Such models are referred to as frozen space charge. For the long bunches, the transverse fields of the Gaussian distribution can be computed with the Bassetti-Erskine formula. In the longitudinal plane, one readily applies a Gaussian line charge density profile. In this work, the above 6D Gaussian bunch shape was assumed and its field map was computed before the simulation with the initial r.m.s values for the transverse and longitudinal planes and it is centred on the computed orbit.

During the simulation, these parameters remain constant and the particles of the tracked distribution are treated as test particles probing this distribution. Firstly, the machine optics (Fig. 6.4) was given as a thin lattice model to SixTrackLib. Further, the bunch parameters from table 6.1 were defined. The lattice was modified with a number of space charge kick points defined by PyHEADTAIL. Schematically this process is shown in Fig. 6.11. Realistic 3D PIC calculation of space charge was done

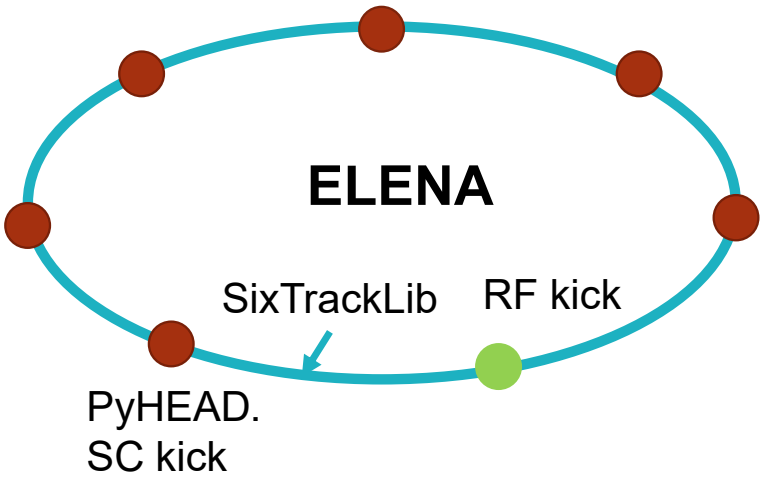

Figure 6.11: *Scheme of tracking simulation with the frozen space charge in SixTrackLib+PyHEADTAIL.*

almost in the same way but with frozen markers replaced by computation on a grid with an optimal resolution (one particle per cell).

Both modes provide an internal benchmark of tracking with space charge in the case of the matched beams when bunch properties do not change significantly over many turns. For unmatched/non-Gaussian beams, the PIC model provides a more accurate estimation.

6.6.3 Long matched and short unmatched bunches. Properties, tune footprint.

The working tune point of the ELENA is carefully selected to avoid the close proximity of resonance lines and also to ensure that available free space is big enough to

accommodate the tune footprint of the bunch.

In this subsection, I will provide a comparison of properties of tune footprints for bunches that have four main different parameters: transverse emittance, bunch length, momentum spread and intensity. All cases are listed in table 6.3. Two types

Table 6.3: *Compared bunch examples and parameters*

Case	Transverse emit., mm mrad	Bunch length r.m.s, m	Momentum spread r.m.s	Bunch intensity
A) Matched long	2.5	0.3284	7×10^{-4}	4.5×10^{6}
B) Matched long (cool.)	1	0.3284	2.5×10^{-5}	4.5×10^{6}
C) Unmatch.long (cool.)	1	0.3284	1×10^{-4}	4.5×10^{6}
D) Matched. short	2.5	0.05	1×10^{-3}	4.5×10^{6}
E) Matched. short	2.5	0.05	1×10^{-3}	4.5×10^{5}

of situations were considered for these bunches: matched (constant bunch length) and unmatched (bunching/bunch rotation) within an RF bucket.

To begin with, Fig. 6.12 demonstrates the tune footprint for the matched bunch without cooling, at the lowest ELENA extraction plateau. The difference between

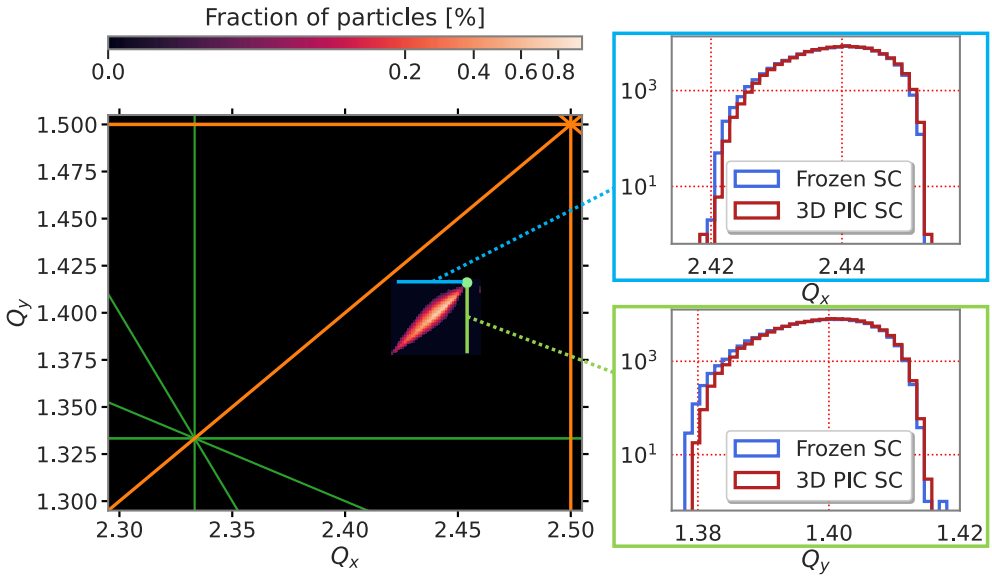

Figure 6.12: *Particle tune distribution from combined SixTrackLib+PyHEADTAIL simulation. Tune footprint on the left from a 3D PIC and frozen simulation models (A).*

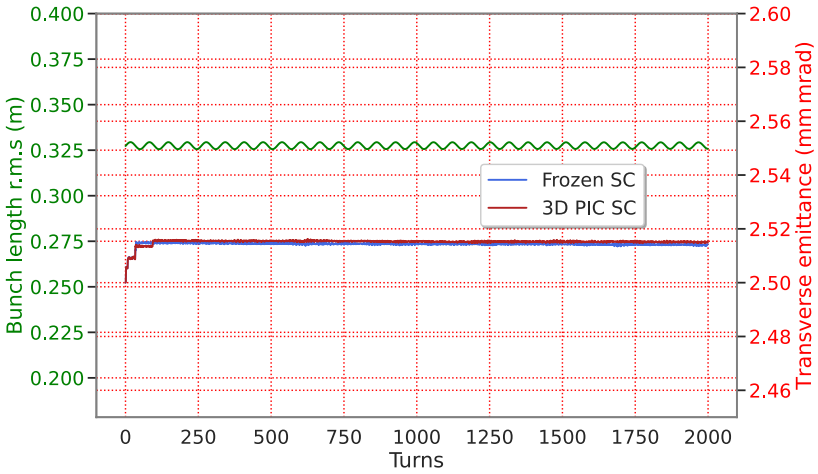

Figure 6.13: *Transverse emittance and bunch length behaviour in the simulation example (A).*

the frozen and PIC space charge models becomes noticeable only at the tail of the distribution, but generally, the static description of space charge is good enough for the first assessment. However, in case of a strong space charge impact, the unmatched bunches, or when a bunch is affected by machine imperfections, PIC will provide a more accurate representation. The transverse emittances stabilise almost on the same value after tens of turns and bunch length oscillates around the initial value, Fig. 6.13.

The next scenario describes bunch behaviour when the momentum spread of the cooled beam, obtained during one of the measurement campaigns [149]. As you may notice, the tune spread in Fig. 6.14 is large enough to cross one of the third-order resonances. Here nothing happened due to the fact that machine errors were disabled, so the bunch length and transverse emittance in this scenario remain at equilibrium, Fig. 6.15. In reality, the main dipole magnets and quadrupoles of the ELENA ring have parasitic multipole components, The multipole components, up to decapole order, were investigated via magnet simulations and magnetic field measurements [179–181]. To demonstrate the impact of errors and to validate created simulation model the closest multipole components were implemented: dipolar, quadrupolar and sextupolar. The maximum amplitudes of the errors were defined as a combination of constant

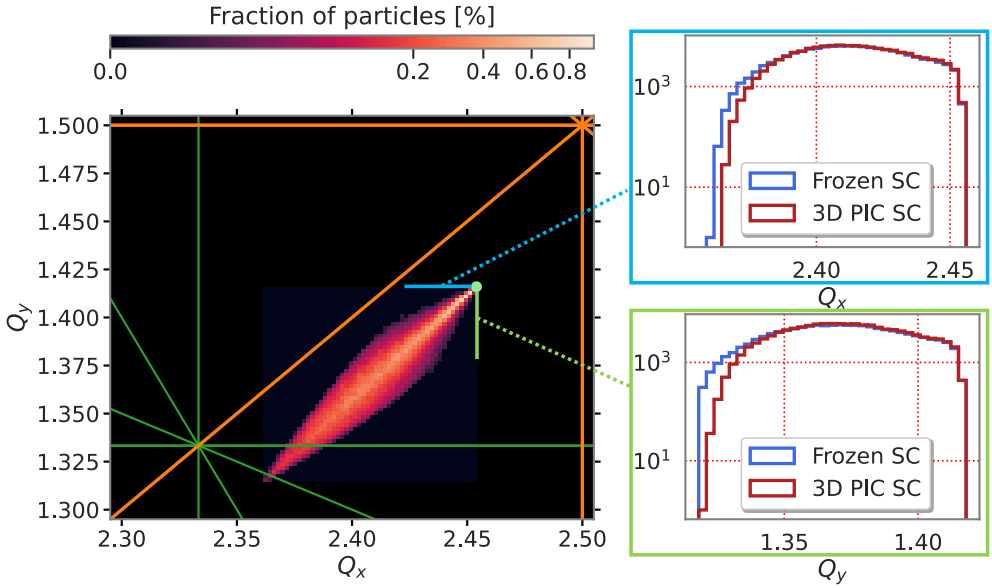

Figure 6.14: *Particle tune distribution from combined SixTrackLib+PyHEADTAIL simulation. Tune footprint on the left from a 3D PIC and frozen simulation models (B).*

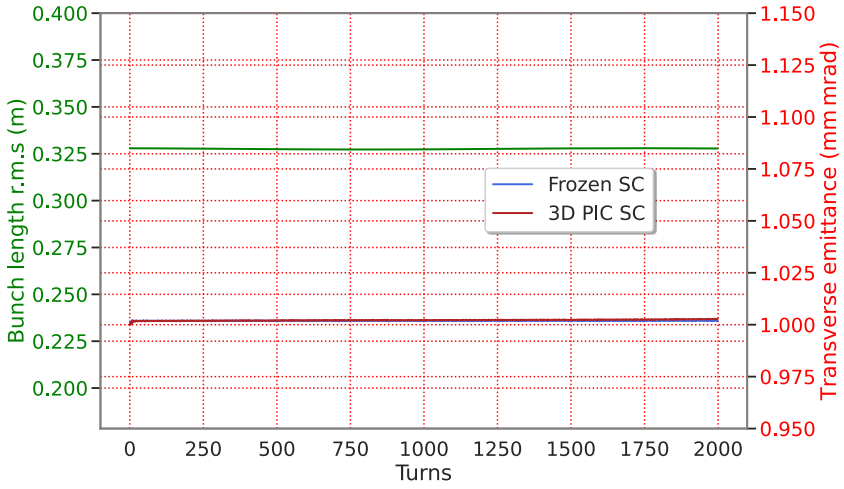

Figure 6.15: *Transverse emittance and bunch length behaviour in the simulation example (B).*

$b_{0..2} = 1 \times 10^{-4}$ and random component up to 1×10^{-4}. Figure 6.16 demonstrates the impact on the tune spread and emittance when the working point is located closer to resonance lines. As one may notice, the coupling resonances capture a portion of the particles and sum resonance increases the emittance, which is also seen as a tune spread blurring.

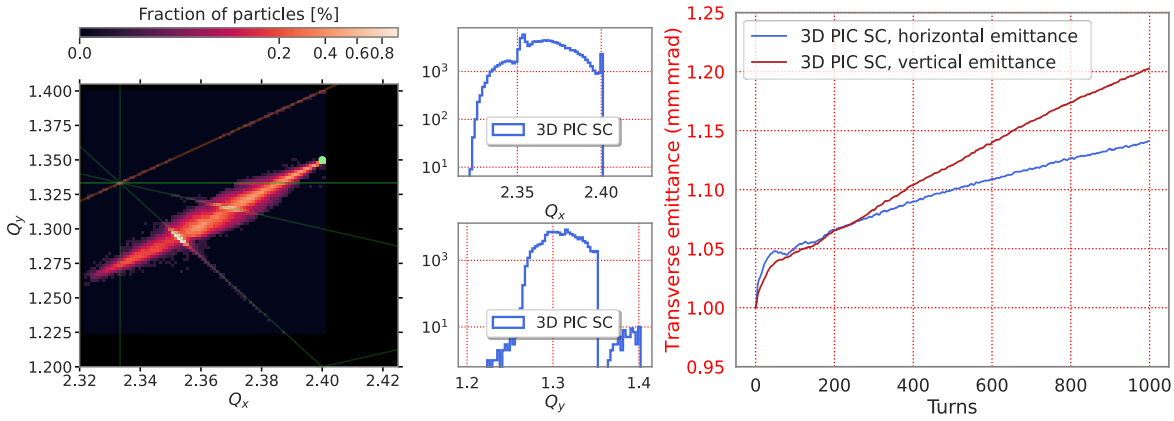

Figure 6.16: *Particle tune distribution obtained from tracking with PIC space charge and randomised lattice errors. Tune footprint highlights resonances that cause emittance growth.*

The best approach to minimise such undesired behaviour of the beam is the selection of proper bunch parameters and machine working points, depending on the existing machine errors. It can be done via a thorough tune scan with all relevant imperfections as demonstrated in [174, 175] and such verification is beyond the scope of the current work.

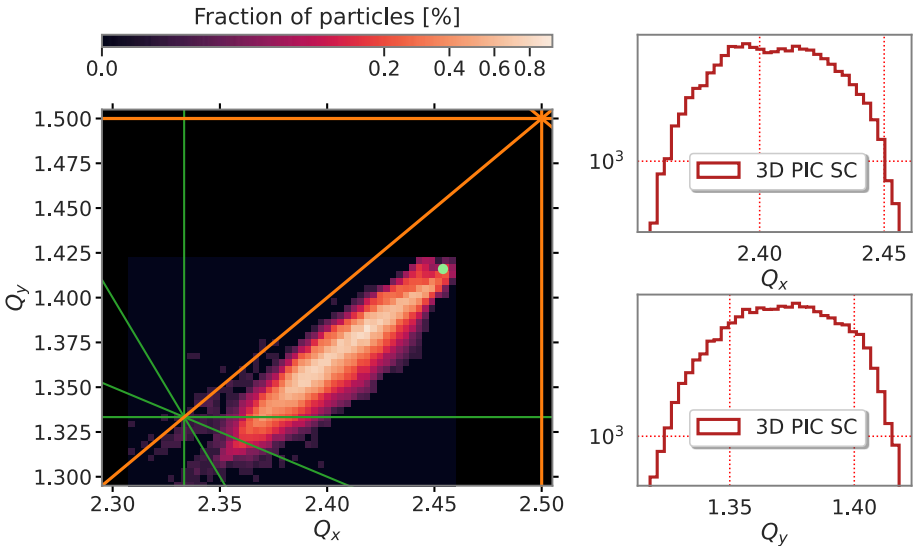

Figure 6.17: *Particle tune distribution from combined SixTrackLib+PyHEADTAIL simulation. Tune footprint demonstrates unmatched case (C).*

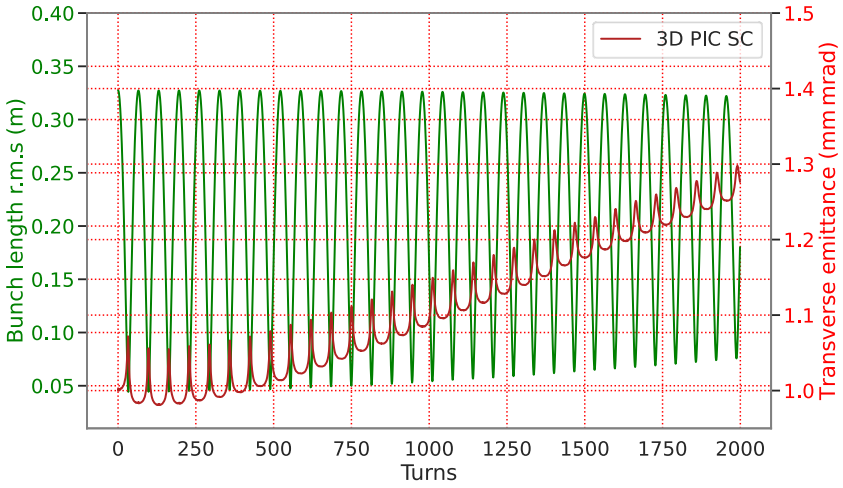

Figure 6.18: *Transverse emittance and bunch length behaviour for the unmatched bunch example (C).*

The following investigated scenario is similar to previously performed in BMAD - bunch rotation combined with 3D space charge. An unmatched bunch was simulated at an RF cavity voltage of 100 V and frequency corresponding to the first RF harmonic. The obtained tune spread can be seen in Fig. 6.17. Interestingly enough, despite the blurriness of the footprint, the distribution mostly resembles the fuzzy matched scenario (Fig. 6.14). It means that bunch rotation is fast enough to distort the beam minimally and this technique can be utilised for experiments that require more extreme bunch conditions unavailable in the matched case for such a bunch length and intensity. Transverse emittance behaviour, Fig 6.18, is in agreement with previously obtained results in BMAD for a larger emittance. When the bunch is fully compressed, an emittance growth is observed due to the dispersive component of the horizontal beam size. After five hundred turns, this instability leads to non-reversible emittance growth. Nevertheless, bunch length degradation is quite slow and changes from the initial 5 cm to 7.5 cm at the end of the simulation. Further studies of such scenarios, combined with magnetic errors, might define more clearly the limitations as well as mitigation methods of beam quality disruption.

The subsequent studied case (D) clearly demonstrates the impossibility of short bunch formation, in the situation when the momentum spread is matched within an

RF bucket and the bunch intensity is the same as for the 32.5 cm case, as shown in Fig. 6.19. This situation corresponds to non-cooled bunch re-capture after the bunch rotation process. The defocusing power of the space charge force is big enough to

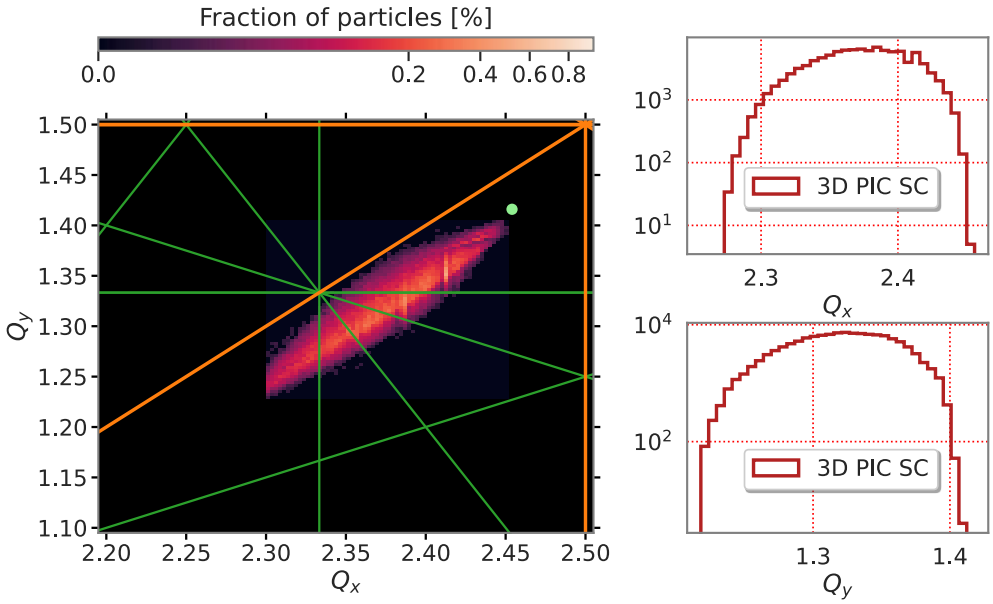

Figure 6.19: *Particle tune distribution from combined SixTrack-Lib+PyHEADTAIL simulation. Tune footprint for the matched case of the short* 5 cm *bunch (D).*

shift the working point of the machine, in the case when this effect was not considered during the lattice matching of tunes.

One of the alternatives in order to obtain a bunch with desired parameters is to decrease bunch intensity, as was shown in the BMAD example. The last considered example is the same bunch as for (D), but with a ten times smaller macro-particle charge. Figure 6.20 shows the tune spread on the resonance diagram, together with the comparison of tune projections with the previous simulation. It is quite close to the very first (A) case, where the long matched bunch was considered. The right side of the image shows a comparison of tune projection for the nominal and decreased intensity. The size of the tune spread is quite small and leaves the possibility for further shortening or cooling to smaller transverse emittances.

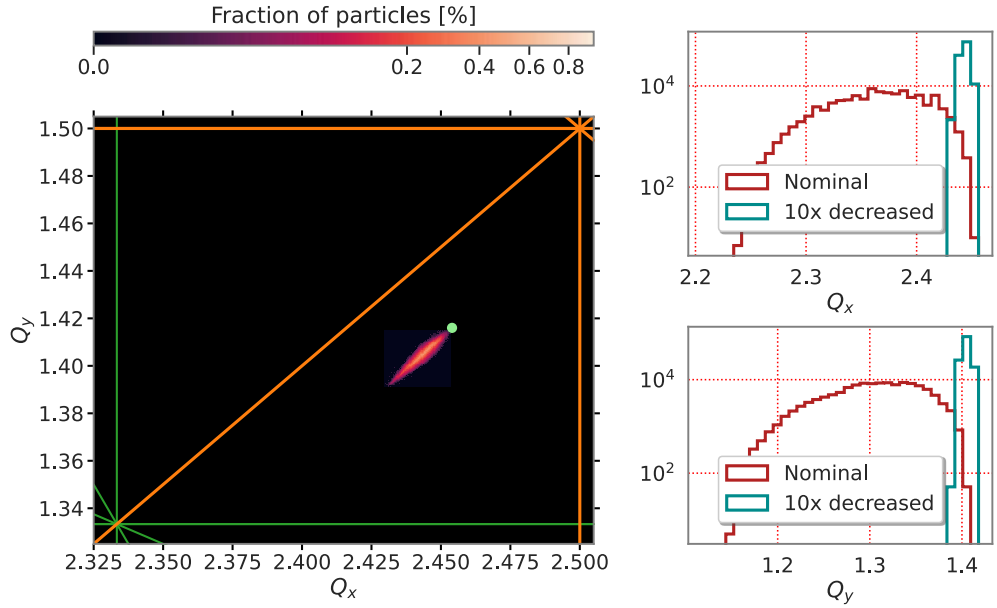

Figure 6.20: *Particle tune distribution from combined SixTrackLib+PyHEADTAIL simulation. Tune footprint for the matched case of the short* 5 cm *bunch with ten times decreased intensity (E).*

6.7 Impact of IBS and electron cooling

The electron cooling system in ELENA is a helpful instrument to overcome IBS and space charge heating during bunch rotation. In the past, predictions about properties of a circulating beam under the presence of IBS and electron cooling, utilising BETACOOL software [182], showed good agreement with experimental values in the case of low-energy machines [183, 184]. In the bunch compression study, a simulation of the cooling process with a bunched beam and the evolution of cooling efficiency in time is calculated.

6.7.1 Model in BETACOOL

The parameters used in the simulation of the ELENA electron cooler are shown in table 6.4. To define lattice properties, the optical functions from Fig. 6.4 were used together with h1 RF voltage of 100 V. The injected macro-particle distribution was directly converted from BMAD to BETACOOL standards and tracked for 1,000 turns to un-

Table 6.4: *Parameters of ELENA electron cooler at 100 keV plateau*

Parameter	Value
Electron beam energy (eV)	55
Beam current (mA)	1
Density of the beam (m^{-3})	1.41×10^{12}
Length of the interaction drift (m)	0.85
Magnetic field in the drift region (kG)	0.1
Electron beam radius (cm)	2.5
Effective temperature of electron beam (eV)	2×10^{-4}
Betatron functions $\beta_{x,y}$ (m)	2.103, 2.186
Horizontal dispersion D_x (m)	1.498

derstand the overall level of beam equilibrium. Additionally, it provided a good benchmark for results obtained in BMAD. The cooling effect was applied using Parkhomchuk friction force model [185] with a uniform cylinder coasting electron beam.

6.7.2 Cooling efficiency

The simulated 1,000 turns correspond to ≈ 7 ms of the cooling process at the 100 keV ELENA working plateau and show the early impact on the beam. Additional collective effects caused slight mismatch and decompression of the bunch as shown in Fig. 6.21a. This happens as a consequence of emittance exchange between the longitudinal and transverse planes. From the emittance evolution, plotted in 6.21b, we can see that continuous electron beam affects the ions mostly in transverse phase space. Figure 6.21c shows the resultant longitudinal growth rates which evolve periodically due to the bunch rotation process and slow decay of the bunch IBS heating due to expansion and decompression. The application of the Martini model results in the coupling between horizontal emittance and bunch length depicted in Fig. 6.21d. Most of the growth happens when the bunch has a minimal momentum spread (growth in steps). The next section brings more attention to the bunch behaviour, via my independent implementation of IBS in Python.

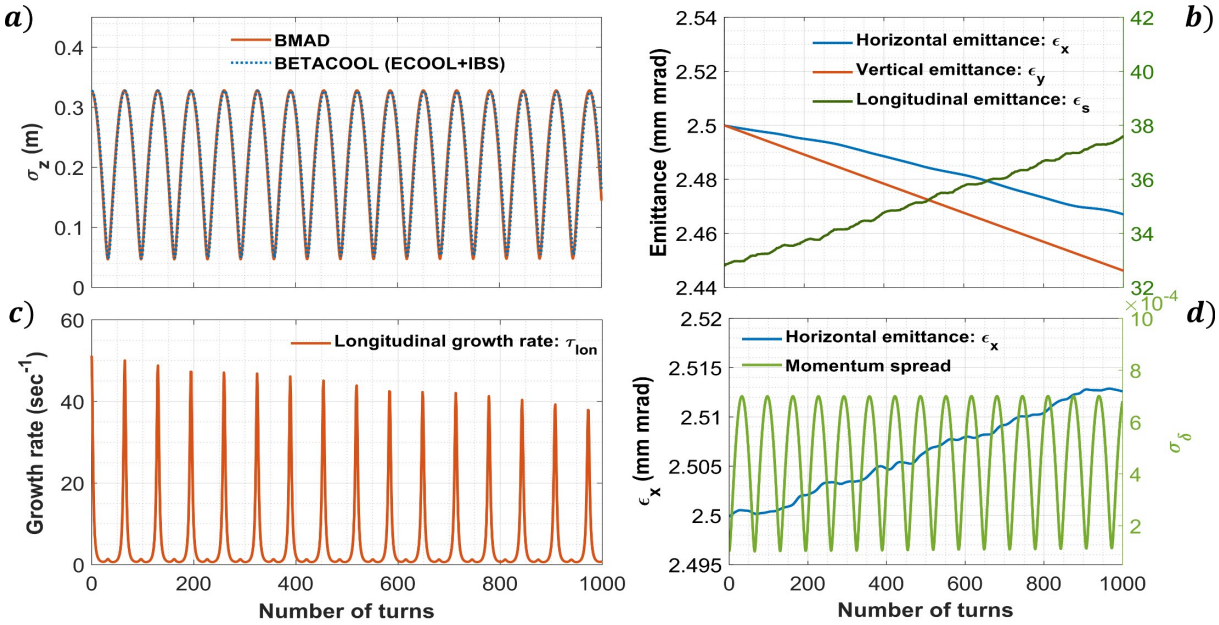

Figure 6.21: *Simulation results from Betacool.* (***a***) *Comparison of bunch length change with h1 and RF voltage* 100 V *for (red) BMAD and (blue) BETACOOL.* (***b***) *Evolution of bunch emittances during bunch rotation with electron cooling and IBS combined.* (***c***) *Changes in longitudinal growth rates may provide a better understanding of overall bunch evolution.* (***d***) *Coupling of horizontal emittance and bunch length during bunch rotation under the impact of IBS solely.*

6.7.3 Simulation of IBS in PyHEADTAIL

In PyHEADTAIL, the accelerator can be represented as a concatenation of elements where various particle tracking steps are performed. A beam is described as a large number of macro-particles that represent a clustered collection of physical particles. It allows large beam intensities to be treated in a realistic manner and within the limitations of computational power. The particle beam itself is transported from one element to another by means of transfer matrices, including detuning effects such as chromaticity and amplitude detuning from octupoles. The machine optics in the transverse planes can be obtained from beam dynamics codes such as MAD-X or BMAD. The tracking of the beam in the longitudinal plane is performed either via linear synchrotron motion or via full non-linear RF kicks which also support multi-harmonic RF

systems. After each tracked segment of the one-turn map collective interactions can be modelled via a kick, e.g., space charge kicks or, like in this study, IBS kicks calculated from an effective (analytical) growth rate model based on the full lattice.

Table 6.5: *Simulation machine and beam parameters for antiprotons in the ELENA ring at the low-energy plateau.*

Parameter	**Value**
Coulomb logarithm C_{log}	12.5
Bunch length rms $\sigma_{z,t}$ (m, ns)	$0.3282, 75$
Relative momentum spread $\Delta P/P_0$	1e-4
Reference momentum P_0 (MeV/c)	13.7
Hor./vert. rms emittance $\epsilon_{x,y}$ (umrad)	2.5, 2.5
Nominal working point $Q_{x,y}$	2.454, 1.416
Bunch intensity N_b	4.5e6
Maximum $\beta_{x,y}$ (m)	14.1, 4.5
RF voltage V_{rf} (Volt)	0 and 100
RF frequency (kHz)	144

6.7.4 Benchmark in multiple tools

In analogy to [186], the ELENA ring was simulated and antiproton beam parameters at the low-energy extraction plateau in order to compare different calculations of IBS growth rates in MAD-X, Betacool [102] and JSPEC against the Python implementation in PyHEADTAIL, that was written by myself. The latter two codes are expected to be in close agreement as their implementation is equivalent. Table 6.5 summarises all important values that were used for the simulation input. MAD-X was used to compute the machine optics. The initial growth rates from all codes are given in table 6.6. When the growth rates are known, it is possible to calculate the mean square of the scattering angle θ as an extra addition to the initial momentum components of the particle. After the random scattering of all particles from this distribution, e.g., the

Table 6.6: *Calculated growth rates.*

Sim. code, (model)	τ_x, s^{-1}	τ_y, s^{-1}	τ_z, s^{-1}
PyHEADTAIL (Martini)	0.2239	-0.3074	51.64
JSPEC (Martini)	0.224	-0.3074	51.65
Betacool (Martini)	0.216	-0.301	51.71
PyHEADTAIL (BM)	0.2208	-0.3061	51.69
JSPEC (BM)	0.221	-0.3062	51.69
MAD-X (Mod. BM)	0.2109	-0.3034	52.48

updated horizontal emittance can be found from

$$\epsilon_{x,new} = \sqrt{\langle (x_i - \langle x \rangle)^2 \rangle \, \langle (x_i' - \langle x' \rangle + \theta)^2 \rangle} \tag{6.8}$$

with $\langle \theta^2 \rangle$ determined by the growth rates and time step dt,

$$\langle \theta_i^2 \rangle = 2 \frac{\epsilon_i dt}{\beta_i \tau_i}. \tag{6.9}$$

The horizontal and vertical emittance growth in tracking simulations with JSPEC and PyHEADTAIL based on the growth rates computed above are demonstrated in Fig. 6.22. The duration of this simulation corresponds to 100 turns.

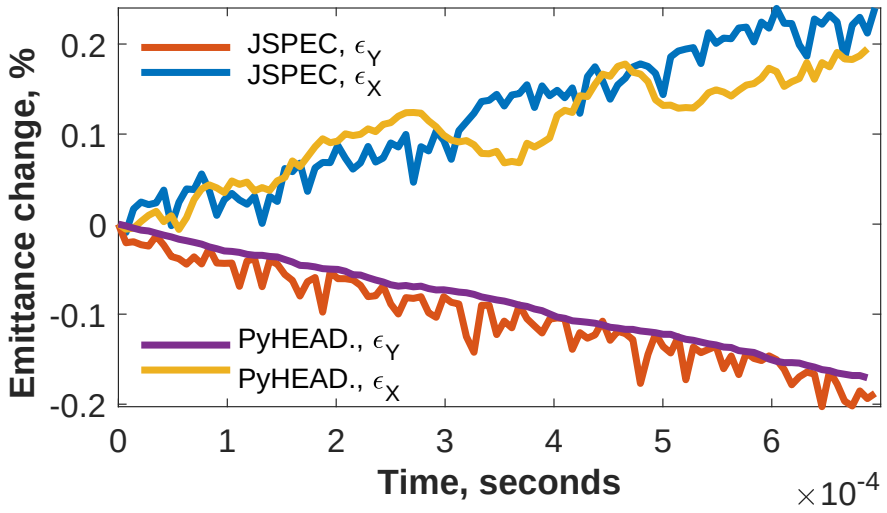

Figure 6.22: *Comparison of transverse rms emittance evolution between JSPEC and PyHEADTAIL.*

Both codes predict the same evolution: increasing horizontal emittance due to positive growth rates and decreasing vertical emittance due to negative growth rates. The jitter in the horizontal plane can be attributed to the random distribution of the applied scattering angle θ in the IBS kick. While PyHEADTAIL continuously tracks the same distribution self-consistently, JSPEC assigns a random phase advance for each particle after the given time step dt (which allows faster tracking and avoids numerical resonance artifacts but inherently leads to jitter). The residual small discrepancy in the vertical plane can thus be attributed to the difference in the particle propagation in PyHEADTAIL and JSPEC.

As an applied benchmark of our module, the dynamic process of bunch rotation has been investigated by employing full 6D tracking. The PyHEADTAIL model of the ring assumes smooth approximation with mean values of the optics calculated from 2.132. The resulting evolution of the bunch length and longitudinal growth rates are shown in Fig. 6.23. The maximum longitudinal growth rate is observed when the bunch

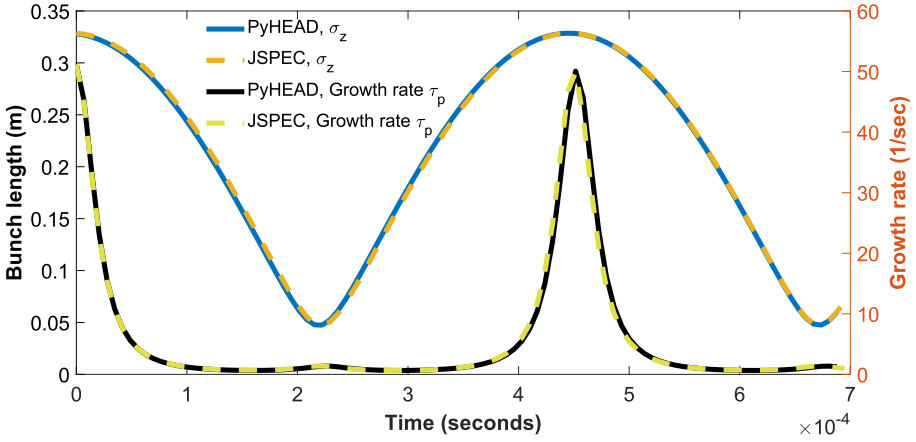

Figure 6.23: *Bunch length and longitudinal growth rate evolution during the bunch rotation process.*

is fully extended and the momentum spread is the smallest, in line with the theoretical scaling to first order: $1/\tau_p \propto \sigma_p$. The overall growth rate value has slightly decreased after one full rotation due to an increase in momentum spread from the IBS heating. The instantaneous growth rates in black compare well to the corresponding statically

computed JSPEC values in red. The top panel in Fig. 6.24 depicts the horizontal growth rate $1/\tau_x$ during the bunch rotation, again agreeing with PyHEADTAIL and static JSPEC predictions. The lower panel displays the evolving horizontal r.m.s emittance ϵ_x: each time the bunch is maximally compressed and $1/\tau_x$ peaks, ϵ_x exhibits a fast increase.

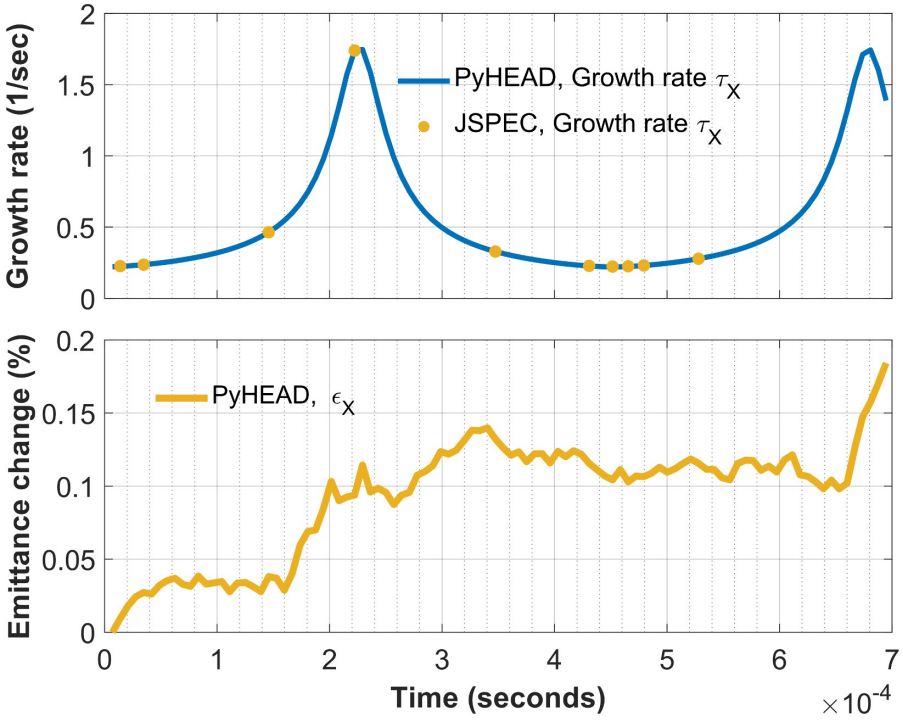

Figure 6.24: *(top) horizontal growth rate τ_x and (bottom) horizontal r.m.s emittance ϵ_x evolution during bunch rotation.*

6.8 Stable conditions for ultra-short bunches

This section combines all previous findings to present stable bunch conditions inside the low-energy machine under high compression.

As we have seen, the ELENA bunch with an initial intensity of 4.5×10^6 antiprotons and bunch length of 5 cm will experience an increase of impact from collective effects. One of the simplest ways to maintain the stability of the short bunches inside the ring is to decrease the initial bunch population by a factor >10.

Thus, I investigated how incoherent tune shift value varies with the bunch length and bunch intensity using the SixTrackLib+PyHEADTAIL simulation framework. The obtained distributions of the particle tune shifts with $\Delta Q_{x,y}$ of -0.07 and -0.1 for 75 or 5 ns matched bunches ($\delta_{75} = 7 \times 10^{-4}$ and $\delta_5 = 4 \times 10^{-4}$) are very close in size and shown in Fig. 6.25. This result coincides well with values that can be obtained analytically for the Gaussian beams.

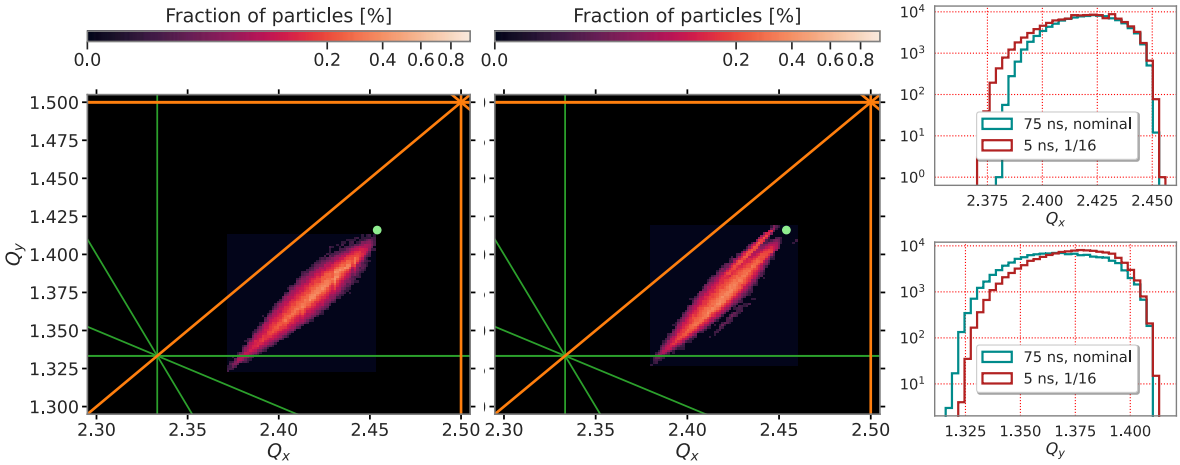

Figure 6.25: *Tune distribution of the matched ELENA bunches. (Left) Bunch length with* 5 ns *r.m.s and intensity of 2.8*×10^5 *antiprotons.(Centre) Bunch length with* 75 ns *r.m.s and intensity of 4.5*×10^6 *antiprotons. (Right) Comparison of tune projections for both cases.*

Presently the ELENA ring operates with four bunches when the RF cavity voltage amplitude is around 50 V and its RF frequency corresponds to the harmonic number h=4. The tolerated bunch intensity in the case of 5 ns long bunch is higher than the intensity threshold due to collective effects. Therefore, a bunch of lower intensity must be used for the bunch shortening procedure. In this example, three bunches are extracted from the ring as shown in Fig. 6.26 and the remaining bunch is adiabatically debunched into a coasting beam and then re-bunched again at the higher harmonic h=16 and cavity voltage of 500 V which are peak operating parameters of ELENA RF system at h16. This limitation is imposed by the maximum power supplied to the cavity.

To demonstrate the feasibility of such a scenario and to check the bunch length

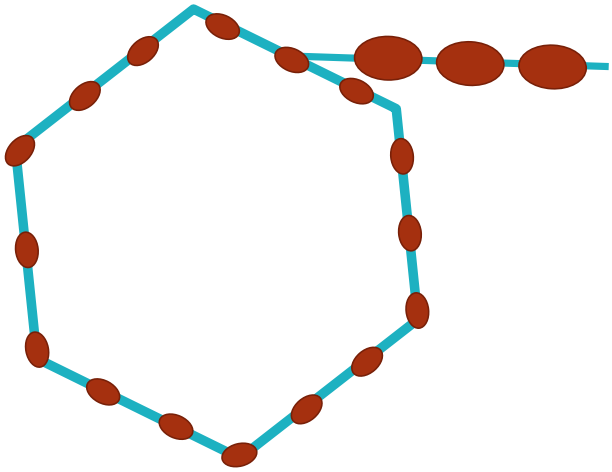

Figure 6.26: *The proposed re-bunching scheme for ELENA ring: (1) Ejection of three bunches from the ring; (2) De-bunching of the remaining bunch; (3) An adiabatic re-bunching at h=16 with RF voltage of 500 V.*

that can be theoretically attainable, I have investigated the re-bunching stage for the cooled coasting beam using the ESME [71] simulation tool.

The initial beam population (KIND=4, from ESME manual) had a random uniform distribution of longitudinal coordinate over the ring ($[-\pi, \pi]$) and a Gaussian distribution in momentum spread, δ, with 2×10^{-5} r.m.s which is achievable according to [149]. This momentum spread determines the final r.m.s of momentum distribution and hence the time span of the matched bunch.

An outcome of the bunching process for 0.5 s is shown in Fig. 6.27. For the initial conditions, the final phase occupation of the single bunch within the selected contour is 0.26° r.m.s which corresponds to the bunch length of 5 ns r.m.s. The final momentum spread δ is equal to 4×10^{-3} r.m.s. The obtained bunch in ESME and the matched 5 ns bunch in Fig. 6.25 from PyHEADTAIL are in quite good agreement with each other.

This result demonstrates one of the stable scenarios for short bunches. More extensive analysis can provide alternative parameters which will keep the tune spread below the dangerous threshold. Ultimately, one can perform an N-dimensional grid parameter scan of this problem to obtain desired bunch properties for specific machine parameters, Fig. 6.28.

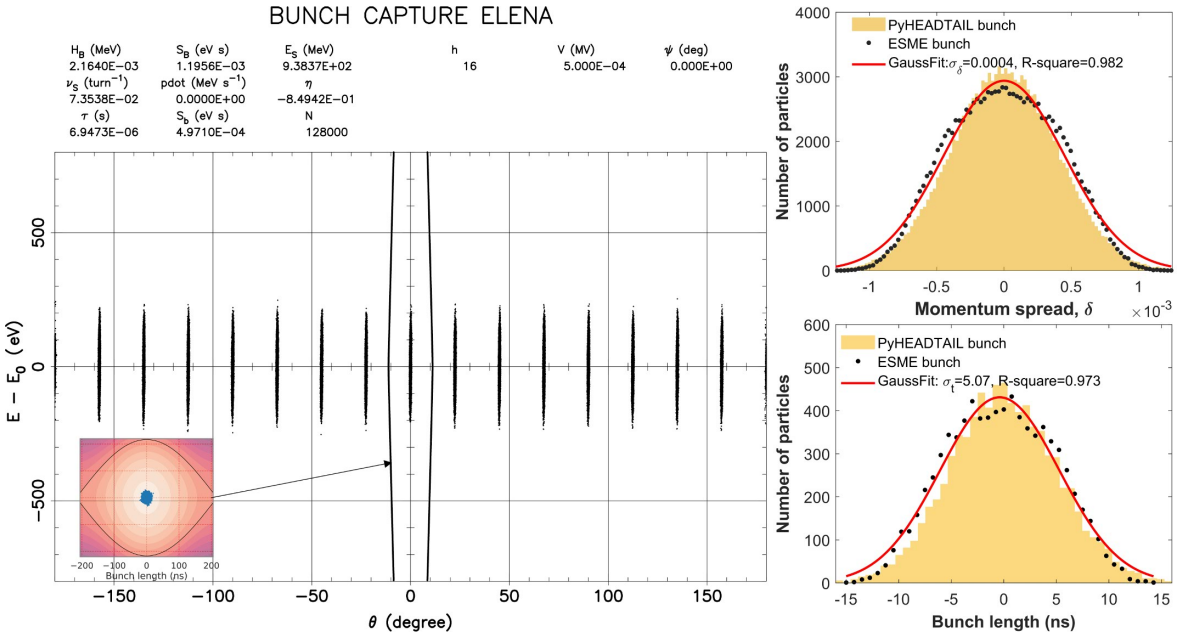

Figure 6.27: *(Left) The longitudinal distribution of 128000 macro particles after the re-bunching process. The miniature image in the left corner demonstrates a single bunch inside the RF bucket in the time domain. (Right) Momentum distribution of particles within the contour at the top and time distribution of the same particles at the bottom after re-bunching.*

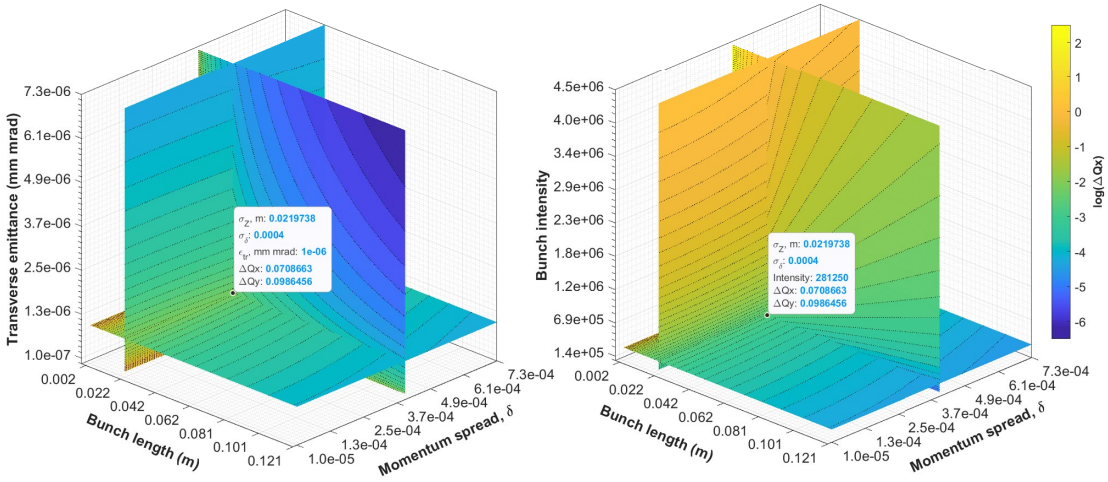

Figure 6.28: *Example of tune shift scan with the analytical equation for Gaussian bunch.*

6.9 Beam-gas target overlap

The collision of a low-energy antiproton beam with the target inside the storage ring has a number of advantages over single-pass experiments in a transfer line. The beam revolution frequency on the order of 2.3 MHz compensates for the loss in interaction luminosity due to the decreased bunch density. Beam cooling processes and small interaction lengths will mitigate multiple particle scattering on a target and improve the energy resolution of detected reaction fragments. However, complex requirements (decreased intensity, large momentum spread, short extraction time) for the circulating beam will likely exclude the possibility of simultaneous operation of other experiments with the same efficiency level.

6.9.1 Gas jet target

The delivered gas jet densities are in the range of 10^{12} – 10^{15} atoms cm^{-2} [187]. To achieve larger densities, the gas is pushed through a cooled nozzle applying a high input pressure.

An acceptable boundary of the target density may be defined by the ability to compensate for the energy loss and scattering of the beam particles via cooling and the RF cavity systems or technical capabilities of the gas-jet system.

The combination of this type of target with the so-called “reaction microscope” provides the opportunity to obtain the full momentum vectors of recoil-ions and electrons in coincidence. The general design and principle of operation are shown in Fig. 6.29. The target gas is crossed by a projectile beam. The produced reaction fragments—ion and the electron(s) are guided towards the position- and time-sensitive detectors by an electric field and propagate through a drift region. An overlaid magnetic field produced by Helmholtz coils forces the particles on a helical trajectory and thereby significantly increases the energy acceptance for detected reaction products.

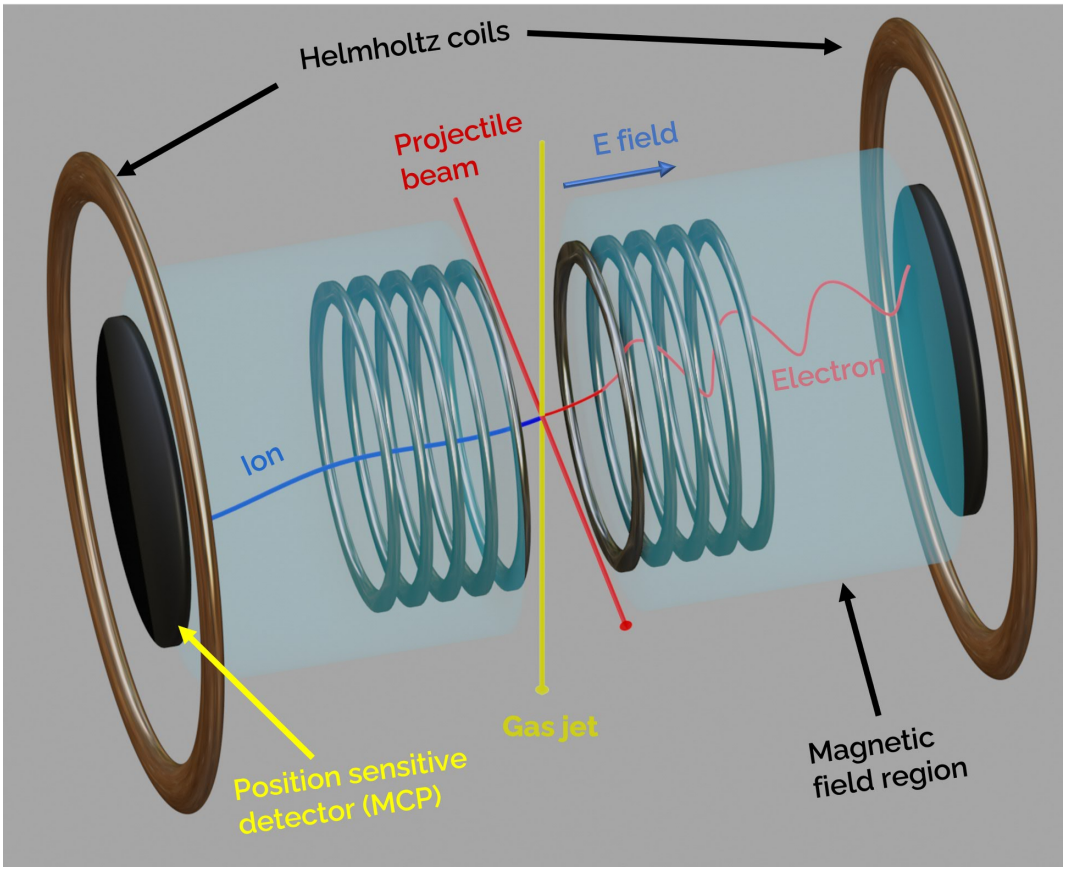

Figure 6.29: *Schematics of reaction-microscope utilising a gas-jet target.*

6.9.2 Geant4 simulation and reaction rates

To apply this technique for 100 keV antiprotons, I have studied the collision of antiprotons with atomic helium gas-jet in Geant4. One of the most straightforward ways to test the theory is to study the single-electron ionisation of the target. Physical models included in Geant4 provide such a possibility via the G4hIonisation method, which offers the continuous energy loss due to ionisation and simulates the "discrete" part of the ionisation, that is, recoil electrons produced by antiprotons. However, to obtain a more realistic reaction rate, I implemented new total cross sections, defining the numbers given by Kirchner [188] for the interaction of 101.6 keV antiprotons with atomic helium. Initially, a default total cross section of 0.128Å^2 (10^{-16} cm^{-2}) provided by a combination of low-energy physics modules QBBC and EMZ were approximately

five times smaller than measured, a comparison is shown in Fig. 6.30. Hadronic cross

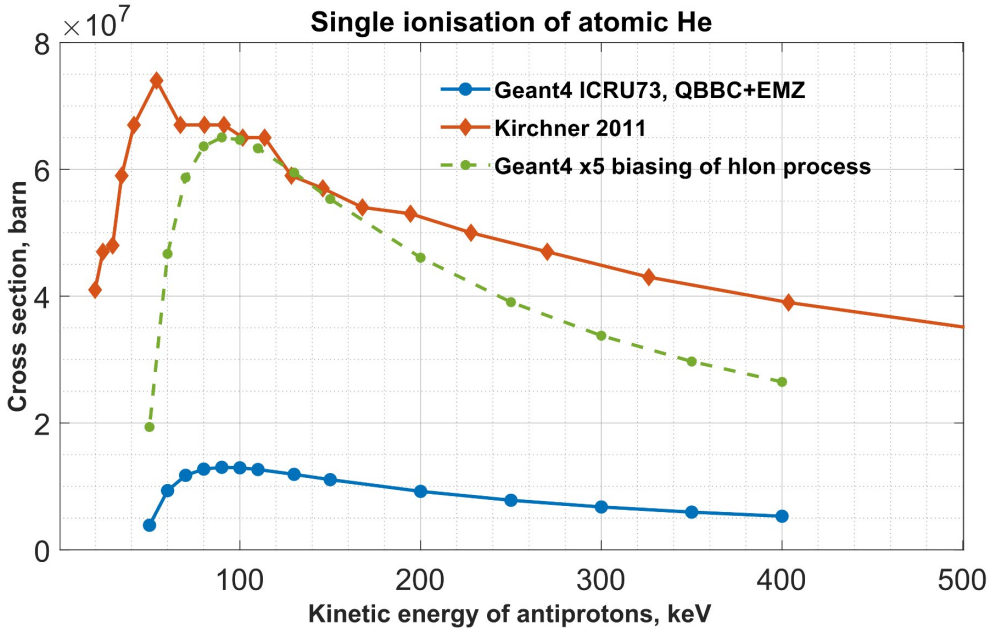

Figure 6.30: *Dependence of the cross section for reaction of single ionisation of atomic He from the kinetic energy of antiprotons.*

sections of elastic and inelastic antiproton/proton collisions with He nucleus are in the order of few barns [189]. The sum of both processes at 100 keV gives only 6 b in this Geant4 physics list. It means that vacuum contamination of the storage rings comes mostly from the gas-jet injection system. The antiproton energy loss is obtained according to the quantum harmonic oscillator model [190] and takes into account the Barkas-Andersen effect [191]. Additionally, my simulation also confirmed the efficiency of the bunch compression, resulting in a decrease in the time spread of the detected signal.

The geometry of the setup is shown in Fig. 6.31, and consists of a gas-jet target made of helium with atomic concentration $2.5 \times 10^{14}\text{cm}^{-3}$, a set of ideal detectors (100 % efficiency) which save properties of entering/leaving beam as well as secondary particles produced by the interaction. A gas jet width of 3 mm was considered, which is equal to $2\sigma_{x,y}$ transverse dimensions of the bunch. The time distributions of secondaries when $\bar{p}$ bunch σ_t set to 1, 5 and 75 ns in orange, red and blue, respectively, are shown in

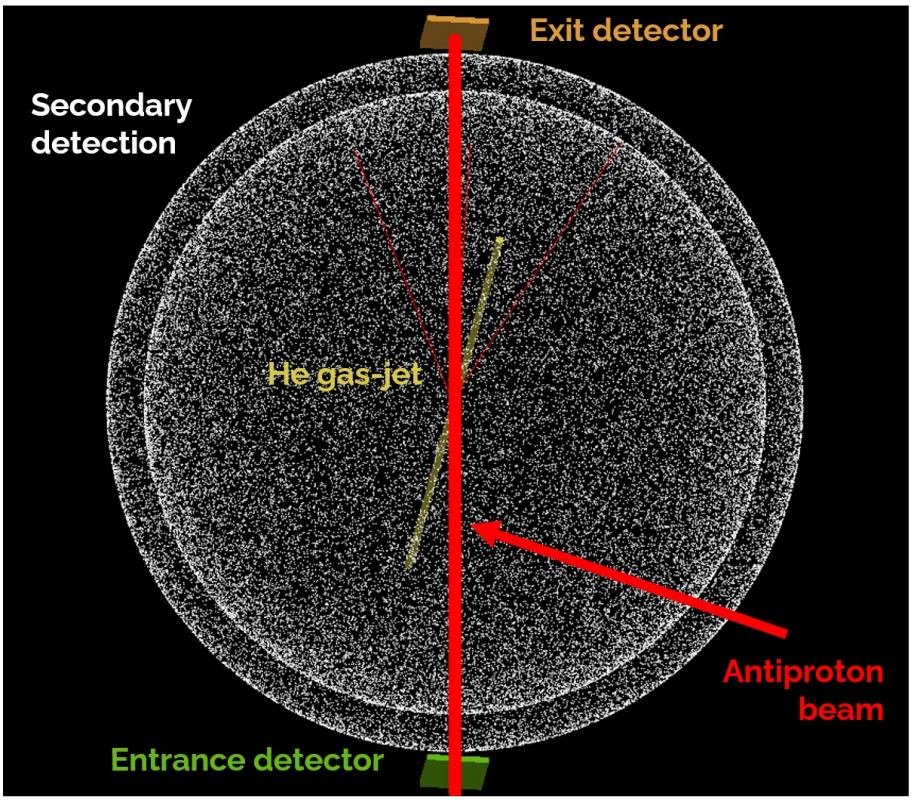

Figure 6.31: *Geant4 simulation of the collision of antiproton bunch with helium gas-jet. The main beam is stored before and after the interaction. The secondary detector records time, position and scattering angles.*

Fig. 6.32b. The total number of beam particles is equal to 45 million, which corresponds to ten turns within the ring or 70 μs. As expected, we can see a significant impact on the time distribution of secondary electrons and the standard deviations of the time signal match pretty well with antiproton bunch lengths until the 4 ns boundary.

Detection time for secondaries consists of the sum of three components: the drift of antiprotons to the target, the time interval of the reaction and the drift of secondaries to the detector. Therefore, further signal compression is limited by the intrinsic energy distribution of secondary electrons and the geometry of the setup. The estimated total reaction rate of such signal in h16 RF mode is $\kappa_{sim}{=}n_{sec} \cdot \nu = 5.52 \times 10^9$ per second in a 4π segment of solid angle, where n_{sec} is a number of detected secondaries, and ν is the frequency of the interaction. Compared to fully analytical calculations of the ionisation process, it gives a close number if we assume uniform gas jet thickness for

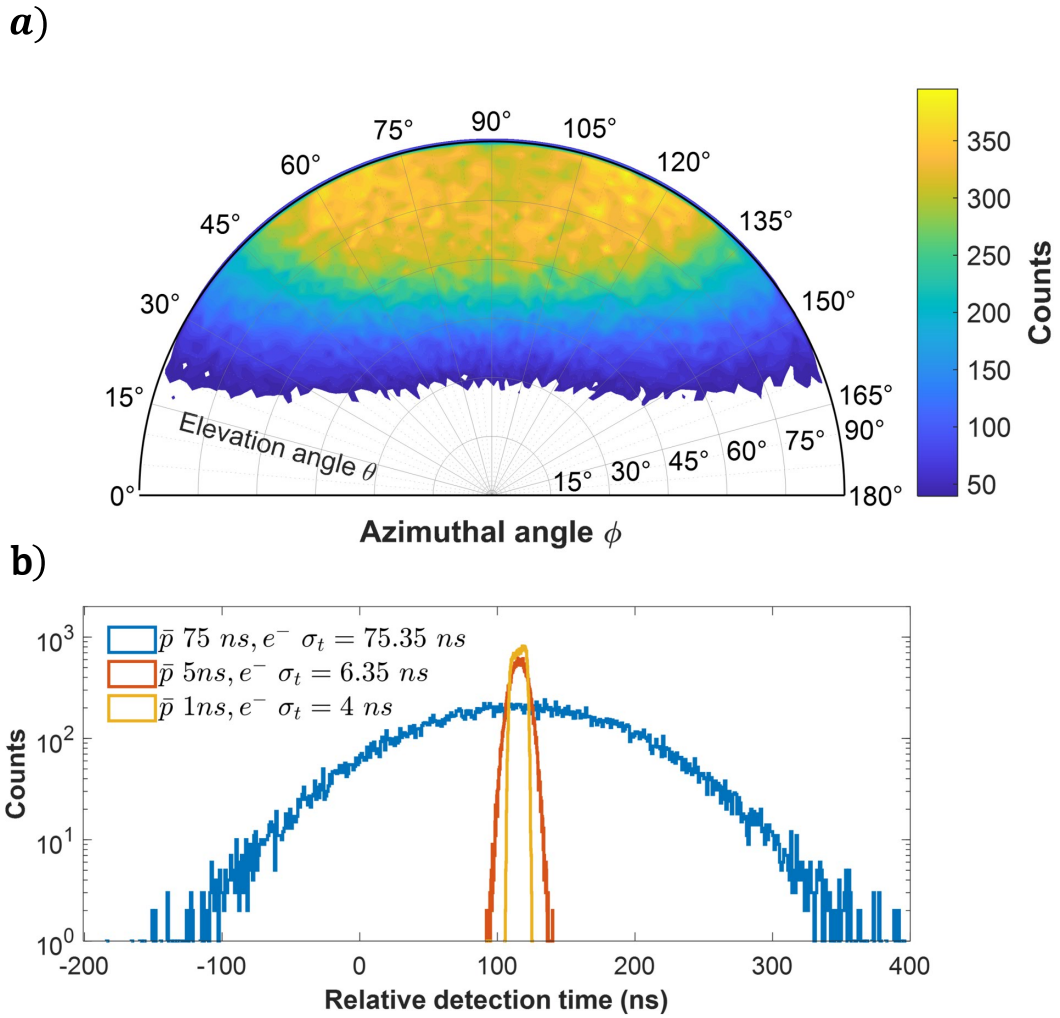

Figure 6.32: *Analysis of the interaction of antiproton bunch with helium gas-jet. (**a**) Angular distribution of secondary electrons, initial mean angles for antiprotons are 90 degrees; (**b**) Time profiles of secondary electrons for different antiproton bunch lengths.*

every antiproton and the absence of other processes:

κ_{calc}=$b_i \cdot \nu \cdot n_g \cdot \sigma_{io} \cdot 0.68 = 7 \times 10^9$, where b_i is simulated antiproton number, n_g is the atomic density of the helium gas-jet, σ_{io} previously mentioned cross section of ionisation and 0.68 stands for one sigma probability to hit the gas-jet. Figure 6.32a demonstrates a polar projection of the angular distribution of secondary electrons stored at the spherical detector. The maximum intensity after scattering is observed at elevation angles close to $\theta = 90$ degrees. This implies that one of the possible ways to decrease

time spread is to narrow a detection solid angle.

However, one should note that this simulation does not consider further behaviour of the recoil ions of the target. All available ionisation models in Geant4 physics lists have a simplified treatment of the hadron ionisation process, where interaction with bound electrons is randomised, and the recoil ion energy is far below 100 eV energy limit for light ions [192]. This model calculates scattering angles according to energy-momentum conservation for incident projectile and electron only. Maximum kinetic energy transfer calculated from simple kinematic relation of head-on elastic collision of two particles:

$$E_{kmax} = \frac{2m_e c^2(\gamma^2 - 1)}{1 + 2\gamma(m_e/M) + (m_e/M)^2}, \tag{6.10}$$

where m_e and M are, respectively, masses of electron and projectile. For 100 keV antiprotons this value is 220 eV.

Next, I would like to discuss the only available experimental data compared to a set of theoretical predictions. This type of experiment was performed in the past for a helium target in case of 945 keV antiprotons from LEIR and then compared with 1 MeV protons [42]. Figure 6.33 demonstrates a comparison of the experiment against Classical Trajectory Monte Carlo (CTMC) [193], Continuum Distorted Wave (CDW) and CDW with the eikonal initial state (EIS) [194]. The last two models give good agreement for the momentum of recoil electrons. Most of the emitted electrons move in a forward direction after an impact ($P_{\|}>0$). For the recoil ion momentum distribution (bottom subplots), CDW–EIS gives the best agreement with the experimental data for both protons and antiprotons. On the other hand, normal CDW underestimates it and CTMC overestimates the peak value. As mentioned in [195], this behaviour is unexpected in light of the agreement between CDW and CDW–EIS for longitudinal electron momentum distribution. Thus, according to these measurements, there is no big difference between antiproton and proton impact at the total cross sections level. Moreover, the shape and maximum locations on Fig. 6.33 are within the experimental

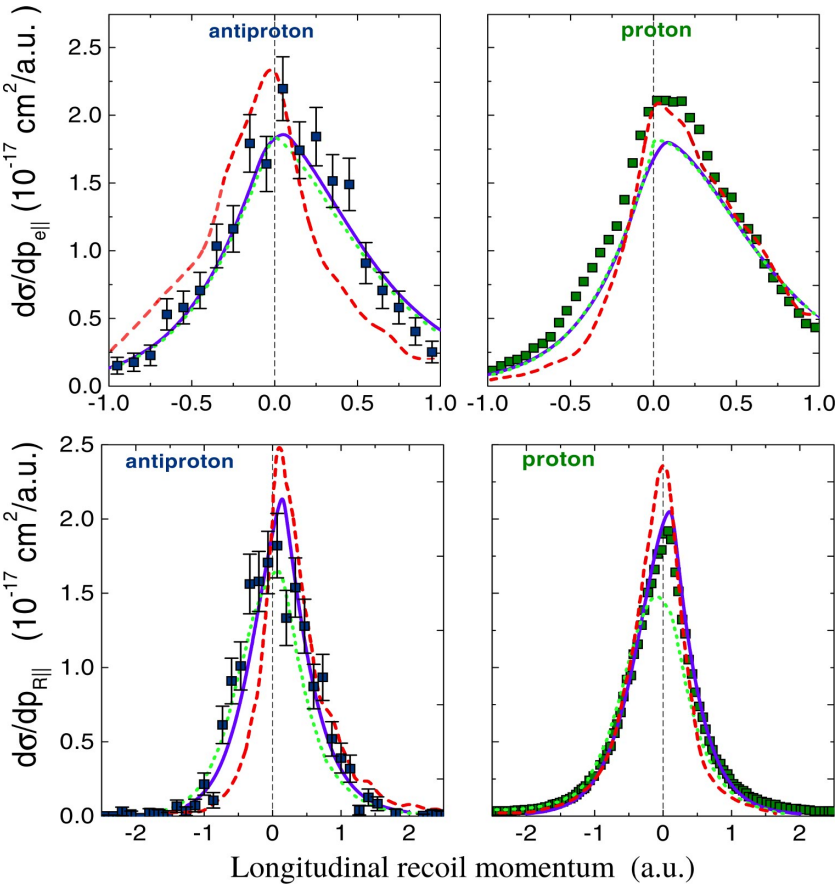

Figure 6.33: *Longitudinal momentum distribution for single ionisation of helium by* 945 keV *antiproton and* 1 MeV *proton (data points) in comparison with theoretical CTMC(dashed red), CDW(dotted green) and CDW-EIS(solid magenta) models. Data obtained and republished with permission from [195]. Momentum is given in atomic units (Hartree unit system).*

uncertainty. So it is not easy to draw a clear contrast between proton and antiproton from the presented results.

But it actually tells us that the ionisation process for these particles is identical at the 1 MeV energy level. The next Fig. 6.34 demonstrates a comparison of the mean longitudinal momentum for recoil ions and emitted electrons in He ionisation by protons and antiprotons as a function of the impact energy. These were calculated using the CDW-EIS model and compared to available data from the next measurements [42, 196, 197] as well as results of performed Geant4 simulation.

The mean longitudinal momentum of recoil electrons is larger in the proton case

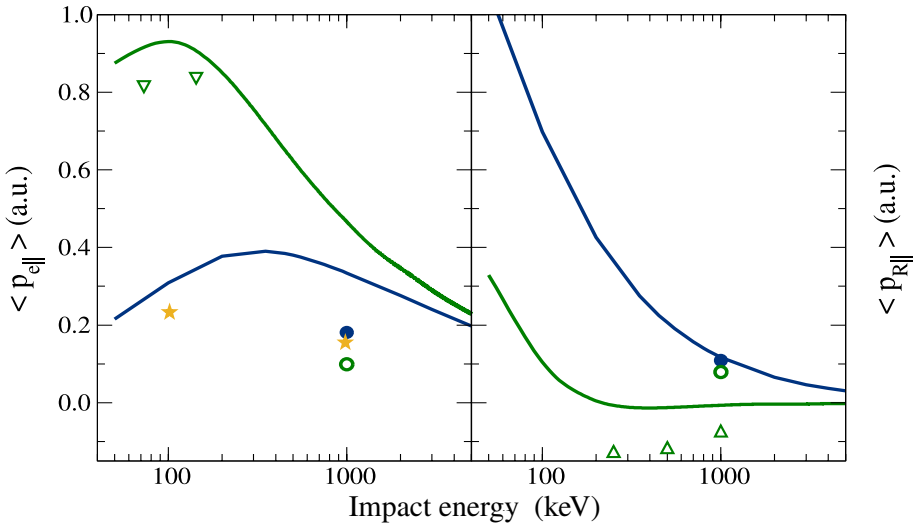

Figure 6.34: *The mean longitudinal momentum of the recoil electron and ion for proton (green) and antiproton (navy) impact on He target as a function of impact energy. Solid curves represent CDW-EIS theory, and experimental data were obtained only for recoil electrons [197] (downward triangles), only recoil ions [196] (upward triangles), and for both recoils [42] (circles). Geant4 simulation results are shown for 100 and* 945 keV *antiproton bunches (yellow stars). Data obtained and reformatted with permission from [195].*

because of the pulling effect after collision in comparison with antiproton repulsion. The opposite behaviour is observed in theory for recoil ions. Also, one may notice surprising differences at high energy, where the theoretical model should work best. Unlike in Fig. 6.33, this recoil property is a responsive quantity to characterise the distributions since results there appear to be a good agreement between theory and experiments. Surprisingly, results from the simplified Geant4 simulation model show good agreement with the measurements, meaning that the recoil ion behaves more like an observer.

Results from this section showed that the most intense secondary emission happens in cone opening below 70 degrees and the time distribution is directly related to the length of the antiproton bunch. Moreover, it also shows that the minimum time signal width of secondary particles depends on the geometry of the setup and momentum exchange with the primary beam. Past experiments and theory show that recoil

longitudinal momentum distributions are less sensitive to the projectile charge sign. An identical experimental setup might be utilised to describe such interaction more precisely.

6.10 Summary

A set of bunch compression methods was discussed and developed in order to perform high-precision experiments within a beam line or storage ring. The first presented method is suitable for a typical crossed-beam atomic physics experiment that uses a single-pass setup, where the projectile beam is given only one chance to interact with the target and afterward may be used for further trapping. The longitudinal focusing, in this case, relies on the bunch rotation principle. However, an exact strategy might be applied to a storage ring when optimal compression is reached within tens of turns.

Next, it was demonstrated that the higher particle density of a compressed bunch leads to instability due to the impact of IBS and space charge processes. Two space charge simulation techniques, frozen and 3D PIC, were utilised depending on bunch properties and machine operation schemes. Additionally, the IBS effect was implemented into the PyHEADTAIL simulation with a future plan to combine it with space charge in a more realistic manner (molecular dynamics algorithm for example). The benchmark study demonstrated perfect agreement with the rest of the simulation codes that implemented the IBS effect. For the ELENA case, it was shown that space charge plays a more dominant role in bunch emittance growth. The nominal intensity is too high to sustain stable beam conditions during bunch compression. Multiple cases were studied and provided a suitable solution for future experiments. A more realistic simulation of a machine will require a detailed implementation of magnet errors and optional compensation of the beam growth with electron cooling.

Finally, the interaction of the compressed bunch with an atomic helium gas jet was studied via created and fine-tuned Geant4 model. A comparison of the results with the available experimental and theoretical data showed that we are still missing

certain aspects of the physics of an interaction process. Additional experimental data in the energy region below 1 MeV is essential for finding the proper conclusion.

Chapter 7

Conclusions

7.1 Summary

The innovative findings of this project demonstrated the possibility of designing and constructing low-energy machines and experiments with a more realistic approach than was done before. Consideration of various limiting factors such as imperfections of magnetic or electrostatic elements, a trade-off between collective effects of the beam, impact of background (stray magnetic fields, vacuum quality, e.g.) ultimately leads to antiproton beams with better quality and controlled properties and beam loss minimisation.

These findings also included new developments for the discovery of unknown antimatter physics. They aim to provide a solid base for the creation of heavy antiprotonic atoms, low-energy antineutrons, and possibly antimatter-induced nuclear micro-fission and fusion.

A novel idea that I had proposed during the project was to utilise existing technology outside the scope of accelerator physics, to characterize complex 3D fields of electrostatic elements. The unique MEMS sensor, developed for this goal, utilises a ray of light fedback through its collimation via electrostatic field strength. Further

improvement of this field sensor may rely on a change of properties of a laser pulse passing through a miniature field-sensitive crystal. A similar approach was also applied in the past [198, 199] as a mostly non-invasive way of field characterisation.

A suite of simulation codes was utilised throughout the presented studies. First of all, two branches of the electrostatic transfer lines from the Antimatter Factory at CERN have been implemented in G4beamline and BMAD, the longest line towards the ALPHA experiment and the AEgIS experiment placed alongside. The main steering components of both beam lines were recreated in CAD and then simulated with CST Particle Studio to generate high-resolution electrostatic field maps. It also allowed benchmarking of the field distribution of electrostatic quadrupole against measurements performed with MEMS. To improve tracking performance in G4beamline, the latest field integration methods and electrostatic quadrupole model were implemented. The fringe field shape was fitted to match the simulated 3D field. Identical maps of electrostatic deflectors were also used in the BMAD model. A beam distribution resembling that after extraction from the ELENA ring was tracked in both codes and showed perfect agreement against the MAD-X baseline model.

Modelling of the AEgIS branch helped to investigate the impact of stray magnetic field produced via two solenoids of the particle trap. Two different representations of the field, numerical CST simulation and G4beamline analytic description via coils, showed good agreement. It clearly demonstrated the importance of an installed corrector system. As an alternative, mitigation of stray magnetic fields by insertion of passive μ-metal shields was studied.

One of the biggest highlights of this work was the design of a low-energy ($<$5 keV) injection beam line for AEgIS collaboration. The final design satisfied a number of requests: system compactness, the passage of three beams, large aperture (20 mm), and the possibility of extraction and trajectory correction under the impact of the stray magnetic field. A realistic CST tracking simulation with space-charge impact demonstrated beam guidance and deceleration before the injection into the AEgIS trap.

This setup will provide the possibility of proof-of-principle studies of antiproton-bound systems with medium-mass elements - iodine and caesium. The AEgIS team plans to demonstrate a solid benchmark of the proposed evolution models of such atoms [200]: 1) antiproton capture process; 2) cascade on lower electron orbits and 3) annihilation with one of the nucleons. Additionally, examinations of these systems allow for tackling a wide range of physics topics, from tests of fundamental symmetries to searches for novel approaches to open questions in atomic and nuclear physics [201].

Multiple methods of longitudinal compression of antiproton bunches from ELENA were investigated. Three different options demonstrated the ability to obtain bunches with $\sim$ ns length:

- **Bunch compression in experimental transfer lines**,

  This method requires an additional RF system with a wave amplitude up to 100 kV. The applied voltage determined the maximum compression spot and the largest momentum spread. Benchmark simulations in G4beamline and BMAD showed a perfect agreement by achieving 1 ns r.m.s bunch in the ALPHA beam line. The main advantages of this method are flexibility in required bunch parameters, minimum disruption to existing beam transport and low impact from collective effects. Intensity loss due to limited momentum acceptance, the necessity of additional RF cavity and inefficiency in bunch usage in single-pass experiments belong to the disadvantages of this proposal.

- **Bunch rotation inside ELENA ring**,

  In this scheme previous method was applied in the ELENA storage ring. It was demonstrated that an initial bunch could be continuously rotated for a prolonged time with controlled decompression due to collective effects, rest gas, and other factors. In this work, the antiproton bunch was compressed to 10 ns r.m.s at the first RF harmonic. With this option, multi-pass target experiments can be performed within the storage ring with activation of the detector triggers only when the bunch is fully compressed. However, due to collective effects,

the intensity of the manipulated bunch needs to be below 3×10^5 antiprotons for stability reasons.

- **Re-bunching at higher harmonics**,

  The last alternative is re-bunching of the single antiproton bunch inside the ELENA ring. It allows bunches of <5 ns r.m.s length at the 16th RF harmonic to be achieved. However, an intensity decrease is required to avoid the strong impact from the space charge, as was demonstrated via 3D PIC PyHEADTAIL simulation. Perfect agreement was found for this re-bunching scheme studied in ESME and PyHEADTAIL.

The bunch rotation inside the ELENA ring was also studied under the impact of IBS process. A much slower emittance increase was observed in comparison with the space-charge effect. It was also discovered that the increase of tune spread in rotation mode is much slower than in continuous operation with ns bunches. This scheme can possibly be used for experiments where higher intensity per target crossing is needed.

Finally, reaction rates after the interaction of ultra-short antiproton bunch with the helium gas-jet were estimated from Geant4 simulation based on available experimental data. Target gas-jet density can be of the order of $10^8\,\mathrm{cm}^{-3}$ and provide a sensible signal per second in 4π solid angle. It was found that the mean momentum value for recoil fragments obtained from the simulation was in better agreement with previously measured data for ≈1 MeV antiprotons than suggested via theoretical predictions.

7.2 Outlook

Further improvements can be focused on improving bunch compression methods and simulation techniques for collective effects. These include investigation of the stable bunch parameters for bunch rotation inside the ELENA ring at the fourth RF harmonic, which should provide compression better than ∼10 ns. Alternatively, one can think

about improving the momentum spread of the antiproton bunch inside the experimental beam lines. Experimental benchmark of demonstrated simulations against the ELENA machine can be performed via excitation of third-order resonance [202].

A better description of the collective effects can be done via a combination of space charge, electron cooling and IBS within a single simulation tool. Since we operate with relatively low bunch intensities, particle propagation can be implemented using relativistic and electromagnetic molecular dynamics techniques [203]. On the experimental side, one may analyse in detail the possible impact of the internal gas-jet target on the vacuum quality of the machine and the most optimal detector setup for the registration of reaction fragments.

The demonstrated simulation methods will be of great benefit to other low-energy machines and experiments. New types of even less invasive measurements of electrostatic or magnetic fields can be developed as a further evolution of the utilised MEMS sensor. The G4beamline code and ELENA transfer lines simulation can be easily extended and include other branches, parts of experiments and additional effects, thanks to the flexibility of the Geant4 toolkit.

Finally, the commissioning of the AEgIS injection line will be done in the near future and will uncover existing limitations of the setup. A study of the extraction of low-energy antiprotons into portable particle traps is also planned. Thus, it will also provide crucial preliminary experience for an even more challenging PUMA experiment.

List of Figures

List of Tables

Bibliography

[1] P. A. M. Dirac. "The quantum theory of the Electron. Part II." In: *Proceedings of the Royal Society of London. Series A, Containing Papers of a Mathematical and Physical Character* 118.779 (Mar. 1928), pp. 351–361. DOI: 10.1098/rspa.1928.0056.

[2] T. Massam et al. "Experimental observation of antideuteron production." In: *Il Nuovo Cimento* 39.1 (Sept. 1965), pp. 10–14. DOI: 10.1007/bf02814251.

[3] D. E. Dorfan et al. "Observation of Antideuterons." In: *Physical Review Letters* 14.24 (June 1965), pp. 1003–1006. DOI: 10.1103/physrevlett.14.1003.

[4] G. Baur et al. "Production of antihydrogen." In: *Physics Letters B* 368.3 (Feb. 1996), pp. 251–258. DOI: 10.1016/0370-2693(96)00005-6.

[5] P. Lefèvre, D. Möhl, and G. Plass. "The CERN Low Energy Antiproton Ring (LEAR) project." In: (1980). URL: https://cds.cern.ch/record/879246.

[6] E. Rutherford. "The scattering of and particles by matter and the structure of the atom." In: *The London, Edinburgh, and Dublin Philosophical Magazine and Journal of Science* 21.125 (May 1911), pp. 669–688. DOI: 10.1080/14786440508637080.

[7] *Geiger and Rutherford experiment.* https://gkscientist.com/rutherford-gold-foil-experiment-1911/.

[8] D. Möhl. *Stochastic Cooling of Particle Beams.* Springer Berlin Heidelberg, 2013. DOI: 10.1007/978-3-642-34979-9.

[9] H. Poth et al. "First results of electron cooling experiments at LEAR." In: *Zeitschrift für Physik A Atomic Nuclei* 332.2 (June 1989), pp. 171–188. DOI: 10.1007/bf01289773.

[10] S. A. Baird et al. "The LEAR stochastic cooling system: present and future." In: (1988). URL: http://cds.cern.ch/record/194352.

[11] H. A. Torii et al. "Atomic Collision Experiments with Ultra-Low-Energy Antiprotons." In: *AIP Conference Proceedings*. AIP, 2008. DOI: 10.1063/1.2977849.

[12] E. Morenzoni. "Ionization by low energy antiprotons." In: *AIP Conference Proceedings*. AIP, 1990. DOI: 10.1063/1.39833.

[13] H. Poth. "Physics with Antiprotonic Atoms." In: *Physics at LEAR with Low-Energy Cooled Antiprotons*. Springer New York, 1984, pp. 567–588. DOI: 10.1007/978-1-4684-8727-5_54.

[14] T. J. Phillips. "Measuring the gravitational acceleration of antimatter with an antihydrogen interferometer." In: *Hyperfine Interactions* 100.1 (Dec. 1996), pp. 163–172. DOI: 10.1007/bf02059941.

[15] G. Gabrielse et al. "First Capture of Antiprotons in a Penning Trap: A Kiloelectronvolt Source." In: *Physical Review Letters* 57.20 (Nov. 1986), pp. 2504–2507. DOI: 10.1103/physrevlett.57.2504.

[16] *AD optics and layout.* https://cern-accelerators-optics.web.cern.ch/AD/defaultAD.htm.

[17] C. Amsler et al. "The ATHENA experiment for the study of antihydrogen." In: *International Journal of Modern Physics A* 29.20 (Aug. 2014), p. 1430035. DOI: 10.1142/s0217751x1430035x.

[18] G. Gabrielse et al. "Background-Free Observation of Cold Antihydrogen with Field-Ionization Analysis of Its States." In: *Physical Review Letters* 89.21 (Oct. 2002), p. 213401. DOI: 10.1103/physrevlett.89.213401.

[19] *Particle trap operation principles.* https://massen.web.cern.ch/hoat/.

[20] Y. Yamazaki. "Trapping, cooling and extraction of antiprotons, and the ASACUSA project." In: *AIP Conference Proceedings*. AIP, 1999. DOI: 10.1063/1.1302100.

[21] V. Chohan et al. *Extra Low ENergy Antiproton (ELENA) ring and its Transfer Lines: Design Report*. CERN Yellow Reports: Monographs. Geneva: CERN, 2014.

[22] *ELENA ring drawings.* https://cern-accelerators-optics.web.cern.ch/ELENA/defaultELENA.htm.

[23] *ELENA ring magnets.* https://indico.cern.ch/event/268237/contributions/1606368/attachments/479864/663745/Magnets_Presentation.pdf.

[24] C. Amole et al. "The ALPHA antihydrogen trapping apparatus." In: *Nuclear Instruments and Methods in Physics Research Section A: Accelerators, Spectrometers, Detectors and Associated Equipment* 735 (Jan. 2014), pp. 319–340. DOI: 10.1016/j.nima.2013.09.043.

[25] G. Yu. Drobychev et al. *Proposal for the AEGIS experiment at the CERN antiproton decelerator (Antimatter Experiment: Gravity, Interferometry, Spectroscopy)*. Tech. rep. Geneva: CERN, 2007. URL: http://cds.cern.ch/record/1037532.

[26] G. Chardin et al. *Proposal to measure the Gravitational Behaviour of Antihydrogen at Rest*. Tech. rep. Geneva: CERN, 2011. URL: https://cds.cern.ch/record/1386684.

[27] S. Ulmer et al. *Direct High-Precision Measurement of the g-Factor of a Single Antiproton Stored in a Cryogenic Penning Trap*. Tech. rep. Geneva: CERN, 2012. URL: https://cds.cern.ch/record/1455847.

[28] T. Aumann et al. *PUMA: antiprotons and radioactive nuclei*. Tech. rep. Geneva: CERN, 2019. URL: https://cds.cern.ch/record/2691045.

[29] C. Smorra et al. *Technical Design Report of BASE-STEP*. Tech. rep. Geneva: CERN, 2021. URL: https://cds.cern.ch/record/2756508.

[30] L. H. Andersen et al. "Single and Double Ionization of Helium by Fast Antiproton and Proton Impact." In: *Physical Review Letters* 57.17 (Oct. 1986), pp. 2147–2150. DOI: 10.1103/physrevlett.57.2147.

[31] A. Kreissl et al. "Remeasurement of the magnetic moment of the antiproton." In: *Zeitschrift für Physik C Particles and Fields* 37.4 (Dec. 1988), pp. 557–561. DOI: 10.1007/bf01549714.

[32] N. Morita et al. "First observation of laser-induced resonant annihilation in metastable antiprotonic helium atoms." In: *Physical Review Letters* 72.8 (Feb. 1994), pp. 1180–1183. DOI: 10.1103/physrevlett.72.1180.

[33] G. Breit and I. I. Rabi. "Measurement of Nuclear Spin." In: *Physical Review* 38.11 (Dec. 1931), pp. 2082–2083. DOI: 10.1103/physrev.38.2082.2.

[34] T. Bergeman, G. Erez, and H. J. Metcalf. "Magnetostatic trapping fields for neutral atoms." In: *Physical Review A* 35.4 (Feb. 1987), pp. 1535–1546. DOI: 10.1103/physreva.35.1535.

[35] S. Aghion et al. "A moiré deflectometer for antimatter." In: *Nature Communications* 5.1 (July 2014). DOI: 10.1038/ncomms5538.

[36] M. J. G. Borge and K. Blaum. "Focus on Exotic Beams at ISOLDE: A Laboratory Portrait." In: *Journal of Physics G: Nuclear and Particle Physics* 45.1 (Nov. 2017), p. 010301. DOI: 10.1088/1361-6471/aa990f.

[37] T. Sowinski. *Personal communication at AEgIS collaboration meeting*. Dec. 1, 2022.

[38] C. J. Baker et al. "Sympathetic cooling of positrons to cryogenic temperatures for antihydrogen production." In: *Nature Communications* 12.1 (Oct. 2021). DOI: 10.1038/s41467-021-26086-1.

[39] S. Sels et al. "Doppler and sympathetic cooling for the investigation of short-lived radioactive ions." In: *Physical Review Research* 4.3 (Sept. 2022), p. 033229. DOI: 10.1103/physrevresearch.4.033229.

[40] R. Rugango et al. “Sympathetic cooling of molecular ion motion to the ground state.” In: *New Journal of Physics* 17.3 (Mar. 2015), p. 035009. DOI: 10.1088/1367-2630/17/3/035009.

[41] S. Truppe et al. “Molecules cooled below the Doppler limit.” In: *Nature Physics* 13.12 (Aug. 2017), pp. 1173–1176. DOI: 10.1038/nphys4241.

[42] Kh. Khayyat and T. Weber. “Differential cross sections in antiproton- and proton-helium collisions.” In: *Journal of Physics B: Atomic, Molecular and Optical Physics* 32.4 (Jan. 1999), pp. L73–L79. DOI: 10.1088/0953-4075/32/4/002. URL: https://doi.org/10.1088%2F0953-4075%2F32%2F4%2F002.

[43] R. von Hahn et al. “The cryogenic storage ring CSR.” In: *Review of Scientific Instruments* 87.6 (June 2016), p. 063115. DOI: 10.1063/1.4953888.

[44] W. Geithner et al. “Status and outlook of the CRYRING@ESR project.” In: *Hyperfine Interactions* 238.1 (Jan. 2017). DOI: 10.1007/s10751-016-1383-5.

[45] M. Durante et al. “All the fun of the FAIR: fundamental physics at the facility for antiproton and ion research.” In: *Physica Scripta* 94.3 (Jan. 2019), p. 033001. DOI: 10.1088/1402-4896/aaf93f.

[46] B. Franzke. “The heavy ion storage and cooler ring project ESR at GSI.” In: *Nuclear Instruments and Methods in Physics Research Section B: Beam Interactions with Materials and Atoms* 24-25 (Apr. 1987), pp. 18–25. DOI: 10.1016/0168-583x(87)90583-0.

[47] T. Stöhlker et al. “SPARC collaboration: new strategy for storage ring physics at FAIR.” In: *Hyperfine Interactions* 227.1-3 (Mar. 2014), pp. 45–53. DOI: 10.1007/s10751-014-1047-2.

[48] T. Katayama et al. “Antiproton chain of the FAIR storage rings.” In: *Physica Scripta* T166 (Nov. 2015), p. 014073. DOI: 10.1088/0031-8949/2015/t166/014073.

[49] E. Widmann. "Low-energy antiprotons physics and the FLAIR facility." In: *Physica Scripta* T166 (Nov. 2015), p. 014074. DOI: 10.1088/0031-8949/2015/t166/014074.

[50] H. Danared, A. Källberg, and A. Simonsson. "CRYRING at the LSR at FLAIR." In: *Hyperfine Interactions* 194.1-3 (Aug. 2009), pp. 129–135. DOI: 10.1007/s10751-009-0040-7.

[51] C. P. Welsch et al. "Ultra-low energy storage ring at FLAIR." In: *Hyperfine Interactions* 213.1-3 (Nov. 2011), pp. 205–215. DOI: 10.1007/s10751-011-0460-z.

[52] T. Morishita et al. "Proton-, antiproton-, and photon-He collisions in the context of ultra fast processes." In: *Photonic, Electronic and Atomic Collisions*. World Scientific, Nov. 2006. DOI: 10.1142/9789812772442_0070.

[53] J. Ullrich. "Sub-femtosecond correlated dynamics explored with antiprotons." In: *AIP Conference Proceedings*. AIP, 2005. DOI: 10.1063/1.2121971.

[54] A. I. Papash and C. P. Welsch. "Realization of nanosecond antiproton pulses in the ultra-low energy storage ring." In: *Nuclear Instruments and Methods in Physics Research Section A: Accelerators, Spectrometers, Detectors and Associated Equipment* 620.2-3 (Aug. 2010), pp. 128–141. DOI: 10.1016/j.nima.2010.03.153.

[55] G. Gaidos et al. "AIMStar: Antimatter initiated microfusion for pre-cursor interstellar missions." In: *AIP Conference Proceedings*. AIP, 1999. DOI: 10.1063/1.57674.

[56] A. Gsponer and J.-P. Hurni. "Antimatter induced fusion and thermonuclear explosions." In: *arXiv: Plasma Physics* (2005). DOI: 10.48550/ARXIV.PHYSICS/0507125.

[57] *ICAN-II concept.* https://science.nasa.gov/science-news/science-at-nasa/1997/msad12nov97_1.

[58] H. Wiedemann. *Particle Accelerator Physics*. Springer International Publishing, 2015. DOI: 10.1007/978-3-319-18317-6.

[59] *Optics of Charged Particles*. Elsevier, 1987. DOI: 10.1016/b978-0-12-762130-2.x5001-8.

[60] R. Garoby et al. "The European Spallation Source Design." In: *Physica Scripta* 93.1 (Dec. 2017), p. 014001. DOI: 10.1088/1402-4896/aa9bff.

[61] S. Y. Lee. *Accelerator Physics*. WORLD SCIENTIFIC, Jan. 2019. DOI: 10.1142/11111.

[62] K. Schindl. *Space charge*. en. 2006. DOI: 10.5170/CERN-2006-002.305.

[63] D. Sagan. "Bmad: A relativistic charged particle simulation library." In: *Nucl. Instrum. Meth.* A558.1 (2006), pp. 356–359. ISSN: 0168-9002. DOI: https://doi.org/10.1016/j.nima.2005.11.001.

[64] *MAD-X simulation tool*. http://mad.web.cern.ch/mad/.

[65] F. Schmidt, E. Forest, and E. McIntosh. *Introduction to the polymorphic tracking code: Fibre bundles, polymorphic Taylor types and "Exact tracking"*. Tech. rep. Geneva: CERN, July 2002. URL: http://cds.cern.ch/record/573082.

[66] T. J. Roberts and D. M. Kaplan. "G4beamline simulation program for matter-dominated beamlines." In: *2007 IEEE Particle Accelerator Conference (PAC)*. IEEE, 2007. DOI: 10.1109/pac.2007.4440461.

[67] S. Agostinelli et al. "Geant4—a simulation toolkit." In: *Nuclear Instruments and Methods in Physics Research Section A: Accelerators, Spectrometers, Detectors and Associated Equipment* 506.3 (July 2003), pp. 250–303. DOI: 10.1016/s0168-9002(03)01368-8.

[68] G. Floquet. "Sur la théorie des équations différentielles linéaires." In: *Annales Scientifiques De L Ecole Normale Superieure* 8 (), pp. 3–132.

[69] E. D. Courant and H. S. Snyder. "Theory of the alternating gradient synchrotron." In: *Annals Phys.* 3 (1958), pp. 1–48. DOI: 10.1016/0003-4916(58)90012-5.

[70] CERN Yellow Reports: Monographs. *CERN Yellow Reports: Monographs, Vol. 6 (2020): Linac4 design report*. en. 2020. DOI: 10.23731/CYRM-2020-006.

[71] J. A. MacLachlan. "Multiparticle Dynamics in the E-φ Tracking Code ESME." In: *AIP Conference Proceedings*. AIP, 2002. DOI: 10.1063/1.1522585.

[72] J. A. MacLachlan. "RF Capture in the NAL Booster." In: (May 1971).

[73] J. E. Griffin, J. A. Maclachlan, and Z. B. Qian. "RF Exercises Associated with Acceleration of Intense Antiproton Bunches at Fermilab." In: *IEEE Trans. Nucl. Sci.* 30 (1983). Ed. by L. S. Taylor, pp. 2627–2629. DOI: 10.1109/TNS.1983.4332905.

[74] J. E. Griffin et al. "Time and Momentum Exchange for Production and Collection of Intense Antiproton Beams at Fermilab." In: *IEEE Trans. Nucl. Sci.* 30 (1983). Ed. by L. S. Taylor, pp. 2630–2632. DOI: 10.1109/TNS.1983.4332906.

[75] R. Cappi et al. "Experiments to test beam behaviour under extreme space charge conditions." In: (June 1994), 4 p. URL: http://cds.cern.ch/record/265952.

[76] R. Garoby and S. Hancock. "New techniques for tailoring longitudinal density in a proton synchrotron." In: (July 1994), 4 p. URL: https://cds.cern.ch/record/265949.

[77] R. Garoby. "Bunch Merging and Splitting Techniques in the Injectors for High Energy Hadron Colliders." In: *17th International Conference on High-Energy Accelerators*. 1998.

[78] H. Damerau et al. "RF Manipulations for Special LHC-Type Beams in the CERN PS." en. In: *Proceedings of the 9th Int. Particle Accelerator Conf.* IPAC2018 (2018), Canada. DOI: 10.18429/JACOW-IPAC2018-WEPAF063.

[79] K. Li et al. “Code development for collective effects.” In: *ICFA Advanced Beam Dynamics Workshop on High-Intensity and High-Brightness Hadron Beams (HB2016)*. 2016, WEAM3X01.

[80] B. Zotter. “Betatron frequency shifts due to image and self fields.” In: (1985). DOI: 10.5170/CERN-1985-019-V-1.253. URL: https://cds.cern.ch/record/165143.

[81] K. Schindl. “Space charge.” In: *Joint US-CERN-Japan-Russia School on Particle Accelerators: Beam Measurement*. 1999.

[82] A. W. Chao. *Physics of collective beam instabilities in high-energy accelerators*. 1993. ISBN: 978-0-471-55184-3.

[83] K. Y. Ng. “Physics of Intensity Dependent Beam Instabilities.” In: *U.S. Particle Accelerator School (USPAS 2002)*. Apr. 2002.

[84] L. Teng. “Primer on beam dynamics in synchrotrons.” In: *AIP Conference Proceedings* 184.2 (1989), pp. 1878–1909. DOI: 10.1063/1.38030. URL: https://aip.scitation.org/doi/abs/10.1063/1.38030.

[85] C. Bhat, L. K. Spentzouris, and P. L. Colestock. “Measurements of intrabeam scattering rates below transition in the Fermilab Antiproton Accumulator.” In: *Proceedings of the 1999 Particle Accelerator Conference (Cat. No.99CH36366)*. Vol. 5. 1999, 3155–3157 vol.5. DOI: 10.1109/PAC.1999.792234.

[86] W. Fischer et al. “Measurements of intra-beam scattering growth times with gold beam below transition in RHIC.” In: (June 2001). URL: https://www.osti.gov/biblio/782957.

[87] P. Zenkevich. “Last advances in analysis of intra-beam scattering in the hadron storage rings.” In: *Nuclear Instruments and Methods in Physics Research Section A: Accelerators, Spectrometers, Detectors and Associated Equipment* 577.1-2 (July 2007), pp. 110–116. DOI: 10.1016/j.nima.2007.02.041.

[88] A. Piwinski. "Intra-beam scattering." In: *Frontiers of Particle Beams*. Ed. by M. Month and S. Turner. Berlin, Heidelberg: Springer Berlin Heidelberg, 1988, pp. 297–309. ISBN: 978-3-540-38935-4.

[89] M. Martini. *Intrabeam scattering in the ACOL-AA machines*. Tech. rep. Geneva: CERN, 1984. URL: https://cds.cern.ch/record/151638.

[90] J. D. Bjorken and S. K. Mtingwa. "Intrabeam Scattering." In: *Part. Accel.* 13 (1983), pp. 115–143.

[91] M. Martini, F. Antoniou, and Y. Papaphilippou. "Intrabeam Scattering." In: *ICFA Beam Dyn. Newslett.* 69 (2016), pp. 38–59.

[92] G. Moliere. "Theorie der Streuung schneller geladener Teilchen II Mehrfach-und Vielfachstreuung." In: *Zeitschrift für Naturforschung A* 3.2 (Feb. 1948), pp. 78–97. DOI: 10.1515/zna-1948-0203.

[93] K. L. F. Bane. "An Accurate, simplified model of intrabeam scattering." In: (May 2002). arXiv: physics/0205058.

[94] S. van der Meer. *Stochastic damping of betatron oscillations in the ISR*. Tech. rep. Geneva: CERN, Aug. 1972. URL: https://cds.cern.ch/record/312939.

[95] S. van der Meer. "Stochastic cooling and the accumulation of antiprotons." In: *Rev. Mod. Phys.* 57 (3 July 1985), pp. 689–697. DOI: 10.1103/RevModPhys.57.689. URL: https://link.aps.org/doi/10.1103/RevModPhys.57.689.

[96] J. Eschner et al. "Laser cooling of trapped ions." In: *Journal of the Optical Society of America B* 20.5 (May 2003), p. 1003. DOI: 10.1364/josab.20.001003.

[97] G. I. Budker. "An effective method of damping particle oscillations in proton and antiproton storage rings." In: *Soviet Atomic Energy* 22.5 (May 1967), pp. 438–440. DOI: 10.1007/bf01175204.

[98] Ya. S. Derbenev and A. N. Skrinsky. "The Physics of Electron Cooling." In: *Sov. Sci. Rev. A* 3 (1981), pp. 165–238.

[99] H. Poth. "Electron cooling: Theory, experiment, application." In: *Physics Reports* 196.3-4 (Nov. 1990), pp. 135–297. DOI: 10.1016/0370-1573(90)90040-9.

[100] I. N. Meshkov. "Electron cooling: Status and perspectives." In: *Phys. Part. Nucl.* 25 (1994), pp. 631–661.

[101] I. Meshkov. "Electron cooling — recent developments and trends." In: *Nuclear Physics A* 626.1-2 (Nov. 1997), pp. 459–471. DOI: 10.1016/s0375-9474(97)00570-8.

[102] A. Sidorin and A. Smirnov. "BETACOOL Code." In: *ICFA Beam Dyn. Newslett.* 65 (2014), pp. 127–135.

[103] V. V. Parkhomchuk. "New insights in the theory of electron cooling." In: *Nuclear Instruments and Methods in Physics Research Section A: Accelerators, Spectrometers, Detectors and Associated Equipment* 441.1-2 (Feb. 2000), pp. 9–17. DOI: 10.1016/s0168-9002(99)01100-6.

[104] V. V. Parkhomchuk and A. N. Skrinsky. "Cooling Methods for Charged Particle Beams." In: *Reviews of Accelerator Science and Technology* 01.01 (Jan. 2008), pp. 237–257. DOI: 10.1142/s1793626808000150.

[105] J. Resta-López, J. R. Hunt, and C. P. Welsch. "Non-Gaussian beam dynamics in low energy antiproton storage rings." In: *Nuclear Instruments and Methods in Physics Research Section A: Accelerators, Spectrometers, Detectors and Associated Equipment* 834 (Oct. 2016), pp. 123–131. DOI: 10.1016/j.nima.2016.08.003.

[106] J. Resta-López et al. "Simulation studies of the beam cooling process in presence of heating effects in the Extra Low ENergy Antiproton ring (ELENA)." In: *Journal of Instrumentation* 10.05 (May 2015), P05012–P05012. DOI: 10.1088/1748-0221/10/05/p05012.

[107] I. Ben-Zvi. "High-Current ERL-Based Electron Cooling System for RHIC." In: *AIP Conference Proceedings*. AIP, 2006. DOI: 10.1063/1.2190095.

[108] V. Bocharov. "Precise Measurements of a Magnetic Field at the Solenoids for Low Energy Coolers." In: *AIP Conference Proceedings*. AIP, 2006. DOI: 10.1063/1.2190135.

[109] M. I. Bryzgunov et al. "System for Measurement of Magnetic Field Line Straightness in Solenoid of Electron Cooler for COSY." In: *Proc. 8th Workshop on Beam Cooling and Related Topics (COOL'11)* (Alushta, Ukraine). JACoW Publishing, Sept. 2011, pp. 107–110.

[110] A. V. Bubley et al. "Compass for Measuring the Magnetic Lines Straightness at the Cooling Section in Vacuum." In: *Proc. 9th Workshop on Beam Cooling and Related Topics (COOL'13)* (Mürren, Switzerland). JACoW Publishing, June 2013, pp. 121–123.

[111] A. Bubley et al. "Low Energy Electron Cooler for the NICA Booster." en. In: *Proceedings of the 11th Workshop on Beam Cooling and Related Topics* COOL2017 (2018), Germany. DOI: 10.18429/JACOW-COOL2017-TUM11.

[112] L. Gr. Ixaru and G. V. Berghe. "Runge-Kutta Solvers for Ordinary Differential Equations." In: *Exponential Fitting*. Springer Netherlands, 2004, pp. 223–304. DOI: 10.1007/978-1-4020-2100-8_6.

[113] *MAD8 Physics Guide*. http://mad8.web.cern.ch/mad8/doc/phys_guide.pdf.

[114] L. Bojtár. "Efficient evaluation of arbitrary static electromagnetic fields with applications for symplectic particle tracking." In: *Nuclear Instruments and Methods in Physics Research Section A: Accelerators, Spectrometers, Detectors and Associated Equipment* 948 (Dec. 2019), p. 162841. DOI: 10.1016/j.nima.2019.162841.

[115] H.-S. Mao and R. Wirz. "Comparison of Charged Particle Tracking Methods for Non-Uniform Magnetic Fields." In: *42nd AIAA Plasmadynamics and Lasers*

Conference. American Institute of Aeronautics and Astronautics, June 2011. DOI: 10.2514/6.2011-3739.

[116] S. P. Møller. "ELISA, and electrostatic storage ring for atomic physics." In: *Nuclear Instruments and Methods in Physics Research Section A: Accelerators, Spectrometers, Detectors and Associated Equipment* 394.3 (July 1997), pp. 281–286. DOI: 10.1016/s0168-9002(97)00673-6.

[117] M. O. A. El Ghazaly. "ELASR – An electrostatic storage ring for atomic and molecular physics at KACST." In: *Results in Physics* 5 (2015), pp. 60–61. DOI: 10.1016/j.rinp.2015.02.001.

[118] D. Krasnicky et al. "AEgIS experiment commissioning at CERN." In: AIP, 2013. DOI: 10.1063/1.4796070.

[119] H. H. Andersen et al. "An apparatus to measure stopping powers for low-energy antiprotons and protons." In: *Nuclear Instruments and Methods in Physics Research Section B: Beam Interactions with Materials and Atoms* 194.3 (Sept. 2002), pp. 217–225. DOI: 10.1016/s0168-583x(02)00692-4.

[120] M. A. Laughton. *Electrical engineer's reference book*. Oxford England Boston: Newnes, 2003. ISBN: 9780750646376.

[121] H. Liebl. *Applied Charged Particle Optics*. Springer Berlin Heidelberg, 2008. DOI: 10.1007/978-3-540-71925-0.

[122] B. Ripperda et al. "A Comprehensive Comparison of Relativistic Particle Integrators." In: *The Astrophysical Journal Supplement Series* 235.1 (Mar. 2018), p. 21. DOI: 10.3847/1538-4365/aab114.

[123] *Numerical Simulations*. https://indico.cern.ch/event/885370/contributions/3732425/attachments/1982938/3303395/008_spring_campus_GI_part1.pdf.

[124] J. Jentzsch et al. “Beam Dynamics Studies of the ELENA Electrostatic Transfer Lines in the Presence of Magnetic Stray Fields.” en. In: *Proceedings of the 7th Int. Particle Accelerator Conf.* IPAC2016 (2016), Korea.

[125] G. de Rijk. *Warm Magnets*. Tech. rep. 20 pages, contribution to the CAS - CERN Accelerator School: Introduction to Accelerator Physics. 2021. arXiv: 2107.03965. URL: http://cds.cern.ch/record/2775676.

[126] H. A. Enge. “Effect of Extended Fringing Fields on Ion-Focusing Properties of Deflecting Magnets.” In: *Review of Scientific Instruments* 35.3 (Mar. 1964), pp. 278–287. DOI: 10.1063/1.1718806.

[127] B. D. Muratori, J. K. Jones, and A. Wolski. “Analytical expressions for fringe fields in multipole magnets.” In: *Physical Review Special Topics - Accelerators and Beams* 18.6 (June 2015). DOI: 10.1103/physrevstab.18.064001.

[128] A. Kainz et al. “Distortion-free measurement of electric field strength with a MEMS sensor.” In: *Nature Electronics* 1.1 (2018), p. 68. DOI: 10.1038/s41928-017-0009-5.

[129] *ZQNA sketch*. https://edms.cern.ch/ui/#!master/navigator/document?D:1555815044:1555815044:subDocs.

[130] A. Kainz et al. “Noninvasive 3D Field Mapping of Complex Static Electric Fields.” In: *Physical Review Letters* 122.24 (June 2019). DOI: 10.1103/physrevlett.122.244801.

[131] COMSOL Multiphysics. “Introduction to COMSOL multiphysics®.” In: *COMSOL Multiphysics, Burlington, MA, accessed Feb* 9 (1998), p. 2018.

[132] A. Kainz et al. “Passive optomechanical electric field strength sensor with built-in vibration suppression.” In: *Applied Physics Letters* 113.14 (2018), p. 143505. DOI: 10.1063/1.5045614. eprint: https://doi.org/10.1063/1.5045614. URL: https://doi.org/10.1063/1.5045614.

[133] L. D. Landau, E. M. Lifshitz, and L. P. Pitaevskii. *Electrodynamics of Continuous Media*. Elsevier Science Technology, Oct. 15, 1984. 480 pp. ISBN: 0750626348.

[134] R. S. Popovic. *Hall Effect Devices, section 5.6, Incorporating a Hall device into a circuit*. Institute of Physics Publishing Bristol and Philadelphia, 2004.

[135] *Feasibility Study for an EDM Storage Ring*. https://indico.cern.ch/event/765096/contributions/3295545/. 2018.

[136] D. Eversmann et al. "New Method for a Continuous Determination of the Spin Tune in Storage Rings and Implications for Precision Experiments." In: *Phys. Rev. Lett.* 115 (9 Aug. 2015), p. 094801. DOI: 10.1103/PhysRevLett.115.094801. URL: https://link.aps.org/doi/10.1103/PhysRevLett.115.094801.

[137] *Transfer Lines Repository*. https://gitlab.cern.ch/acc-models/acc-models-tls/-/tree/4a2306bda3a3ecdf7790448a9e6272be9868d90b/elena_extraction.

[138] J. R. Hunt. "Beam Quality Characterisation and the Optimisation of Next Generation Antimatter Facilities." In: (2019). DOI: 10.17638/03039086.

[139] L. J. Nevay et al. "BDSIM: An accelerator tracking code with particle–matter interactions." In: *Computer Physics Communications* 252 (July 2020), p. 107200. DOI: 10.1016/j.cpc.2020.107200.

[140] C. Ahdida et al. "Measurement of the muon flux from 400 GeV/c protons interacting in a thick molybdenum/tungsten target." In: *The European Physical Journal C* 80.3 (Mar. 2020). DOI: 10.1140/epjc/s10052-020-7788-y.

[141] A. Mereghetti et al. "The FLUKA LineBuilder and Element DataBase: Tools for Building Complex Models of Accelerator Beam Lines." In: *Conf. Proc. C* 1205201 (2012). Ed. by Vic Suller, pp. 2687–2689.

[142] S. Aghion et al. "Measurement of antiproton annihilation on Cu, Ag and Au with emulsion films." In: *JINST* 12.04 (2017), P04021. DOI: 10.1088/1748-0221/12/04/P04021. arXiv: 1701.06306 [hep-ex].

[143] S. Chauvie, P. Nieminen, and M. G. Pia. "Geant4 model for the stopping power of low energy negatively charged hadrons." In: *2006 IEEE Nuclear Science Symposium Conference Record*. IEEE, 2006. DOI: 10.1109/nssmic.2006.356235.

[144] MATLAB. *version 7.10.0 (R2010a)*. Natick, Massachusetts: The MathWorks Inc., 2010.

[145] J. Borburgh et al. "Concept for ELENA Extraction and Beam Transfer Elements." In: *Conf. Proc.* C130512 (July 2013), MOPFI061. 4 p. URL: https://cds.cern.ch/record/1574727.

[146] *Electrostatic Deflectors*. https://edms5.cern.ch/cdd/plsql/c4w.equip_list?cookie=2714623&p_cat_id=Z.

[147] *Transfer Lines CERN Report*. https://indico.cern.ch/event/497132/contributions/2017582/attachments/1230820/1804122/LNA-LJ-ES-0001-00-40.pdf.

[148] S. Boogert et al. "Pyg4ometry : A Tool to Create Geometries for Geant4, BDSIM, G4Beamline and FLUKA for Particle Loss and Energy Deposit Studies." en. In: *Proceedings of the 10th Int. Particle Accelerator Conf.* IPAC2019 (2019), Australia. DOI: 10.18429/JACOW-IPAC2019-WEPTS054.

[149] J. R. Hunt et al. "Novel transverse emittance measurements for electron cooling characterization." In: *Physical Review Accelerators and Beams* 23.3 (Mar. 2020). DOI: 10.1103/physrevaccelbeams.23.032802.

[150] D. Gamba et al. "AD/ELENA Electron Cooling Experience During and after CERNs Long Shutdown (LS2)." en. In: *Proceedings of the 13th International Workshop on Beam Cooling and Related Topics* COOL2021 (2021), Russia. DOI: 10.18429/JACOW-COOL2021-S503.

[151] *PyTao software*. https://bmad-sim.github.io/pytao/.

[152] W. H. Press et al. *Numerical Recipes*. Cambridge University Pr., Sept. 6, 2007. 1248 pp. ISBN: 0521880688. URL: https://www.ebook.de/de/product/6504686/william_h_press_saul_a_teukolsky_william_t_vetterling_brian_p_flannery_numerical_recipes.html.

[153] R. Storn and K. Price. In: *Journal of Global Optimization* 11.4 (1997), pp. 341–359. DOI: 10.1023/a:1008202821328.

[154] K. Nordlund. "Slowing down of 100 keV antiprotons in Al foils." In: *Results in Physics* 8 (Mar. 2018), pp. 683–685. DOI: 10.1016/j.rinp.2017.12.073.

[155] V. Rodin et al. "Multi-objective Optimization of 3D Beam Tracking in Electrostatic Beamlines." In: *10th International Particle Accelerator Conference*. 2019, WEPTS060. DOI: 10.18429/JACoW-IPAC2019-WEPTS060.

[156] *HistoRoot software*. http://www.muonsinternal.com/muons3/HistoRoot.

[157] *Matlab Runtime*. https://uk.mathworks.com/products/compiler/matlab-runtime.html.

[158] J. C. Simpson et al. "Simple Analytic Expressions for the Magnetic Field of a Circular Current Loop." In: 2001.

[159] V. Rodin et al. "Realistic Simulations of Stray Field Impact on Low Energy Transfer Lines." en. In: *Proceedings of the 12th International Particle Accelerator Conference* IPAC2021 (2021), Brazil. DOI: 10.18429/JACOW-IPAC2021-WEPAB214.

[160] *Magnetic Field of Earth*. https://www.ngdc.noaa.gov/geomag/WMM/.

[161] T. Bryś et al. "Magnetic field stabilization for magnetically shielded volumes by external field coils." In: *Nuclear Instruments and Methods in Physics Research Section A: Accelerators, Spectrometers, Detectors and Associated Equipment* 554.1-3 (Dec. 2005), pp. 527–539. DOI: 10.1016/j.nima.2005.08.040.

[162] C. Holmlund et al. “Novel Concepts in Magnetic Shielding.” In: (Dec. 2001). DOI: 10.1.1.4.5448.

[163] V. Kelha et al. “Design, construction, and performance of a large-volume magnetic shield.” In: *IEEE Transactions on Magnetics* 18.1 (1982), pp. 260–270. DOI: 10.1109/TMAG.1982.1061780.

[164] R. M. Faradzhaev et al. “Performances investigation and material selection of PMT magnetic shields for the space experiments with GRIS and PING-M instruments.” In: *Journal of Physics: Conference Series* 675.4 (Feb. 2016), p. 042008. DOI: 10.1088/1742-6596/675/4/042008.

[165] E. Harting. *Electrostatic lenses*. Amsterdam New York: Elsevier Scientific Pub. Co, 1976. ISBN: 9780444413192.

[166] M. Ferrario, D. Alesini, et al. “Experimental Demonstration of Emittance Compensation with Velocity Bunching.” In: *Phys. Rev. Lett.* 104 (5 Feb. 2010), p. 054801. DOI: 10.1103/PhysRevLett.104.054801. URL: https://link.aps.org/doi/10.1103/PhysRevLett.104.054801.

[167] https://www.hitachi-metals.co.jp.

[168] C. Ohmori et al. “RF systems for JHF synchrotrons.” In: *Conf. Proc. C* 9803233 (1998). Ed. by Y.H. Chin et al., p. 602.

[169] M. Paoluzzi et al. “The new 1-18 MHz wideband RF system for the CERN PS Booster.” In: CERN-ACC-2019-120 (2019), WEPRB107. 3 p. DOI: 10.18429/JACoW-IPAC2019-WEPRB107. URL: http://cds.cern.ch/record/2693249.

[170] M. E. Angoletta et al. “A new digital Low-Level RF and longitudinal diagnostic system for CERN’s AD.” In: *10th International Particle Accelerator Conference*. 2019, THPRB070. DOI: 10.18429/JACoW-IPAC2019-THPRB070.

[171] C. Ohmori, M. Aoki, et al. "Ultra-High Field Gradient RF for Bunch Rotation." In: *Nuclear Physics B - Proceedings Supplements* 149 (2005). NuFact04, pp. 280–282. ISSN: 0920-5632. DOI: https://doi.org/10.1016/j.nuclphysbps.2005.05.046. URL: http://www.sciencedirect.com/science/article/pii/S0920563205007140.

[172] C. Ohmori. "A magnetic alloy loaded RF cavity system for EMMA." In: *IPAC 2010 - 1st International Particle Accelerator Conference* (May 2010), pp. 3714–3716.

[173] M. Bassetti and G. A. Erskine. "Closed Expression for the Electrical Field of a Two-dimensional Gaussian Charge." In: (Mar. 1980).

[174] V. Kornilov et al. "Beam quality and beam loss predictions with space charge for SIS100." In: *Journal of Instrumentation* 15.07 (July 2020), P07020–P07020. DOI: 10.1088/1748-0221/15/07/p07020.

[175] A. Oeftiger et al. "Simulation study of the space charge limit in heavy-ion synchrotrons." In: *Physical Review Accelerators and Beams* 25.5 (May 2022), p. 054402. DOI: 10.1103/physrevaccelbeams.25.054402.

[176] C. Mayes, Ryne R., and D. Sagan. "3D Space Charge in Bmad." In: *9th International Particle Accelerator Conference*. 2018, THPAK085. DOI: 10.18429/JACoW-IPAC2018-THPAK085.

[177] I. Hofmann and O. Boine-Frankenheim. "Grid dependent noise and entropy growth in anisotropic 3d particle-in-cell simulation of high intensity beams." In: *Phys. Rev. ST Accel. Beams* 17 (2014), p. 124201. DOI: 10.1103/PhysRevSTAB.17.124201. arXiv: 1405.4153 [physics.acc-ph].

[178] Y.-S. Yuan, O. Boine-Frankenheim, and I. Hofmann. "Intensity limitations due to space charge for bunch compression in synchrotrons." In: *Phys. Rev. Accel. Beams* 21.7 (2018), p. 074201. DOI: 10.1103/PhysRevAccelBeams.21.074201.

[179] D. Schoerling. "Case study of a magnetic system for low-energy machines." In: *Phys. Rev. Accel. Beams* 19 (8 Aug. 2016), p. 082401. DOI: 10.1103/PhysRevAccelBeams.19.082401. URL: https://link.aps.org/doi/10.1103/PhysRevAccelBeams.19.082401.

[180] *Design Report: ELENA Bending Magnet.* https://edms.cern.ch/file/1311860/2.0/LNA-MBHEK-ER-0001-20-00.pdf.

[181] *Magnetic measurements in ELENA ring.* https://indico.cern.ch/event/638836/contributions/2589330/attachments/1457587/2250374/MM_on_MBR_MQ_correctors_for_elena_Fiscarelli_a.pdf.

[182] A. O. Sidorin, I. N. Meshkov, et al. "BETACOOL program for simulation of beam dynamics in storage rings." In: *Nuclear Instruments and Methods in Physics Research Section A: Accelerators, Spectrometers, Detectors and Associated Equipment* 558.1 (2006). Proceedings of the 8th International Computational Accelerator Physics Conference, pp. 325–328. ISSN: 0168-9002. DOI: https://doi.org/10.1016/j.nima.2005.11.041. URL: http://www.sciencedirect.com/science/article/pii/S0168900205021479.

[183] J. R. Hunt et al. "Novel transverse emittance measurements for electron cooling characterization." In: *Phys. Rev. Accel. Beams* 23 (3 Mar. 2020), p. 032802. DOI: 10.1103/PhysRevAccelBeams.23.032802. URL: https://link.aps.org/doi/10.1103/PhysRevAccelBeams.23.032802.

[184] A. I. Papash, A. V. Smirnov, and C. P. Welsch. "Nonlinear and long-term beam dynamics in low energy storage rings." In: *Phys. Rev. ST Accel. Beams* 16 (6 June 2013), p. 060101. DOI: 10.1103/PhysRevSTAB.16.060101. URL: https://link.aps.org/doi/10.1103/PhysRevSTAB.16.060101.

[185] V. V. Parkhomchuk. "New insights in the theory of electron cooling." In: *Nuclear Instruments and Methods in Physics Research Section A: Accelerators, Spectrometers, Detectors and Associated Equipment* 441.1 (2000), pp. 9–17. ISSN:

0168-9002. DOI: https://doi.org/10.1016/S0168-9002(99)01100-6. URL: http://www.sciencedirect.com/science/article/pii/S0168900299011006.

[186] M. Martini. *Intrabeam Scattering*. https://indico.cern.ch/event/362960/contributions/1776154/attachments/1178496/1715142/Slides.pdf. Accessed: 2021–05-26. 2017.

[187] N. Petridis et al. "Energy loss and cooling of relativistic highly charged uranium ions interacting with an internal hydrogen droplet target beam." In: *Nucl. Instrum. Meth. A* 656 (2011), pp. 1–4. DOI: 10.1016/j.nima.2011.07.035.

[188] T. Kirchner and H. Knudsen. "Current status of antiproton impact ionization of atoms and molecules: theoretical and experimental perspectives." In: *Journal of Physics B: Atomic, Molecular and Optical Physics* 44.12 (June 2011), p. 122001. DOI: 10.1088/0953-4075/44/12/122001.

[189] V. Godinho et al. "Characterization and Validation of a-Si Magnetron-Sputtered Thin Films as Solid He Targets with High Stability for Nuclear Reactions." In: *ACS Omega* 1.6 (Dec. 2016), pp. 1229–1238. DOI: 10.1021/acsomega.6b00270.

[190] "Stopping of Ions Heavier than Helium: CONTENTS." In: *Journal of the International Commission on Radiation Units and Measurements* 5.1 (June 2005), pp. iii–viii. ISSN: 1473-6691. DOI: 10.1093/jicru/ndi002. eprint: https://academic.oup.com/jicru/article-pdf/5/1/iii/2523831/ndi002.pdf. URL: https://doi.org/10.1093/jicru/ndi002.

[191] L. H. Andersen et al. "Measurement of the Z_1^3 contribution to the stopping power using MeV protons and antiprotons: The Barkas effect." In: *Phys. Rev. Lett.* 62 (15 Apr. 1989), pp. 1731–1734. DOI: 10.1103/PhysRevLett.62.1731. URL: https://link.aps.org/doi/10.1103/PhysRevLett.62.1731.

[192] *Hadron and Ion Ionisation in Geant4*. https://geant4-userdoc.web.cern.ch/UsersGuides/PhysicsReferenceManual/html/electromagnetic/charged_hadron_incident/hion.html.

[193] R. E. Olson and A. Salop. "Charge-transfer and impact-ionization cross sections for fully and partially stripped positive ions colliding with atomic hydrogen." In: *Physical Review A* 16.2 (Aug. 1977), pp. 531–541. DOI: 10.1103/physreva.16.531.

[194] D. S. F. Crothers and J. F. McCann. "Ionisation of atoms by ion impact." In: *Journal of Physics B: Atomic and Molecular Physics* 16.17 (Sept. 1983), pp. 3229–3242. DOI: 10.1088/0022-3700/16/17/015.

[195] P. D. Fainstein and V. D. Rodríguez. "Mean recoil-ion and electron longitudinal momentum in He single ionization by proton and antiproton impact." In: *Journal of Physics B: Atomic, Molecular and Optical Physics* 33.21 (Oct. 2000), pp. 4637–4645. DOI: 10.1088/0953-4075/33/21/309.

[196] R. Dorner et al. "Three-body final-state momentum distributions for swift Hsup/supand Hesup2/supon He collisions." In: *Journal of Physics B: Atomic, Molecular and Optical Physics* 28.3 (Feb. 1995), pp. 435–444. DOI: 10.1088/0953-4075/28/3/014.

[197] S. D. Kravis et al. "Single ionization of He by low-velocity protons and C^{6+}: Ejected electron momentum distributions." In: *Phys. Rev. A* 54 (2 Aug. 1996), pp. 1394–1403. DOI: 10.1103/PhysRevA.54.1394. URL: https://link.aps.org/doi/10.1103/PhysRevA.54.1394.

[198] L. Duvillaret, S. Rialland, and J.-L. Coutaz. "Electro-optic sensors for electric field measurements II Choice of the crystals and complete optimization of their orientation." In: *Journal of the Optical Society of America B* 19.11 (Nov. 2002), p. 2704. DOI: 10.1364/josab.19.002704.

[199] L. Sun, S. Jiang, and J. R. Marciante. "All-fiber optical magnetic-field sensor based on Faraday rotation in highly terbium-doped fiber." In: *Optics Express* 18.6 (Mar. 2010), p. 5407. DOI: 10.1364/oe.18.005407.

[200] A. Bamberger et al. “Observation of antiprotonic atoms.” In: *Physics Letters B* 33.3 (Oct. 1970), pp. 233–235. DOI: 10.1016/0370-2693(70)90582-4.

[201] M. Doser. “Antiprotonic bound systems.” In: *Progress in Particle and Nuclear Physics* 125 (July 2022), p. 103964. DOI: 10.1016/j.ppnp.2022.103964.

[202] G. Franchetti et al. “Space charge effects on the third order coupled resonance.” In: *Physical Review Accelerators and Beams* 20.8 (Aug. 2017), p. 081006. DOI: 10.1103/physrevaccelbeams.20.081006.

[203] M. Tanaka and M. Murakami. “Relativistic and electromagnetic molecular dynamics simulations for a carbon-gold nanotube accelerator.” In: *Computer Physics Communications* 241 (Aug. 2019), pp. 56–63. DOI: 10.1016/j.cpc.2019.03.012.